Understanding the nature of fluctuations in the edge of I-mode and L-mode plasmas at ASDEX Upgrade

by

Rachel S. Bielajew

B.S.E., University of Michigan (2014)

Submitted to the Department of Nuclear Science and Engineering
in partial fulfillment of the requirements for the degree of

DOCTOR OF PHILOSOPHY IN NUCLEAR SCIENCE AND ENGINEERING

at the

MASSACHUSETTS INSTITUTE OF TECHNOLOGY

February 2024

Authored by: Rachel S. Bielajew
Department of Nuclear Science and Engineering
December 4, 2023

Certified by: Anne E. White
Vice Provost and Associate Vice President for Research Administration
Thesis Supervisor

Accepted by: Ju Li
Battelle Energy Alliance Professor of Nuclear Science and Engineering
Chairman, Department Committee on Graduate Theses

Understanding the nature of fluctuations in the edge of I-mode and L-mode plasmas at ASDEX Upgrade

by

Rachel S. Bielajew

Submitted to the Department of Nuclear Science and Engineering
on December 4, 2023 in partial fulfillment of the requirements for the degree of

DOCTOR OF PHILOSOPHY IN NUCLEAR SCIENCE AND ENGINEERING

ABSTRACT

Changes in turbulence at the plasma edge are thought to lead to the formation of the edge transport barrier in tokamak plasmas, which defines the transition from low confinement (L-mode) to high confinement operation such as H-mode or the "improved" confinement regime I-mode. I-mode is of particular interest for future reactor operation because its unique transport barrier in heat but not particles prevents impurity accumulation and keeps the I-mode edge away from instability boundaries which lead to damaging Edge-Localized Modes. The mechanism for the formation of the edge transport barrier is an open question across high confinement regimes. The unique transport barrier formed in I-mode, with separated heat and particle transport channels, must be understood. This thesis explores fluctuations in the edge region of plasmas at ASDEX Upgrade (AUG) to better understand how changes in fluctuations relate to changes in transport between L and I-mode, as well as L-modes across different magnetic configurations (favorable and unfavorable ∇B drift). An extensive turbulence diagnostic suite at AUG is used for experimental exploration of edge turbulence, with special focus on measurements of radiated temperature (T_{rad}) fluctuations from the Correlation Electron Cyclotron Emission diagnostic.

Comparative studies of L-mode and I-mode edge turbulence reveal that the Weakly Coherent Mode (WCM), previously considered a marker of I-mode, is present in both regimes. The WCM is present across a wide parameter space of collisionality in both L-mode and I-mode. The presence of the WCM and its T_e fluctuation amplitude are not correlated with the quality of the global confinement. Properties of the WCM are compared in detail between L and I-mode, with a focus on unfavorable ∇B drift plasmas. While some properties of the WCM are consistent between L and I-mode, such as its wavenumbers and radial location, other WCM properties change between the confinement regimes, such as its coupling to a low frequency edge oscillation. Additionally, studies of matched L-modes in favorable and unfavorable ∇B drift magnetic configurations show that the WCM can form in L-modes of both magnetic configurations, and that its onset can occur even at power levels far below the L to I-mode and L to H-mode transition. While the nature of fluctuations in the edge of the matched plasmas is seen to be dominated by a WCM-like feature in both the favorable and unfavorable configurations, differences in turbulence damping from $E \times B$ velocity shear and the resulting differences in turbulence fluctuation amplitude seem to play into the different H-mode power threshold between the configurations. In addition to these experimental studies, gyrokinetic studies of the L-mode and I-mode are performed at radial locations inside the transport barrier region, with a focus on the outer core. These gyrokinetic studies reveal that the nature of L-mode and I-mode turbulence is very similar in the outer core in terms of the identities of instabilities present, and the response of turbulent heat flux to changes in gradient drives. The fluctuations associated with the I-mode WCM are not inconsistent with the edge transport required for the unique I-mode transport barrier in heat and not particles, however, the presence of the WCM in L-mode shows that this fluctuation is not a unique marker of I-mode. These findings improve our understanding of I-mode phenomenology overall, which is important for its extrapolation to future reactors.

Thesis supervisor: Anne E. White
Title: Vice Provost and Associate Vice President for Research Administration

Acknowledgments

I would not have been able to complete this work without incredible support along the way. I feel very lucky to have been surrounded by so many wonderful people during my PhD journey.

First, I would like to thank my advisor, Professor Anne White. Anne provided invaluable scientific guidance and professional support. She has been an example to me of what a good scientist, leader, and advisor look like. I could not have asked for a better mentor.

I would like to express sincere gratitude to Dr. Garrard Conway for his mentorship throughout my PhD. I have learned so much from Garrard, and am so thankful that he was always willing to share his immense scientific and technical expertise. I also thank Garrard for serving as my thesis reader.

I would like to thank Dr. Pablo Rodriguez-Fernandez for his guidance on this thesis, and my other scientific contributions during the PhD. Pablo's support has ranged from guiding my scientific questions to troubleshooting computing workflows. I thank him for his incredibly patient and consistent support.

I am very grateful to the rest of the CECE team for making this work possible. I thank Willy Burke for his engineering expertise, and for implementing our seemingly consistent stream of diagnostic upgrades. I thank Dr. Branka Vanovac the many good discussions on science and hardware, and deeply appreciate her insightful questions. Branka's friendship helped make stays at IPP fun and productive. I also thank Christian Yoo his development of CECE workflows as well as his friendship along the way.

A number of scientists at the PSFC have had a significant impact on my work, and I am grateful for the opportunity to learn from and work with them. I would like to thank Dr. Nathan Howard for sharing his knowledge of transport simulations with me. I so appreciate the many hours he has spent helping me understand the intricacies of running CGYRO and interpreting results. I would also like to thank Dr. Peter Catto for being such a wonderful teacher over the last two years of my PhD. I have enjoyed learning about neoclassical physics from him, and appreciate Peter's endless patience as I grappled with new topics. I would also like to acknowledge Dr. Amanda Hubbard for her guidance and sharing her knowledge with me. Our discussions of edge turbulence and I-mode have been so valuable to my learning.

In addition to the PSFC, I have received immense support from the ASDEX Upgrade team. In particular, I would like to thank Dr. Tim Happel for sharing his I-mode expertise and guidance, Dr. Ulrike Plank for helping me learn about H-mode transitions, Dr. Davide Silvagni for help with experimental design, and Dr. Michael Griener and Dr. Takashi Nishizawa for providing and analyzing thermal He beam data. I am grateful to have gained experimental experience with a team so supportive of students, and my time at IPP was an incredible learning experience.

The staff in NSE and at the PSFC have helped me get so much done during my time in grad school. In particular, I would like to thank Valerie Censabella for helping with all the purchasing for CECE diagnostic upgrades, and for making sure all my travel to IPP went smoothly.

I am thankful for the community of students at the PSFC who have provided me with friendship and camaraderie along the way. Christina, Evan, and Richard - you were the best cohort with whom to do all this. I am also so grateful for the support and friendship of Audrey, Will, Abhi, and the many other friendly faces of NW17 and NW16.

Outside of lab, I am so fortunate for my wonderful support network. Tally and Francesca, thank you for being such steadfast friends and for all the dog walks and shared meals. Allayna and Morgan, thank you for sending me so much love from afar. To my siblings Ben, Liz, and Lexi and my parents Karen and Alex, your unwavering support has gotten me here. Finally, to Kade (and Dobby and Winky), thank you for being there and cheering me on during every step of this process.

Contents

List of Figures

List of Tables

Chapter 1

Introduction

Fusion energy holds great potential as a carbon free energy source. The hydrogen isotopes which fuel fusion reactions are derived from abundant materials on Earth. Other merits of fusion include the lack of long-lived radioactive waste and the potential for reliable energy generation that could meet baseload electricity needs. However, fusion faces technological challenges which have so far prevented its realization as a viable energy source. Research at fusion experiments around the world aims to develop the scientific understanding needed to deploy fusion as an energy source and move fusion along the pathway to commercialization.

The tokamak fusion scheme has been the focus of a significant portion of fusion energy research efforts over the past 60 years, and this scheme is currently closest to commercialization. A tokamak uses strong magnetic fields to confine a plasma in a torus shape. Due to the Lorentz force, charged particles comprising the plasma follow helical orbits around magnetic field lines, shown in Figure 1.1. A temperature of roughly one million Kelvin is needed in order for the plasma ions to overcome Coulomb repulsion and undergo fusion reactions. Therefore, external heating is applied to achieve very high temperatures in the plasma core.

One criterion for the success of fusion is the achievement of “breakeven”, where more energy is produced from fusion reactions than is applied by external heating. Although the Tokamak Fusion Test Reactor (TFTR) and the Joint European Torus (JET) both demonstrated measurable fusion energy output during experiments with deuterium and tritium fuel [1], [2], the scientific milestone of breakeven has not yet been attained. Tokamak performance is challenged in part due to turbulent processes in the plasma which reduce the timescale on which heat remains in the plasma core. The large temperature and density gradients between the plasma core and edge are sources of free energy for the growth of instabilities and turbulence. Understanding and controlling anomalous transport caused by this gradient-driven turbulence is one of the big challenges of fusion. In order to predict the performance of future fusion devices, a fundamental understanding of turbulence and transport processes is necessary.

Previous experimental, modeling, and theory work has made significant contributions to our knowledge of tokamak turbulence and transport. Core anomalous transport has been found to be primarily caused by drift wave type turbulence, comprised of ion temperature gradient, electron temperature gradient, and trapped electron turbulent modes [3], [4]. The nature of the core turbulence has been studied experimentally with diagnostics that measure fluctuations in plasma density and temperature. The validation of turbulent transport

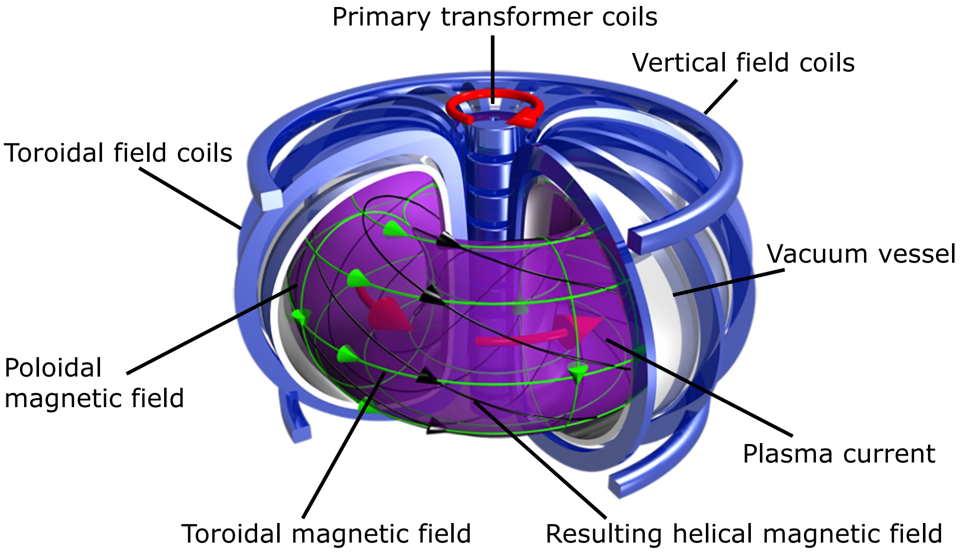

Figure 1.1: Tokamak schematic, showing the toroidal (green horizontal arrows) and poloidal magnetic fields (green vertical arrows), which combine to create a helical magnetic field (black arrows). The toroidal magnetic field is generated by the toroidal magnetic field coils, and the poloidal magnetic field is generated from the plasma current (red counterclockwise arrows), which is driven by the electric field induced by the central transformer. Adapted from Christian Brandt, Max Planck Institute for Plasma Physics.

simulations using experimental measurements of turbulence in the plasma core is currently an active effort, and under certain circumstances core transport can be accurately predicted with models [5]–[9].

The turbulence and transport processes in the edge region of the plasma are less well understood. As will be explained in more detail in Chapter 2, changes in turbulence at the tokamak edge can lead to changes in the energy confinement. When edge turbulence is damped by sheared plasma flows, a so-called edge transport barrier forms. This barrier forms only at the very edge of the plasma, and results in a higher core plasma pressure, as if the radial profiles of density and temperature are lifted to sit on a pedestal. The formation of this pedestal marks the transition from the so-called low confinement regime L-mode to the so-called high confinement regime H-mode, and this transition occurs at a certain threshold in external heating power. Next generation research reactors such as ITER and SPARC will rely on the H-mode operation as their baseline scenario for demonstrating energy breakeven. An understanding of the changes in turbulence across the L to H-mode transition a prerequisite for predicting high confinement operation in these future tokamaks. One open question related to the L to H-mode transition is the reason for the difference in H-mode access between the so-called "favorable" and "unfavorable" ion $B \times \nabla B$ drift configurations, as will be described in further detail in Chapter 2.

Although operation in H-mode allows the high energy confinement needed for future reactors, this "standard" H-mode is not a feasible operational scenario for long-term operation of fusion power plants. The steep edge pressure gradients in H-mode lead to Edge Localized Mode (ELM) instabilities that expel plasma and cause damage to the reactor materials.

Ultimately, high confinement regimes that are free from ELMs will be needed. Candidate regimes exist, but they are understudied in comparison to the ELMy H-mode, and more work is thus needed to understand their operational access, underlying mechanisms, and extrapolation to future reactors.

One candidate ELM-free high confinement regime is the "improved" confinement regime I-mode [10]. As will be described in more detail in Chapter 2, I-mode is typically accessed in the unfavorable $B \times \nabla B$ configuration and exhibits a transport barrier in energy. This leads to the energy confinement needed for high performance operation. However, I-mode does not form an edge transport barrier in particles. This prevents the accumulation of impurities, and keeps the edge pressure and pressure gradient below stability limits which lead to ELMs. These characteristics could make I-mode an ideal regime for future reactor operation. However, we currently lack fundamental understanding of the mechanism behind the I-mode regime. The reason for the separation of the particle and energy transport channels in I-mode is an open question. The role of turbulence in regulating the unique transport properties of I-mode are not yet understood.

Early investigations indicated that the I-mode was accompanied by a characteristic pedestal fluctuation, named the Weakly Coherent Mode (WCM) for its broadband frequency structure [10], [11]. Despite years of study, a detailed understanding of the WCM's identity and physical properties is not yet clear. It is known that the WCM is localized to the pedestal and causes fluctuations in electron temperature and density [11], [12]. It is not yet known what radial transport, if any, the WCM causes. The study of the properties of the WCM provides insight to its identity, drive, and impact on plasma transport, thereby increasing our understanding of the I-mode regime as a whole.

Theoretical and modeling attempts at capturing the physics of the I-mode regime vary widely in their approach. Some modeling and theory efforts connect the WCM to specific instabilities [13]–[15], while others claim the WCM is broadband turbulence leftover when large and small scale fluctuations are damped [16]. These models link the WCM fluctuations with the unique transport properties of I-mode. Other models do not consider the WCM as specifically important in I-mode, instead attributing changes in radial transport between L-mode and I-mode to changes in the phase between fluctuating quantities [17] or claim that particle transport can be explained through a neoclassical picture [18].

Experimental measurements provide invaluable contributions to our understanding of I-mode. Measurements can be used to test theories and to validate or invalidate models for I-mode. Measurements can also be used as inspiration to construct new hypotheses and build new theories, when current understanding fails to explain the complete picture of I-mode. This thesis reports on experimental work performed at the ASDEX Upgrade (AUG) tokamak housed at the Max Planck Institute for Plasma Physics in Garching, Germany. AUG is equipped with diagnostics capable of measuring the micro-scale fluctuations associated with turbulence in the plasma core and edge. In particular, the Correlation Electron Cyclotron Emission (CECE) diagnostic is used in this thesis for detailed studies of electron temperature fluctuations. For the experiments of this thesis, the diagnostic was configured to optimize measurements in the edge region, where the character of turbulence changes across confinement regime transitions. The combination of measurements, computational modeling, and theory are the pathway for an improved understanding of I-mode.

Summary of thesis

The following chapters of this thesis describe theoretical and modeling investigations of edge turbulence across confinement regime transitions. Chapter 2 gives the necessary background on tokamak turbulence and transport, and confinement regime transitions. The formation of the edge transport barrier is discussed in the context of the L to H transition. The impact of the magnetic field configuration on the L to H transition power threshold is discussed. The I-mode confinement regime is also explained in greater detail in this chapter.

Chapter 3 describes the methodology for studying turbulence in tokamaks. The process of the experimental discharge design at AUG is explained, and the diagnostic suite used for measuring radial profiles and turbulent fluctuations is described. A brief introduction to the gyrofluid and gyrokinetic modeling tools used is also given.

This thesis' unique contributions to the field are given in Chapters 4 to 6. Chapter 4 describes a detailed experimental investigation of the WCM in L-mode and I-mode. A key finding of this work is the presence of the WCM in L-mode across a wide parameter space. An example of an experiment with a WCM in both L-mode and I-mode can be seen in Figure 1.2, which shows a spectrogram of CECE fluctuations in the pedestal. Through the use of AUG's diagnostic suite, details of the WCM properties in L-mode and I-mode are compared, including the electron temperature fluctuation spectra, fluctuation amplitude, and radial correlation distance. The WCM dispersion relation, the "cross" phase between electron temperature and density fluctuations, and the mode's coupling with a strongly coherent low frequency fluctuation are also presented. The presence of the WCM is found to be independent of the global plasma confinement quality and plasma collisionality.

Chapter 5 extends the study of the L-mode WCM to both the favorable and unfavorable $B \times \nabla B$ magnetic configurations. The WCM is found to exist in L-mode in both configurations at power levels far below the L to I-mode transition. This experimental study correlates changes in the edge radial electric field, and the resulting $E \times B$ velocity shear, with changes in edge fluctuations. The strength of the edge electron temperature fluctuations, in terms of coherence and fluctuation amplitude, is found to be negatively correlated with the velocity flow shear in the pedestal. The favorable $B \times \nabla B$ configuration, which has easier access to H-mode, is found to have higher shear and lower electron temperature fluctuations in L-mode phases just prior to confinement regime transitions, compared to matched L-modes in the unfavorable $B \times \nabla B$ configuration.

Chapter 6 investigates the difference between outer core and pedestal top turbulence in L-mode and I-mode through gyrokinetic simulations. These simulations are based on experiments described in Chapter 4. Because the WCM is found to be present in both L-mode and I-mode and is found to be independent of confinement quality, we seek additional explanations for the change in transport and confinement between L-mode and I-mode. The simulation results indicate that the nature of the turbulence is similar in these locations between L-mode and I-mode in terms of instabilities present and their sensitivity to drive terms. This points to the importance of processes in the plasma edge, including transport barrier formation and the behavior of the WCM, in determining the difference between L-mode and I-mode.

Finally, Chapter 7 provides a summary of findings and indicates directions for the next steps in research on this topic. This thesis delivers a new set of observations of the nature of

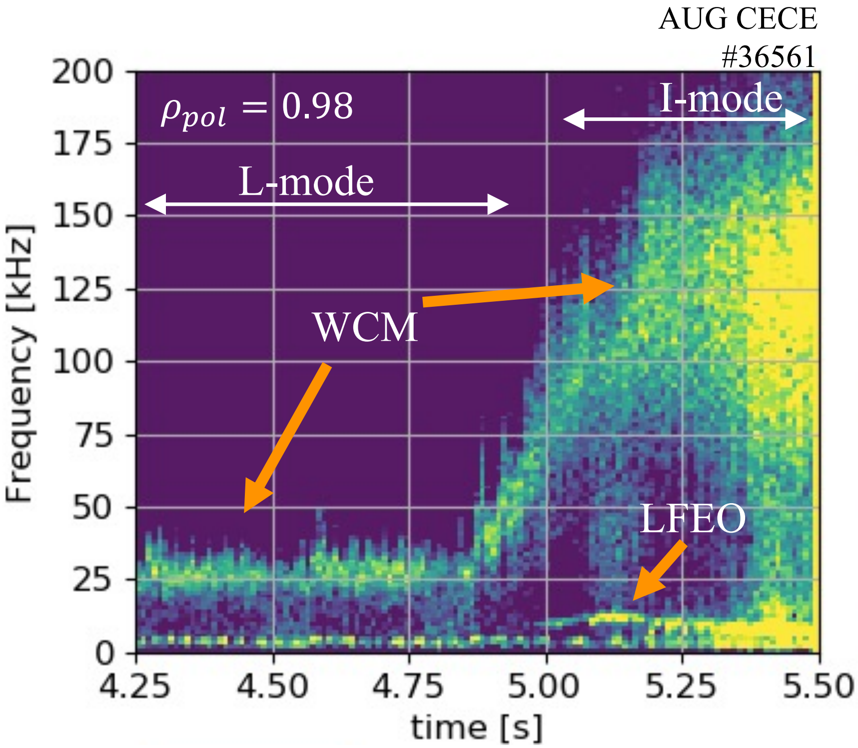

Figure 1.2: Spectrogram from single CECE channel near the WCM peak amplitude of $\rho_{pol} = 0.98$ during a discharge with L-mode and I-mode phases. The WCM appears as the 25 kHz mode in L-mode which spins up to 80-160 kHz in I-mode. A Low Frequency Edge Oscillation (LFEO) also appears in I-mode only as narrowband mode at 8 kHz.

edge turbulence in L-mode and I-mode, which adds to our knowledge of these regimes and the transitions between regimes.

Chapter 2

Background

The anomalous transport driven by turbulence challenges the energy confinement of tokamaks. Therefore, turbulence and its resulting transport must be understood at a fundamental level in order to access high energy confinement and predict performance of future reactors. In particular, fluctuations at the plasma edge must be understood because changes in edge turbulence play a key role in the transition between low confinement and high confinement operation. This chapter will briefly describe key concepts and areas of research addressed in this thesis, including the drift wave picture of turbulence, turbulence-driven transport, and the high confinement regimes H-mode and I-mode.

2.1 Turbulence and transport in tokamaks

2.1.1 The drift wave turbulence picture

Turbulence in a tokamak is the result of free energy that is converted to kinetic energy in the form of fluctuating modes, which nonlinearly evolve to a saturated state. Pressure gradients are a source of free energy that are always present in magnetic confinement fusion devices, due to the necessity of a hot and dense plasma core for fusion reactions and a cooler and less dense plasma edge for acceptable material interactions.

Drift wave modes have been shown to be responsible for the majority of the anomalous transport in the core of tokamak plasmas [3], [4]. Drift waves are generated from a gradient in pressure, which leads to diamagnetic currents in the plasma. A simple picture of the drift wave model in a slab geometry is shown in Figure 2.1, where the background magnetic field $\vec{B}$ is in the $\hat{z}$ direction and there is a density gradient in the $\hat{x}$ direction. Electrons are assumed to have a Boltzmann response, satisfying $\frac{\delta n_e}{n_e} = \frac{e\phi}{T_e}$, and flow rapidly along field lines. If an initial density perturbation is applied in the $\hat{y}$ direction, then differences of charge accumulation will lead to an electric field also in the $\hat{y}$ direction. This electric field leads to an $E \times B$ drift in the $\hat{x}$ direction, which causes the density perturbations to propagate along the $\hat{y}$ direction. This drift wave phase velocity is the electron diamagnetic drift velocity, $v_{De} = \frac{\nabla n_e}{n_e}\frac{T_e}{eB}$ and the dispersion relation is $\omega = k_y v_{De}$.

With this dispersion relation, the drift wave is purely propagating because its frequency does not have an imaginary component. In order for drift waves to grow and become unsta-

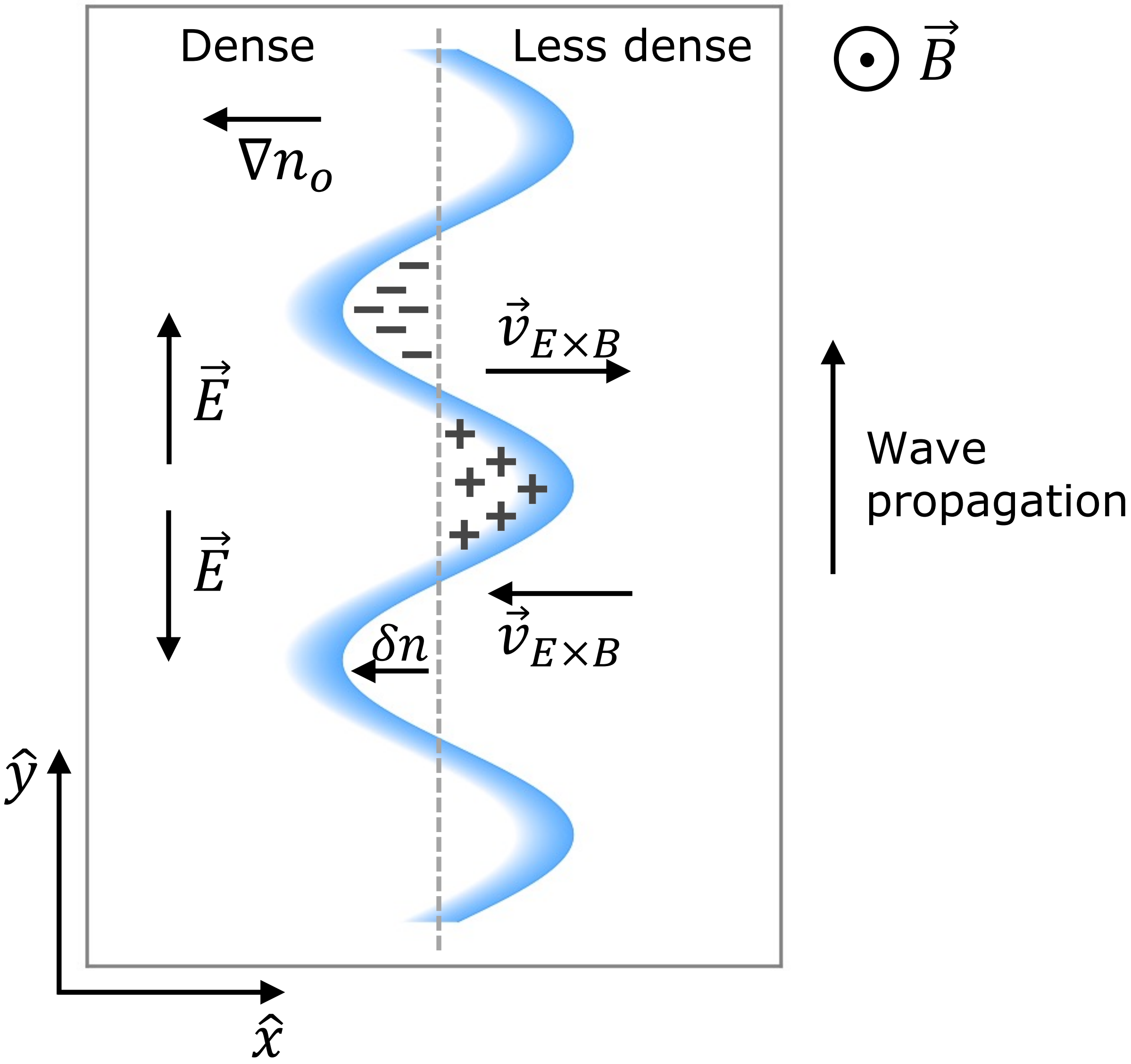

Figure 2.1: The drift wave mechanism in a plane geometry. Figure based on Reference [19], Figure 6-14.

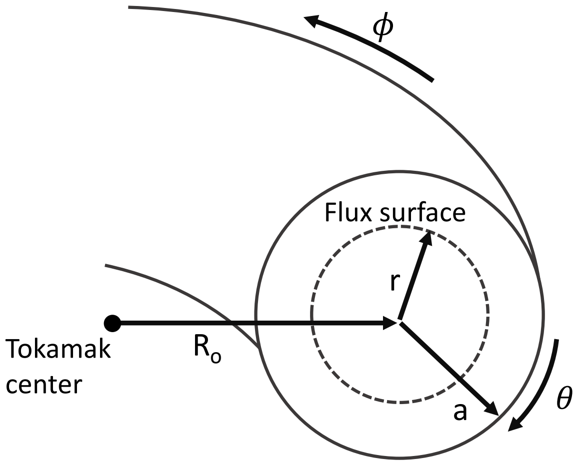

Figure 2.2: Poloidal cross section of a tokamak, showing the important geometrical definitions. These include the major radius R_o, minor radius a, minor radial coordinate r, and the toroidal (ϕ) and poloidal (θ) directions.

ble, the electron parallel motion along field lines must be limited by a mechanism such as resistivity, such that a phase shift δ occurs between the density and potential perturbations. This phase shift gives a modified Boltzmann relation: $\frac{\delta n_e}{n_e} = \frac{e\phi}{T_e}(1 - i\delta)$, and a modified dispersion relation $\omega = k_y v_{De}(1 - i\delta)$. This wave has a growth rate $\gamma = k_y v_{De}\delta$.

This simple slab picture of the drift wave instability is not a full representation of the drift wave picture in a tokamak, where toroidal geometry, additional gradients, and kinetic effects can all occur, but it captures the fundamental nature of the instability. The tokamak geometry under consideration is displayed in Figure 2.2, which shows the toroidal (ϕ), poloidal (θ), and minor radial (r) directions. With the inclusion of these additional effects, the drift wave picture can be extended to describe the instabilities that are most prevalent in the plasma core, including the ion temperature gradient (ITG) mode, the electron temperature gradient (ETG) mode, and the trapped electron mode (TEM). A more detailed picture of drift waves can be found in several plasma physics textbooks, including References [19]–[21].

In a tokamak, the saturated state of turbulence is determined through the nonlinear interaction of unstable modes across different scales. Turbulent energy cascades from large scales to small scales, where it is dissipated via collisional processes. Energy also moves from smaller scales to large scales to form zonal flows. Zonal flows are reviewed in Reference [22]. These turbulence-driven flows are radially localized and flow perpendicular to the background gradients which drive the turbulence. Velocity shear in these self-generated flows can act to radially shear apart turbulent eddies, thereby acting to suppress the turbulence. Figure 2.3 gives a simplifeid summary of the interactions between heating, turbulence, zonal flows, and transport in a tokamak.

2.1.2 Fluctuation induced transport

The turbulence caused by unstable drift waves leads to anomalous transport of heat and particles. This cross-field transport can be understood by relating fluctuating quantities

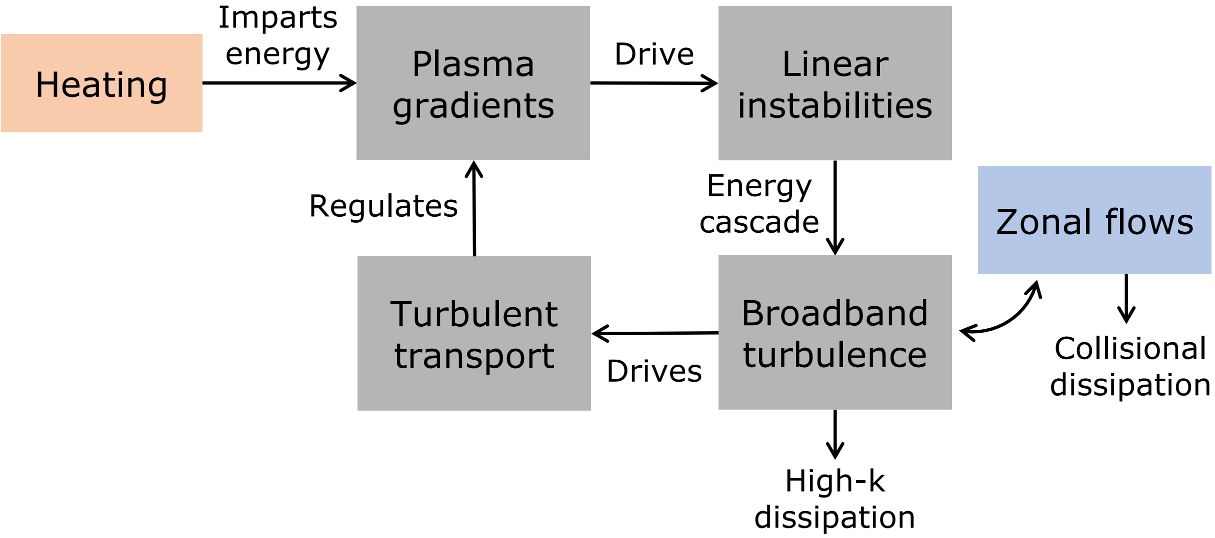

Figure 2.3: Summary of the interactions between turbulence and transport in a tokamak. Auxiliary heating introduces a source of energy and leads to gradients in the plasma profiles. These gradients drive linear instabilities, which nonlinearly saturate to form broadband turbulence. This turbulence self-generates zonal flows, which in turn regulates the turbulence. The turbulence, which is regulated by flows, drives the cross-field transport of heat and particles. This cross-field transport plays a role in determining the plasma profiles. Figure based on Reference [23] Figure 2.1 and [24] Figure 1.

($\widetilde{n}, \widetilde{T}$, $\widetilde{\phi}$, $\widetilde{B}$, etc.), to the particle and heat fluxes, Γ and Q respectively. Turbulence-induced fluxes for species s are given by [25]:

$$\Gamma_s = \langle \widetilde{n}_s \widetilde{v}_r \rangle \tag{2.1}$$

$$Q_s = \langle \frac{3}{2} \widetilde{p}_s \widetilde{v}_r \rangle \tag{2.2}$$

where the particle flux is the time averaged product of the density fluctuations and radial velocity fluctuations and the energy flux is the time averaged product of the energy (equivalent to $\frac{3}{2}p$ where p is pressure) and radial velocity fluctuations. The angle brackets denote and ensemble average, which includes the phase between the fluctuating quantities within the average. In the electrostatic limit, for a fluctuating electric field $\widetilde{E} = \nabla\widetilde{\phi}$, the fluctuating radial velocity $\widetilde{v}_r$ comes from the fluctuating $E \times B$ velocity:

$$\widetilde{v}_r = \frac{[\nabla\phi \times \vec{B}] \cdot \hat{r}}{B^2} \simeq \frac{E_\theta}{B} \tag{2.3}$$

where the product of the toroidal electric field and poloidal magnetic field is small because $k_\parallel \ll k_\perp$ for drift waves. Using $p_s = n_s T_s$, equations 2.1 and 2.2 can be rewritten as:

$$\Gamma_s = \frac{1}{B} \langle \widetilde{n}_s \widetilde{E}_\theta \rangle \tag{2.4}$$

$$Q_s = \frac{3}{2}\frac{1}{B}\langle \widetilde{p}_s \widetilde{E}_\theta \rangle = \frac{3}{2}\frac{1}{B}\left(T_s \langle \widetilde{n}_s \widetilde{E}_\theta \rangle + n_s \langle \widetilde{T}_s \widetilde{E}_\theta \rangle \right) \tag{2.5}$$

From equations 2.4 and 2.5, we can see that determination of electrostatic particle and heat fluxes would require determining the density, temperature, and potential fluctuation amplitudes as well as the cross phases between fluctuating density and potential ($\alpha_{n\phi}$) and temperature and potential ($\alpha_{T\phi}$). In the case of electromagnetic transport, which can occur in high β plasmas or edge plasmas, measurements of magnetic field fluctuations and the associated phase relationships must also be determined. In the confined plasma, current diagnostics do not have the ability to simultaneously measure all these quantities to provide precise experimental measurements of turbulence-driven transport. However, the measurement of any single one of the quantities can provide valuable constraints on the possible transport. Measured changes in fluctuation amplitudes or phase angles between different plasmas can indicate changes in transport. This thesis will focus on comparisons of $\widetilde{T}_e$ between different operational regimes.

2.1.3 Core turbulence and transport

The drift wave turbulence that causes the majority of the core anomalous transport is primarily dominated by the gradient-driven modes. The drive of these modes is often expressed as a normalized gradient a/L_x or R/L_x where a and R are the minor and major radii and $L_x = x/\nabla x$ is the gradient scale length of quantity x.

- The Ion Temperature Gradient (ITG) mode [26], [27]:
  The ITG mode is driven by a gradient in T_i. This mode is sometimes referred to as the η_i mode where $\eta_i = L_n/L_{T_i}$, indicating that this mode occurs when the ion temperature gradient is stronger than the density gradient. ITG modes occur when the normalized ion temperature gradient a/L_{T_i} exceeds a critical gradient. ITG stability also depends on the normalized density gradient a/L_n and the ion to electron temperature ratio T_i/T_e [26], [27]. ITG modes drive the majority of the core ion heat flux, but can also play a role in the electron heat flux. ITG modes propagate in the direction of the ion diamagnetic drift (v_{Di}). The direction of v_{Di} depends on the magnetic field direction (see Figure 2.8). This mode exists at low wavenumbers, typically with $k_\theta \rho_s \sim 0.1 - 1.0$ where k_θ is the poloidal wavenumber and ρ_s is the ion gyroradius evaluated at the sound speed, defined as $\rho_s = c_s/\Omega_{ci}$ with $c_s = \sqrt{T_e/m_i}$ and $\Omega_{ci} = qB/m_i$.

- The Trapped Electron Mode (TEM) [28], [29]:
  TEMs exist because of a trapped population of electrons, which undergo banana orbits on the low-field side of the tokamak. TEMs can be driven by either a/L_{T_e} or a/L_n, and exhibit a critical gradient affected by these quantities. TEMs are dependent on the collisionality of the plasma. At high collisionality, TEMs are damped because trapped electrons become de-trapped due to collisions. In low collisionality plasmas where TEMs are unstable, this mode can drive the majority of the electron heat flux. TEMs propagate in the electron diamagnetic drift direction and have a characteristic scale of $k_\theta \rho_s \sim 1.0$.

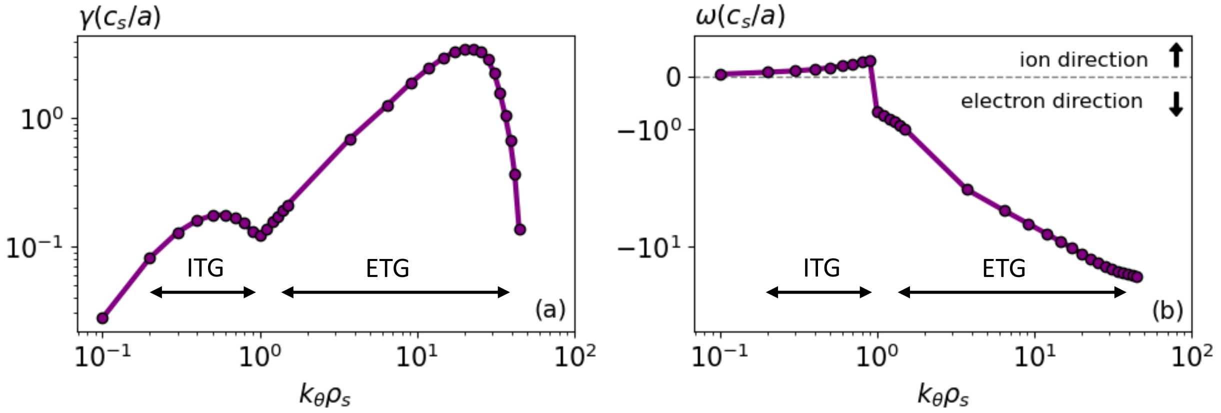

Figure 2.4: Dominant mode liner growth rate (a) and real frequency (b) over $k_\theta\rho_s$. This example represents the linear turbulence of an I-mode plasma at $\rho_{pol} = 0.90$, and will be discussed further in Chatper 6.

- The Electron Temperature Gradient (ETG) mode [30]–[32]:
  The ETG mode can be thought of as the electron version of the ITG mode. ETG is driven by a/L_{T_e}, and has a critical gradient in this quantity. The ETG mode drives electron heat flux, propagates in the electron diamagnetic direction, and occupies the small spatial scales $k_\theta\rho_s > 1.0$. Due to its small spatial scale, in some scenarios ETG does not play a dominant role in heat transport. However, it has also been shown through simulations of core core plasmas that ETG can form radially elongated streamers that can enhance transport and cause cross-scale interaction between the ion and electron-scales [32], [33]. Due to the small spatial scale of ETG, its experimental measurement is not possible by current diagnostics.

ITG, TEM, and ETG modes can coexist and typically occupy different regions of wavenumber space $k_\theta\rho_s$. Figure 2.4 shows a typical spectrum of the linear growth rate (γ) and real frequency (ω) for the dominant turbulent mode over $k_\theta\rho_s$. In this example, ITG is seen to dominate the low wavenumber portion of the spectra, while ETG dominates the high wavenumber portion. Turbulent modes at different wavenumbers nonlinearly saturate through the interaction across different scales, and through the generation of zonal flows.

Core transport in tokamaks is generally found to lead to "stiff" profiles. Stiffness can be thought of as the resistance of a particular profile to change, when that profile has a gradient above a particular threshold for turbulence drive. An example of stiff core profiles is shown in Figure 2.5, where the electron pressure profiles of an L and H-mode are shown using a logarithmic scale. In the plasma core, the profiles are self-similar, while the non-stiff edge region the profile gradients change between L and H-mode.

The explanation for these clamped profiles is that an increase in heating power that would further increase the gradient in turn increases the turbulence drive, and thereby increases the transport which regulates the profile. Stiffness can by quantified either as the closeness of a normalized gradient a/L_x to its critical value, or as the change in heat or particle flux with a change in a/L_x. Fusion reactors require peaked profiles to achieve high core densities and temperatures, but turbulence-induced stiffness in profiles challenges this peaking. The

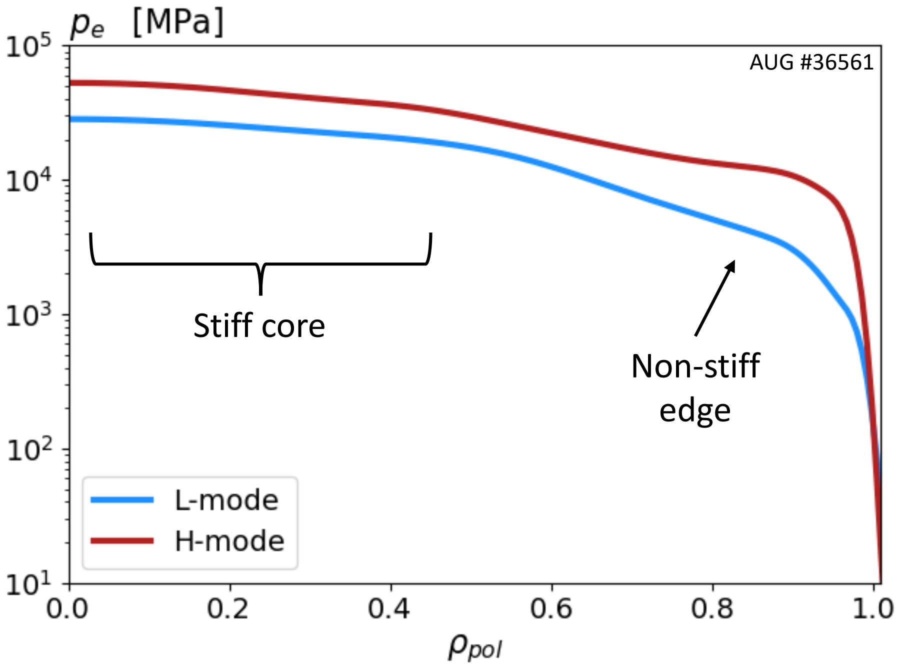

Figure 2.5: Log-scale electron pressure profiles from L-mode and H-mode, showing the self-similarity of profiles in the core (stiffness), while the slope of the edge profiles change between L and H-mode.

opportunity for achieving high core temperature therefore comes from the edge boundary condition, where a "pedestal" can form in the profiles, leading to increased core density and temperature by raising the whole profile.

2.1.4 Edge turbulence and transport

The edge of the confined plasma plays an important role in determining global confinement. In this section we define the edge as the radial range from the pedestal top to the separatrix. The pedestal region is characterized by the steep pressure gradients which separate the cool SOL region from the hot and dense core plasma. The formation of the pedestal (see Figure 2.6) and its connection to confinement will be discussed in Section 2.2. The steep gradients of this region can drive turbulence distinct from the core modes previously discussed. While ITG, TEM, and ETG modes can all be driven at the edge, additional instabilities can also be found. These include:

- The Micro-Tearing Mode (MTM) [34]–[36]:
  MTMs are electromagnetic, small-scale tearing modes driven by the steep T_e gradients in the pedestal and are dependent on collisionality. MTMs cause electron heat transport, and while they are damped in the core they can play a significant role in the pedestal. As the name suggests, MTMs cause tearing and reconnection of the magnetic field lines. These modes are electromagnetic, so they can be identified through

their magnetic field fluctuations. MTMs propagate in the electron diamagnetic drift direction and typically exist in the ion-scale range of wavenumbers $k_\theta \rho_s < 1.0$.

- The Kinetic Ballooning Mode (KBM) [37], [38]:
  KBMs are destabilized by the pedestal pressure gradient and magnetic curvature, and are stabilized by magnetic shear. The ideal ballooning mode can be described by the ideal MHD equations, and refers to a pressure gradient driven mode which has a ballooning structure, meaning its amplitude grows on the "bad curvature" low field side of the tokamak. The KBM is similar to the ideal ballooning mode, with modifications from kinetic effects such as finite Larmor radius and Landau resonances. These kinetic modifications make the KBM instability threshold lower than that for ideal ballooning modes. KBMs and other MHD-type modes are thought not to contribute significantly to heat transport, but can play a role in pedestal particle transport [39]. KBMs propagate in the ion diamagnetic drift direction and occur at the ion scale with $k_\theta \rho_s < 1.0$.

MTMs and KBMs are not always present in the pedestal region. In fact, in high confinement regimes with strong pedestals, ITG and TEM may also be damped. In such cases, ETG is thought to regulate the pedestal heat transport. In edge scenarios, the ETG wavenumber extent may extend below $k_\theta \rho_s = 1.0$.

Edge turbulence is of different nature than core turbulence. The steep gradients in the pedestal lead to instabilities not present in the core, and also to large growth rates which result in a large turbulent fluctuation amplitude. Turbulence at the edge can be more bursty in nature than the core, with the large gradients and strong turbulence generating “blobs” that can carry particles and energy across the last closed flux surface (LCFS) to the scrape-off-layer (SOL). Understanding the nature of this edge turbulence is an active area of research, and the experimental observations of edge and pedestal turbulence have been limited due to diagnostic limitations. This thesis will focus on adding to our understanding of the fluctuations present in this region.

2.2 High confinement operation and the pedestal

2.2.1 The L to H transition

The low confinement regime L-mode was the first operational regime explored on tokamaks and has high levels or turbulence, leading to poor confinement of heat and particles. The high confinement regime H-mode was discovered on ASDEX in 1982 [40] and has since been studied on tokamaks around the world. H-mode is the reference scenario for demonstrating net energy gain on next generation experiments such as ITER.

H-mode can be reached if sufficient heating power is applied, above a power threshold P_{LH}. Compared to L-mode, H-mode exhibits higher confinement of heat and particles. During the L to H transition, a pedestal forms at the edge of the pressure profile, in both the density and temperature. This pedestal forms in both the ion and electron channels. The formation of a pedestal increases the energy confinement and particle confinement of the plasma because the pedestal top sets a boundary condition for the core profiles. Core

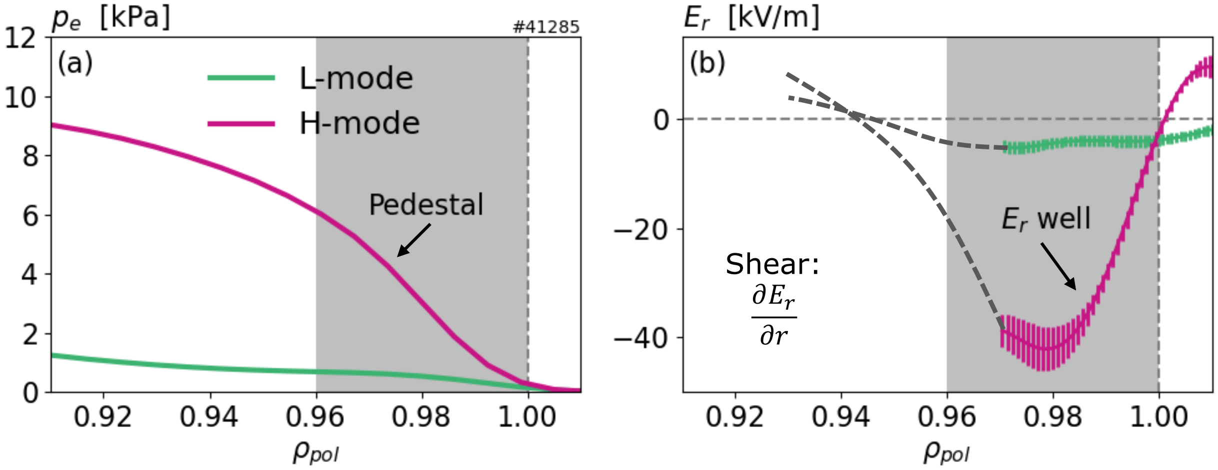

Figure 2.6: (a) The radial profile of electron pressure in L-mode and H-mode, with the H-mode pedestal region shaded. (b) The radial profile of E_r in the same L-mode and H-mode phases. The colored portions of the E_r profiles are fitted to data from the HES diagnostic, while the dashed lines indicate the estimated E_r inside of $\rho_{pol} = 0.97$, where experimental data is not available. Figure is inspired from References [41] and [42].

profiles of both L-mode and H-mode are stiff, and display similar normalized gradients. High pressure pedestals lead to the high core plasma pressure desired for fusion reactors.

At the L to H transition, the radial electric field (E_r) profile forms a “well” in the edge region. For any plasma species s, the E_r can be related to the pressure p_s and the plasma particle flows through:

$$E_r = \frac{1}{n_s Z_s e} \nabla_r p_s + v_{\phi,s} B_\theta - v_{\theta,s} B_\phi \tag{2.6}$$

where $v_{\theta,s}$ and $v_{\phi,s}$ are the toroidal and poloidal flows respectively and B_ϕ and B_θ are the toroidal and poloidal magnetic field components respectively. Examples of L-mode and H-mode pressure profiles and E_r profiles are shown in Figure 2.6.

The increased pedestal E_r leads to an increased $E \times B$ velocity. This flow is strongly sheared in the radial direction due to the well structure of E_r. This sheared flow is believed to suppress turbulence and its associated transport by decorrelating (i.e. distorting and shearing apart) turbulent eddies [43]. The commensurate reduction in transport in the edge leads to the pedestal formation in the kinetic profiles, which is also called a “transport barrier”. In H-mode, the balance of turbulence drive from these steepened profiles and damping from the sheared $E \times B$ flow is different than the balance of turbulence drive and damping in L-mode.

When a transport barrier is formed in H-mode, the pedestal pressure and pressure gradient increase dynamically until an MHD limit is reached, and an Edge Localized Mode (ELM) is triggered. The classic type I ELMs are a coupling of pressure gradient-driven peeling modes and pressure driven peeling modes [44], [45]. ELMs are explosive instabilities that eject particles and energy and relax the pedestal. ELMs occur in a quasi-periodic cycle: once the pedestal is relaxed by an ELM, the transport barrier is re-established and the pressure profiles and gradients grow again until the next ELM is triggered. ELMs are useful

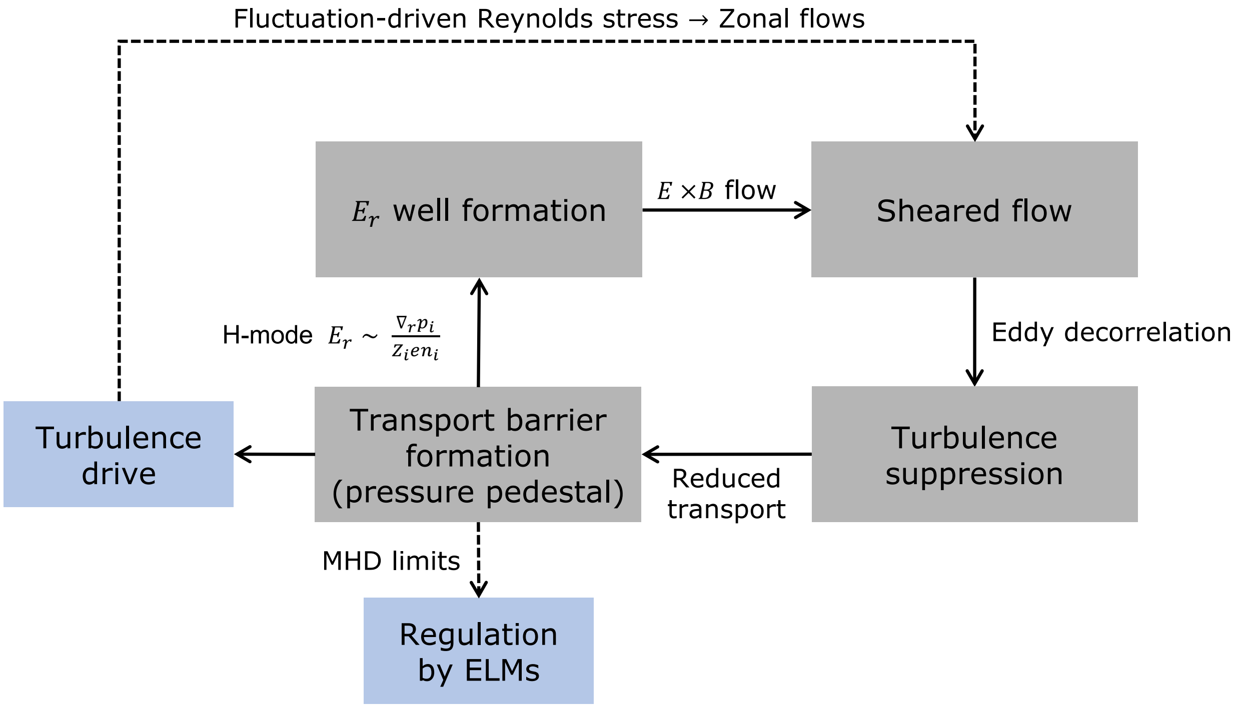

Figure 2.7: Feedback loop representing some of the processes impacting the L to H transition.

for maintaining a steady-state H-mode plasma because they expel impurities, which would otherwise lead to radiative collapse of the plasma if accumulated. However, ELMs can be damaging to the wall and divertor, with each ELM crash releasing up to 20% of the plasma stored energy in a time period less than 1ms. High confinement operation without ELMs will be necessary for future fusion power plants, and naturally ELM-free, high confinement regimes such as I-mode could meet this need.

The paradigm of edge transport barrier formation and the L to H transition is still an active area of research, in particular the triggering of the transition. One widely accepted model is that L to H transition occurs when turbulence damping by $E \times B$ shear exceeds the turbulence growth rate [46]. The onset of this flow shear is not yet completely understood. One possible feedback loop is represented in Figure 2.7. It is possible that growth of the pressure pedestal may be sufficient to explain the flow shear via the $\nabla_r p_i$ contribution to the E_r well. The edge sheared $E \times B$ flow will stabilize edge turbulence. Reduced turbulence will mean reduced edge heat and particle transport, which leads to the steepening of edge profiles. A steepened edge pressure profile reinforces the edge E_r well, which in turn leads to a sheared $E \times B$ flow. This is a positive feedback loop, and the edge pressure profiles grow until an ELM appears to relax the pedestal.

The turbulence itself, which is strongly driven due to steep pedestal gradients, can generate zonal flows via Reynolds stress [47]. These zonal flows contribute to the sheared $E \times B$ flow, forming a predator-prey system with the turbulence. Some theories define the transition criterion as a point where the transfer of energy from turbulence to zonal flows exceeds the turbulence drive from kinetic profiles [48]. Several types of zonal flows can receive energy from turbulence and play a role in shearing turbulent eddies, depending on the exact plasma conditions. These zonal flows can include zero frequency zonal flows, low frequency zonal flow oscillations, and finite frequency geodesic acoustic modes (GAMs) [49]. These different branches of zonal flows can coexist and may compete in gaining energy from turbulence. A full description of the L to H transition must include a self-consistent picture zonal flows, turbulent eddies, transport, and sheared flows, and their intertwined in feedback loops. Pedestal turbulence measurements and E_r measurements across the L to H transition can provide valuable information to test hypotheses related to the pedestal and confinement regime transitions.

2.2.2 H-mode scaling laws

Although a complete physical understanding of the L to H-mode transition is still under investigation, empirical scalings have been constructed to capture the important parameter dependencies of the L to H transition and H-mode operation. Of particular interest to planning tokamak operation is the power threshold for the L to H transition, P_{LH}. For plasmas above a minimum density, the most frequently used power threshold derived from a multi-machine database is [50]:

$$P_{LH} = 0.0488\, \bar{n}_e^{0.72}\, B_\phi^{0.80}\, S^{0.94} \tag{2.7}$$

where P_{LH} is expressed in MW, $\bar{n}_e$ is the line averaged density in 10^{20}m^{-3}, B_ϕ is the magnetic field in T, and S is the plasma surface area in m^2. This scaling has been constructed using only deuterium plasmas in the favorable $B \times \nabla B$ drift configuration, meaning the ion $B \times \nabla B$ drift points towards the active X-point.

The predicted energy confinement time, τ_E, is also of interest when predicting performance for future reactors. Similar to the power threshold scaling, multi-machine databases can be fit to relate τ_E to its important dependencies. The most commonly used τ_E scaling for H-mode is the ITER-98(y,2) scaling, compiled from a set of ELMy H-modes across 8 tokamaks [51]. In terms of engineering parameters, this scaling is:

$$\tau_E^{98(y,2)} = 0.0562\, I_p^{0.93} B_\phi^{0.15} P^{-0.69} \bar{n}^{0.41} M^{0.19} R^{1.97} \epsilon^{0.58} \kappa^{0.78} \tag{2.8}$$

where I_p is the plasma current in MA, P is the absorbed power in MW, M is the isotope mass, R is the major radius, ϵ is the inverse aspect ratio, and κ is the elongation.

The confinement time scaling can also be expressed in terms of dimensionless "physics" parameters:

$$\tau_E^{98(y,2)} \propto \tau_B\, \rho_*^{-0.80} \beta^{-0.90} \nu_*^{-0.01} M^{0.96} q^{-3.0} \epsilon^{0.73} \kappa_a^{2.3} \tag{2.9}$$

where $\tau_B = \frac{(\text{minor radius})^2}{\text{Bohm diffusion coefficient}}$ is the Bohm confinement time, ρ_* is the ion gyroradius normalized by a, ν_* is the effective collision frequency for particle detrapping normalized to the trapped particle bounce frequency, β is the plasma pressure normalized to magnetic pressure, and q is the safety factor. For more details on these normalizations, see Reference [51].

Using these confinement time scalings, a "confinement improvement factor" H_{98} can be defined as the ratio between the confinement time measured during an experiment τ_E^{exp}, and the confinement time that would be predicted by $\tau_E^{98(y,2)}$:

$$H_{98} = \tau_E^{exp} / \tau_E^{98(y,2)} \tag{2.10}$$

τ_E^{exp} can be measured via magnetics measurements of stored energy and knowledge of the input power. The confinement improvement factor is often used to quantify the quality of the confinement of a discharge, with $H_{98} > 1$ considered to be particularly good confinement.

Confinement time scalings for L-mode plasmas have also been determined using an L-mode database. The most commonly used L-mode scaling is the ITER89 scaling, to give L-mode confinement time τ_E^{89} [52]. Similar to H_{98}, a confinement improvement factor H_{89} is constructed with τ_E^{89} to compare the confinement time of an experiment with the L-mode confinement time predicted from this scaling law.

2.2.3 Magnetic configuration and the H-mode power threshold

The magnetic configuration has a strong impact on the input power required to access the L to H transition. Figure 2.8 shows poloidal cross sections of magnetic flux surfaces, comparing four different magnetic configurations possible with a single magnetic flux X-point. A lower single null (LSN) configuration features a single X-point at the bottom of the plasma and upper single null (USN) has a single X-point at the top. Depending on the direction of the toroidal magnetic field, the ion $B \times \nabla B$ drift will point either towards the bottom or top of the plasma. The "favorable" $B \times \nabla B$ drift direction refers to a configuration where the ion $B \times \nabla B$ drift points towards the active X-point, and the "unfavorable" $B \times \nabla B$ drift direction refers to a configuration where the ion $B \times \nabla B$ drift points away from the active X-point. Depending on plasma shaping, more than one X-point may be created in the magnetic flux, but the "active" X-point refers to the one closest to the closed flux surfaces. In unfavorable magnetic configuration, the power threshold for transition from L to H-mode is roughly twice the favorable configuration threshold for a matched plasma [40], [53], [54]. This difference in power requirement is the origin of the "favorable" and "unfavorable" terminology. The reason for the difference in power threshold is an open question.

Differences in E_r between favorable and unfavorable configuration plasmas have been observed in both the confined region of the plasma [54]–[58] and the scrape-off layer (SOL) [59], [60]. These differences in E_r could lead to differences in turbulence suppression by $E \times B$ flow shear between the two configurations. At Alcator C-Mod, the direction of the SOL turbulence-driven flows changed when the configuration was switched from favorable to unfavorable by switching from LSN to USN topology while keeping the field and current directions unchanged [61]. These SOL flows were suggested to impose a boundary condition on confined plasma toroidal rotation, which effects the E_r. At AUG, the direction of SOL flow is always in the v_{De} direction and does not change with the magnetic configuration, and so cannot explain the difference in power threshold between favorable and unfavorable configuration [54]. Differences in ion orbit losses and neutral penetration into the plasma are also candidates for explaining differences in E_r and the difference in the L-H power threshold between the two configurations [62], [63]. In addition, in the confined region of the plasma, the magnetic configuration is theorized to effect the turbulent eddy tilt and thus Reynolds stress, which may also effect the E_r [64], [65].

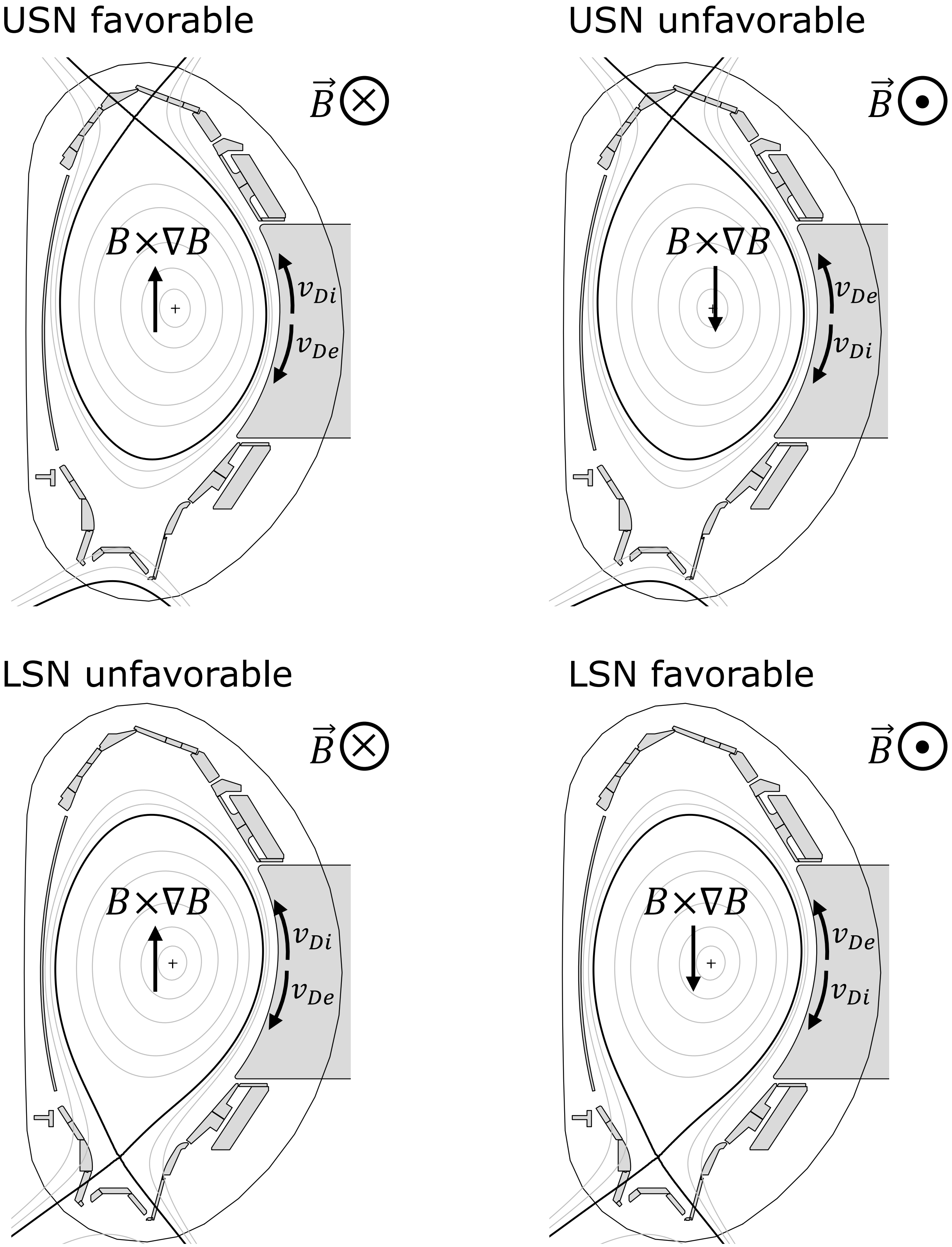

Figure 2.8: Four different combinations of X-point and magnetic field direction, resulting in either favorable or unfavorable ion $B \times \nabla B$ drift direction. The directions of the ion and electron diamagnetic drift, v_{Di} and v_{De} respectively, are also indicated.

2.3 The I-mode confinement regime

The I-mode confinement regime is a naturally ELM-free high confinement regime characterized by a heat transport barrier but without a particle transport barrier [10]. The high energy confinement without impurity accumulation or ELMs makes the I-mode a promising regime for future reactor operation. First discovered at AUG [66], I-mode has been studied at Alcator C-Mod [10], AUG [53], DIII-D [67], and EAST [68].

The experimental recipe for I-mode and the features of this confinement regime are common across these tokamaks. I-mode is typically accessed in the unfavorable ion $B \times \nabla B$ drift direction. In comparison with the favorable $B \times \nabla B$ configuration, the unfavorable configuration allows more external heating power to be applied before the plasma transitions from L-mode to H-mode. I-mode exists in the operational space between L-mode and H-mode. The L to I power threshold was studied at C-Mod, and appears to have a weaker scaling with magnetic field as compared to the L to H transition [69]. Therefore, the power window for I-mode access is wider at higher magnetic field. Robust I-modes have been achieved with ICRH, ECRH, and NBI heating and have covered a wide range of operational space in terms of magnetic field B_t, plasma current I_p, edge n_e, edge T_e [69], [70].

I-mode is characterized by its unique transport barrier in heat but not particles, as seen by the formation of a pedestal in T_e while the n_e profile is very similar between L and I-mode. Typical n_e and T_e profiles of L, I, and H-mode at AUG are shown in Figure 2.9. The n_e profile always forms a slight pedestal in AUG plasmas with X-points, but the L and I-mode n_e pedestals are very weak compared to those in H-mode. I and H-mode both form a pedestal in T_e. The weak density pedestal of I-mode means that the plasma edge does not have pressure and pressure gradients that approach the MHD stability limits leading to ELMs. The lack of particle transport barrier also means that impurities do not accumulate in I-mode plasmas, and impurity and main ion particle transport are similar to L-mode levels [69]. I-mode is accompanied by a deepening of the E_r well in comparison to L-mode, and an accompanying $E \times B$ sheared flow. The I-mode E_r spans the parameter space between L-mode and H-mode, and some I-mode E_r minima can be as deep as those typical in weak H-modes [12]. The confinement improvement factor, $H_{98}(y, 2)$ in I-mode also falls between L-mode and a good H-mode [12].

I-mode is also characterized by distinctive pedestal fluctuations. The most prominent feature is the Weakly Coherent Mode (WCM), which is a mid-frequency broadband fluctuation. The WCM has also been observed in L-mode phases directly preceding the L to I transition [72]. This thesis will study the L-mode WCM in greater detail, but prior to this work, the detailed studies of the WCM were limited to I-mode plasmas. In AUG I-modes, the WCM exists in the 50-150 kHz range. The WCM features fluctuations in n_e and T_e. The C-Mod WCM also had magnetic field fluctuations, but this has not been observed at AUG. The amplitude of the n_e fluctuations is several times higher than that of the T_e fluctuations [72]. A coherent edge fluctuation known as the Low Frequency Edge Oscillation (LFEO) can also be present in the I-mode pedestal. This mode has been proposed to be a modified Geodesic Acoustic Mode (GAM) [73] or a low frequency zonal flow. The identification of the LFEO, and its implications for transport, is still actively under investigation. A spectrogram of WCM and LFEO fluctuations are shown in Figure 2.10. The LFEO and the WCM have

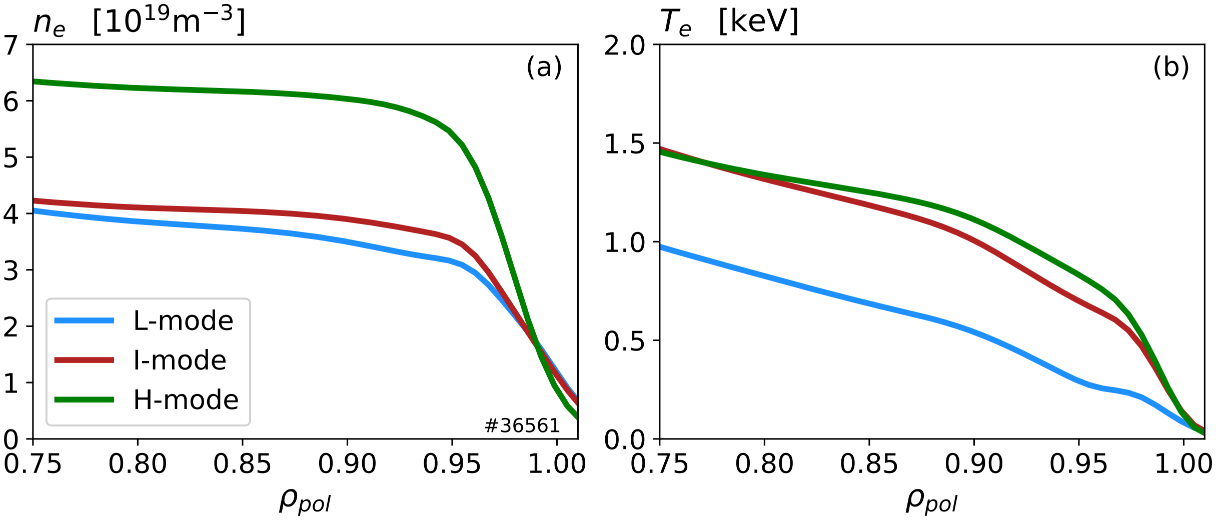

Figure 2.9: Electron density and temperature profile fits of the L, I, and H-mode phases of a discharge. Profiles fits were obtained using the integrated data analysis method [71]. The density profile is similar between L-mode and I-mode, but the temperature profile forms a pedestal in I-mode. H-mode features a strong pedestal in both temperature and density.

been shown to couple during I-mode, with the LFEO receiving energy from the WCM and the LFEO responsible for the frequency broadening of the WCM [74].

Despite these experimental observations in I-mode, a complete understanding of this operating regime does not yet exist. The mechanism for separation of the particle and heat transport channels is still an open question, and the role of turbulence in determining the unique transport of I-mode is not yet understood. The identity of the WCM and the transport caused by the WCM have not been determined. A more complete physical understanding of I-mode is necessary if this regime is to be extrapolated to future fusion reactors.

There exists a limited amount of modeling and theory work related to explaining the phenomena of I-mode regime. The only modeling work related to the I-mode core is a set of validation studies which explain the reduction in core turbulence between L-mode and I-mode as related to an increase in $E \times B$ velocity shear and profile stiffness in I-mode [75], [76]. Much of the rest of the body of modeling work in I-mode focuses on the pedestal region and attempts to identify the WCM and the transport it causes. A study using the numerical fluid simulation code BOUT++ found that the C-Mod I-mode pedestal is unstable to both the drift Alfvén wave instability and the resistive ballooning mode [14]. One gyrokinetic study of the I-mode edge at C-Mod found that the WCM could be explained by an ion temperature gradient mode affected by the impurity density gradient [77], despite the low expected imurity accumulation in I-mode. Another gyrokinetic study found that the WCM is a type of instability not yet named by the literature which is sensitive to the T_e gradient and has long wavelength and low frequency [15]. Meanwhile, some theoretical work has identified the WCM as as heavy particle impurity mode [13], [78]. Other more recent theory work identifies the WCM as the leftover broadband turbulence when large and small scale

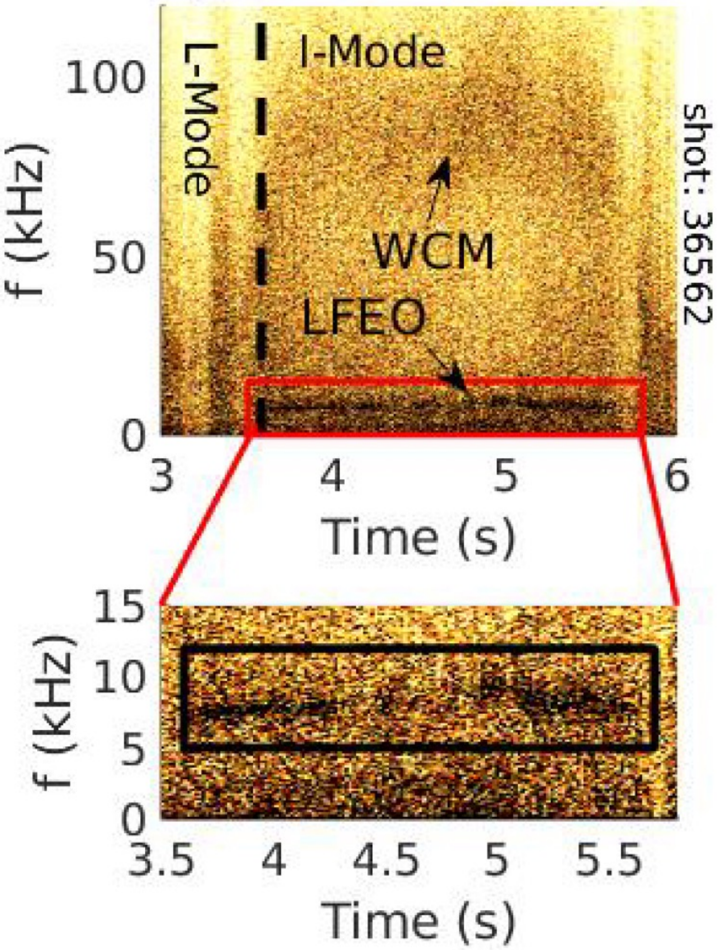

Figure 2.10: Spectrogram of reflectometer (i.e. density) fluctuations showing the WCM and LFEO during an I-mode. Figure adapted from Reference [73].

fluctuations are suppressed by phase randomization and finite-Larmor-radius effects [16]. The broad range of experimental, modeling, and theoretical observations about I-mode motivate the need for further study to gain a more complete understanding of the physics underlying this regime.

2.4 Conclusions

Gradient-driven turbulence in tokamaks limits confinement by driving the transport of heat and particle, so a fundamental understanding of turbulence phenomenology is necessary for planning future high performance fusion reactors. Changes in edge turbulence lead to high confinement operation, and the L to H transition occurs when turbulence is damped by sheared flows. This transition happens when external heating power surpasses a threshold. The power threshold is about twice as high in the unfavorable configuration compared to the favorable configuration for reasons not yet fully understood.

I-mode exists in the parameter space between L-mode and H-mode and is typically accessed in the unfavorable drift configuration. I-mode is a promising regime because it offers ELM-free, high confinement operation. These favorable properties originate because of I-mode's unique transport barrier in energy but not particles. The I-mode pedestal features the WCM fluctuation, but the identity of this mode and its associated transport are not yet understood. This thesis will show that the WCM also exists in L-mode across a wide parameter space of density and heating power.

Our picture of edge turbulence and its relation to different confinement regimes is incomplete. Experimental and modeling efforts are required to better understand the interplay of E_r, sheared flow, and turbulence across confinement regime transitions in different magnetic configurations. Further study of I-mode is needed to understand how the fluctuations in the I-mode pedestal compare with edge fluctuations in L-mode and H-mode. The next chapter will discuss the experimental and modeling techniques used in this thesis to understand edge fluctuations.

Chapter 3

Turbulence investigation techniques at ASDEX Upgrade

This thesis presents investigations of turbulence in L-mode and I-mode tokamak discharges, with a focus on fluctuations in the edge and pedestal region. To perform this investigation, the current state of the art turbulence measurement techniques and modeling routines are applied. The experimental and modeling tools are described in this chapter.

3.1 The ASDEX Upgrade tokamak

The experimental work of this thesis was carried out on the ASDEX Upgrade (AUG) tokamak at the Max Planck Institute for Plasma Physics in Garching, Germany [79]. A picture of the inside of the tokamak vacuum vessel and a schematic poloidal cross section are shown in Figure 3.1. AUG is a diverted, tungsten-walled, midsize tokamak with major radius $R_0 = 1.65$ m and minor radius $a \sim 0.5$ m, maximum magnetic field $B_T = 3.2$ T, and a maximum current $I_p = 1.4$ MA. Auxiliary heating systems include up to 20 MW of Neutral Beam Injection (NBI), 6 MW of Electron Cyclotron Resonance Heating (ECRH), and 6 MW of Ion Cyclotron Resonance Heating (ICRH).

AUG's operational goal is to prepare the physics basis for the ITER and DEMO tokamaks, and it hosts an extensive suite of over 40 diagnostics. These diagnostics allow for detailed studies of the plasma behavior, in particular the micro-scale turbulence (mm-cm characteristic scale) of interest to this thesis. AUG is a leading tokamak in the study of high confinement operation, including ELM-free high confinement regimes, and the transition from low to high confinement. Experimental studies of the H-mode power threshold [66], H-mode density limit [80], and E_r across the L to H transition [81] have increased our understanding of the transition from L-mode to ELMy H-mode operation. ELM-free high confinement regimes such as I-mode, EDA H-mode, and QH-mode have also been studied at AUG [12], [82], [83].

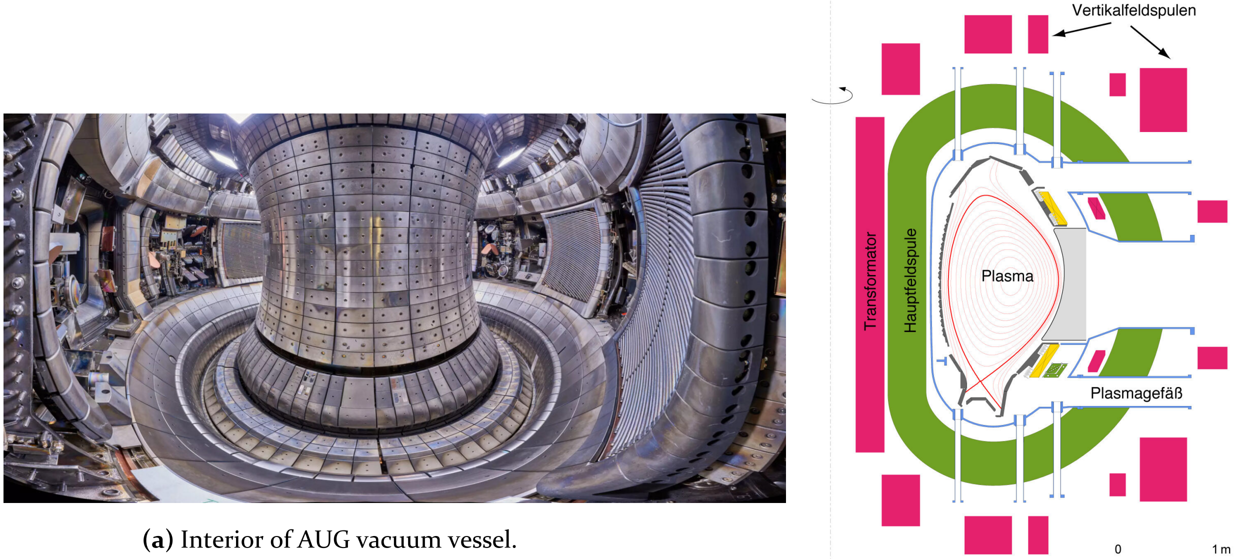

(a) Interior of AUG vacuum vessel.
Source: EUROfusion, image credit: Volker Rohde

(b) AUG poloidal cross section
Source: IPP MPG

Figure 3.1: Images of AUG interior including (a) vacuum vessel and (b) a poloidal cross section.

3.2 Experimental design at AUG

The experimental work of this thesis uses discharges at AUG specifically designed for studying different confinement regimes, with good conditions for turbulence diagnostic measurements. Several discharge parameters may be prescribed by engineering design in order to obtain plasmas of interest, including magnetic field, current, flux surface shaping, heating, density control, and others. The time histories of some of these quantities, as well as the resulting resulting core T_e and n_e obtained, are shown in Figure 3.2 for a discharge designed to study L-mode turbulence [84].

This discharge was designed with a constant -2.5 T field, which is the typical toroidal magnetic field for AUG discharges, and was designed with a Lower Single Null (LSN) with the X-point at the bottom of the plasma (as shown in Figure 2.8). The divertor at the bottom of the tokamak is equipped with cryogenic vacuum pumps for strong density control. In contrast to this L-mode discharge, I-mode plasmas at AUG are often designed with an Upper Single Null (USN) because the typical field and current directions determine this to be the unfavorable $B \times \nabla B$ direction.

The heating design (method and power waveform) of an experiment requires careful consideration when performing turbulence measurements. Although AUG is equipped with NBI, ECRH, and ICRH heating, the former two are the most often used. Both NBI and ECRH can affect turbulence measurement. NBI perturbs the plasma through the addition of hot neutrals and can affect the toroidal rotation, and ECRH can lead to nonthermal electron distributions. Also important to note is that NBI heats preferentially ions, while ECH heats electrons. NBI also injects torque and can effect toroidal rotation. Either heating source

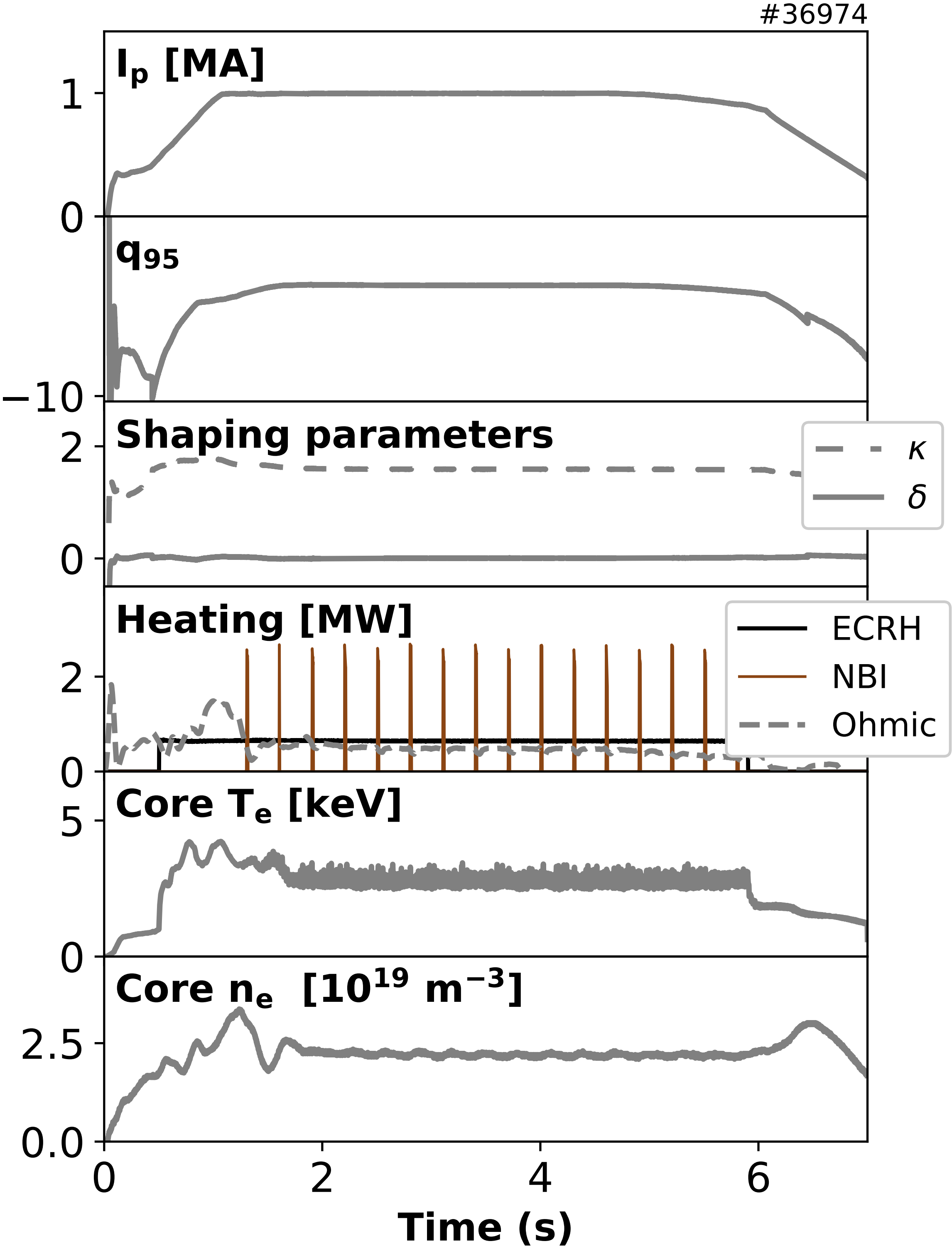

Figure 3.2: Time histories of an L-mode discharge, including pre-programmed parameters such as current, shaping, and heating, as well as the resulting core T_e and n_e.

can be used in a feedback method to maintain steady-state plasmas. For example, in I-mode experiments NBI heating has been applied in feedback to obtain a constant β_{pol} target value within a known I-mode parameter space [72]. Short NBI power blips are also required for CXRS measurements, even when NBI is not chosen as a primary method for heating.

3.2.1 Profile diagnostics

Measurements of the radial profiles of the density, temperature, rotation, etc. are important to quantify the character of the plasma and the strength of the turbulence drive and damping during an experiment. The key diagnostics used for profile measurements in this thesis are:

- Thomson scattering [85], [86], which measures n_e and T_e through laser light scattered by plasma electrons. The total scattered intensity is related to n_e and the Doppler frequency shift of the scattered spectrum is related to T_e.

- Electron Cyclotron Emission (ECE) [87], [88], which measures T_e by collecting ECE from the plasma, the intensity of which is directly proportional to electron temperature and its frequency to radial position. ECE diagnostics are discussed in detail in Section 3.3.1.

- Charge Exchange Recombination Spectroscopy (CXRS) [89], [90], which measures T_i from the light emitted from charge exchange interactions between injected neutrals and fully ionized impurity ions. The plasma velocity (v_{tor} and v_{pol}) can also be obtained through spectra Doppler shifts. Through the radial force balance, the E_r can be obtained with these measurements.

- Doppler Reflectometry [91], [92], which measures the plasma $E_r \times B$ velocity, $v_{E\times B}$, directly from the Doppler shift of a fluctuation spectrum from a backscattered microwave beam that is launched and received at a known poloidal angle to the plasma cutoff layer. The measured velocity, $v_\perp$ is given by $v_\perp = v_{E\times B} + v_{ph}$, where $v_{ph} \ll v_{E\times B}$ is the turbulence propagation velocity in the $E \times B$ frame of reference.

- Helium II spectroscopy [41] uses active spectroscopy of singly ionized helium (He) atoms to measure the E_r from the pedestal region to the scrape off layer (SOL). The methodology is the same as the determination of the E_r from CXRS, with the He pressure gradient and poloidal and toroidal velocities used in the radial force balance equation.

An integrated data analysis tool, IDA [71], [93], is often used to generate fitted n_e and T_e profiles at AUG. IDA combines diagnostic measurements for n_e and T_e using a Bayesian probability framework to calculate best quality fitted profiles. The Thomson Scattering and ECE measurements are used, as well as data from lithium beam emission spectroscopy (LIB) and deuterium cyanide laser interferometry. IDA profiles face challenges in properly capturing the pedestal, where large scatter can occur in diagnostic data.

3.3 Turbulence measurement diagnostics for the confined plasma

AUG is equipped with several diagnostics specially designed for the measurement of fluctuations. We will describe here the main diagnostics used in this work: the Correlation Electron Cyclotron Emission (CECE) diagnostic, a coupled CECE-reflectometer system, and the Thermal He beam diagnostic. In particular, the CECE diagnostic at AUG was extended as part of the work of this thesis, so its hardware and measurement technique will be explained in detail.

3.3.1 The Correlation Electron Cyclotron Emission diagnostic

ECE principles

ECE radiometer diagnostics measure the electron temperature by collecting the ECE radiation, emitted by electrons as they undergo gyro-motion around the tokamak magnetic field lines. The blackbody intensity of this emission is directly related to the plasma electron temperature, $I(f) \propto T_e(f)$. The reader is referred to Reference [94] Chapter 5 for a detailed derivation of the principles of ECE emission. The electron cyclotron frequency, ω_{ce}, is given by:

$$\omega_{ce} = \frac{eB}{m_e} \tag{3.1}$$

where e is the electron charge, B is the magnetic field, and m_e is the mass of the electron. Because $\omega_{ce} \propto B$ and the toroidal field in a tokamak varies as $B \propto 1/R$, ECE from a particular location in the tokamak can be observed by using an ECE diagnostic to collect radiation at a particular frequency.

The frequency of ECE radiation, ω, occurs in harmonics and when considering a particular diagnostic viewing angle and an electron traveling with velocity v, the emission layer is described more generally as:

$$\omega = m\omega_{ce}\frac{\sqrt{1-\beta^2}}{1-\beta_{||}\cos\theta} \tag{3.2}$$

where m is the harmonic number, $\beta = v/c$ is the relativistic factor, and θ is the angle between the diagnostic line of sight and magnetic field line about which the electron undergoes gyro-motion. The numerator, $\sqrt{1-\beta^2}$, is the relativistic mass correction and the denominator, $1-\beta_{||}\cos\theta$, is the Doppler broadening. Therefore, a population of electrons with a given distribution function will have an ECE linewidth determined by the velocity distribution and the diagnostic viewing angle.

The ECE resonance layer sets the minimum possible radial resolution of ECE diagnostics, and it is therefore beneficial to minimize the ECE linewidth. Doppler broadening can be minimized by collecting ECE perpendicular to the magnetic field. Broadening from the relativistic mass correction then sets the minimum linewidth. Hot plasmas with high thermal velocities will have wide emission layers. Non-Maxwellian distribution functions with nonthermal electron populations can also broaden the emission layer. This nonthermal emis-

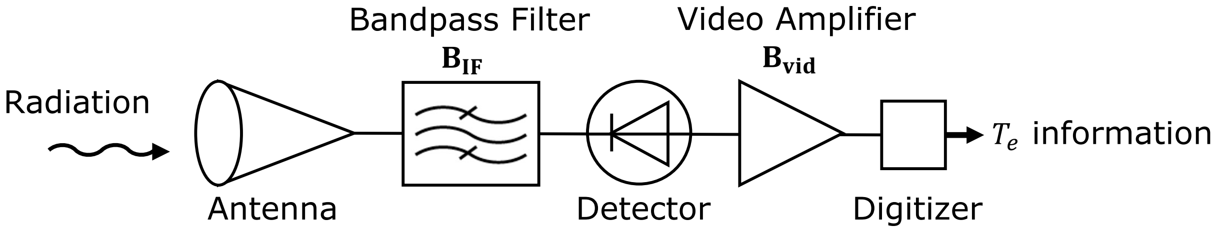

Figure 3.3: Simple radiometer hardware schematic. The ECE power received by the antenna is proportional to output voltage. The IF and video amplifiers set the sensitivity limit.

sion is of particular consideration during experiments with ECRH current drive, runaway electrons, or ELMs.

The electron temperature can be directly related to the intensity of ECE, under the assumption that the plasma acts as a blackbody and perfectly emits and absorbs all radiation at the ECE frequency. The blackbody intensity, $I_{BB}(\omega_{ce})$, of the ECE is related to the frequency and electron temperature through the Rayleigh-Jeans approximation for blackbody radiation at low frequencies:

$$I_{BB}(\omega_{ce}) = \frac{\omega_{ce} T_e}{8\pi^3 c^2} \tag{3.3}$$

The ECE is collected and processed through radiometer hardware in order to extract information about electron temperature. A radiometer is a diagnostic used to measure radiation power within a defined frequency range. A simple schematic of a radiometer is shown in figure 3.3. The ECE radiation is collected by an antenna, then frequency downshifted from the radio-frequency (RF) range to the intermediate frequency (IF) range. A bandpass filter of bandwidth B_{IF} then determines the frequency range over which radiation is detected. The power, P, measured by the radiometer is $P = TB_{IF}$, where T is the radiation temperature of the incoming signal, which will be T_e if the plasma is optically thick and acts as a blackbody. Note that the temperature here is defined in energy units. The radiation power is then detected by a square law detector and low-pass filtered by a video amplifier with bandwidth B_{vid}.

Standard ECE systems are limited in their ability to measure temperature fluctuations. The fluctuating portion of ECE signals are in part comprised by thermal noise fluctuations, which set a floor below which RMS temperature fluctuations cannot be measured. The sensitivity limit of a single radiometer channel is given by:

$$\left.\frac{\delta T}{T}\right|_{\text{lim}} = \sqrt{\frac{2B_{vid}}{B_{IF}}} \tag{3.4}$$

In standard ECE radiometers, given typical choices for B_{IF} and B_{vid}, this statistical limit may be well above 5%.

Correlation techniques

The Correlation ECE (CECE) diagnostic extracts information about electron temperature fluctuations from thermal noise by applying correlation techniques to an ECE diagnostic specially designed for these turbulence measurements. The principle of CECE is that two separate measurements of the same turbulence will have uncorrelated noise. Suppose that the fluctuating parts of two ECE signals are given by $\widetilde{T}_{e,1} = \widetilde{T}_e + N_1$ and $\widetilde{T}_{e,2} = \widetilde{T}_e + N_2$, where $\widetilde{T}_e$ is the turbulent temperature fluctuation common to both signals, and N_1 and N_2 are the incoherent noise specific to signals 1 and 2. The correlation between signals 1 and 2 is given by $R_{1,2} = \langle \widetilde{T}_{e,1}\widetilde{T}_{e,2} \rangle = \langle \widetilde{T}_e^2 \rangle + \langle N_1\widetilde{T}_{e,2} \rangle + \langle N_2\widetilde{T}_{e,1} \rangle + \langle N_1 N_2 \rangle$. Since the noise is not correlated with the temperature fluctuations, and the noise one channel is not correlated with the noise of the other, $\langle N_1\widetilde{T}_{e,2} \rangle = \langle N_2\widetilde{T}_{e,1} \rangle = \langle N_1 N_2 \rangle = 0$ and therefore $R_{1,2} = \langle \widetilde{T}_e^2 \rangle$. The background noise is removed by this correlation analysis and only information about the temperature fluctuations remains.

Correlation techniques may be used to extract fluctuation spectra and RMS fluctuation amplitude. The correlation and fluctuation amplitude calculations used in this thesis are explained in detail in Reference [95], but a summary will be given here. The complex coherence spectrum as a function of frequency, $\gamma_c(f)$, is given by:

$$\gamma_c(f) = \frac{G_{1,2}(f)}{\sqrt{G_{1,1}(f)G_{1,1}(f)}} \tag{3.5}$$

for ECE signals 1 and 2, where $G_{1,1}(f)$ and $G_{2,2}(f)$ are the one-sided auto-spectral density functions and $G_{1,2}(f)$ is the one-sided cross-spectral density function between signals x and y, given by:

$$G_{x,y} = 2F_x^*(f)F_y(f) \tag{3.6}$$

.
Here, $F_x(f)$ is the Fourier transform of signal x, made using ensemble averaging with a 50% overlapping Hanning window [96]. $F_x^*(f)$ is the complex conjugate of $F_x(f)$.

The complex coherency can be used directly in obtaining an electron temperature fluctuation amplitude, $\delta T/T$:

$$\frac{\delta T}{T} = \sqrt{\frac{2}{B_{IF}} \int_{f_1}^{f_2} \frac{Re\{\gamma_c(f) - \gamma_{bg}\}}{1 - Re\{\gamma_c(f) - \gamma_{bg}\}} df} \tag{3.7}$$

were B_{IF} is the bandwidth of the bandpass filter, f_1 and f_2 bound the frequency range of the turbulent feature, $\gamma_c(f)$ is the complex coherence, and γ_{bg} is the mean background coherence. γ_{bg} is calculated by averaging $\gamma_c(f)$ over a frequency range above the turbulent features of interest. This background coherence is similar to the coherency bias error, and the subtraction of the background level is implemented to ensure that noise unrelated to temperature fluctuations, such as that from overlapping IF filters, does not enter into the calculation of fluctuation amplitude. An example coherence spectrum is shown in Figure 3.4, which displays a turbulent feature from $f_1 = 15$ kHz to $f_2 = 175$ kHz. The value of γ_{bg}, and the frequency range over which γ_{bg} is averaged, are also shown.

The standard deviation of the complex coherence is given by [97]:

$$\sigma_{\gamma_c}(f) = \sqrt{\frac{1}{2n_d}} \left(1 - |\gamma_c(f)|^2\right) \tag{3.8}$$

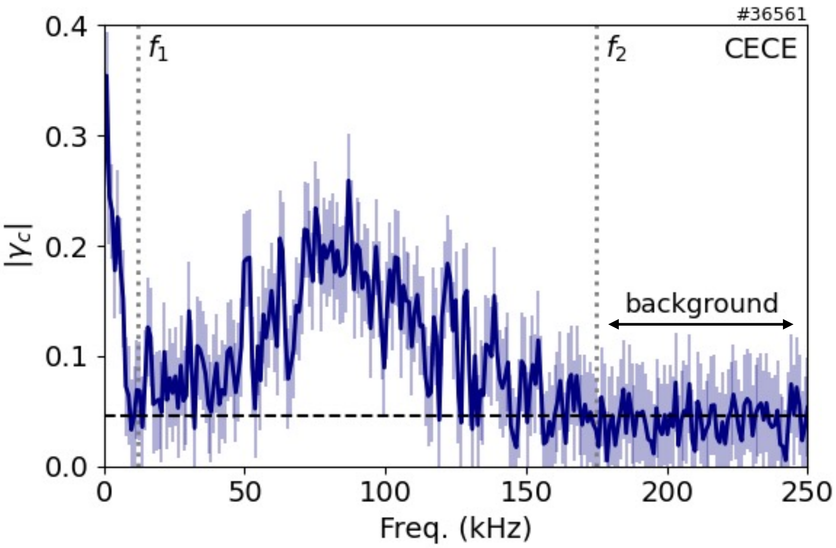

Figure 3.4: Example coherence spectrum (modulus $\gamma_c(f)$) over frequency for an I-mode discharge at the outer core radial location $\rho_{pol} = 0.93$. The frequency bounds for integration to produce $\delta T/T$ are shown by the dotted lines at f_1 and f_2. The region over which γ_c may be averaged to produce the background coherence level γ_{bg} is indicated. The horizontal black dashed line represents this averaged γ_{bg}.

where n_d is the number of windows used in the FFT ensemble averaging. The uncertainty (i.e. confidence interval or error bar) on the fluctuation amplitude is then given by:

$$\sigma_{\delta T/T} = \frac{1}{\delta T/T} \frac{1}{B_{IF}} \int_{f_1}^{f_2} \frac{\sigma_{\gamma_c(f)}}{(1 - |\gamma_c(f) - \gamma_{bg}|)^2} df \tag{3.9}$$

This uncertainty is derived by propagating the error on $\gamma_c(f)$ though Eq. 3.7. The error on B_{IF} is ignored in this analysis. This uncertainty differs from that in Ref. [95] because it does not take the limit of small $\gamma_c(f)$, but rather allows $\gamma_c(f)$ to be large, as is often the case for edge fluctuations.

Using this correlation analysis, the ideal sensitivity limit of CECE is given by [98], [99]:

$$\left.\frac{\delta T}{T}\right|_{\text{lim}} = \sqrt{\frac{2}{\sqrt{N}} \frac{B_{vid}}{B_{IF}}} \tag{3.10}$$

where N is the number of independent data points. If the statistical limit is instead determined by integrating $\sigma_{\gamma_c}(f)$ over the signal bandwidth, $B_{sig} = f_2 - f_1$, the statistical limit becomes:

$$\delta T/T|_{lim} = \sqrt{\frac{2}{\sqrt{N}} \frac{B_{sig}}{B_{IF}} \sqrt{\frac{B_{vid}}{2B_{sig}}}} \tag{3.11}$$

This adjusted statistical limit is typically lower than the the classic CECE limit, Eq. 3.10.

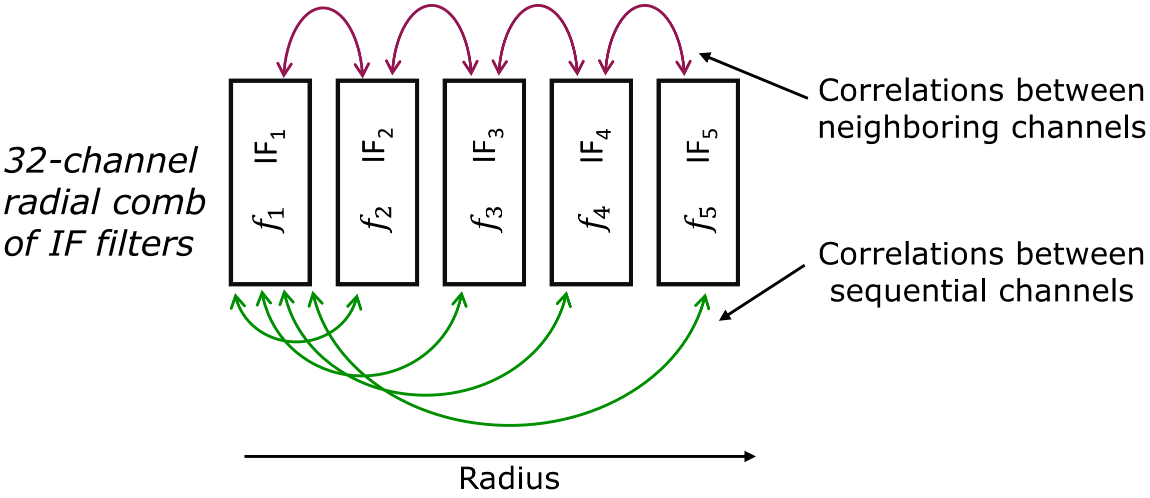

Figure 3.5: Representation of a CECE radial comb of IF filters of frequency f_1-f_5, and the possible correlations between radially neighboring or sequential channels.

Using the calculations outlined in this section, a CECE diagnostic can be used for detailed study of temperature fluctuations over radius. Examples of the correlations that can be performed with a radial comb CECE system are shown in Figure 3.5. By calculating $\gamma_c(f)$ and $\delta T/T$ between neighboring channels, the T_e turbulence fluctuation amplitude over radius may be determined. By calculating $\gamma_c(f)$ over sequential channels, the radial extent over which fluctuations are correlated may be determined. Figure 3.6 shows examples of $\delta T/T$ over radius (panel a) and the radial correlation length (panel b). Both these examples are taken from Reference [7], which performed a detailed study of core T_e turbulence at AUG using CECE.

Limitations of CECE

CECE is limited in its measurement capabilities by a number of factors inherent to ECE physics. The plasma edge is particularly susceptible to effects which make interpretation of CECE signals challenging, and special care must be taken when reporting edge T_e fluctuations.

Cutoffs

ECE measurements require that emitted radiation travels to the diagnostic receiver and be detected. For the radiation to propagate through the plasma, cutoffs must be avoided. ECE occurs in both O-mode polarization, with the emitted radiation electric field parallel to background magnetic field, and X-mode polarization, with the emitted radiation electric field perpendicular to background magnetic field. The relative strength of the polarizations are different at different ECE harmonics. At the 1st harmonic, the intensity X-mode emission is very weak, but at the 2nd harmonic X-mode emission intensity is somewhat stronger than O-mode [94]. The O and X-mode waves face different cutoffs in the plasma, past which the refractive index for the wave is below zero and the wave cannot propagate. The cutoff frequencies are visualized over the radius of a typical AUG discharge in Figure 3.7.

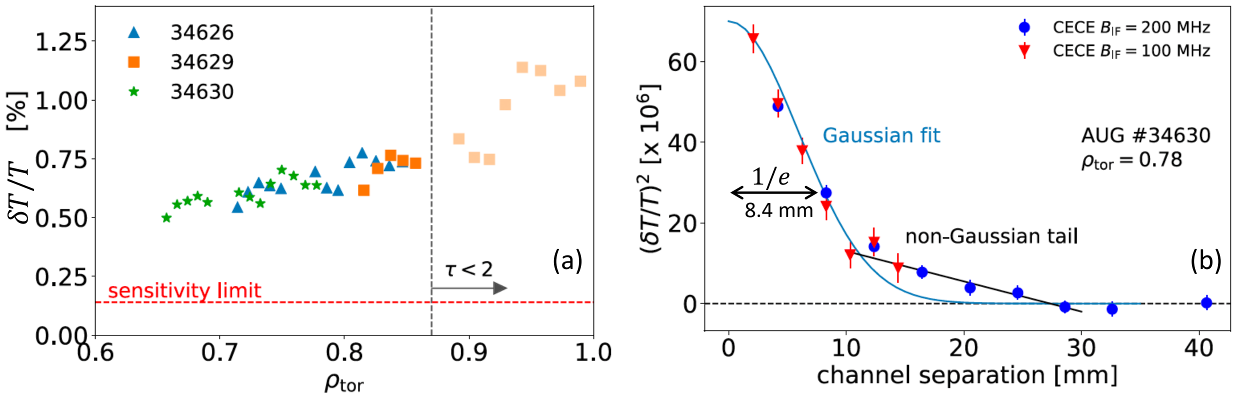

Figure 3.6: Examples of CECE measurements which give information about the radial structure of T_e turbulence, adapted from Reference [7]. (a) $\delta T_e/T_e$ over normalized radius (ρ_{tor} here) can be determined through correlations of radially neighboring CECE channels. The optically thin $\tau < 2$ region is indicated. (b) the radial correlation length of T_e turbulence is calculated through correlations of radially sequential channels. The correlation function has a Gaussian shape with an elongated tail, and the $1/e$ with of the Gaussian portion is 8.4mm.

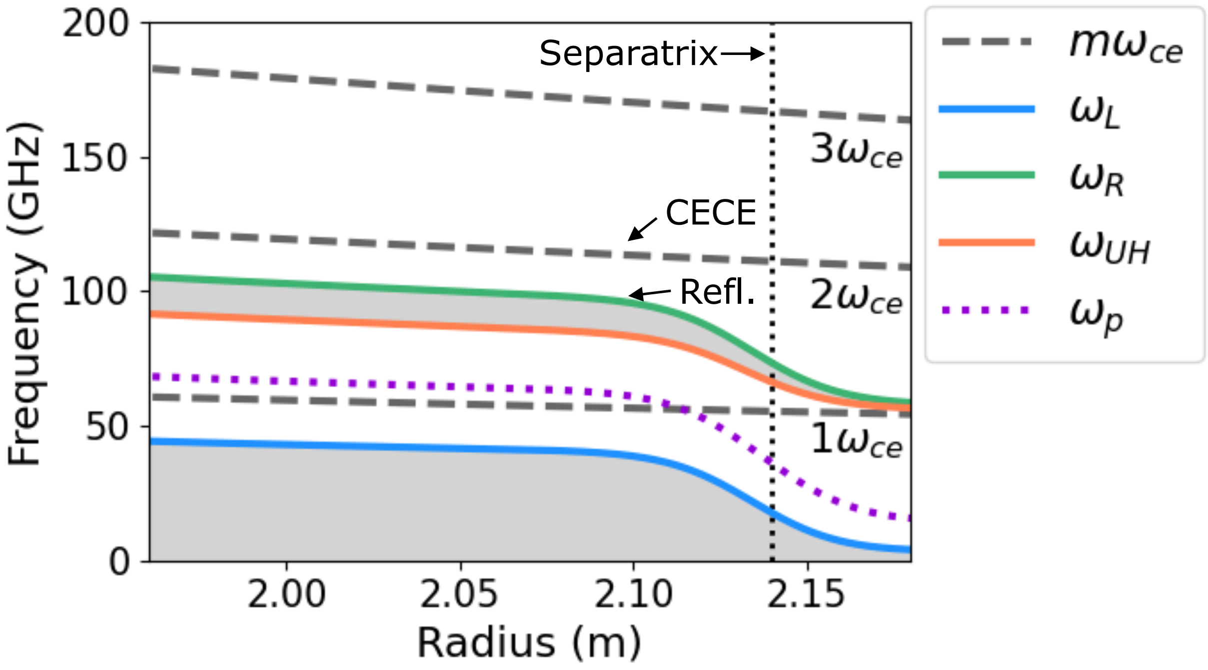

Figure 3.7: The first three harmonics of the electron cyclotron resonance frequency and the cutoffs relevant to ECE diagnostics for a typical AUG magnetic field ($B_{T0} = -2.5$ T) and L-mode density profile (with core $n_0 = 7.1 \times 10^{19}$ m^{-3}). The regions cutoff for X-mode ECE are shaded. The right-hand cutoff determines the location of X-mode reflectometer measurements and the 2nd harmonic ECE resonance determines the location of CECE measurements.

The O-mode cut-off occurs when the wave frequency ω is less than the plasma frequency ω_p, or:

$$\omega < \omega_p = \sqrt{\frac{n_e e^2}{m_e \epsilon_o}} \tag{3.12}$$

where e is the electron charge, m_e is the electron mass, and ϵ_o is the vacuum permittivity. In cases where n_e is too high, significant regions of the plasma may be cutoff, therefore O-mode polarization is not a common choice for ECE diagnostics.

X-mode waves of frequency ω are cut-off when $\omega_{UH} < \omega < \omega_R$ and $\omega < \omega_L$ where ω_{UH} is the Upper Hybrid resonance frequency:

$$\omega_{UH} = \sqrt{\omega_{ce}^2 + \omega_p^2} \tag{3.13}$$

and ω_R and ω_L are the right and left-hand cut-off frequencies:

$$\omega_{R,L} = \frac{1}{2}\left(\sqrt{1 + 4\left(\frac{\omega_p}{\omega_{ce}}\right)^2} \pm \omega_{ce}\right) \tag{3.14}$$

In addition to very weak X-mode emission at the 1st ECE harmonic, X-mode emission at this harmonic is also always cut off on the low field side of the plasma. Therefore, the 2nd harmonic X-mode is a popular choice for tokamak ECE diagnostics. n_e enters into the X-mode cutoffs through ω_p, and at high enough density, 2nd harmonic X-mode ECE can also face cutoff. At densities close to the cutoff density, the EC wave index of refraction can differ from 1. In these cases, the plasma curvature can cause and bending of the ECE rays due to refraction, resulting in a deflection of the diagnostic line of sight.

Optical depth

The plasma's ability to act as a blackbody for ECE at a particular location depends on the local electron density and temperature. The transport of ECE through plasma may be described by:

$$\frac{dI(\omega_{ce})}{ds} = j(\omega_{ce}) - I(\omega_{ce})\alpha(\omega_{ce}) \tag{3.15}$$

where $I(\omega_{ce})$ is the intensity, or the radiative power per unit frequency per unit solid angle. s is the radiation path length. $j(\omega_{ce})$ is the emissivity, or the rate of emission of energy per unit frequency per unit solid angle. $\alpha(\omega_{ce})$ is the fractional rate of absorption of radiation per unit path length. The optical depth, τ is determined by the absorption coefficient by:

$$\tau = \int \alpha(\omega_{ce}) ds \tag{3.16}$$

When the plasma is optically thick, Kirchoff's law determines that:

$$I_{BB}(\omega_{ce}) = \frac{j(\omega_{ce})}{\alpha(\omega_{ce})} \tag{3.17}$$

where I_{BB} is the blackbody intensity.

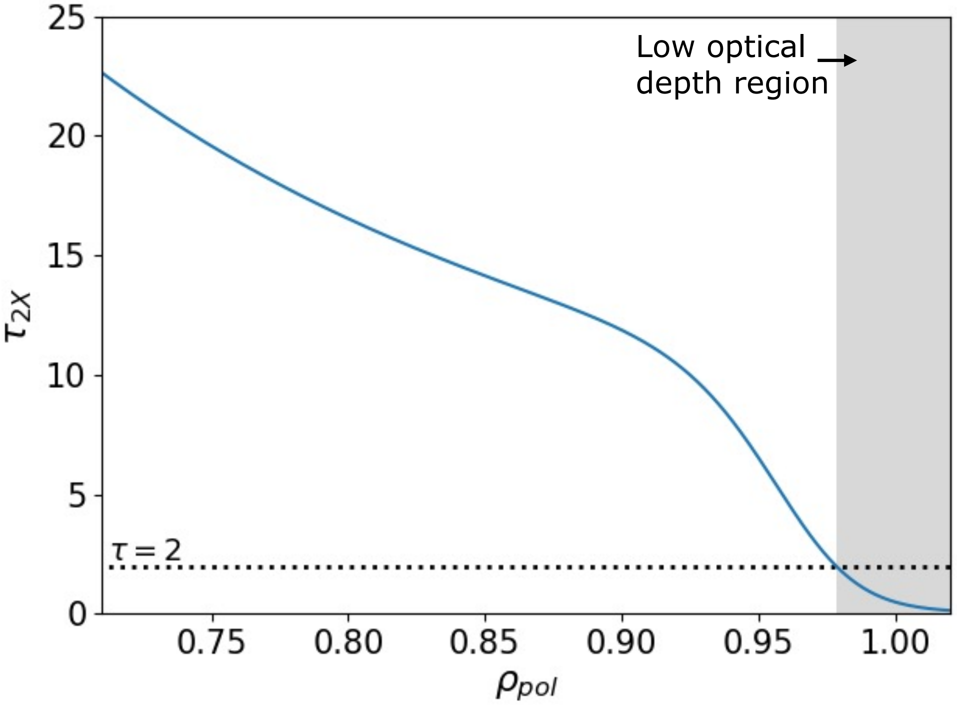

Figure 3.8: Example profile of τ_{2X} over normalized radius ρ_{pol} for typical AUG L-mode kinetic profiles. The region of low optical depth ($\tau < 2$) is shaded, starting at $\rho_{pol} \sim 0.98$ and continuing outwards.

The measured intensity can be solved for, and is given by:

$$I = \frac{\omega_{ce}^2 T}{8\pi^3 c^2}(1 - e^{-\tau}) \tag{3.18}$$

When $\tau \gg 1$, $I = \frac{\omega_{ce}^2 T}{8\pi^3 c^2}$ and the temperature can be directly determined by collecting ECE emissions. Plasmas with $\tau > 2$ are considered "optically thick".

By integrating the absorption coefficient, the optical depth may be determined, as performed in References [100] and [101]. For the case of perpendicular 2nd harmonic X-mode radiation far from cutoff, a simplification is:

$$\tau_{2X} = \frac{2\pi^2 R_o}{\lambda_o} \frac{\omega_p^2}{\omega_{ce}^2} \left(\frac{v_t}{c}\right)^2 \tag{3.19}$$

Where R_o is the plasma major radius, $\lambda_o = 2\pi c/\omega_{ce}$, and the thermal velocity $v_t = \sqrt{T_e/m_e}$. The important dependencies are that τ_{2X} is proportional to the plasma density through ω_p and temperature through v_t^2.

Optical depth has implications for edge turbulence measurements performed with CECE. One consideration is the localization of the birthplace distribution of ECE in the optically thin edge. For example, a "shine-through" peak can occur in the pedestal and SOL region of H-mode plasmas [88], [102], [103]. Shine-through occurs when EC absorption is low at the cold resonance position, and downshifted radiation from the tail of the Maxwellian distribution originating at the pedestal top can pass through cold resonance layers and contribute to an nonphysical peak in T_e in the pedestal or SOL. When mapping ECE measurements to radial locations in the edge, a local approximation for ECE may not hold, to properly capture CECE measurement locations, ECE forward modeling may be needed to capture ECE resonance position [103].

An additional consideration for low optical depth measurements is that density fluctuations, $\delta n_e/n_e$, may have an impact on the measured radiated temperature fluctuations, $\delta T_{rad}/T_{rad}$, from CECE. In optically thin plasmas, one may not assume $\delta T_{rad}/T_{rad} = \delta T_e/T_e$. The effect of these density fluctuations is derived in Ref. [104]. The electron density and temperature fluctuation contributions to $\delta T_{rad}/T_{rad}$ can be represented by:

$$\frac{\delta T_{rad}}{T_{rad}} = \left((1+A)^2 \left(\frac{\delta T_e}{T_e} \right)^2 + A^2 \left(\frac{\delta n_e}{n_e} \right)^2 + 2A\,(1+A)\,\frac{\mathrm{Re}[\langle \delta T_e \delta n_e \rangle]}{T_e n_e} \right)^{1/2} \tag{3.20}$$

where

$$A = \frac{\tau e^{-\tau}}{1-e^{-\tau}} \left(1 - \chi \frac{1-e^{-\tau}}{1-\chi e^{-\tau}} \right) \tag{3.21}$$

and χ is the reflectivity of the tokamak wall. Information about the phase between the density and temperature fluctuations, α_{nT}, is contained within the $\langle \delta T_e \delta n_e \rangle$ term. One cannot exactly quantify the effect of n_e fluctuations on CECE signals without measurements of $\delta n_e/n_e$, χ, and α_{nT}, none of which are standard measurements.

In order to understand the possible effects of n_e fluctuations under different conditions, a calculation of T_{rad} fluctuation amplitude from Eq. 3.20 is shown in Figure 4.10. For $\delta T_e/T_e = 1.0\%$, the value of $\delta T_{rad}/T_{rad}$ which would be measured by CECE is plotted over a range of τ for a number of plausible $\delta n_e/n_e$ values. Low and high wall reflectivity are investigated, using $\chi = 0.31$ to approximate a low reflectivity silicon carbide wall and $\chi = 0.85$ to approximate a high reflectivity metal wall [105]. In panels (a) and (b), $\alpha_{nT} = 170°$ (close to out-of-phase n_e and T_e fluctuations) is investigated, and in panels (c) and (d) $\alpha_{nT} = 10°$ (close to in-phase n_e and T_e fluctuations) is investigated. Previous α_{nT} measurements have indicated that n_e and T_e fluctuations for typical drift wave turbulence are usually out-of-phase [7], [106]–[108], and the tungsten metal walls of AUG are expected to be highly reflective. Panel (b) is therefore most closely represents the expected impact of density fluctuations on the measurements presented in this thesis, but without measurements of all quantities in Eq. 3.20, there is uncertainty on the relationship between $\delta T_{rad}/T_{rad}$ and $\delta T_e/T_e$. This thesis will present measurements of edge and pedestal plasmas, which are in some cases regions of marginal optical depth. For this reason, many of the reported pedestal measurements will be reported as T_{rad} rather than T_e. Information about T_{rad} is still rich in physics and provides valuable information about edge turbulence behavior.

CECE design at AUG

The CECE system at AUG has been expanded in the work of this thesis from its original 24-channel radial comb, described in Reference [95] to a modular 60 channel system, with

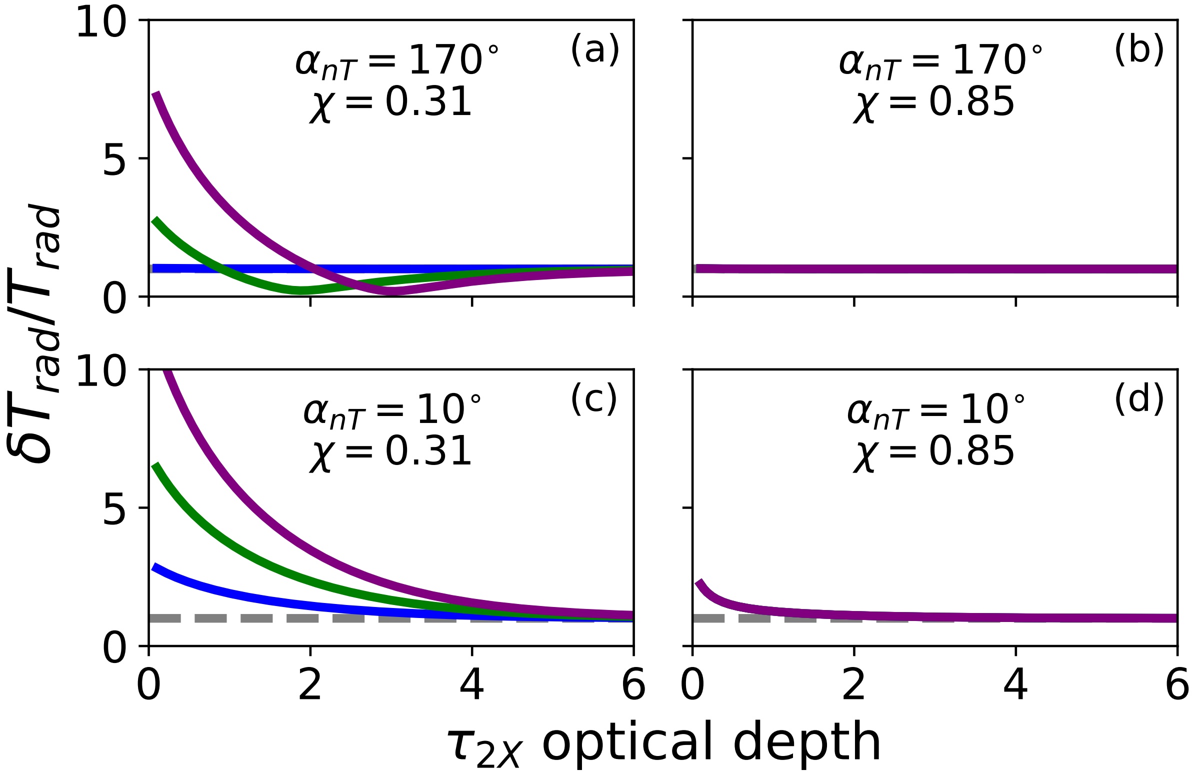

Figure 3.9: The value of $\delta T_{rad}/T_{rad}$ which would be measured by CECE as a function of optical depth, over a range of $\delta n_e/n_e$ if the actual $\delta T_e/T_e = 1\%$, for a variety of α_{nT} and χ values. Panel (b) with out-of-phase density and temperature fluctuations, and high wall reflectivity is likely closest representation of the measurement scenario at AUG.

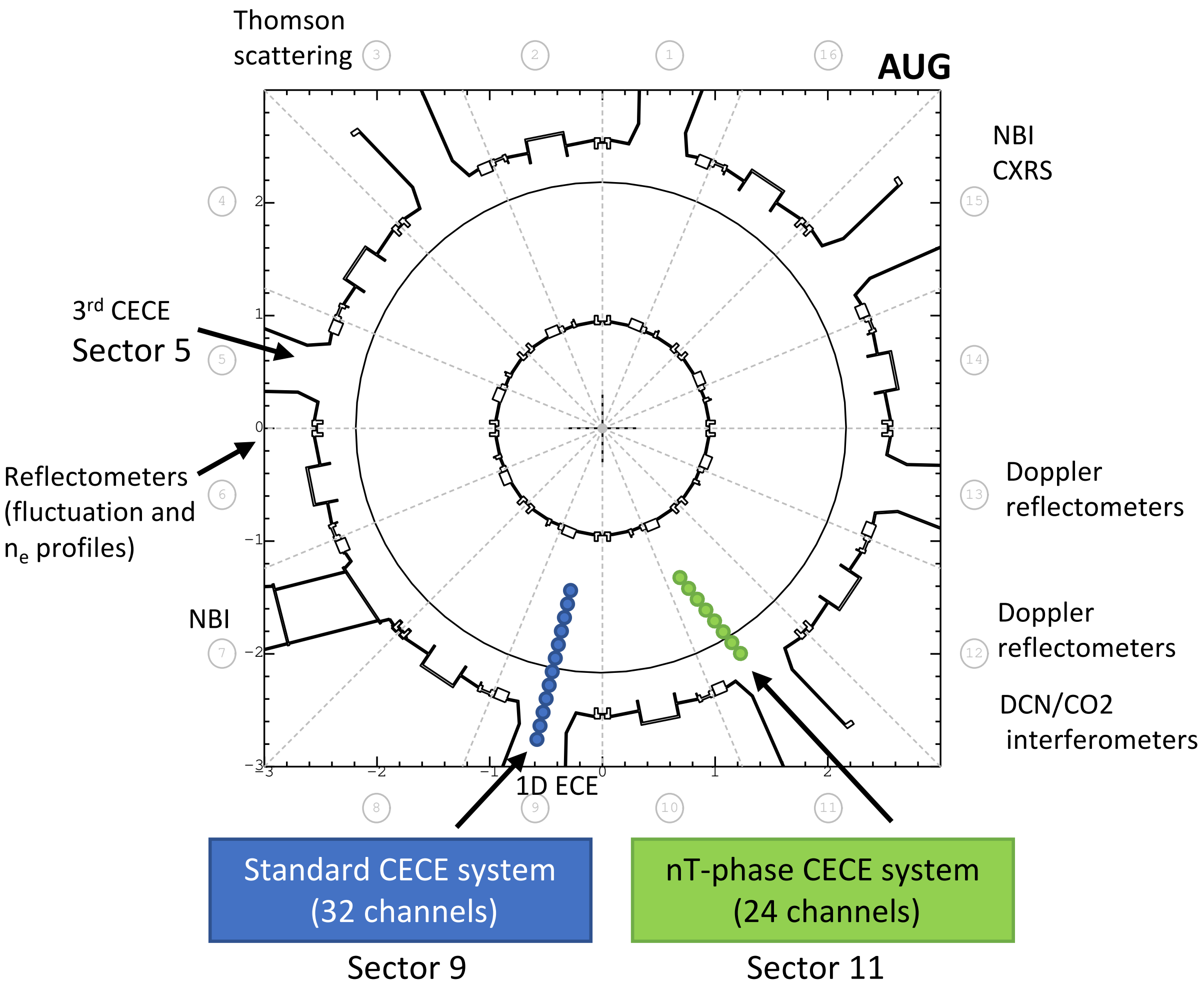

Figure 3.10: Top down schematic view of the AUG vessel, with the toroidal locations of the standard CECE and nT-phase CECE systems indicated. The toroidal locations of other important diagnostic and heating systems are also shown.

interchangeable front end RF sections and plasma access at a number of different toroidal locations on AUG. A top-down view of the tokamak and the CECE system locations is shown in Figure 3.10. The current system is comprised of the "standard" CECE system, which has 32 channels and shares optics with the ECE system at AUG, in the toroidal "sector 9" of the tokamak. The "nT-phase" CECE system was comprised of 24 channels and was placed in "sector 11" a toroidally separate location than the standard CECE system. The hardware schematic of the CECE design at AUG is shown in Figure 3.11. A third CECE location in toroidal "sector 5" was also explored during the work of this thesis, but results from this setup will not be presented.

The front-end optics determines the turbulence wavenumbers to which the CECE system is sensitive. CECE can only detect turbulence with characteristic wavelengths larger than the $1/e$ beam power width determined by the optical setup. The optical setup for the standard CECE system, shared with the 1D ECE system in sector 9, is comprised of a

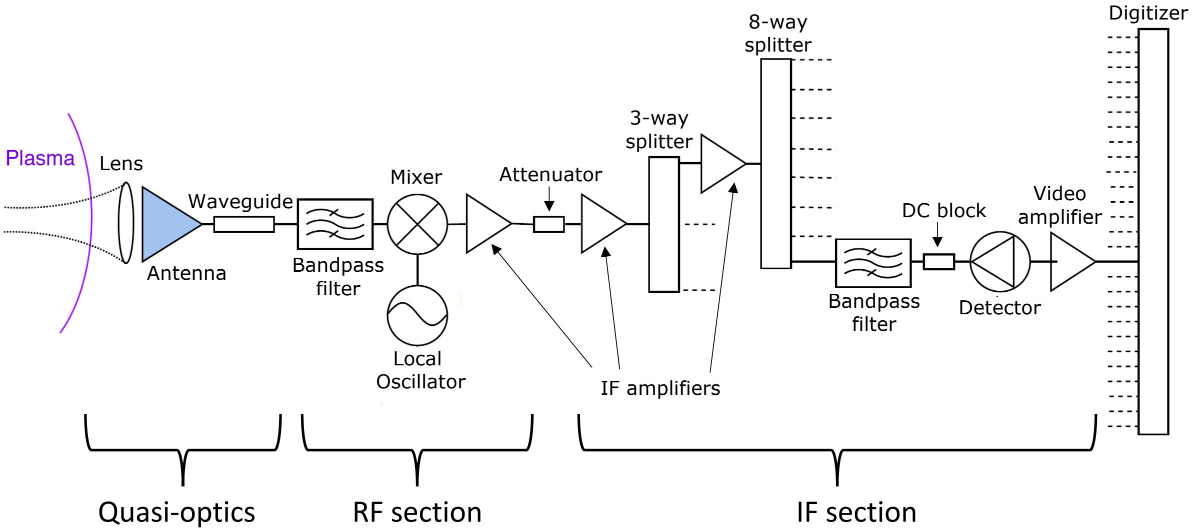

Figure 3.11: Hardware schematic of the AUG CECE designs. From the plasma out, the components include quasi-optics, an RF section, an IF sections, and a digitizer.

quartz window to the vacuum vessel, three high-density polyethylene focusing lenses, and an X-mode polarizing grid. ECE is collected with a 25dB gain D-band rectangular horn antenna, and a waveguide transition couples the D-band to F-band waveguide. The F-band waveguide connects the optics to the radiofrequency (RF) section, which sits on a sliding rail. The rail can move the antenna along a radial distance of 60mm to optimize the location of the beam waist for core versus edge measurements. Gaussian optics calculations determine that the beam diameter within the plasma reaches a minimum of 1.4 cm [84].

The front-end optics of the nT-phase CECE system in sector 11 were shared with the steerable Doppler reflectometers during the measurements presented in this thesis. This optical system consisted of a steerable elliptical mirror, a smooth-bore broadband Gaussian-beam antenna, an oversized circular waveguide, two waveguide tapers and transitions, and a short section of fundamental F-band waveguide. The beam diameter from this optical setup reaches a minimum of approximately 3.0 cm in the plasma outer core [7]. With a beam waist approximately twice as large as the standard CECE system, the nT-phase system is somewhat less sensitive to small-scale fluctuations.

The CECE systems at AUG have interchangeable RF front ends (downconvertor, mixer, and tunable Gunn diode source) which can be swapped to optimize for either core or edge measurements. The RF section is designed to downconvert the frequency of the incoming ECE signal to the IF range of frequencies (2-12 GHz here) for ease of signal collection. First, an F-band waveguide bandpass filter selects a range of incoming ECE signal with which to mix the local oscillator (LO) frequency. The RF bandpass filter frequency range may be the upper sideband (USB) or lower sideband (LSB) with respect to the LO frequency. The LO frequency is generated by a V-band varactor-tuned Gunn Oscillator and isolator. This tuning (±1GHz) allows for flexibility in the measurement range. The Gunn oscillator pumps a subharmonic mixer and the IF output is followed by a first stage of IF amplification with a

LO frequency (GHz)	Sideband filter (GHz)	CECE locations (ρ_{pol})
12em107	USB: 109-125	0.81-1.04
12em112	USB: 114-128	0.65-0.85
22em115	USB: 117-125	0.48-0.80
	LSB: 105-113	0.97-1.16

Table 3.1: RF section LO frequency, sideband filter frequency range, and resulting CECE measurement location range for a discharge with typical 2.5 T magnetic field and typical shaping.

43dB gain low-noise amplifier. The specifications of the interchangeable RF sections at AUG are shown in Table 3.1, including the LO frequencies, bandpass filter range, and estimated CECE measurement range for the 32 channel standard CECE system during a typical AUG discharge with $B_o = 2.5$T. The interchangeable RF sections give the possibility of core or edge measurements during a given experiment. Expansions are currently underway to make simultaneous core and edge measurements possible.

The IF sections (2-12 GHz) of both systems begin with a amplifier/divider chassis. The standard CECE system uses two 30dB low noise amplifiers and the nT-phase system uses a 30dB and 40dB amplifier prior to splitting the signal by 4 or 6 ways with power dividers before continuing to the IF "filter chassis". Additional low-noise amplifiers follow the power dividers. These are 30dB amplifiers in the standard CECE system and 20dB amplifiers in the nT phase system. In between are various IF attenuators to optimize the signal levels at each stage.

The IF filter chassis are modular, 8-channel chassis with identical hardware in each chassis except for the frequencies of the bandpass filters. Each chassis contains an eight-way power splitter, IF bandpass filters, DC blocks, Schottky diode detectors, and video amplifiers with custom-fitted 1 MHz low-pass anti-aliasing filters. The IF filters have a 200 MHz bandwidth and are arranged in a comb of frequencies spaced 250 MHz apart, with center frequencies covering the IF range (2-12 GHz). The last stage of the CECE hardware is digitization. Each CECE system uses two pairs of synchronized 16-channel, 14 bit digitizers, which sample at 4 MHz.

3.3.2 Coupled CECE-reflectometer system

The phase between electron density and temperature fluctuations, α_{nT}, can be measured through coupled CECE and reflectometer diagnostics. A description of the first α_{nT} measurements at AUG is given in Ref. [7], and the α_{nT} measurements in this thesis use an identical diagnostic setup. An nT-phase diagnostic is created with the 24-channel nT-phase CECE system coupled with an X-mode W-band (75-110 GHz) and two O-mode V-band (50-75 GHz) reflectometers. These reflectometers are usually operated in "Doppler" mode by tilting a poloidally steerable mirror. However, during α_{nT} measurements, the reflectometers are operated in standard normal incidence mode. As shown in Figure 3.12, the CECE and reflectometer systems share the same oversized waveguide and both systems are focused with the ellipsoidal mirror share a line of sight. The systems are coupled with a 3dB wire-grid

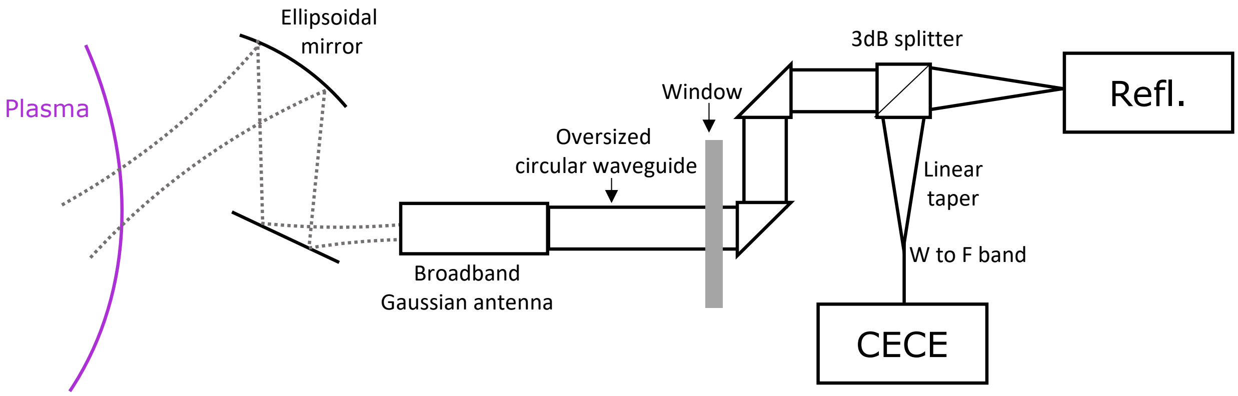

Figure 3.12: Hardware schematic of the AUG nT-phase quasi-optical components, shared by the reflectometer and CECE systems during α_{nT} measurements. The reflectometer launch antenna is not pictured.

splitter in the oversized circular waveguide section. The reflectometers and the CECE system also shares the same digitization system.

Reflectometers measure density by launching an electromagnetic wave towards the plasma, which reflects off the plasma cutoff and returns to the receiver. The time delay between the launched and received waves gives information about the location of the cutoff layer. Fluctuations in the cutoff layer correspond with fluctuations in density. The cutoffs of X-mode and O-mode systems are represented in Figure 3.7. In order to measure α_{nT}, the locations of the reflectometer cutoff and the CECE 2nd harmonic resonance must align closely, within a turbulence correlation length (typically sub-centimeter). These measurements often require repeat discharges so that the plasma density profile can be determined and the appropriate reflectometer probe frequency chosen. The reflectometers may also be swept over several frequencies to probe several different cutoff locations.

The reflectometer heterodyne receiver has in-phase (I) and quadrature (Q) detection. For the α_{nT} measurements presented in this thesis, the reflectometer amplitude, $\sqrt{I^2+Q^2}$, is used in the correlations with the CECE signals. At low density fluctuation levels, modeling has shown that fluctuations in the reflectometer phase signal are proportional to the density fluctuation amplitude, while at higher density fluctuation levels (as expected towards the plasma edge), fluctuations in the reflectometer amplitude signal are proportional to the density fluctuation amplitude [109]–[112]. The reflectometer amplitude has been seen to have higher correlation with CECE as compared to its phase [106]. When there is a frequency range in which the CECE and reflectometer signals (S_{T_e} and S_{n_e} respectively) display a detectable level of coherency, γ_c, then α_{nT} may be calculated as:

$$\alpha_{nT} = \arg\left(S^*_{T_e} S_{n_e}\right) \tag{3.22}$$

with a statistical uncertainty in radians given by [97]:

$$\sigma_{\alpha_{nT}} = \sqrt{\frac{1}{2n_d}\left(\frac{1}{|\gamma_c|^2 - 1}\right)} \tag{3.23}$$

where n_d is the number of independent samples used to calculate γ_c.

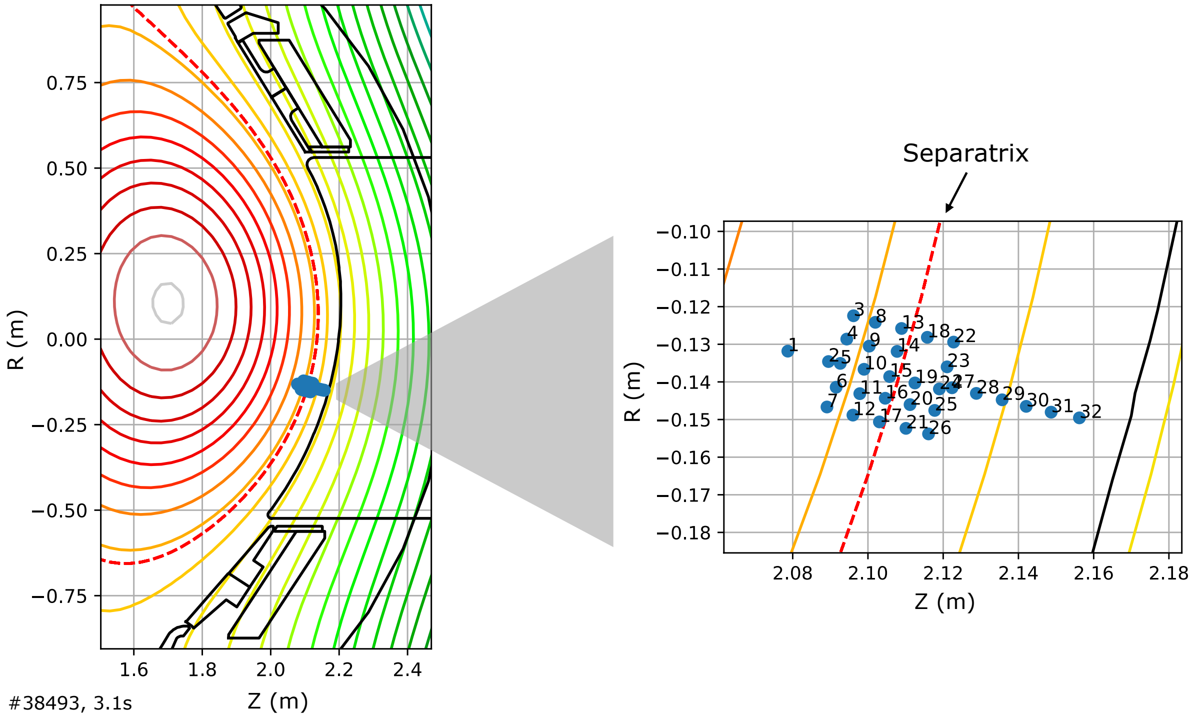

Figure 3.13: Geometry of the Helium beam spectroscopy system is shown, including its poloidal location in the vacuum vessel (left) and the 2D 32-channel array (right). The dashed red line is the separatrix ($\rho_{pol} = 1.0$) and the colored contours represent ρ_{pol} surfaces.

3.3.3 Thermal Helium beam diagnostic

The thermal He beam spectroscopy diagnostic at AUG is used to study the 2D structure of edge fluctuations in the experiments presented in this thesis. Details of the diagnostic operation are presented in [113] and [114]. The He beam emission spectroscopy system measures local He I emission in 32 radially and poloidally spaced channels. The geometry of the 32 channels is shown in Figure 3.13. The 2D grid of channels has 3mm spatial resolution. The diagnostic line-of-sight covers a radial range of 8.5 cm, spanning both the confined plasma inside the separatrix and the SOL plasma. The poloidal location is below the midplane. Correlations between radially and poloidally spaced channels may be performed similarly to the CECE correlation analysis previously presented.

To measure emission from excited He, neutral He is injected to the plasma by a piezo valve. Emitted light at the intersection of injected He beam and the diagnostic LOS is collected by an optical head and focused onto optical fibers. A polychromater separates the light from each channel into different spectral lines (587.6 nm, 667.8 nm, 706.5 nm, and 728.1 nm), and then detected by fast photo-multiplier tubes which allow a 900 kHz temporal resolution.

The intensity of the collected light is proportional to both the plasma electron density and temperature. The intensity, I_x, for a particular He I line, x, can be represented as:

$$I_x = n_{He} n_e \mathrm{PEC}_x(n_e, T_e) \tag{3.24}$$

where $\mathrm{PEC}_x(n_e, T_e)$ is the photon emissivity coefficient for the particular He I line. The He I singlet and triplet states respond differently to changes in n_e and T_e. The ratio of singlet to triplet states can be used for determining T_e, and a collisional radiative model combined with the ratio of singlet or the ratio of triplet states can determine n_e. For the He beam spectroscopy measurements presented in this thesis, no attempt is made to distinguish between the density and temperature fluctuation components, and the fluctuations of signal intensity are expected to be a mixture of both quantities.

3.4 Modeling techniques

Diagnostics provide valuable information about the plasma turbulence in experiment, but are constrained by diagnostic limits and data processing techniques. Computational (e.g. gyrokinetic turbulence) models are a useful way to gain deeper insights into turbulence behavior, as modeling outputs generally contain more complete information about the plasma state. However, well validated models are only as reliable as their inputs. In the case of plasma turbulence and transport codes, validation is still an ongoing exercise and models are not well validated for all regions of the plasma. Models are used in this thesis, with careful consideration of their caveats, because they add valuable information about the nature of plasma turbulence in L-mode and I-mode states. The two models used in this work are gyrokinetic (GK) and gyrofluid (GF) models.

The basis of these models is a kinetic formulation of the plasma, coupled with Maxwell's equations. A kinetic treatment of the plasma involves the distribution function $f_s(\vec{x}, \vec{v}, t)$ for species s which depends on three-dimensional position $\vec{x}$ and velocity $\vec{v}$. The evolution of the distribution can be described by the Boltzmann Equation:

$$\frac{Df_s}{Dt} = \frac{\partial f_s}{\partial t} + \vec{v} \cdot \nabla f_s + \vec{a} \cdot \nabla_v f_s = C\left(f_s\right) \tag{3.25}$$

where $\vec{a}$ is the acceleration experienced by particles due the Lorentz force: $\vec{a} = \frac{q_s}{m_s}\left(\vec{E} + \vec{v} \times \vec{B}\right)$ where q_s and m_s are the charge and mass respectively of species s, and $\vec{E} = E\left(\vec{x}, t\right)$ and $\vec{B} = B\left(\vec{x}, t\right)$ are the electric and magnetic fields respectively. $C\left(f_s\right)$ is a collision operator, which accounts for the effect of collisions on the phase-space distribution of particles.

The Boltzmann equation is coupled to Maxwell's equations:

$$\nabla \cdot \vec{E} = \frac{\rho_c}{\epsilon_o} \tag{3.26}$$

$$\nabla \cdot \vec{B} = 0 \tag{3.27}$$

$$\nabla \times \vec{E} = -\frac{\partial \vec{B}}{\partial t} \tag{3.28}$$

$$\nabla \times \vec{B} = \mu_o\left(\vec{J} + \epsilon_o \frac{\partial \vec{E}}{\partial t}\right) \tag{3.29}$$

where ϵ_o and μ_o are the vacuum permittivity and permeability respectively, charge density $\rho_c = \sum_s q_s n_s$, and current density $\vec{J} = \sum_s \vec{J}_s$. The number density n_s and current density J_s of species s are defined as:

$$n_s = \int f_s d\vec{v} \tag{3.30}$$

and

$$\vec{J}_s = q_s \int \vec{v} f_s d\vec{v} \tag{3.31}$$

This kinetic formulation contains extensive detail of the plasma behavior, but it is a six-dimensional problem with three spacial dimensions and three velocity dimensions. To ease analytical and computational requirements, this model is reduced.

3.4.1 Gyrokinetic models

The gyrokinetic model makes the six-dimensional kinetic problem into a five-dimensional problem. Rather than tracking the complete gyro-motion of particles, the gyrokinetics formulation instead tracks the guiding center, and only considers the velocities parallel and perpendicular to the magnetic field, thereby reducing the velocity space dimensions from three to two.

A key assumption of the gyrokinetic formulation is that the important transport processes occur at frequencies much lower than the cyclotron frequency of the species considered, ω_s. The ordering assumptions included in the gyrokinetic model are given by [115]:

$$\frac{\omega}{\omega_s} \sim \frac{k_\parallel}{k_\perp} \sim \frac{\delta v_E}{v_{ts}} \sim \frac{\delta n_s}{n_o} \sim \frac{B_1}{B_o} \sim \frac{\rho_s}{L_n} \sim \mathcal{O}(\epsilon_g) \tag{3.32}$$

where ϵ_g is the smallness parameter (e.g. $\omega \ll \omega_s$) and ω is the characteristic turbulence frequency. $k_\parallel$ and $k_\perp$ are the parallel and perpendicular components respectively of the turbulence wavenumbers. δv_E is the perturbed $E \times B$ drift velocity and $v_{t,s}$ is the thermal velocity of the species. δn_s and n_o are the perturbed and background density of the species. B_1 and B_o are the perturbed and background magnetic field. ρ_s is the Larmor radius of species s and L_n is the density gradient scale length.

A derivation of the theoretical formulation of gyrokinetics is beyond the scope of this thesis, but its details can be found in several references [115]–[119]. In this work, we use gyrokinetic codes as tools to better understand the nature of the turbulence in the plasmas also studied experimentally. The gyrokinetic ordering assumptions help us understand the regions in which it is valid to apply gyrokinetics codes. For example, the orderings state that the gyroradius of the species investigated is small compared to background gradient scale length. Although this assumption holds in the plasma core, it can break down in the steep gradient region of the pedestal. The assumption that the perturbed density is small compared to its background value is true for drift wave turbulence, but may not hold for the large fluctuations present in the plasma edge. Overall, gyrokinetics is a useful formulation for exploring turbulence physics, but great care must be taken when applying this model to the plasma edge.

Computational approach to gyrokinetics

Several gyrokinetic codes have been created for application to tokamak plasmas. The CGYRO code is the computational gyrokinetic tool used in this thesis. A description of the CGYRO approach to evolving the gyrokinetic system is given in [120]. The form of the collision operator differentiates CGYRO from predecessor codes. The CGYRO treatment of collisions is optimized for the more collisional edge region. Although several options of collision operators are included in the CGYRO code, the most complete is the Sugama operator [121], which is a model for the complete linearized, gyroaveraged Fokker-Planck operator [122], and includes unlike particle collisions.

CGYRO uses a unique spectral formulation and a Eulerian solver to evolve the distribution function and fields. The space coordinates are field-aligned and the discretization is fully spectral in the radial and binormal directions. In order to optimize the implementation of the collision operator, velocity space is represented by energy and pitch angle with pseudo-spectral meshes. CGYRO is a δf code, meaning it solves for the perturbed, non-adiabatic part of the distribution function, approximating the background distribution function as a Maxwellian. Once the distribution function is determined, the fluxes may be determined by integrating over the appropriate quantities.

CGYRO is a local or "flux-tube" code, which simulates the plasma only in the vicinity of a single magnetic field line. A local solver uses fixed background gradients and periodic boundary conditions. In contrast, global codes simulate an extended domain and allow equilibrium parameters to vary across the domain. Local simulations cannot self-consistently evolve profiles or study time-dependent phenomena as global simulations can, but local simulations are computationally cheaper.

Linear stability analysis can be performed by running CGYRO in the linear initial value mode. In this mode, the real frequency (ω_r) and growth rate (γ) of the most unstable mode in the plasma can be obtained. A linearly unstable mode will have the form:

$$\widetilde{\phi}(t) = \widetilde{\phi} e^{-i\omega_r t + \gamma t} \tag{3.33}$$

where we have taken the example of potential fluctuations, $\widetilde{\phi}$. The spectra of ω_r and γ give information about the dominant unstable mode identity. However, the characteristics of the dominant mode do not always clearly correlate with the nonlinear, fully saturated state of turbulence. During a nonlinear simulation, the interactions between the different modes are considered and the plasma reaches a saturated state of turbulence. This nonlinear interaction transfers energy between modes at different wavenumbers, providing a dissipation mechanism for the the exponentially linearly unstable modes.

The CGYRO code is formulated such that different physics can be included or excluded depending on which flags are selected in the input file. The following considerations have been taken when running the simulations presented in this thesis:

- Electromagnetic effects: CGYRO has a choice of whether to include only fluctuations of potential ($\delta\phi$) for an electrostatic simulation, or to include fluctuations of the magnetic field (both $\delta A_\parallel$ and $\delta B_\parallel$) for a fully electromagnetic simulation. While core transport is largely dominated by electrostatic turbulence, electromagnetic effects can be important in the edge. In the simulations performed here, we take a reduced electromagnetic approach and include $\delta A_{\parallel}$ only because $\delta B_{\parallel}$ is expected to be small.

- Gyrokinetic electrons: CGYRO has several choices for the treatment of the electrons. By assuming adiabatic ($\delta n \sim \frac{e}{T_e}\delta\phi$) or drift kinetic ($k_\theta \rho_e \to 0$) electrons, the computational expense of running the simulation can be reduced. For this work, fully gyrokinetic electrons were used because this is a more exact treatment and details of electron dynamics have been shown to be important to the turbulence and resulting transport.

- Simulation resolution: The CGYRO input file allows the user to set the the number of poloidal gridpoints, pitch angle gridpoints, and energy gridpoints. These resolutions should be set to be large enough that the simulation outputs converge, and otherwise kept as small as possible to reduce computing time. The number of radial and binormal wavenumbers is also set by the user, and the radial and binormal domain size must be defined.

  The choice of domain size and wavenumber extent defines whether a simulation is ion-scale, electron-scale, or multi-scale. Ion-scale simulations typically simulate $k_y \rho_s < 1.0$ where k_y is the binormal wavenumber and ρ_s is the ion sound speed. These simulations must have a domain that captures ion-scale dynamics, with radial an binormal extents typically $\sim 100\rho_s$. Electron-scale simulations will extend to higher wavenumber in the ETG range ($k_\theta \rho_s > 1.0$), but can have a smaller domain size sufficient only for capturing electron-scale dynamics. Multi-scale simulations must extend to wavenumber high enough to capture electron-scale dynamics, but must have a domain size large enough to capture ion-scale structures. Thus, multi-scale simulations are very computationally expensive and are only run in rare cases.

3.4.2 The gyrofluid model

Nonlinear gyrokinetic simulations require significant computational resources, even in the single-scale, electrostatic limit. Gyrofluid simulations are much cheaper to run and in well-validated regimes can recover much of the same physics as gyrokinetics. The Trapped Gyro Landau Fluid code TGLF is used in this work to study turbulence behavior in situations where extensive gyrokinetic runs are not possible. A description of the TGLF model and efforts towards validation with gyrokinetic models are given in References [123]–[126].

The gyrofluid model is obtained by taking moments of the gyrokinetic equations to obtain a fluid description of the plasma. When taking a moments approach, a closure is needed to form a complete set of equations. The closure in the TGLF model is formulated to accurately represent the trapped particle response and finite Larmor radius effects. The TFGL system of equations uses six velocity moments of the linearized gyrokinetic equation, and then forms a closure by defining higher velocity moments as linear combinations of the lower moments.

TGLF is a quasilinear code, meaning it calculates linear growth rates of turbulent modes and uses a saturation rule to determine the nonlinear saturated state. The linear instabilities are calculated by finding the eigenmodes of this gyrofluid system. ITG, TEM, ETG, and KBM modes can all be investigated. In general, a quasilinear solver assumes that the total flux can be expressed as a sum over unstable linear modes at each wavenumber. This summation includes the non-interacting linear response at each wavenumber, which can be found by solving the gyrofluid eigenvalue problem, as well as the saturated electrostatic potential at each wavenumber.

Since TGLF cannot describe the nonlinear interactions between modes, a saturation rule is used for determining the saturated potential. A heuristic mixing-length argument is used for determining the saturated potential, in which the growth of linear modes is balanced by turbulent diffusion. TGLF saturation rules are fitted to sets of nonlinear gyrokinetic simulations. The TGLF saturation rule SAT2 [127] is used in the simulations presented in this thesis, which has been fitted 64 gyrokinetic simulations. SAT2 is the third iteration of TGLF saturation rules, after predecessors SAT0 and SAT1. SAT2 is designed to represent the full 3D dependence of wavenumber coupling (radial and poloidal wavenumber, and poloidal angle), mediated by zonal flow mixing. SAT2 also includes multiscale effects.

The quasilinear approach of TGLF makes it significantly computationally cheaper to run than CGYRO. TGLF was used in this thesis for cases where fine parameter scans are desired, such as the stiffness tests performed in Chapter 6. A downside of the TGLF code is that it is not well validated in all plasma regimes, and one must be wary of its application to areas of the plasma not yet extensively studied with gyrokinetics. The saturation rule was built based on mid-radius L-mode plasmas, however I-modes were not covered in the database. TGLF is also not well-suited to the edge region of the plasma, where the code has not been validated and where more unusual instabilities such as MTMs may be present, which cannot be resolved by the code.

3.5 Conclusions

In this chapter a set of experimental and modeling techniques for studying tokamak turbulence has been presented. The experiments in this thesis are performed on AUG, which has an extensive diagnostic suite for measuring turbulent fluctuations. These experiments are specifically designed to optimize for edge turbulence measurements so that open questions in the area of I-mode and pedestal physics can be probed. Kinetic profiles are determined using the Thomson Scattering, ECE, and CXRS diagnostics, as well as the AUG's integrated data analysis tool IDA. The E_r profiles are determined with Doppler reflectometers and the HES system in this thesis. These measurements form the basis for understanding the plasma confinement and the transitions between L-mode and higher confinement regimes, during which an edge velocity shear layer forms and the kinetic profiles develop a pedestal. The CECE diagnostic is the main turbulence diagnostic featured in this work, but a coupled CECE-reflectometer system and a Helium beam spectroscopy system add additional details about edge turbulence, in particular the I-mode WCM.

Gyrokinetic and gyrofluid simulations are performed for plasmas similar to those obtained experimentally. The purpose of these computational studies is not validation, but rather to gain further physical insight to the nature of turbulence in L-mode and I-mode plasmas. The application of these experimental and modeling tools to L-mode, I-mode, and H-mode plasmas will be presented the next three chapters. By combining findings from these difference techniques, a more complete picture of I-mode physics is uncovered.

Chapter 4

Detailed investigation of the Weakly Coherent Mode in L-mode and I-mode

4.1 Introduction

The I-mode confinement regime was introduced in Section 2.3 as a promising operational regime for future reactors. I-mode is also a regime for which we lack full understanding of its formation and unique transport properties. The mechanism for separation of particle and heat transport channels in I-mode is an open question, and the role of turbulence in regulating the I-mode pedestal has not yet been determined. The I-mode WCM has been hypothesized to play a role in particle and impurity transport, similar to how ELMs regulate the ELMy H-mode pedestal. However, the instability causing the WCM has not yet been determined and the connection between the WCM and transport has not yet been established.

Theoretical work elucidates the importance of collisionality in determining the turbulence and the transport properties of the I-mode pedestal. One theorized regime of turbulence for I-mode is the reduction of electron heat transport with the decreased collisionality of the I-mode pedestal and therefore increased electron conductivity[16]. In this model, as temperature increases, electrons become more adiabatic and fast parallel equilibration levels out electron temperature fluctuations. The WCM is hypothesized to be the residual broadband turbulence when large and small scales are stabilized. However, sizeable electron temperature fluctuations associated with the WCM have been measured at both C-Mod and AUG, albeit smaller in amplitude than density fluctuations [12], [128]. Separate neoclassical theory work has postulated that the WCM is not necessary to I-mode transport at Alcator C-Mod and that neoclassical transport alone can account for I-mode impurity transport [18]. This work requires the pedestal to be in the banana regime of collisionality, which is often the case for I-mode pedestals while H-mode pedestals are often in the plateau regime[129]. As shown in Appendix A, extension of this neoclassical work shows that when the pedestal is in the plateau regime, neoclassical radial transport is negligible [130].

The importance of collisionality in determining the nature of the turbulence and resulting transport in the pedestal region motivates the need for the study of the I-mode turbulence across a range of collisionality values. The first major results of this thesis are the results of a study of L and I-mode pedestal fluctuations in low and high collisionality plasmas. These

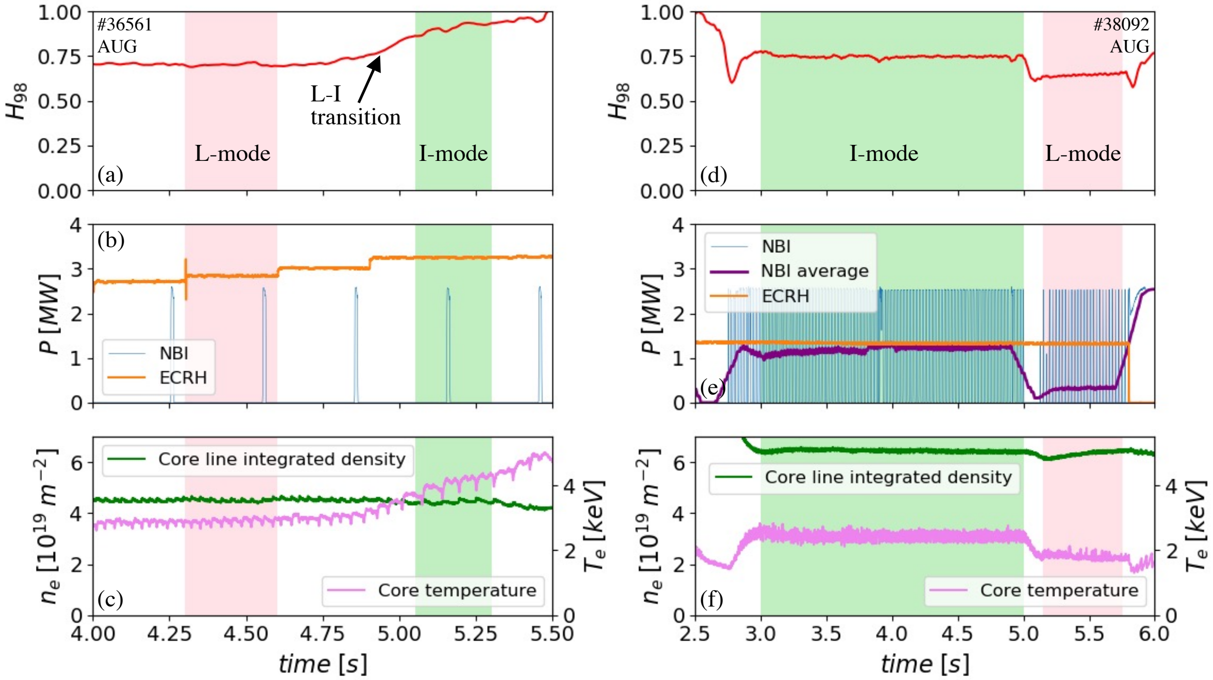

Figure 4.1: Time histories of the low n_e (a-c) discharge #36561 and the high n_e discharge (d-f) #38092 with the phases of L-mode and I-mode used in the following turbulence analysis. (a) and (d) show the confinement improvement factor H_{98}. (b) and (e) show the heating schemes with ECRH steps and NBI beam blips in (b) and NBI in feedback with steady ECRH in (e). (c) shows the core line integrated electron density from DCN interferometry and (f) shows the on-axis temperature from core ECE. Both discharges display constant density in L-mode and I-mode with a higher temperature in I-mode than L-mode. The low n_e discharge has higher quality confinement than the high n_e discharge.

results increase our understanding of edge transport in L and I-mode and the behavior of the WCM. Much of the material in this chapter is reproduced from a previously published article [131], with the permission of AIP Publishing.

4.2 Experimental description

In order to study the parameter space of collisionality and compare L and I-mode pedestal fluctuations, discharges with L and I-mode phases across a range of densities were designed for dedicated experiment. Plasma parameters for the two such discharges are shown in Figure 4.1. These two discharges represent two types of experiments used to study pedestal turbulence across a wide parameter space. Both discharges have steady-state L and I-mode phases but they were designed with different densities and heating schemes. Several discharges are used in this chapter to investigate the fluctuations in the L-mode and I-mode edge, but we will explore in the most detail two discharges that represent the opposite ends of the experimental parameter space: the “low n_e ECRH heated L-mode/I-mode discharge" and the “high n_e NBI heated L-mode/I-mode discharge".

The low n_e L-mode/I-mode discharge was heated by electron cyclotron resonance heating (ECRH) in small power steps from the L to I-mode threshold and neutral beam injection (NBI) beam blips were present only for ion temperature measurements obtained with the charge exchange recombination spectroscopy (CXRS) system [132]. This discharge has a core line integrated density of $\sim 4.4 \times 10^{19}\,\mathrm{m}^{-2}$. The core density stays the same between the L and I-mode phases, but the core electron temperature rises from $\sim 3.0\,\mathrm{keV}$ in L-mode to ~ 4.0 keV in I-mode, and the edge temperature ($\rho_{pol} = 0.95$) rises from $\sim 0.3\,\mathrm{keV}$ to $\sim 0.7\,\mathrm{keV}$. The confinement enhancement factor H_{98} relative to the IPB98(y,2) scaling law [51] for the thermal confinement time rises from 0.70 in L-mode to 0.91 in I-mode.

The high n_e L-mode/I-mode discharge was designed with the I-mode phase first, followed by the L-mode. In contrast to the low n_e discharge, this plasma was heated by NBI feedback controlled on the β_{pol} value of the plasma with ECRH at a constant level of 1.4 MW. This discharge has a core line integrated density of $\overline{n}_e = 6.4 \times 10^{19}\,\mathrm{m}^{-2}$. The core electron temperature drops from $\sim 2.5\,\mathrm{keV}$ in I-mode to $\sim 1.8\,\mathrm{keV}$ in L-mode, and the edge temperature ($\rho_{pol} = 0.95$) drops from ~ 0.4 keV to ~ 0.2 keV. The confinement of this discharge is comparatively worse than the low n_e case, with H_{98} reaching only 0.75 in I-mode and falling to 0.64 in L-mode.

The profile comparison of the two discharges is shown in Figure 4.2. Integrated Data Analysis (IDA) [133] is used to determine n_e and T_e profile fits from standard profile diagnostics including Thomson scattering and 1D ECE. T_i profiles are made using CXRS data and Gaussian Process Regression (GPR) fits. The electron to ion temperature ratio T_e/T_i is determined from these fits, and the effective collisionality ν_{eff} is determined through the fitted profiles and Equation 2 in [132]:

$$\nu_{eff} = 0.00279 \times \left(15.94 - 0.5 \log\frac{n_e}{T_e^2}\right) \times \frac{n_e}{T_e^2} R \sqrt{m_A} Z_{eff} \tag{4.1}$$

where n_e here is in units of $10^{19}\,\mathrm{m}^{-3}$, T_e is in keV, R is the major radius in meters, m_A is the main ion mass in amu, Z_{eff} is the effective charge.

Both discharges display the characteristic n_e profiles that change minimally between L-mode and I-mode while the T_e and T_i profiles form a pedestal in I-mode. The low n_e discharge has a more marked development of a T_e pedestal in I-mode than the high n_e discharge, which displays a relatively weak T_e pedestal. The ion temperature in the L-mode phase of the high n_e discharge is taken from a previous discharge, which had matched parameters but more frequent CXRS ion measurements. The lower density and higher temperatures in the low n_e I-mode/L-mode case lead to lower collisionality than in the high n_e case. Collisionality is tied to the degree of electron and ion temperature coupling, or equilibration of temperature between the two species. The L-mode edges often have coupled T_e and T_i, while higher confinement regimes have decoupled edges due to higher overall temperatures and therefore lower collisionality. In the low n_e discharge, there is a change in coupling between the L-mode and I-mode edges as shown by the T_e/T_i ratios between L-mode and I-mode. The high n_e discharge has a higher degree of temperature coupling and little change in coupling between L and I-mode.

The E_r profiles during the L-mode and I-mode phases of the low and high n_e discharges are shown in Figure 4.3. The E_r profiles are measured using Doppler reflectometry [92],

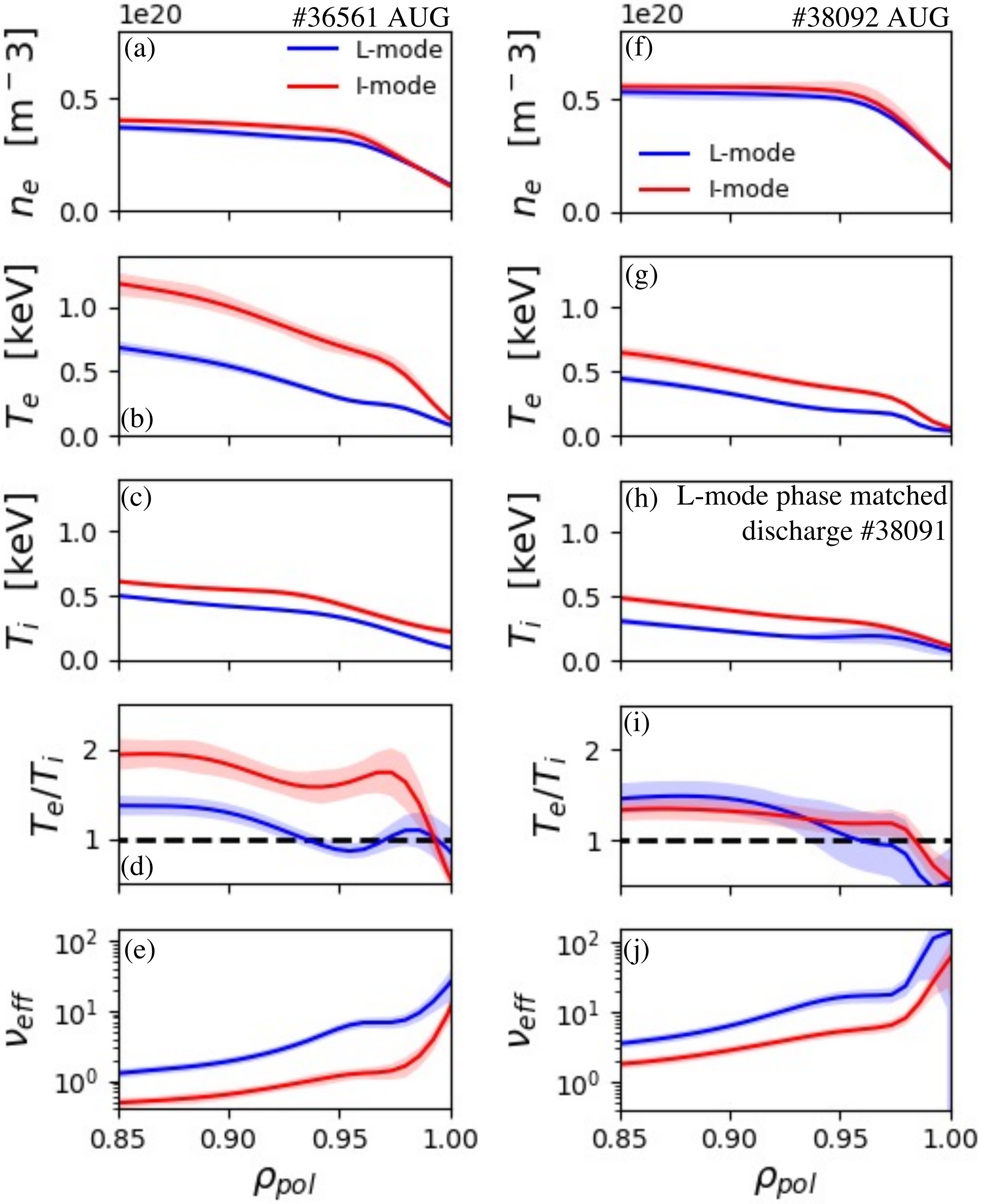

Figure 4.2: Radial profiles of the low n_e (a-e) discharge #36561 and the high n_e discharge (f-g) #38092 from steady state phases of L-mode and I-mode shown in Figure 4.1. (a) and (f) electron density and (b) and (g) electron temperature from IDA. (c) and (h) ion temperature fitted with GPR. (d) and (i) electron to ion temperature ratios. (e) and (j) effective collisionality as defined in [132]. The high n_e discharge displays lower T_e and T_i, stronger temperature coupling, and higher collisionality than the low n_e discharge.

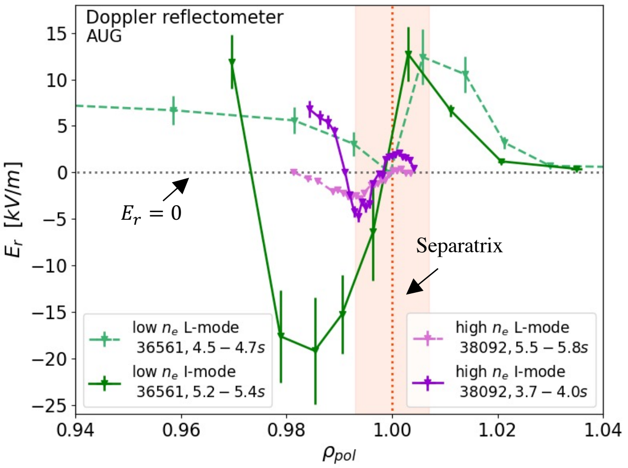

Figure 4.3: Radial profiles of E_r for the low n_e discharge (#36561) and the high n_e discharge (#38092) as measured by Doppler reflectometers during I-mode and L-mode phases of these two discharges. Both discharges display a deepened E_r well in I-mode as compared to L-mode. The low n_e I-mode forms a much deeper well than the high n_e I-mode. The shaded region represents the maximum error on the separatrix position during these discharge phases.

[134]. In both the low and high n_e discharges, the E_r well deepens between L-mode and I-mode. The change in E_r slope leads to a change in sheared $E \times B$ flow in both cases. The E_r well is significantly deeper and wider in the low n_e I-mode than in the high n_e I-mode. The large positive value of E_r in the low n_e SOL indicate that the SOL is warm in these plasmas.

4.3 Observation of the L-mode WCM

Previous to the work of this thesis, the observations of the WCM in L-mode were limited to observations of a WCM precursor prior to L to I transitions [72]. The work of this thesis identifies for the first time a steady-state L-mode WCM which can exist in L-modes even far from the power threshold for the L to I transition. The spectrograms of WCM fluctuations from the low and high n_e L-mode/I-mode discharges are shown in Figure 4.4 using a single CECE channel at the location corresponding to the WCM peak amplitude ($\rho_{pol} \sim 0.98$). In both cases, the WCM can be seen spinning up in frequency at the transition from L-mode to I-mode. The low n_e case undergoes a single L to I transition over the course of the discharge. In the high n_e case, an L to I transition occurs early in the discharge. A brief H-mode occurs at around 2.6s, during which the WCM is not visible. The discharge returns to I-mode at $\sim$ 2.75s, and the WCM reappears. The WCM is seen to transition back to lower frequency at the I to L back-transition at 5.0s.

At the onset of I-mode in both the low and high n_e cases, a coherent low frequency mode also appears (arrows on Figure 4.4). This mode is identified as the Low Frequency Edge Oscillation (LFEO) [73]. The LFEO is not present in L-mode phases in these discharges. A

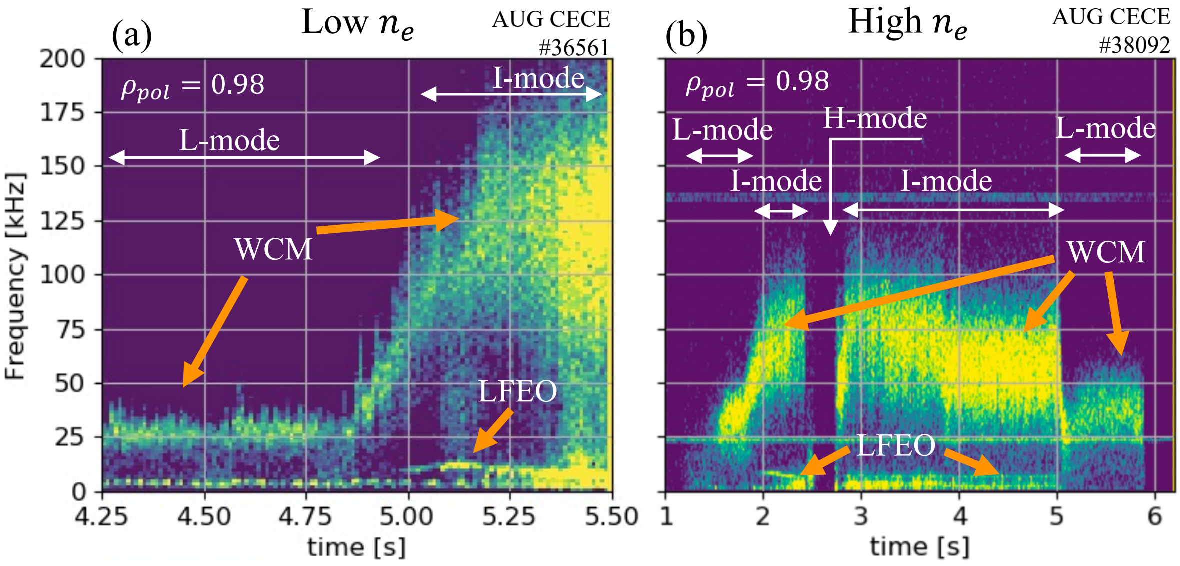

Figure 4.4: Spectrogram from single CECE channel near the WCM peak amplitude of $\rho_{pol} = 0.98$ during the (a) low n_e and (b) high n_e discharges. In the low n_e discharge, the WCM appears as the 25 kHz mode in L-mode which spins up to 80-160 kHz in I-mode, and the LFEO is the narrowband mode at 8 kHz which appears in the I-mode phase only. The high n_e discharge has L and I-mode phases early in the discharge, followed by a brief H-mode, followed by steady-state I and L-mode phases. In this discharge, the WCM appears as the 40-80 kHz mode in I-mode and the 25-50 kHz mode in L-mode. The LFEO is again the narrowband mode at 8 kHz which appears in the I-mode phases only.

modulation of the LFEO frequency during the onset of I-mode (spin-up in the low n_e case and spin-down in the high n_e case) is observed. A feature at low frequency ($<$ 2kHz) is also observed in these spectra, in both L and I-mode in the low n_e discharge and in I-mode alone in the high n_e discharge. The investigation and identification of these very low frequency fluctuations are left for future work.

4.4 WCM decoupled from collisionality, confinement, and E_r

A small database of 18 plasma phases in which edge turbulence was investigated with CECE is shown in the parameter space of collisionality and H_{98}, as well as collisionality and τ_E in Figure 4.5. The confinement improvement factor H_{98} is commonly used for quantifying the quality of confinement in I-mode plasmas [11], [12], despite the fact that this factor is meant to describe H-modes. The plasmas contributing to the database in Figure 4.5 all displayed L-mode and I-mode phases with a WCM. The confinement factor H_{98} is negatively correlated with collisionality in these plasmas, which is also observed in other devices and confinement regimes [135], [136]. This trend is the same when instead using the H_{89} confinement enhancement factor calculated with L-mode scaling [52], as well as an I-mode

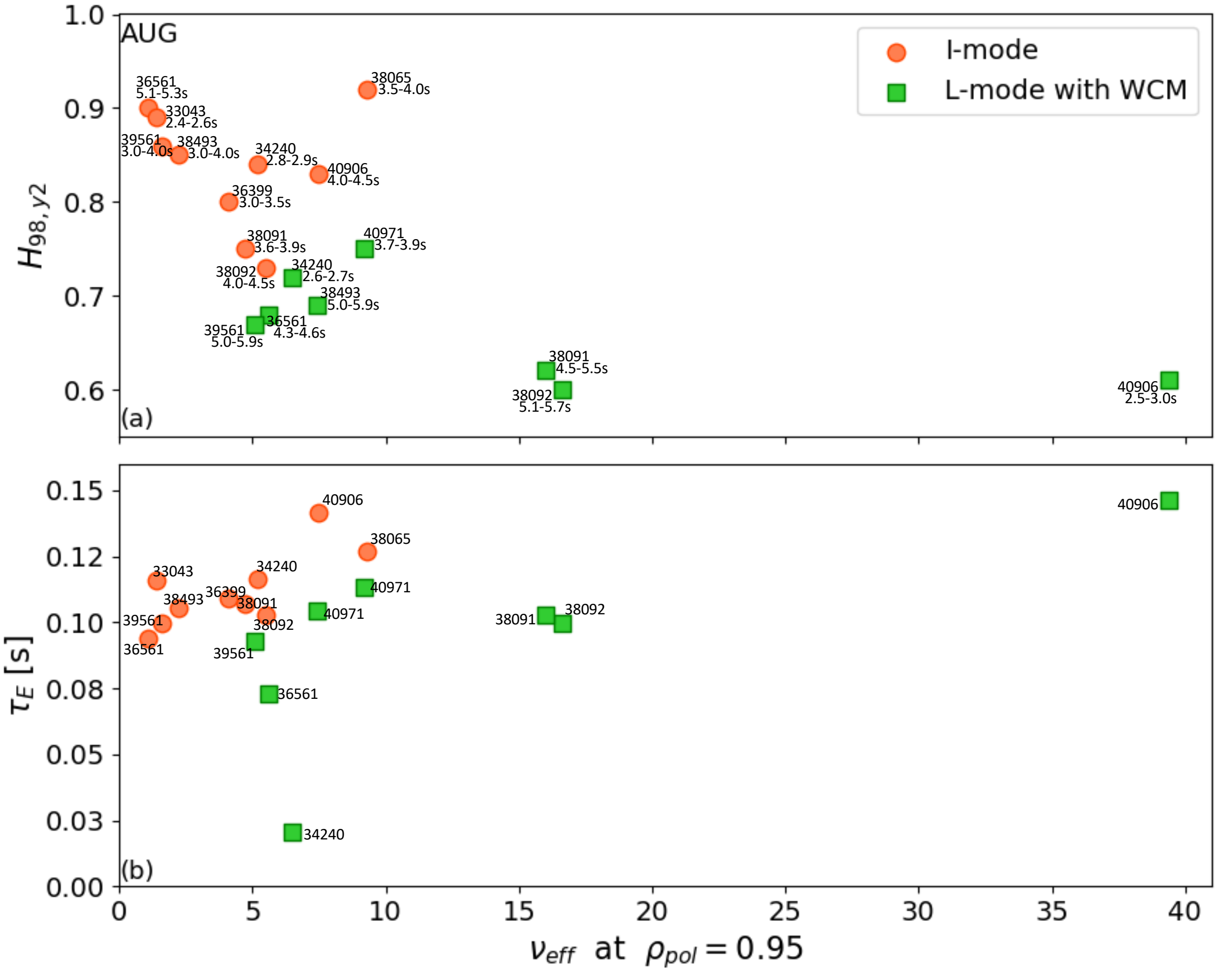

Figure 4.5: Confinement quality trends with ν_{eff}, including (a) confinement improvement factor $H_{98,y2}$ and (b) stored energy τ_E plotted against effective ν_{eff} evaluated at $\rho_{pol} = 0.95$.

confinement time scaling [137]. A clear trend in τ_E with collisionality is not observed, with τ_E staying relatively constant over the collisionality range. This could indicate that current scaling laws do not effectively capture the effect of collisionality on confinement quality in L and I-mode. The presence of the WCM is not correlated with either collisionality or confinement. The WCM $\delta T_e/T_e$ fluctuation level is generally higher in the I-mode phase than in that plasma's corresponding L-mode phase, but within the L-mode and I-mode phases alone there is no correlation between collisionality and WCM $\delta T_e/T_e$ amplitude or confinement and WCM $\delta T_e/T_e$ amplitude.

A simple experimental thermal transport analysis of the pedestal region was used for the low and high n_e L-mode/I-mode plasmas, following the method of Ref [138]. Although L-mode does not have an edge pedestal, this terminology will be used when referring to the region $\rho_{pol} = 0.95 - 1.0$ for ease of comparison between L-mode and I-mode. This analysis is shown in Table 4.1. The thermal diffusivity, χ_{eff}, is estimated from $\chi_{eff} = -P_{net}/\left(2An_e\nabla T_e\right)$ with P_{net} the power crossing the last closed flux surface (LCFS) and A

Table 4.1: Comparisons of thermal diffusivity, H_{98}, and the minimum value of E_r from Figure 4.3. Experimental transport analysis of low and high density discharges to determine χ_{eff} uses T_e gradients and n_e values from the profiles in Figure 4.2

Shot	Phase	χ_{eff} (m^2/s)	H_{98}	E_r, min (kV/m)
Low n_e (36561)	L	0.28	0.70	-0.04
	I	0.22	0.91	-19.18
High n_e (38092)	L	0.36	0.66	-2.86
	I	0.27	0.75	-4.68

the surface area of the LCFS. P_{net} is calculated as the heating input power minus the radiated power inside the LCFS as measured by bolometry. The pedestal T_e gradient is determined as the linear slope between the T_e values at $\rho_{pol} = 0.96$ to 0.99, the and mid-pedestal n_e value is taken at $\rho_{pol} = 0.975$. In both the low and high n_e discharges, the thermal diffusivity decreases with the increasing profile steepness from L to I-mode. The fractional change in diffusivity between the L and I-mode phases is similar in both discharges. Lower thermal diffusivity values correspond with higher H_{98} and deeper E_r minimum values both when comparing L to I-mode and when comparing low n_e with high n_e cases. This makes intuitive sense, as lower transport is expected to lead to higher confinement, and reduced transport is linked to the $E \times B$ flow shear occurring due to the radial variation in E_r.

The WCM was present for all pedestals analyzed in Table 4.1, therefore the WCM presence or fluctuation level also cannot be correlated with thermal diffusivity or E_r well depth. This suggests that the existence of WCM alone does not play a significant role in the difference in heat transport and energy confinement between L and I-mode plasmas. The existence and consistent properties of the WCM over this entire parameter space of E_r, ν_{eff}, χ_{eff}, and H_{98} motivates further study to determine the parameters to which this fluctuation is sensitive.

4.5 Comparison of L-mode and I-mode edge fluctuations

The existence of the WCM in both L and I-mode across a wide parameter space of plasma collisionality and performance is a new finding. This motivates the need for detailed experimental study to understand the nature of pedestal fluctuations in both L and I-mode, and whether the character of the WCM changes between these regimes. The diagnostic capabilities of AUG allow for a detailed study of pedestal fluctuations. Here we compare the properties of the L and I-mode edge fluctuations with particular focus on the WCM using CECE radiometers, the thermal He beam diagnostic, and the n_eT_e phase system.

4.5.1 Electron temperature fluctuations

The T_e fluctuations in these L-mode/I-mode discharges are primarily studied with the Correlation Electron Cyclotron Emission (CECE) diagnostic, described in Chapter 2. The T_e turbulence frequency spectra from the low and high n_e discharges described in Section 4.2 taken with the CECE diagnostic are shown in Figure 4.6. The spectra show the modulus of the complex coherence between neighboring CECE channels, with the location stated as the average location of the two correlated channels. The fluctuation measurements span the outer core ($\rho_{pol} = 0.90$) through the LCFS, and the selection of these measurements shown in Figure 4.6 display the typical features of L and I-mode turbulence in the outer core ($\rho_{pol} = 0.93$), inner pedestal top ($\rho_{pol} = 0.95$), and WCM location ($\rho_{pol} = 0.98$).

The most prominent element in the spectra is the WCM, shown as the feature with the highest value of coherence in the pink spectra. In all cases studied, this mode is localized near $\rho_{pol} = 0.98$. In the low n_e discharge, the WCM is centered at 20 kHz in L-mode with a full-width half maximum (FWHM) of 40 kHz. In the low n_e I-mode, the WCM is centered at 90 kHz and has a FWHM of 120 kHz. In the high n_e L-mode, the WCM is centered at 40 kHz with a FWHM of 50 kHz and in the high n_e I-mode, the WCM is centered at 60 kHz and has a FWHM of 90 kHz. In addition to the WCM, broadband turbulence is seen on the CECE coherence spectra throughout the outer core and pedestal measurement locations ($\rho_{pol} = 0.90 - 0.97$). These broadband features in some cases shift frequency between L-mode and I-mode phases, such as the spectra at $\rho_{pol} = 0.93$ in the high n_e discharge, but generally have a similar structure between L-mode and I-mode.

The change in E_r between the I-mode and L-mode phases of the discharges is sufficient to increase the $E \times B$ flow and Doppler shift the spectra to higher frequencies, with a larger frequency shift occurring in the low n_e discharge, with a larger change in E_r between L-mode and I-mode. The frequency of turbulence captured by CECE is given by $f = f_{turbulence} + f_{Doppler}$ where $f_{turbulence}$ is the frequency of the turbulence in the $v_{E\times B}$ frame and $f_{Doppler} = k_\theta v_\theta + k_\phi v_\phi$ is the Doppler shift due to the plasma velocity in the poloidal and toroidal directions (v_θ and v_ϕ) for a turbulent mode with a given poloidal and toroidal wavenumber (k_θ and k_ϕ). The radial velocity is assumed to be negligible. The $k_\phi v_\phi$ term can also often be neglected due to the very small toroidal wavenumber expected for turbulent modes. The $k_\theta v_\theta$ term can be calculated assuming that $v_\theta = E_r \times B_\phi$ and assuming a turbulent feature with a given wavenumber k_θ. The frequency shifts observed between L-mode and I-mode for low and high n_e WCM are consistent with the frequency shift expected for a low wavenumber turbulent mode, with $k_\theta > 0.3$ cm^{-1}.

The normalized electron temperature fluctuation amplitude, $\delta T_e/T_e$, is derived from integration of the coherence spectra, subtraction of the background coherence, and incorporation of IF filter bandwidth, as explained in Section 2.3. The radial profile of $\delta T_e/T_e$ in the high and low n_e L-mode/I-mode phases is shown in Figure 4.7. The WCM in L-mode and I-mode leads to a marked increase in fluctuation amplitude in the pedestal region. The fluctuation amplitude rises from close to 1% in the outer core to several times higher at the WCM location in all cases. In the low n_e case, the WCM fluctuation amplitude is 2.3% and 3.8% in L-mode and I-mode respectively, and in the high n_e case is 2.8% and 4.2% in L-mode and I-mode respectively. From these T_e fluctuation radial profiles, the WCM in both the low and high n_e cases, in both L-modes and I-modes, is localized at $\rho_{pol} \sim 0.97 - 0.99$. This corresponds in real space to a WCM width of around 1.8cm. The regions of marginal optical depth ($\tau < 2$) are marked with a grey box. In all cases the region of low optical depth occurs outside the region of peak WCM amplitude. The error bars typically associated with $\delta T_e/T_e$ measurements are of a statistical nature and for these analyses of turbulence in the edge with high $\delta T_e/T_e$ are in many cases smaller than the plotted points themselves.

The location of the E_r well can be compared from Figure 4.3 with the WCM peak

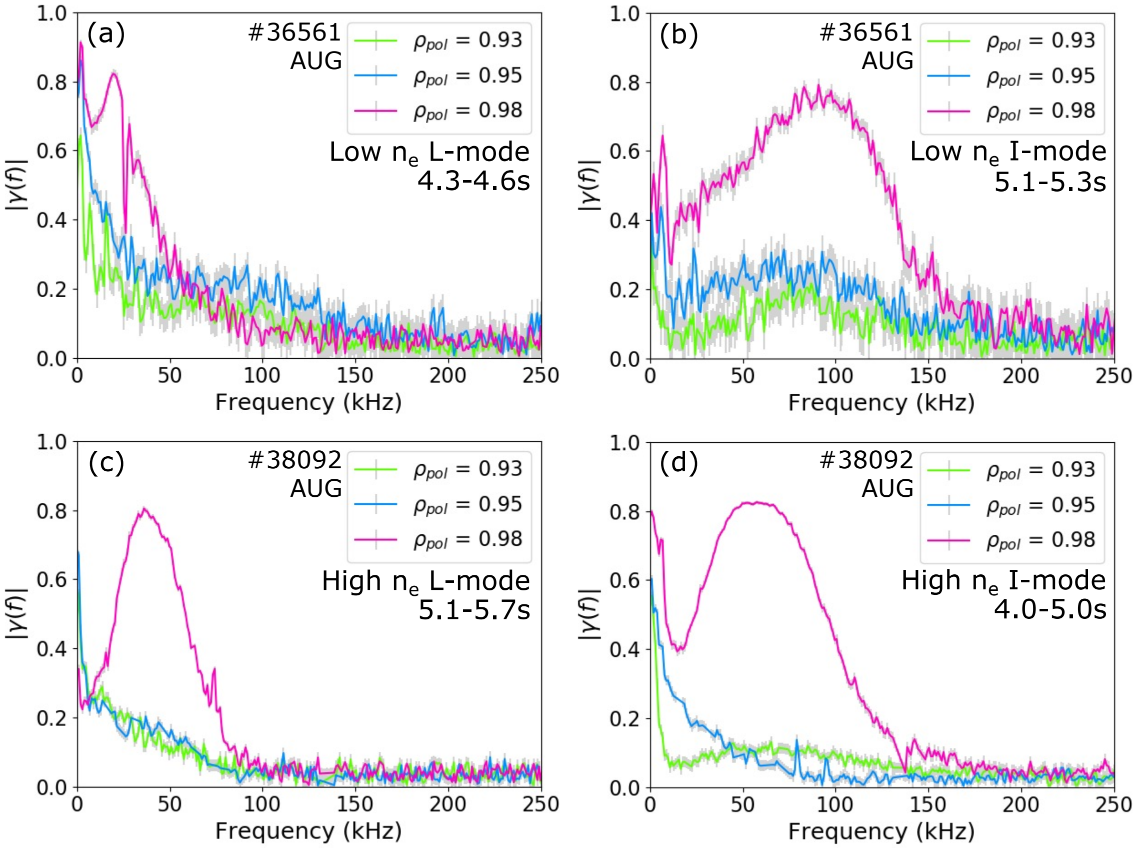

Figure 4.6: T_e fluctuation coherence spectra as measured by CECE in the low n_e discharge (#36561) (a) L-mode and (b) I-mode phases and the high n_e discharge (#38092) (c) L-mode and (d) I-mode phases. Spectra range from $\rho_{pol} = 0.93 - 0.98$. The WCM can be seen in all cases at $\rho_{pol} = 0.98$ and broadband turbulence is seen in the outer core ($\rho_{pol} = 0.93$) and pedestal top ($\rho_{pol} = 0.95$) locations.

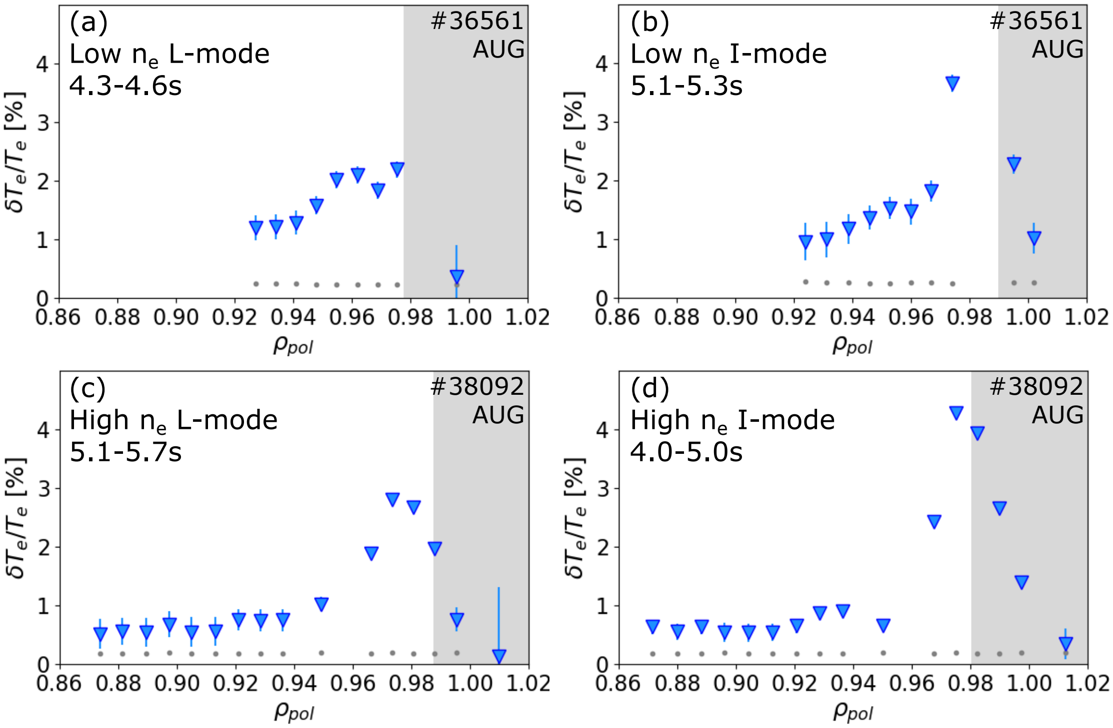

Figure 4.7: Electron temperature fluctuation level over radius from low n_e discharge (#36561) (a) L-mode and (b) I-mode and the high n_e discharge (#38092) (c) L-mode and (d) I-mode. All phases use 10-250 kHz as the turbulence integration band and 250-270 kHz for background subtraction in the calculation of fluctuation amplitude. Regions of marginal optical depth $\tau < 2$ are shaded in grey. Fluctuation levels rise from $\sim 1\%$ in the outer core to $2.3 - 4.2\%$ in the WCM range from $\rho_{pol} = 0.97 - 0.99$.

amplitude region from Figure 4.7. In the low n_e I-mode, the E_r well extends from $\rho_{pol} = 0.978$ to $\rho_{pol} = 0.99$, and the WCM amplitude peaks just inside $\rho_{pol} = 0.98$. In the high n_e I-mode, the E_r well is farther towards the separatrix, with a minimum around $\rho_{pol} = 0.99$, while the WCM once again peaks just inside $\rho_{pol} = 0.98$. These mappings indicate that the peak amplitude of the WCM occurs towards the inside of the region of high $E \times B$ shear in I-mode, but that the WCM persists throughout the E_r well region. These findings are consistent with previous WCM vs E_r localizations from EAST [68], but they are inconsistent with findings from C-Mod, which place the WCM in the outer shear layer of the E_r well [139]. These localizations are subject to uncertainties in E_r locations due to density profile fits and equilibrium reconstruction and mapping. CECE localizations are subject to the same uncertainty in equilibrium reconstruction and mapping. The separatrix position has an uncertainty as large as 4.5 mm in these plasma phases, which translates to $\Delta\rho_{pol} \sim 0.007$, indicative of significant uncertainties in mapping of edge CECE measurements and motivating a need for future studies.

4.5.2 WCM dispersion relation

The thermal helium (He) beam diagnostic is capable of measuring density and temperature fluctuations in the edge of AUG plasmas[113], [114]. Helium is injected into the plasma and line ratio spectroscopy is performed to determine density and temperature. The diagnostic's 32 lines of sight enable correlation analysis.

The He beam diagnostic can capture information about the WCM poloidal structure and propagation velocity, in addition to frequency spectra. Figure 4.8 shows the dispersion relation of edge fluctuations during the L and I-mode phases of a medium density L-mode/I-mode discharge (core line integrated density of $\overline{n}_e = 5.1 \times 10^{19}\,\mathrm{m}^{-2}$) with steady-state L and I-mode phases. This dispersion relation was calculated from poloidally separated channels using the spectral analysis method from [140]. The channels used in the correlations were not neighboring, but separated by ~ 2.5 cm. The WCM is the feature with wavenumbers in the range of -0.5 to -1.0 cm^{-1}, and the wavenumber extent stays the same between L and I-mode. These wavenumbers are similar to the WCM wavenumber extent reported from similar analysis on C-Mod and AUG [74], [141]. The WCM is centered around a frequency of ~ 20 kHz in L-mode and broadening to the range of 30 to 90 kHz in I-mode with a peak amplitude at ~ 60 kHz. This frequency shift of the WCM between L-mode and I-mode is again consistent with a Doppler shift due to increased $E \times B$ velocity, with a larger frequency shift occurring at larger wavenumber absolute value. The structure that appears near 4 kHz centered around $k = 0$ cm^{-1} is the LFEO and appears in the I-mode phase only.

The He beam diagnostic can also determine the WCM propagation velocity by using the phase angle between coherent fluctuations in poloidally separated channels and the spacing between the channels. During the L-mode phase of this mid n_e discharge, the WCM fluctuation peak at ~ 20 kHz propagates with a velocity of ~ -1.5 km/s. The negative sign indicates the electron diamagnetic direction. During the I-mode phase, the WCM peak at ~ 60 kHz propagates at ~ -6 km/s. This change of -4.5 km/s in velocity is consistent with a change in the $E \times B$ flow resulting from the change in E_r from L to I-mode. These WCM propagation velocity measurements include the contribution from the plasma $E \times B$ flow ($v_{\text{propagation}} = v_{\text{phase}} + v_{E\times B}$), and the phase velocity of the WCM in the plasma frame

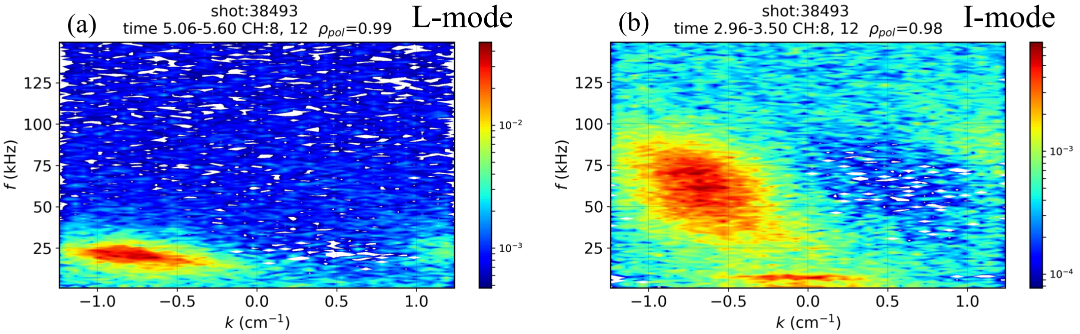

Figure 4.8: Dispersion relation of fluctuations at $\rho_{pol} = 0.98$ and 0.99 from poloidally separated channels of the thermal Helium beam. The WCM is seen in the L-mode phase (a) at 25 KHz and in the I-mode phase (b) at 45-75 kHz. The wavenumber extent of the WCM does not change between L-mode and I-mode, and the frequency change is consistent with a Doppler shift between the two regimes. The LFEO also appears in the I-mode phase at 4 kHz.

cannot determined from these measurements alone.

4.5.3 WCM n_eT_e cross phase

The phase angle between electron density and temperature fluctuations (α_{n_eTe}) can be obtained with a reflectometer and CECE system that share a line of sight to the plasma. By choosing the appropriate frequencies for 2nd harmonic EC emission and density cutoff, the reflectometer and radiometer can be made to measure approximately the same plasma volume [7], [107]. The reflectometer does not share electronics other than the data acquisition board with the CECE system and does not suffer from thermal noise, therefore a correlation between the reflectometer and radiometer signals will yield information about coherent turbulent quantities. Details of the n_eT_e phase calculation and the associated uncertainty are found in Reference [7].

Measurements of the n_eT_e cross-phase in L and I-mode with a coupled CECE-reflectometer system find that the WCM has a finite, out of phase $\alpha_{n_eT_e}$ in both L and I-mode. For these measurements, an O-mode, V-band reflectometer was used (launch frequency 50/51 GHz in L-mode/I-mode) and the reflectometer amplitude signal was used in correlating with the CECE signal. These measurements find that $\alpha_{n_eT_e}$ changes slightly between L and I-mode. The coherence between CECE and reflectometer channels and the n_eT_e phase during the L and I-mode phases are shown in Figure 4.9. The coherence spectra show that the fluctuations associated with the WCM are coherent between the radiometer and reflectometer. The n_eT_e cross-phase at the spectral peak of the WCM is 171° in L-mode and shifts to 143° in I-mode. The error associated with the n_eT_e cross-phase is of a statistical nature and is small in regions of coherence between the reflectometer and CECE, so this change in phase angle is statistically significant. It is within the realm of possibilities that the measured values of $\alpha_{n_eT_e}$ could correspond to small or negative heat flux associated with the WCM and a positive particle flux, but the turbulent transport cannot be quantified without simultaneous

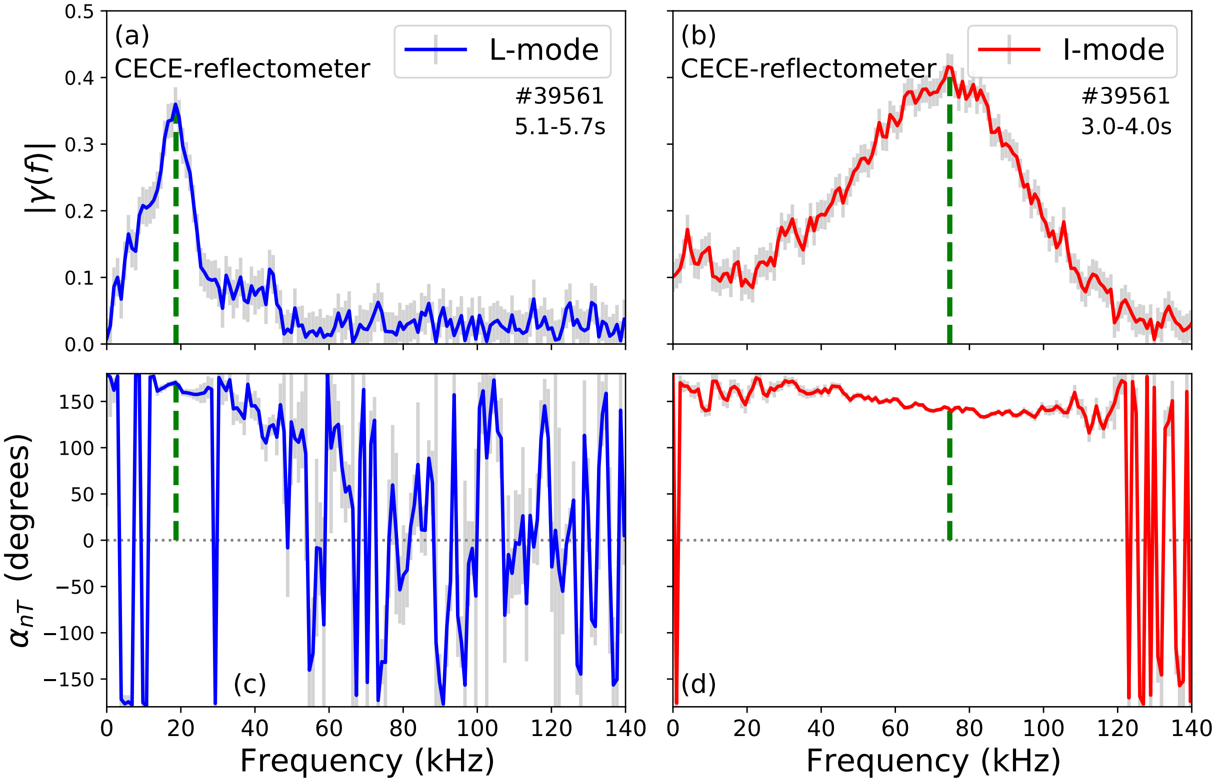

Figure 4.9: Coherence between a CECE channel and V-band reflectometer at $\rho_{pol} = 0.97$ in the (a) L-mode and (b) I-mode phases of a middle density discharge (#39561) showing the WCM in both cases. (c) L-mode and (d) I-mode n_eT_e phase over frequency. The n_eT_e cross-phase at the spectral peak of the WCM is 171° in L-mode and shifts to 143° in I-mode.

measurements of the amplitude of fluctuations in T_e, n_e, plasma potential ϕ, magnetic field B, and T_e-ϕ and n_e-ϕ cross-phases, as shown in Equations 2.4 and 2.5. While $\alpha_{n_eT_e}$ does not enter directly into the turbulence-driven flux equations, comparisons of this measurement with theory and simulation can provide valuable new information about the physics of the WCM.

The $\alpha_{n_eT_e}$ measurement assists in quantifying the effects of density fluctuations in CECE measurements. To follow the analysis in Reference [104], an n_e fluctuation level of 20% is assumed, corresponding with the upper limit of the WCM n_e fluctuations reported in [72]. We then calculate the impact of n_e fluctuations on signal intensity if the T_e fluctuation level is 3%, in line with the typical CECE values for the AUG WCM. Reflective tungsten walls with a reflectivity value of $\chi = 0.85$ are assumed. The n_eT_e cross-phase angles measured in L and I-mode were used in this calculation. The impact of n_e fluctuations under these assumptions is shown in Figure 4.10. The possibility of a greater than unity contribution of T_e fluctuations at low optical depth ($\tau_{2X} < 2$) is due to out of phase n_e fluctuations reducing the fluctuation signal intensity and leading to a smaller intensity fluctuation amplitude. In all WCM measurements presented in this chapter, the peak WCM amplitude occurs in a region of high optical depth ($\tau_{2X} > 2$), therefore CECE $\delta T_e/T_e$ amplitude measurements

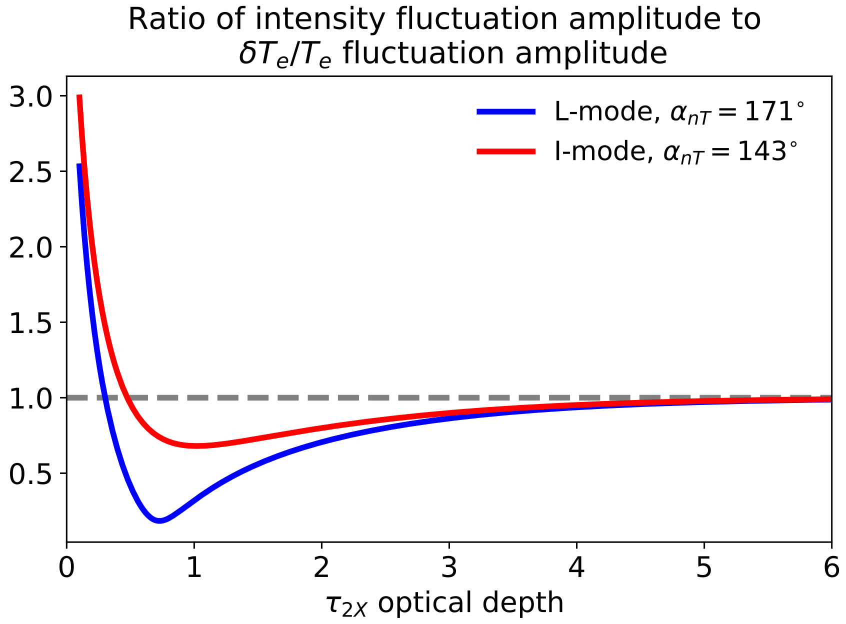

Figure 4.10: Ratio of the CECE intensity fluctuation amplitude to the true $\delta T_e/T_e$ fluctuation amplitude as a function of optical depth for two values of the n_eT_e cross-phase angle. For this toy calculation, the measured n_eT_e phases of the WCM in L-mode and I-mode were used, but estimates were used for fluctuation amplitudes ($\delta T_e/T_e = 3\%$ and $\delta n_e/n_e = 20\%$) and wall reflectivity ($\chi = 0.85$). At an optical depth of $\tau > 2$, the CECE intensity fluctuation amplitude corresponds well to the $\delta T_e/T_e$ fluctuation amplitude.

are assumed to be due primarily to T_e fluctuations, with a minor ($< 30\%$) impact from n_e fluctuations. There is little change between L-mode and I-mode in terms of the impact of density fluctuations in regions of high optical depth. However, because the L-mode $n_e T_e$ cross-phase is farther out of phase than the I-mode $n_e T_e$ phase, the interpretation of the WCM fluctuation amplitude in a marginal optical depth L-mode would be that the measured fluctuation intensity is slightly lower than the true $\delta T_e / T_e$ amplitude.

4.5.4 Long range toroidal correlations

Toroidally separated CECE systems in different tokamak toroidal sectors allow for long-range toroidal correlation calculations and study of the three-dimensional nature of turbulence. For these long-range measurements during an L-mode/I-mode discharge, two CECE systems were placed in toroidal locations of the tokamak separated by 60°. The lines of sight (LOS) at these two toroidal locations have a poloidal difference of 11.3° between the two systems. The WCM peak amplitude occurred near $\rho_{pol} = 0.99$ in this experiment and the safety factor at this radial location was $q_{99} \sim 5$. This geometry allowed the magnetic field lines near the WCM location to pass through both CECE systems. The coherence between the toroidally separated channels at $\rho_{pol} = 0.99$ is shown in Figure 4.11, with standard CECE analysis from radially neighboring channels overplotted to compare the WCM spectral features. During the L-mode phase, the long-range correlations do not display clear spectral features above the level of the standard deviation. However, during the I-mode phase, the WCM centered at 70 kHz is clearly seen in the long-range correlations. The LFEO is also seen in these long-range correlations during the I-mode phase. The long physical range of these correlations thus limits both the WCM and LFEO mode to low toroidal mode numbers. While the lack of long-range L-mode WCM measurements could be due to a change in the three-dimensional structure of the WCM between L-mode and I-mode, it is also possible that L-mode correlations were not captured due to a slight change in safety factor ($< 10\%$) changing the field line orientation with respect to CECE lines of sight, or the weaker fluctuation amplitude of the L-mode WCM. More measurements are needed to determine the three-dimensional nature of the L-mode WCM.

4.6 Coupling between the WCM and Low Frequency Edge Oscillation

The LFEO appears only in the I-mode phase of the L-mode/I-mode discharges in this chapter. The LFEO onset occurs as the WCM ramps up to its I-mode frequency range. The LFEO presence may not be ubiquitous in I-mode, as I-mode phases have been observed to occur without an observed LFEO[73]. In cases where the LFEO does appear in I-mode, it is coupled to the T_e fluctuations associated with the WCM. Figure 4.12 shows the cross-bicoherence between neighboring CECE channels at the WCM location during an L-mode and I-mode phase of a discharge. The squared cross-bicoherence $\hat{b}^2$ of two fluctuation electron

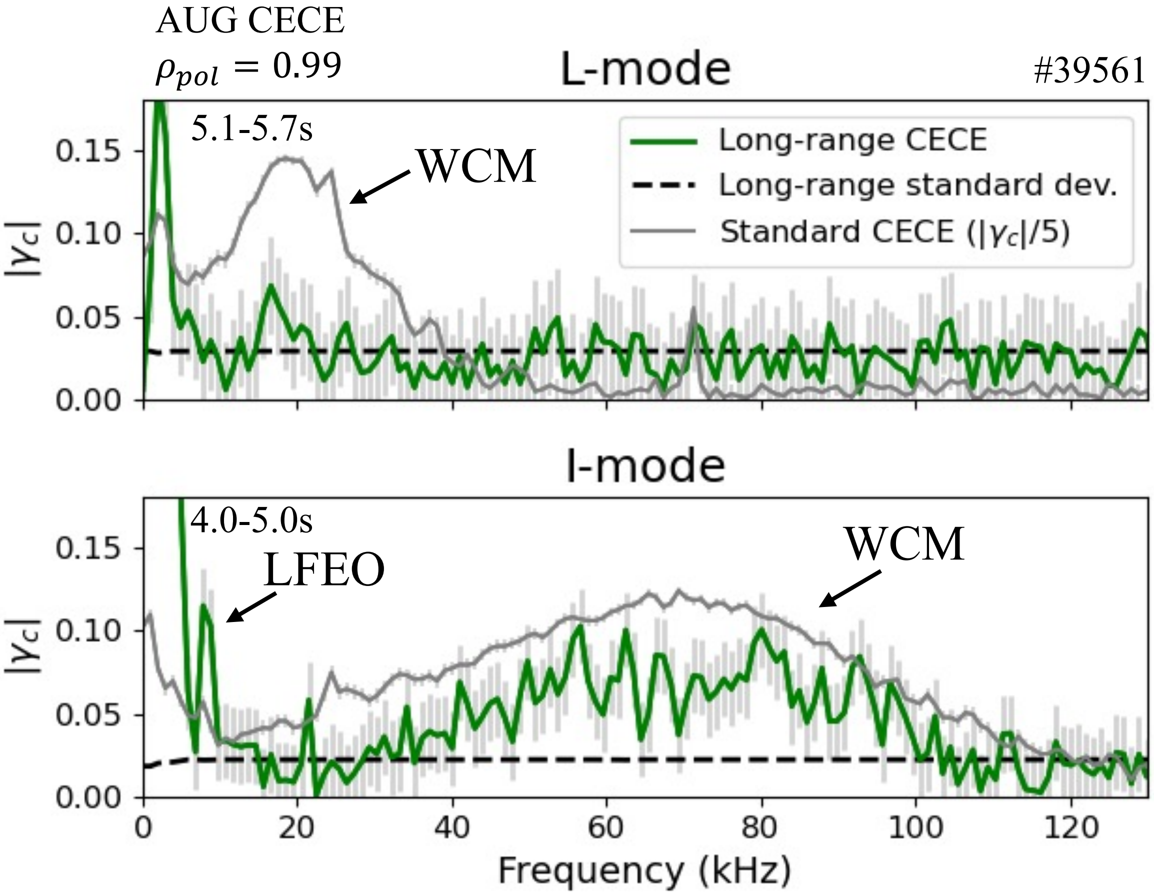

Figure 4.11: Coherence spectra from CECE channels at $\rho_{pol} = 0.99$ at toroidally separate locations, with normalized standard CECE spectra from a single CECE toroidal location overlaid for comparison. The standard deviation of the long-range coherence is given by the dashed line. The WCM feature is seen in both the L-mode and I-mode phases of the standard CECE analysis and is also present in the I-mode phase of the long-range CECE correlation.

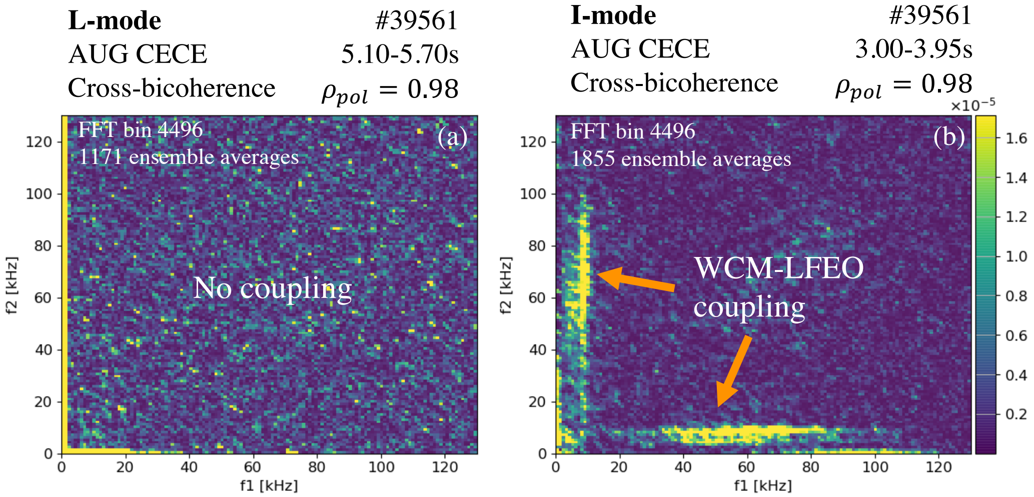

Figure 4.12: Cross-bicoherence of neighboring CECE channels near the WCM peak location of $\rho_{pol} = 0.98$ during a medium density discharge (39561). The L-mode phase (a) shows no coupling while the I-mode phase (b) shows coupling between the WCM (40-60 kHz) and the LFEO (5 kHz).

temperature signals $X(t)$ and $Y(t)$ is given by:

$$\hat{b}^2 = \frac{|\langle X(f_1)Y(f_2)X^*(f_1+f_2)\rangle|^2}{\langle|X(f_1)Y(f_2)|^2\rangle\langle|X^*(f_1+f_2)|^2\rangle} \tag{4.2}$$

where $X(f)$ and $Y(f)$ are the Fourier transforms of $x(t)$ and $y(t)$ and frequency coupling is investigated between f_1, f_2, and f_1+f_2. This bicoherence analysis was applied to a medium n_e discharge (core line integrated density of $\overline{n}_e = 5.3\times10^{19}\mathrm{m}^{-2}$) which was designed similar to the high n_e discharge for steady state L-mode and I-mode phases and the WCM appeared in both phases. For the cross-bicoherence calculation, FFT bins of 4096 are used with a Hanning window, with 1171 overlapping ensembles used for the L-mode period and 1855 used for the I-mode period. This analysis finds that in the L-mode phase of the discharge, despite the presence of the WCM, there is no three-wave coupling between different frequencies within the T_e fluctuation signals. In contrast, the I-mode phase displays coupling between the WCM frequency band (40-80 kHz) with the LFEO at $\sim$ 5 kHz. The coupling between the WCM and the LFEO is also seen in the auto-bicoherence of the thermal He beam channels during I-mode phases where these two fluctuations are present.

The localization of the LFEO, WCM, and the coupling between these two modes can be determined through CECE coherence spectra and bicoherence analysis. Figure 4.13 shows the maximum value of the CECE coherence in the LFEO and WCM range of frequencies over the radial ranges where these features exist. The LFEO and WCM have a peak amplitude at the same radial location near $\rho_{pol} = 0.99$. The WCM amplitude is nearly as high slightly farther inside near $\rho_{pol} = 0.98$ but the WCM amplitude is significantly lower inside $\rho_{pol} = 0.98$. The LFEO is visible over a slightly larger radial region than the WCM, extending to $\rho_{pol} = 0.97$. The degree of coupling is shown in 4.13 and is determined by calculating the maximum of the cross-bicoherence between neighboring CECE channels in the region of

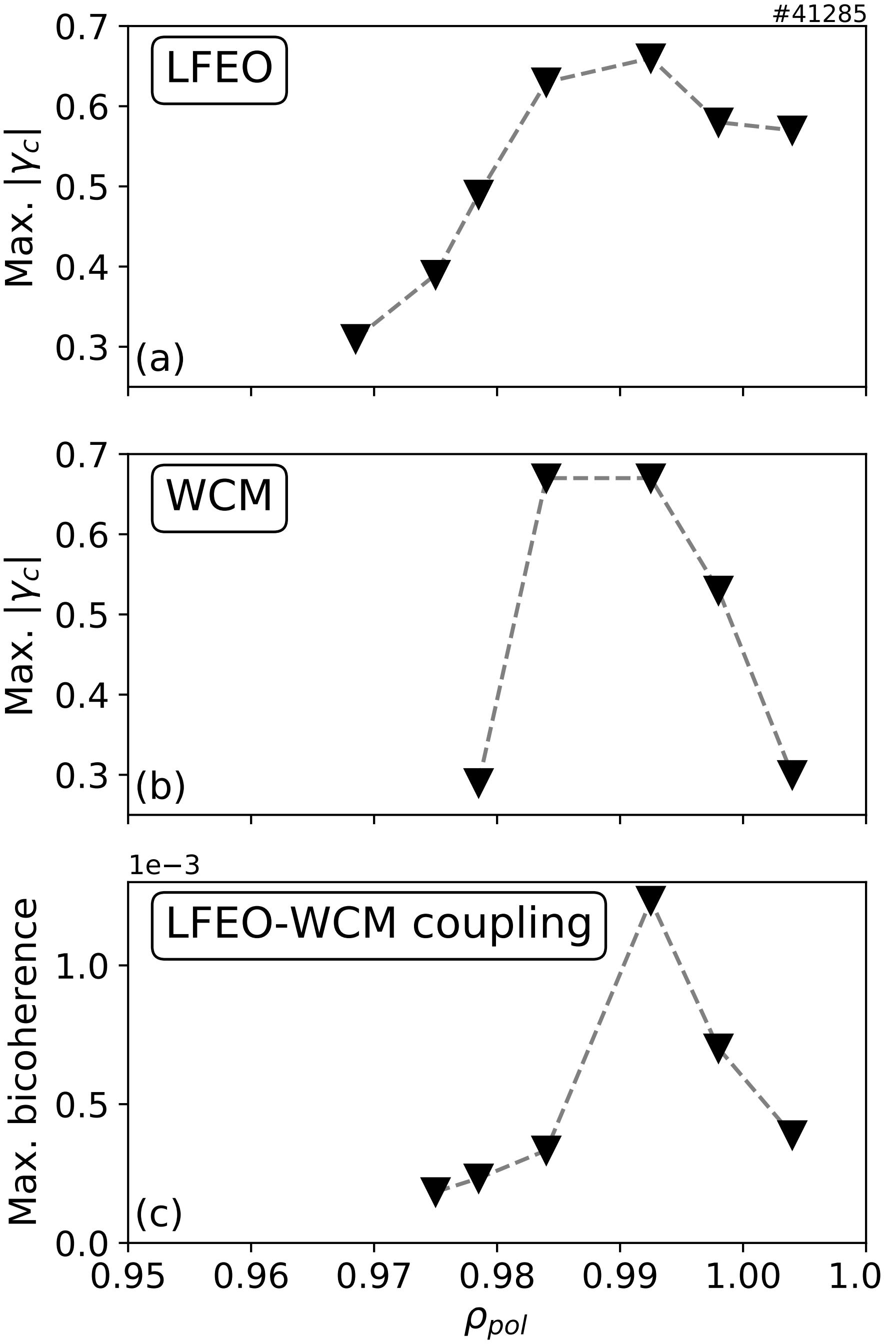

Figure 4.13: LFEO and WCM localization and coupling during an I-mode phase. (a) shows the maximum value of coherence of the LFEO over radius and (b) shows the maximum value of the coherence of the WCM feature over radius. (c) shows the the maximum value of the coupling calculated from the cross-bicoherence between neighboring CECE channels in the LFEO-WCM coupling range of frequencies.

frequency coupling between the WCM and LFEO. The coupling is maximum at the location where the WCM and the LFEO have the maximum amplitude, but falls off with radius more sharply than the WCM or LFEO coherence values fall off. This analysis suggests that the LFEO-WCM coupling is a highly localized process and that the WCM drive, LFEO drive, and the coupling between these modes is sensitive to properties near the LCFS.

Auto and cross-bicoherence analysis of CECE signals alone does not give information about energy transfer between the coupled modes, however frequency coupling is a prerequisite for the transfer of energy. The coupling shown here through CECE bicoherence analysis indicates that energy transfer between the WCM and LFEO may be possible. Through such transfer of energy, the LFEO could play a role in the overall state of the turbulence drive and damping, which in turn determines the turbulence-driven transport in the I-mode pedestal. In order to confirm this energy transfer and to determine its direction (whether the WCM transfers energy to or receives energy from the LFEO), additional measurements and analysis would be needed. These could include measurements of density and velocity fluctuations and the calculation of their spectral transfer, as performed in Reference [74].

4.7 Summary and discussion

In this chapter we investigated the pedestal fluctuations across a parameter space of density and collisionality in L-mode and I-mode, in particular the WCM which dominates the edge fluctuations. The presence of the WCM is not found to be correlated with the quality of confinement of the discharge, the depth of E_r, or the pedestal collisionality. However, the quality of confinement (as determined by the H_{98} factor) is negatively correlated with collisionality, with low confinement and high collisionality plasmas being L-modes and high confinement and low collisionality plasmas being I-modes.

This work is the first detailed study of the L-mode WCM. A summary of WCM properties observed with AUG's diagnostic suite is shown in Table 4.2. The consistency of wavenumber and radial location of the WCM between L-mode and I-mode indicate that this mode is the same in nature in the two regimes. The consistency of the frequency shift with a Doppler shift from increased $E \times B$ velocity in I-mode is further indication that this mode is the same between the two regimes. The increase in $\delta T_e/T_e$ and the change in $\alpha_{n_e T_e}$ between L-mode and I-mode could be explained as consequences of an increased pedestal ∇T_e in I-mode. This change in gradient could both drive the WCM more strongly leading to higher fluctuations, and cause a change in phase angle. Despite this higher ∇T_e drive and higher fluctuation amplitude in I-mode, the thermal diffusivity of I-mode is lower, indicating lower heat transport. These trends still remain to be explained. The coupling of the WCM and LFEO is a signature of the I-mode regime alone. This coupling has been shown to only occur in some I-modes [73], however it is present in all experiments presented in this thesis. One explanation for this coupling in I-mode alone could be that the increased WCM drive from increased ∇T_e crosses a coupling threshold where the WCM energy is strong enough to drive the zonal flow oscillation of the LFEO. The GAM review presented in Reference [49] discusses such drive thresholds in relation to the GAM. The coupling between the LFEO and WCM in I-mode is found to be highly localized, with the maximum value of the coupling occurring at the location of peak amplitude for the LFEO and WCM. This localized behavior

Table 4.2: Summary table of WCM observations in L-mode and I-mode

	L-mode	I-mode	Comparison
Radial location (ρ_{pol})	0.97-0.99	0.97-0.99	Same
Wavenumber (cm^{-1})	-0.5 to -1.0	-0.5 to -1.0	Same
Frequency (kHz)	20-50	40-150	Consistent with Doppler shift
$\delta T_e/T_e$ (%)	1.5-3%	2.5-4.5%	Higher in I-mode
n_eT_e cross-phase	171°	143°	Less out-of-phase in I-mode
WCM-LFEO coupling	None	Present	Marked difference
Long-range correlations	Not observed	Present	More measurements needed

suggests that the WCM drive, such as a critical ∇T_e, is highly localized.

This work has not definitively connected the WCM in L-mode or I-mode to transport of either energy or particles. The presence of the WCM across confinement regimes and across discharges of both low and high energy confinement indicates that it may not be the dominant contributor to the differences in transport between the two regimes. The question of the WCM's particle transport is still open. The fact that the WCM exists in both L-mode and I-mode could be consistent with the WCM driving particle transport, as particle transport and the density profile are constant between L-mode and I-mode. The $\alpha_{n_eT_e}$ measurements cannot alone determine the direction of heat and particle transport caused by the WCM. The pedestal fluctuations of L-modes and I-modes will be further investigated in the next chapter, with an expansion of the parameter space to both favorable and unfavorable magnetic configurations.

Chapter 5

Edge turbulence measurements across magnetic configurations in L-mode, I-mode, and H-mode plasmas

5.1 Introduction

In Chapter 4, edge fluctuations in L-mode and I-mode were studied and found to be of a similar nature in the two regimes and in particular, the WCM was found to dominate pedestal fluctuations in both L-mode and I-mode. In this chapter we will expand the study of pedestal turbulence to a wider parameter space of magnetic configuration and confinement regimes. As discussed in Section 2.2, the unfavorable magnetic configuration, with the ion $B \times \nabla B$ drift pointing away from the active X-point, has a wider power window for I-mode access due to the higher power threshold for the L to H transition. I-mode experiments at AUG, such as the studies in Chapter 4, are therefore designed in the unfavorable magnetic configuration. The L-mode phases with the WCM studied in Chapter 4 are also in the unfavorable configuration. A comparison of edge L-mode T_e turbulence in favorable and unfavorable magnetic configurations has until now not been performed.

The reason for the difference in power threshold in the favorable and unfavorable configurations is still unknown. Previous investigations and theories to explain the difference between favorable and unfavorable configuration are discussed in Section 2.2.3. To review, some candidates to explain the difference between the configurations include differences in the direction of SOL flows [61], differences in turbulence poloidal group velocity [55], [142], and differences in E_r in the confined region of the plasma [54]–[58] and the scrape-off layer (SOL) [59], [60]. Differences in the amplitude of turbulent fluctuations have not yet been reported. Several open questions remain to be answered about the favorable versus unfavorable configurations: whether there are real differences in the turbulence, what is the nature and cause of these possible differences, and what is the link between such differences and the L to H transition.

In this chapter an experimental study is described, which explores edge turbulence in favorable and unfavorable configurations in L-mode, I-mode, and H-mode. Much of the material in this chapter is reproduce from a previously published article [143] (© IOP

Publishing. Reproduced with permission. All rights reserved.) Differences between power-matched L-mode phases of favorable and unfavorable configuration discharges are found in edge T_{rad} fluctuations. The I-mode phase only exists in the unfavorable configuration discharge. Edge T_{rad} fluctuations in the favorable H-mode discharge show that the presence of edge fluctuations does not necessarily correlate with heat transport.

5.2 Experimental design

Dedicated experiments were performed on AUG to investigate the nature of edge turbulence across confinement regime transitions in the favorable and unfavorable magnetic field configurations. Two plasma scenarios will be described in detail in this section, in which the experimental design aimed to match *all* plasma characteristics, aside from the $B \times \nabla B$ direction. The time evolution of these discharges is shown in Figure 5.1. To access confinement regime transitions, Electron Cyclotron Resonance Heating (ECRH) was applied in power steps. The comparison between the favorable and unfavorable plasmas was performed by holding all programmed quantities of the plasma fixed between discharges, but changing the *direction* of the magnetic field between discharges from -2.5 T to $+2.5$ T. At AUG, counter-clockwise is taken the positive direction, and is the standard direction for the plasma current. Both discharges were performed in USN with the x-point at the top of the plasma, making the $+2.5$ T plasma the case with favorable $B \times \nabla B$ drift and the -2.5 T plasma the case with unfavorable $B \times \nabla B$ drift.

Both the favorable and unfavorable configuration discharges are in L-mode during the first two power steps and have matched ECRH power, stored energy, core electron temperature as determined by ECE, and edge density as determined by interferometry. In the following sections of this chapter, the first power phase at 0.2 MW ECRH is called the "low power L-mode" and the second power phase as 0.6 MW ECRH is called the "high power L-mode". At the end of the second ECRH power step, the favorable discharge undergoes a confinement regime to an ELMy H-mode with Type I ELMs. This L to H transition coincides with the timing of a diagnostic Neutral Beam Injection (NBI) blip. During the transition to H-mode, the density and stored energy increase. This H-mode is interrupted by a brief back-transition to L-mode accompanied by a spike in radiation, but then the plasma returns to H-mode. The unfavorable configuration discharge remains in L-mode during the 1.2 MW power step but enters I-mode with the fourth power step at 1.8 MW, during which the density does not increase but the electron temperature and stored energy increase moderately. With the fifth power step at 2.2 MW, the unfavorable configuration discharge transitions from I-mode to ELMy H-mode.

The low and high power L-mode phases were intended to match between the favorable and unfavorable configuration experiments so that direct comparisons of turbulence could be made. Figure 5.2 shows the electron density n_e, electron temperature T_e, and ion temperature T_i profiles from Thomson scattering and charge exchange recombination spectroscopy (CXRS). The profiles match within the scatter of the data except for core T_i. The equilibria are very closely matched, with the exception of the direction of the toroidal magnetic field. Because this study focuses on the edge ($\rho_{pol} = 0.95 - 1.0$) turbulence, the edge kinetic profiles are shown in more detail in Figure 5.3 with profile fits made to the data. The fits

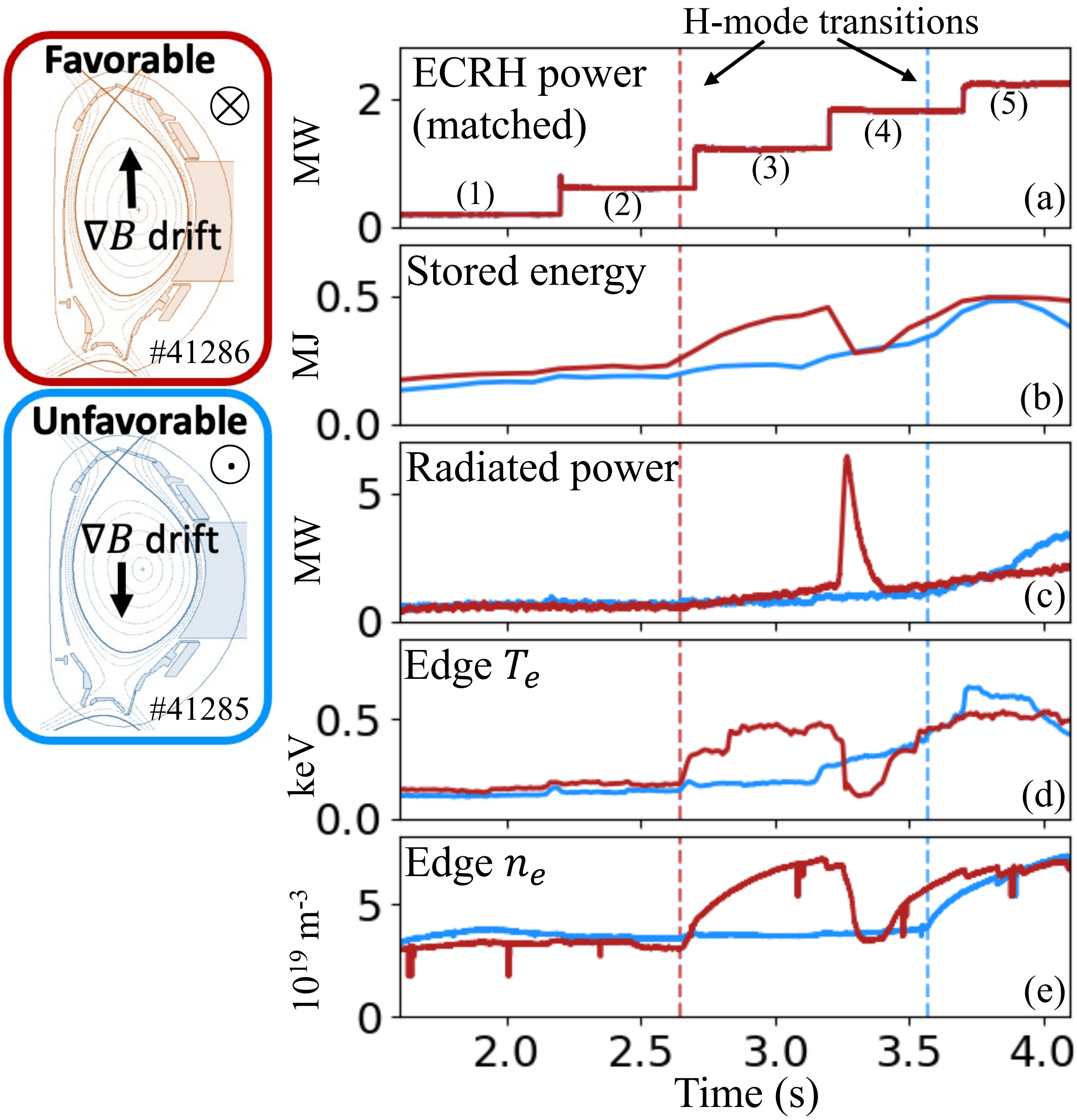

Figure 5.1: Time histories of favorable discharge #41286 (red) and unfavorable discharge #41285 (blue). (a) shows the ECRH power, (b) shows stored energy (W_{MHD}), (c) shows the radiated power, (d) shows the edge T_e at $\rho_{pol} = 0.95$ from Integrated Data Analysis (IDA), and (d) shows the edge n_e from interferometry. The H-mode transition is observed for the favorable discharge at 2.6s at the end of the 2nd ECRH power step, while the unfavorable discharge undergoes an H-mode transition in the 4th ECRH power step.

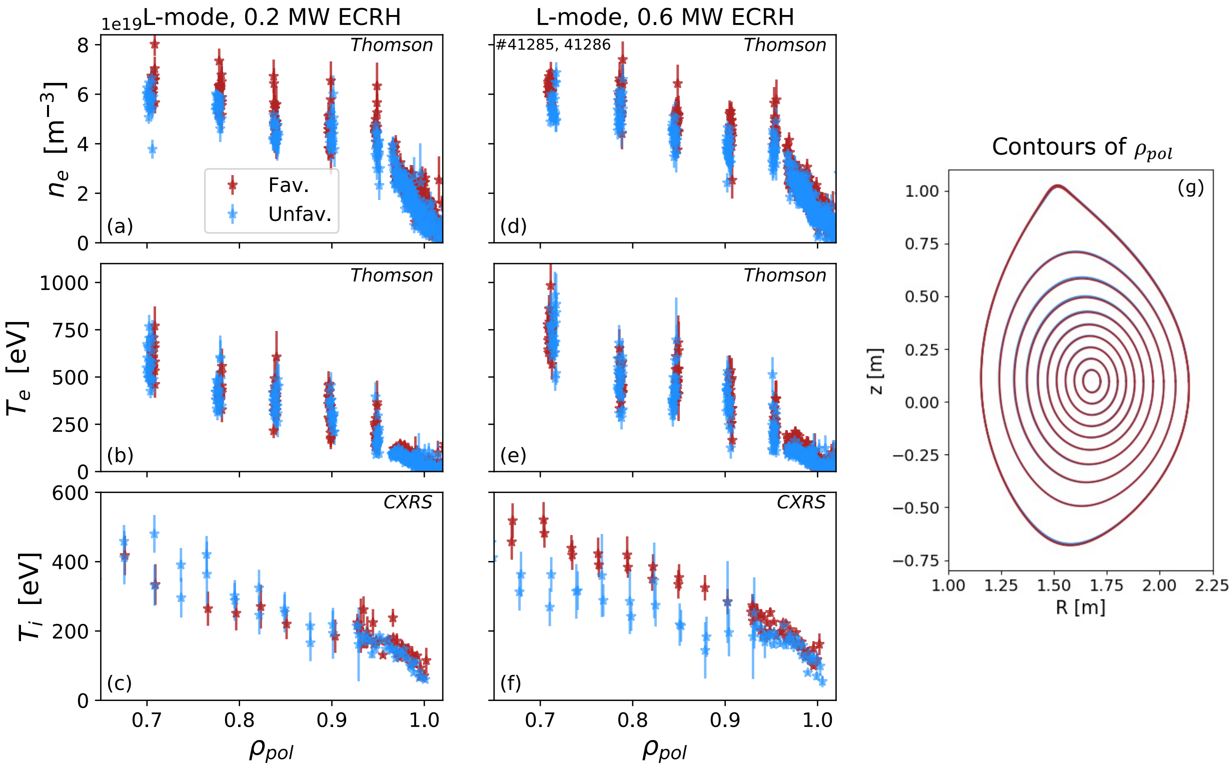

Figure 5.2: Kinetic profiles of the favorable (red) and unfavorable (blue) configuration discharges during the low power (a-c) and high power (d-f) L-mode phases from the outer core to separatrix. n_e (a, d) and T_e (b, e) measurements are from Thomson scattering and T_i measurements are from CXRS. Equilibria of the favorable and unfavorable discharges are shown to overlap closely in (g)

are modified hyperbolic tangents, made with a Monte Carlo approach varying measurement data within their error bars. In this edge region, the difference in the fits to the profiles is as high as 25% in the steepest gradient region of the edge ($\sim \rho_{pol} = 0.98$), with the favorable discharge having slightly higher values of n_e, T_e, and T_i than the unfavorable discharge. The difference in the mean of the data in favorable and unfavorable configurations is similar to the standard deviation of the data around a particular radial location for n_e, T_e, and T_i.

5.3 Edge turbulence in the unfavorable magnetic configuration

Pedestal ($\rho_{pol} = 0.95 - 1.0$) radiated temperature (T_{rad}) fluctuations were measured with the CECE diagnostic. As described in Section 3.3.1, several properties of edge T_{rad} fluctuations may be determined from CECE measurements, including the frequency coherence spectra $|\gamma(f)|$, the normalized fluctuation amplitude $\delta T_{rad}/T_{rad}$, and the radial correlation length of

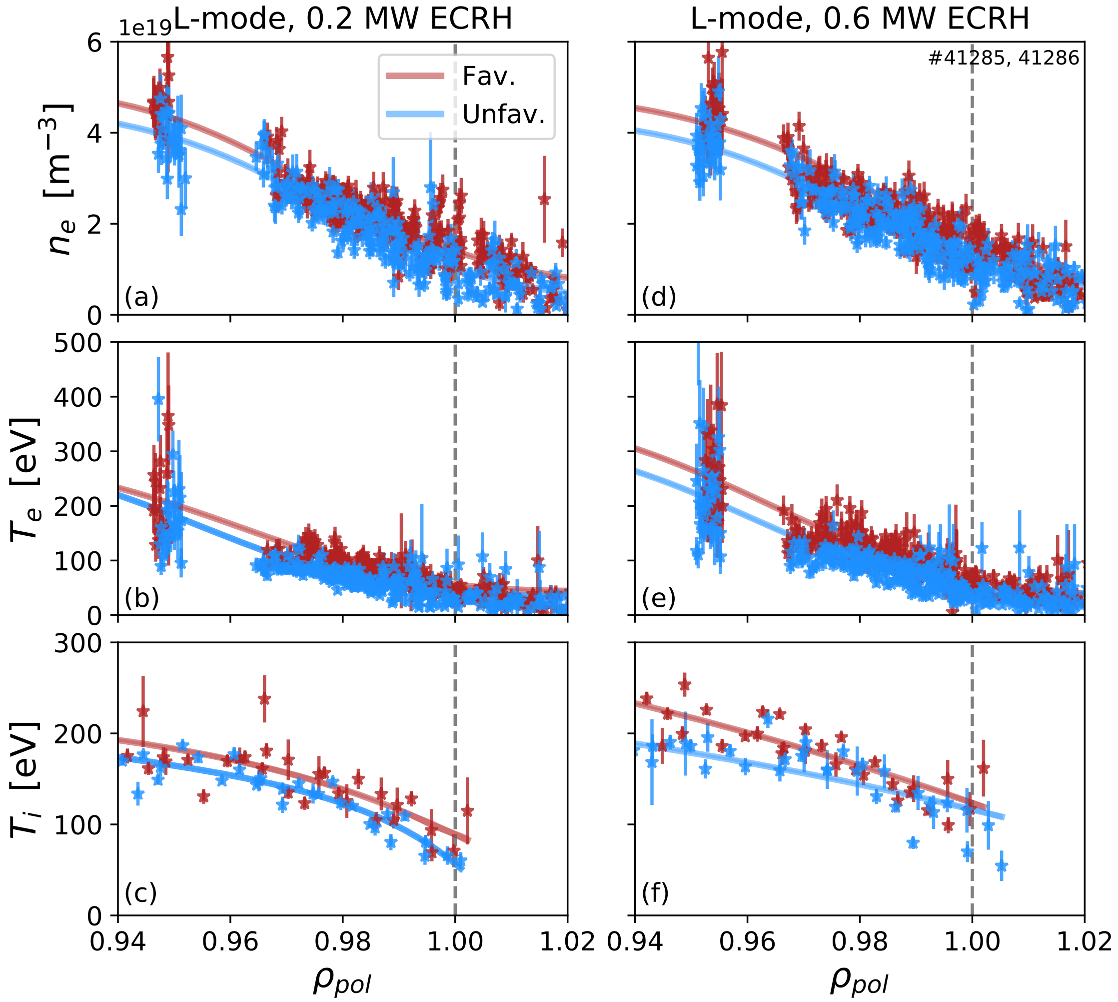

Figure 5.3: Edge kinetic profiles of the favorable (red) and unfavorable (blue) configuration discharges during the low power (a-c) and high power (d-f) L-mode phases with fits generated with modified hyperbolic tangent functions. The separatrix is shown by the vertical dashed grey lines at $\rho_{pol} = 1.0$.

T_e turbulence. We report here only on radiated temperature T_{rad} fluctuations rather than electron temperature T_e fluctuations because of the optically thin nature of edge plasmas. The radial electric field E_r was measured in these experiments using the He II spectroscopy (HES) system which uses active spectroscopy to measure E_r from the pedestal region to the scrape off layer (SOL) [41].

The development of the WCM can be seen during the L-mode phase of the unfavorable configuration discharge and is studied here for the first time during L-mode phases at low heating power, far below the L to I transition. Figure 5.4 shows the evolution of the unfavorable configuration CECE coherence spectra near the last closed flux surface (LCFS) and E_r during a low power L-mode phase (1.65-2.15s, 0.2 MW ECRH), high power L-mode phase (2.23-2.63s, 0.6 MW ECRH), and an I-mode phase (3.30-3.55s, 1.8 MW ECRH). The development of the WCM is seen in the coherence spectra over the course of the discharge, starting as a feature centered at 35 kHz in the L-mode phases and growing in power until the I-mode phase at which point the WCM center frequency increases to 85 kHz. During the I-mode phase, the LFEO can also be seen in the coherence spectra as a narrow-band mode at 7.8 kHz. The LFEO appears only in the I-mode phase of this discharge.

The E_r profiles are flat in both L-mode phases and a moderate well forms during the I-mode phase, reaching a depth of -14 kV/m. From the E_r profile and the magnetic field, the $E \times B$ velocity shearing rate ($\gamma_{E\times B}$) is calculated at $\rho_{pol} = 0.99$. The shearing rate increases from 0.4 to 1.2×10^5 s^{-1} in the L-mode phases, to 5.2×10^5 s^{-1} in I-mode. We also estimate the expected Doppler shifts of turbulent features at $\rho_{pol} = 0.99$. As discussed in Chapter 4, the Doppler frequency shift, $f_{Doppler}$, may be determined by $f_{Doppler} \sim k_\theta v_\theta$ with $v_\theta = E_r/B_\phi$ and k_θ the poloidal wavenumber of the turbulent mode. The average WCM poloidal wavenumber, shown in Chapter 4 to be $k_\theta \sim 0.75$ cm^{-1}, is used for these Doppler shift estimations. The Doppler shift increases from 15 kHz in L-mode just prior to the L to I-mode transition, to 63 kHz in I-mode. The shift in the WCM center frequency between L and I-mode WCM could be consistent with this estimated Doppler shift due to increased $v_{E\times B}$, although other candidates exist to explain the difference in frequency of the WCM between L and I-mode, such as a change in the drive or nature of the mode, or the coupling between the WCM and the LFEO.

5.4 Edge turbulence in the favorable magnetic configuration

Figure 5.5 shows the development of the favorable configuration CECE coherence spectra at the pedestal bottom ($\rho_{pol} \sim 0.99$) and E_r during a low power L-mode phase (1.65-2.15s, 0.2 MW ECRH), high power L-mode phase (2.23-2.63s, 0.6 MW ECRH), and the inter-ELM period of an H-mode phase (3.96-4.0s, 2.2 MW ECRH). The L-mode phases in this favorable configuration discharge are power-matched with the L-mode phases of the unfavorable configuration discharge described in the previous section. The edge kinetic profiles of this favorable configuration discharge match within the scatter of the data, as described in Section 5.2. The H-mode of this favorable configuration discharge is not comparable to the I-mode phase of the unfavorable configuration discharge because during H-mode the particle

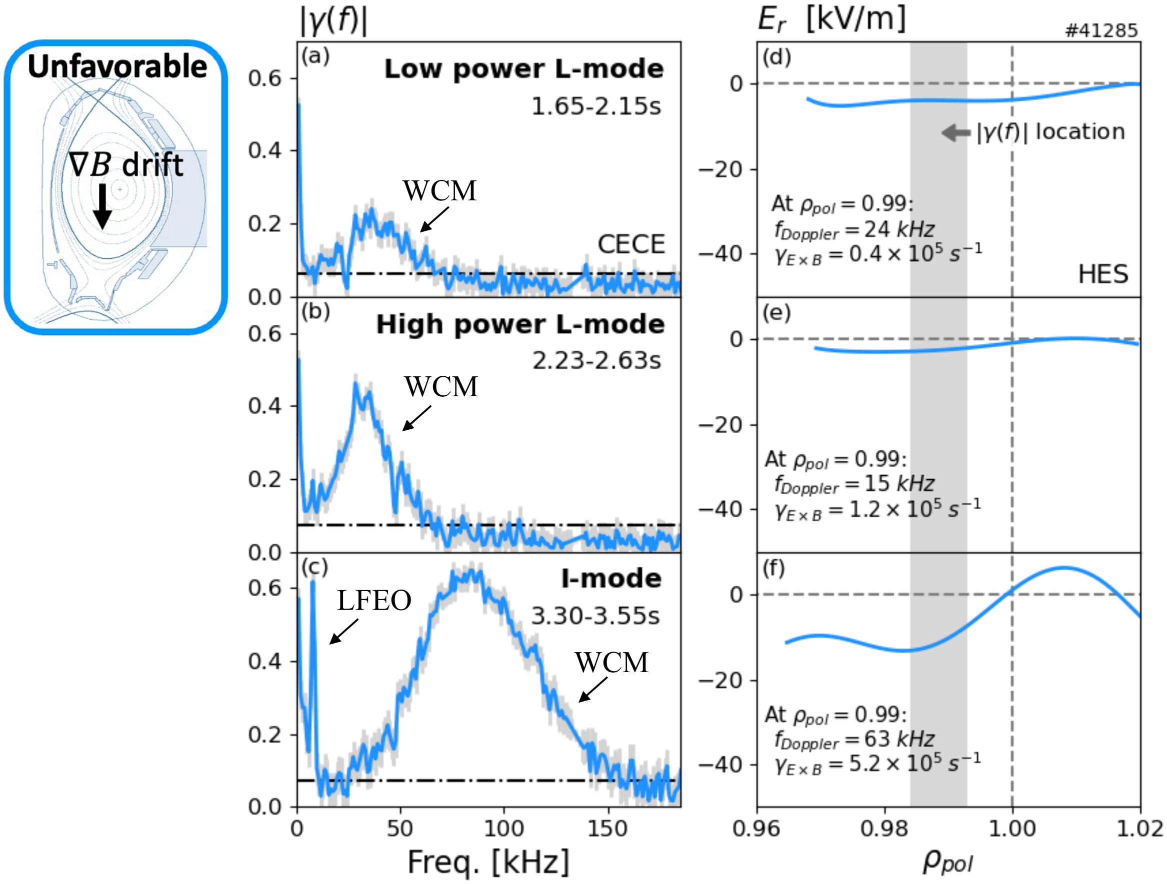

Figure 5.4: Development of T_{rad} CECE coherence $|\gamma(f)|$ spectra (a-c) in the edge (channel 16, $\rho_{pol} \sim 0.99$) and pedestal E_r (d-f) over the unfavorable configuration discharge, #41285. The WCM centered at 35 kHz is present in the $|\gamma(f)|$ spectra of both the low and high power L-mode phases, and at 85 kHz during the I-mode phase. E_r develops from a weak E_r well in the L-mode phases to a moderate well in I-mode. Also shown are the calculated $E \times B$ shearing rate at $\rho_{pol} = 0.99$, as well as the expected Doppler shift due to the $E \times B$ velocity at $\rho_{pol} = 0.99$ for a large-scale mode with wavenumber $k = 0.75$ cm^{-1}. The black dashed line in (a-c) is the CECE statistical limit.

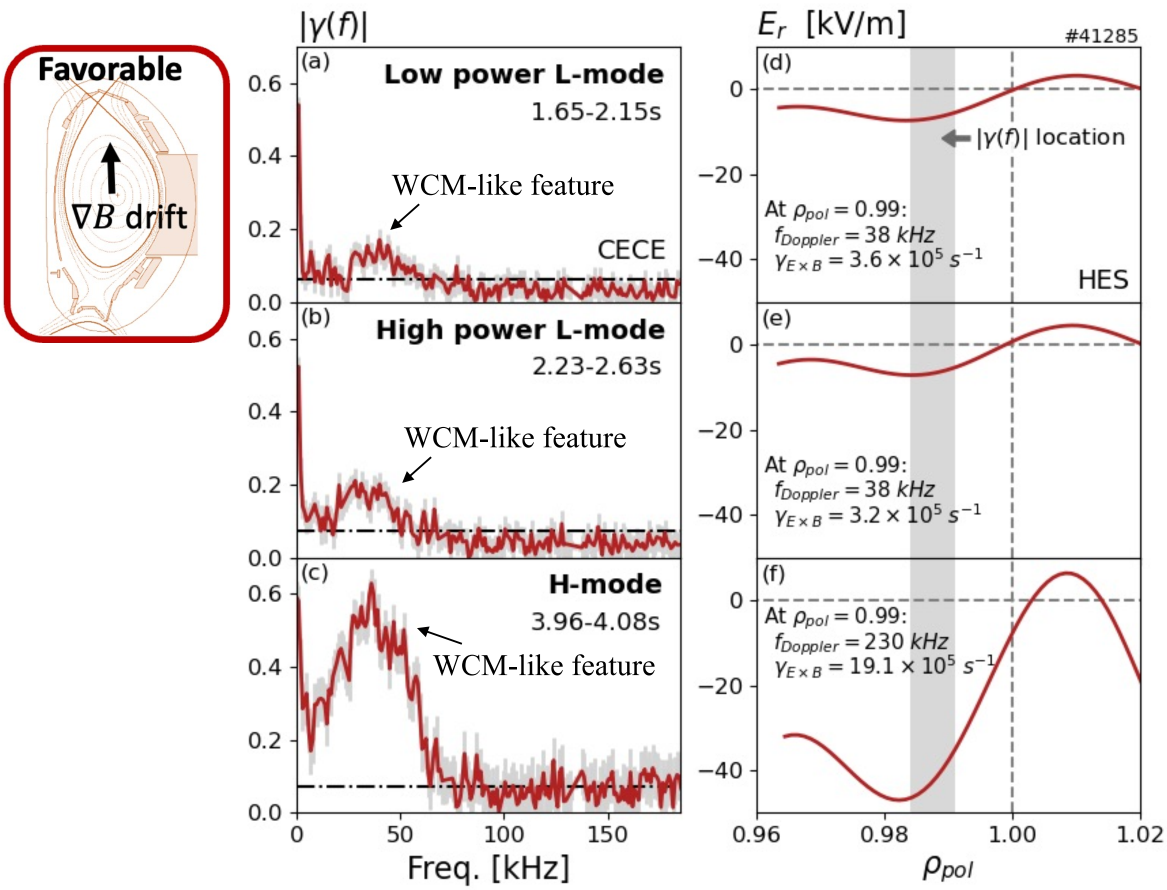

Figure 5.5: Development of T_{rad} CECE coherence $|\gamma(f)|$ spectra (a-c) in the edge (channel 16, $\rho_{pol} \sim 0.99$) and pedestal E_r (d-f) over the favorable configuration discharge, 41286. A structure centered at 35 kHz is present in the $|\gamma(f)|$ spectra of both the low and high power L-mode phases as well as the H-mode phase. E_r develops from a shallow well structure in the L-mode phases to a deep well in H-mode. Also shown are the calculated $E \times B$ shearing rate at $\rho_{pol} = 0.99$, as well as the expected Doppler shift due to the $E \times B$ velocity at $\rho_{pol} = 0.99$ for a large-scale mode with wavenumber $k = 0.75$ cm^{-1}. The black dashed line in (a-c) is the CECE statistical limit.

		Favorable		Unfavorable	
Regime	Time [s]	ΔR_{WCM} [cm]	Peak Location [ρ_{pol}]	ΔR_{WCM} [cm]	Peak Location [ρ_{pol}]
L-mode	1.65-2.15s	0.4	0.984	0.4	0.984
L-mode	2.23-2.63s	1.0	0.991	1.8	0.993
I-mode	3.30-3.55s	–	–	2.1	0.991

Table 5.1: Properties of the WCM and WCM-like features in the pedestal of the different phases of the favorable and unfavorable configuration plasmas. The feature grows in radial extent over the course of the discharges with larger radial growth occurring in the unfavorable configuration discharge. The location of the peak of the WCM and WCM-like features is the same in both discharges and the L and I confinement regimes. The radial extent and peak location in H-mode cannot be determined due to ECE cutoff near the pedestal top.

transport barrier is formed and the density increases as compared to L-mode and I-mode.

A WCM-like spectral feature is seen in the coherence spectra centered at 35 kHz in both L-mode phases and the H-mode phase. The strength of this WCM-like feature grows during the H-mode phase. The E_r profiles display shallow wells of -5 to -8 kV/m during the L-mode phases and a deep well during the H-mode phase of the discharge, reaching -47 kV/m. The shearing rate $\gamma_{E\times B}$ calculated at $\rho_{pol} = 0.99$ increases by more than five times between L-mode and H-mode at this radial location, from 3.2 to 3.6×10^5 s^{-1} in L-mode, to 19.1×10^5 s^{-1} in I-mode. The estimated Doppler shift of a turbulent feature at $\rho_{pol} = 0.99$ due to the calculated $E \times B$ velocity for a feature with wavenumber $k = 0.75$ cm^{-1} increases between L-mode and H-mode from 38 kHz to 230 kHz as the E_r well develops. However, despite this increased Doppler shift, the feature does not change in frequency between L-mode and H-mode.

5.5 Comparison of matched favorable and unfavorable configuration fluctuations

To understand the differences in edge turbulence between favorable and unfavorable configurations, a side-by-side comparison of the power-matched discharges is useful. Comparison of power-matched phases shows differences between favorable and unfavorable configurations in the radial extent of the WCM, differences in edge E_r, and differences in T_{rad} fluctuation amplitude.

The development of the radial extent of the WCM in the unfavorable configuration discharge and WCM-like feature in the favorable configuration discharge is shown in Table 5.1. The radial extent of the WCM or WCM-like feature, ΔR_{WCM}, is calculated by correlating sequential CECE channels spanning increasing radial distance. The radial extent ΔR_{WCM} is defined as the maximum radial distance between CECE channels for which the WCM or WCM-like feature is apparent in the coherence spectrum between channels. An example of the determination of ΔR_{WCM} for the I-mode phase of the unfavorable discharge is shown in Figure 5.6. Correlations are performed between CECE channel 17 and sequentially farther channels in each direction (from channel 14 to channel 20). The WCM appears in the coherence spectrum between 15 and 17, which are spaced apart by 1.2 cm. The WCM does not appear in the coherence between channels 14 and 17. In the other direction, the WCM is apparent in the coherence spectrum between channels 19 and 17, which are spaced apart by 0.9 cm, but not apparent in the coherence spectrum of channels 20 and 17. The WCM radial extent therefore spans channels 15 to 19, which are radially separated by a total distance of 2.1cm.

The WCM peak location is the location at which the WCM or WCM-like feature has the maximum value of $|\gamma(f)|$ between neighboring CECE channels. The WCM and WCM-like feature in the unfavorable and favorable configurations respectively share the same radial extent (0.4 cm) and same peak location ($\rho_{pol} = 0.984$) during the low power L-mode phase early in the discharge. During the second L-mode phase at higher power, the WCM and WCM-like feature share a similar peak location in favorable ($\rho_{pol} = 0.991$) and unfavorable ($\rho_{pol} = 0.993$) configurations, but the mode grows to a wider radial extent in the unfavorable configuration (1.8 cm) compared to the favorable configuration (1.0 cm). During the I-mode phase of the unfavorable configuration discharge, the peak amplitude of the WCM remains at a similar peak location ($\rho_{pol} = 0.991$) as during the L-mode phases and grows to a yet larger radial extent (2.1 cm). The favorable configuration discharge does not have an I-mode phase. During the H-mode phase of the favorable configuration discharge the WCM-like feature's peak location and radial extent could not be clearly determined due to ECE cutoff occurring near the pedestal top. This investigation shows that the WCM and WCM-like feature grows in radial extent during the L-mode phases of both favorable and unfavorable configuration plasmas. The location of the peak of this feature is similar in the favorable and unfavorable configuration L-modes, and remains similar during the unfavorable configuration I-mode phase. This analysis suggests that the WCM-like feature in favorable configuration L-mode may be the same WCM as appears in unfavorable configuration L-modes.

A comparison of the matched high power (0.6 MW ECRH) L-mode phases of the favorable and unfavorable configuration discharges reveals important differences in edge plasma properties close to confinement regime transitions. The difference in E_r during this phase is shown in Figure 5.7. The favorable configuration discharge forms a more significant E_r well and region of shear during this L-mode than the unfavorable configuration discharge. This is consistent with previous observations of deeper wells in favorable compared to unfavorable configuration plasmas at AUG and other tokamaks [55]–[58]. A comparison of the T_{rad} fluctuation properties across the pedestal in favorable and unfavorable configurations is shown in Figure 5.8. By integrating the coherence spectra, as in Ref. [95], the normalized fluctuation amplitude $\delta T_{rad}/T_{rad}$ may be determined. The frequency range 10-150 kHz was used for this integration, with the background coherence averaged over the range 150-200 kHz. At $\rho_{pol} = 0.95$, neither the favorable or unfavorable configuration discharges display significant turbulent features above the CECE statistical limit, $|\gamma(f)| = 0.07$. At this location, $\delta T_{rad/}T_{rad}$ is 0.3% in the favorable configuration and 0.4% in the unfavorable configuration, but both measurements are within error bars of the CECE $\delta T_{rad}/T_{rad}$ statistical limit of 0.2%. In the steeper gradient region of $\rho_{pol} = 0.97$, broadband turbulence can be seen in the CECE coherence spectra, with a higher coherence in the unfavorable case than the favorable case. At this location, the favorable configuration discharge $\delta T_{rad}/T_{rad} = 0.5\%$ while the unfavorable configuration discharge $\delta T_{rad}/T_{rad} = 1.1\%$. Near the last closed flux

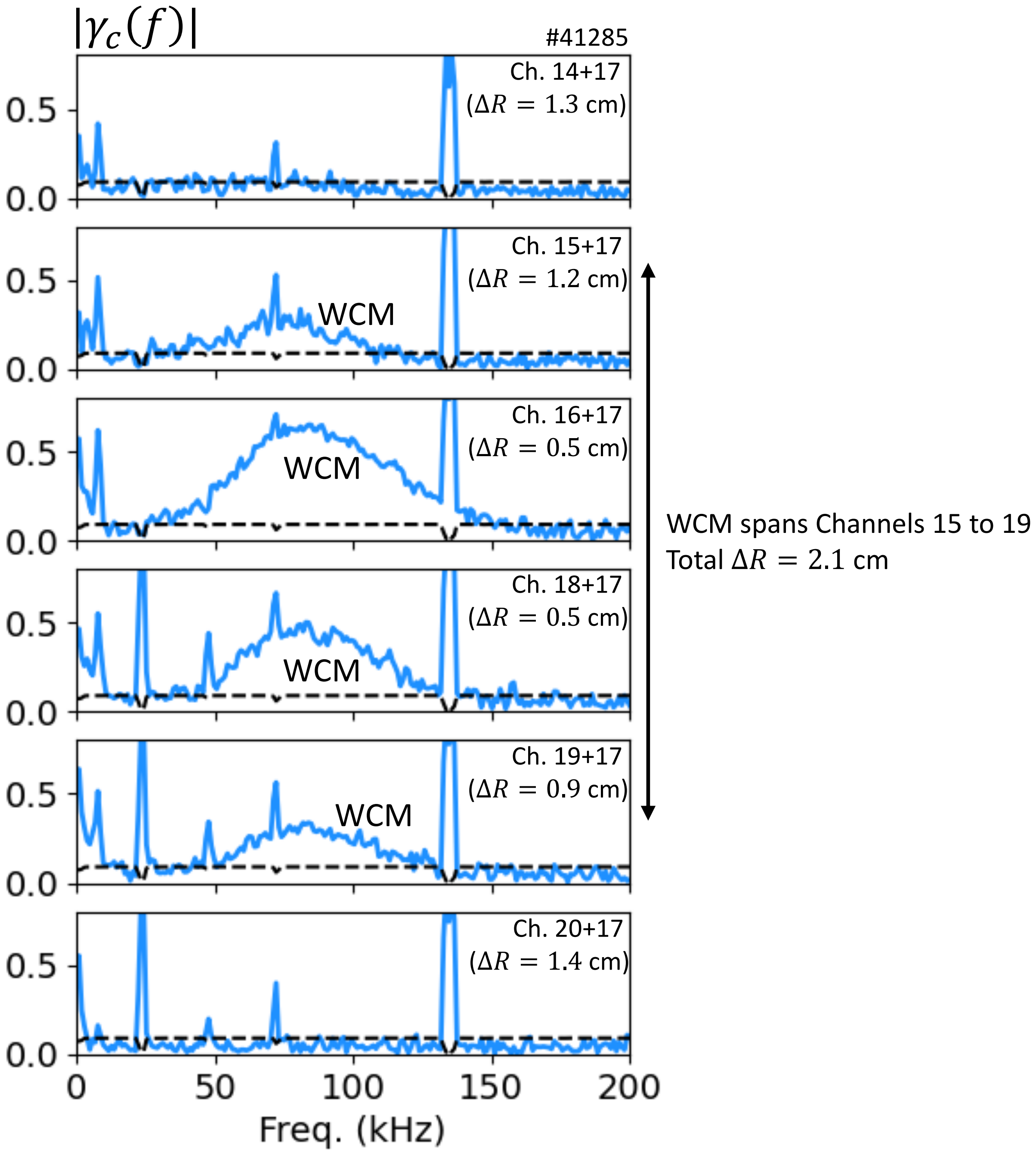

Figure 5.6: Coherence spectra performed between sequential CECE channels (14 to 20) and channel 17 during the I-mode phase (3.30-3.55s) of the unfavorable discharge (#48215). The WCM is apparent in the coherence between channel 17 and the channels ranging from 14 to 19. $\Delta R_{WCM} = 2.1$ cm, equivalent to the radial distance between channel 14 and 19.

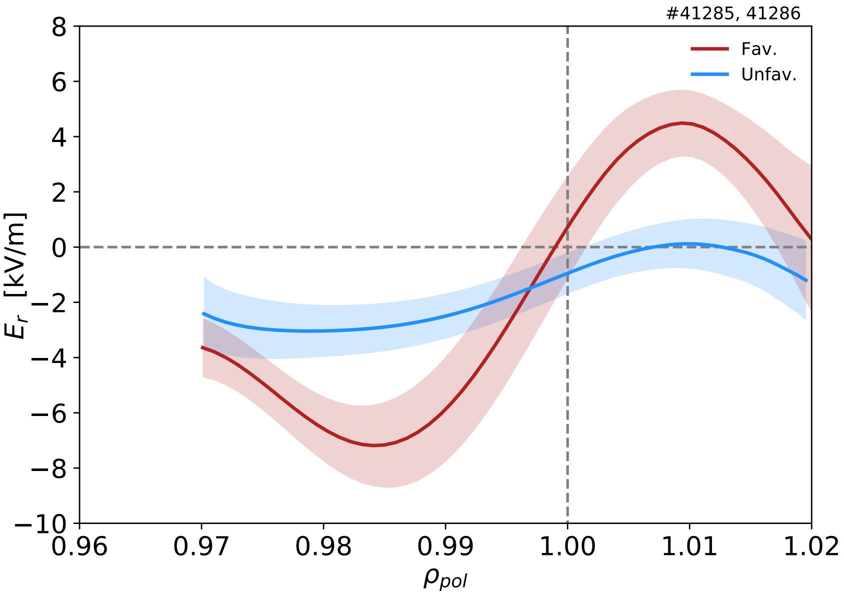

Figure 5.7: E_r profiles during the matched high power (0.6MW ECRH) phases of the favorable and unfavorable configuration discharges. The favorable configuration plasma (red) is deeper and has a more well-like structure than the unfavorable configuration plasma (blue).

surface at $\rho_{pol} = 0.99$, the favorable and unfavorable configuration spectra are dominated by the L-mode WCM. Here the favorable configuration discharge $\delta T_{rad}/T_{rad} = 0.7\%$ while the unfavorable configuration discharge $\delta T_{rad}/T_{rad} = 1.2\%$. In both the favorable and unfavorable configuration plasmas, $\delta T_{rad}/T_{rad}$ increases from the outer core towards the pedestal bottom, but the increase is larger in the unfavorable configuration than the favorable configuration. The difference in fluctuation amplitude correlates with the difference in E_r in these L-mode phases, with the E_r well formation in the favorable configuration coinciding with lower pedestal turbulence.

5.6 Three wave mode coupling across L, I, and H-modes

The WCM feature in the lower pedestal appears to develop in both favorable and unfavorable configuration L-modes, and may remain during the inter-ELM period of favorable configuration H-modes. The LFEO only occurs during the unfavorable configuration I-mode. To study the coupling properties of edge T_{rad} fluctuations, the cross-bicoherence was calculated between neighboring CECE channels near the LCFS ($\rho_{pol} = 0.99$) where the WCM and WCM-like feature is present. The CECE cross-bicoherence from L-mode, I-mode, and H-mode phases is shown in Figure 5.9. The L-mode phase of the favorable and unfavorable discharges do not show any significant coupling. When the LFEO appears during I-mode, it couples to the WCM, as seen by the coupling between the WCM band of frequencies (70-100kHz in I-mode) and the LFEO frequency (7.8kHz). During the H-mode phase of the favorable configuration discharge, the cross-bicoherence shows coupling between the WCM-like feature range of frequencies (25-60kHz) and a range of frequencies below 10kHz. This

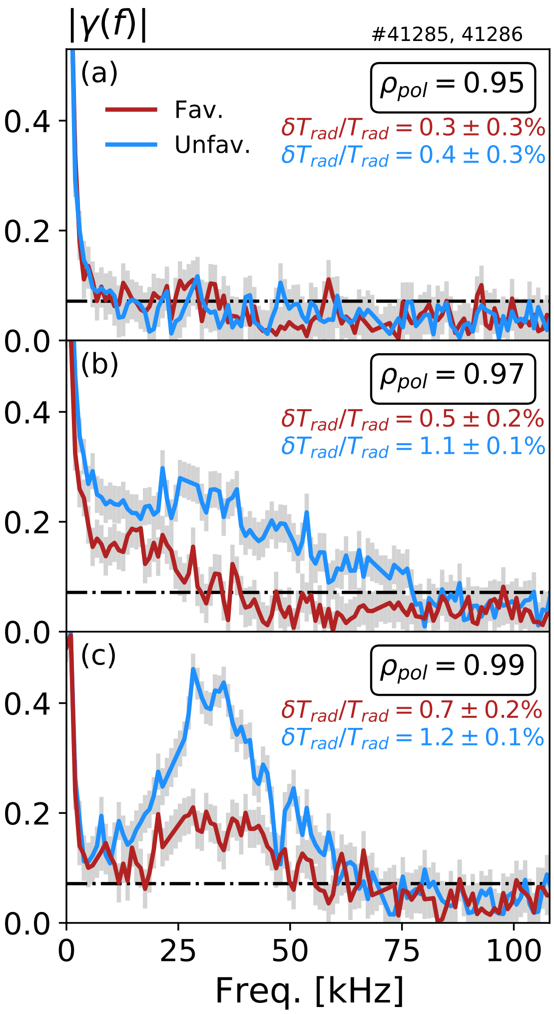

Figure 5.8: T_{rad} CECE coherence $|\gamma(f)|$ spectra in power matched favorable (red) and unfavorable (blue) configuration discharges at three radial positions (a) $\rho_{pol} = 0.95$, (b) $\rho_{pol} = 0.97$, and (c) $\rho_{pol} = 0.99$ during the high power L-mode phase prior to confinement regime transitions. The fluctuation amplitude $\delta T_{rad}/T_{rad}$ near the sensitivity limit at $\rho_{pol} = 0.95$. $\delta T_{rad}/T_{rad}$ grows as radius increases and is higher in the unfavorable configuration than the favorable configuration at $\rho_{pol} = 0.97$ and 0.99.

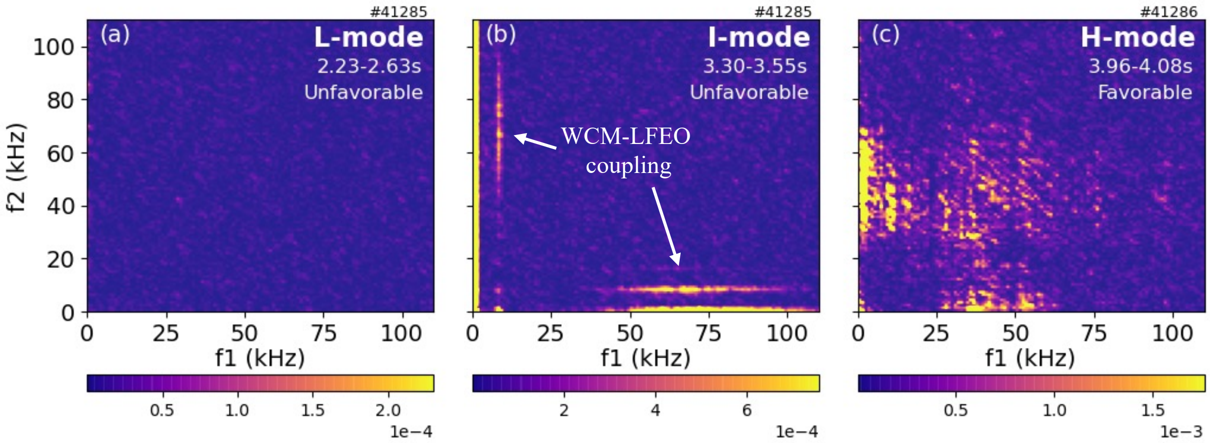

Figure 5.9: Cross-bicoherence of neighboring CECE channels at $\rho_{pol} = 0.99$ during (a) unfavorable configuration L-mode, (b) unfavorable configuration I-mode, and (c) favorable configuration H-mode phases. The L-mode phase shows no coupling. The I-mode phase shows coupling between the WCM range of frequencies (50-100 kHz) and the LFEO frequency (7.8 kHz). The H-mode case shows diffuse coupling between the WCM-like feature range of frequencies (25-60 kHz) and low frequencies (<10 kHz). In all cases FFT bins of 4096 were used and 781, 488, and 238 overlapping (50%) ensemble averages used in L, I, and H mode respectively.

frequency coupling is more diffuse than the clear WCM-LFEO coupling of I-mode. Bicoherence analysis shows only frequency coupling and does not provide information about energy transfer, but this coupling is a prerequisite for energy transfer.

The WCM and GAM or LFEO are known to couple and exchange energy, with the GAM receiving energy from the WCM and possibly responsible for the frequency broadening of the WCM [74], [144]. A review of GAMs is presented in Reference [49]. The transfer of energy between turbulence and GAMs and zonal flows (ZF) are thought to be important to confinement regime transitions. One physical explanation for the L (or I) to H transition is that the transfer of energy from turbulence to ZFs reaches a threshold corresponding with turbulence drive [145], [146]. A competition between the transfer of energy from turbulence to ZFs and to GAMs may be possible during I-mode in the unfavorable configuration, but contrasting views exist about the existence of a ZF/GAM competition in the direct L to H transition in favorable magnetic configuration [145], [146]. The coupling investigation presented here is in agreement with this previous work in that only the I-mode phase features coupling between the GAM and LFEO/GAM, while the H-mode phase is not accompanied by a GAM but does feature possible coupling between turbulence and low-frequency ZFs.

5.7 Summary and discussion

In this chapter we investigated edge turbulence in favorable and unfavorable magnetic configurations in power-matched L-modes and after confinement regime transitions to I-mode and

H-mode. We find that the WCM develops in both the favorable and unfavorable configuration L-modes, but has a higher coherence $|\gamma(f)|$ and a larger radial extent in the unfavorable configuration than the favorable configuration in the higher power L-mode phase close to confinement regime transitions. The differences in fluctuation amplitude are correlated with differences in E_r, with the shallower well of the unfavorable configuration accompanying the higher $|\gamma(f)|$ and $\delta T_{rad}/T_{rad}$. The unfavorable configuration discharge undergoes a confinement regime transition to I-mode, during which the WCM shifts to higher frequency, grows in coherence and radial extent, and couples with the LFEO. The favorable configuration discharge undergoes a confinement regime transition to H-mode. During an inter-ELM period of the H-mode phase, a WCM-like feature appears at the same location as the L-mode WCM.

The nature of the L-mode edge T_{rad} turbulence appears similar between favorable and unfavorable configurations, as evidenced by the WCM formation in both configurations. However, the fluctuation amplitude of edge turbulence is higher in the unfavorable configuration than the favorable configuration, in correlation with a deeper E_r well and stronger $E \times B$ shear. One candidate to explain this correlation could be that plasmas in the favorable configuration more effectively transfer energy from turbulence to sheared flows. Another candidate could be that the three dimensional nature of turbulence is different between favorable and unfavorable configurations due to different SOL conditions, leading to differences in $E \times B$ flow and shear. These SOL flows place a boundary condition on the confined region $E \times B$ flow, and therefore could lead to differences in fluctuations in the confined region. More measurements are needed to test these hypotheses.

The observations presented in this chapter suggest that one interpretation of the I-mode confinement regime is an extension of the unfavorable configuration L-mode parameter space. In the I-mode regime of operation, sufficient auxiliary heating power enables the plasma to become hot and form a temperature pedestal. However, due to the higher power threshold for the L to H transition in the unfavorable configuration, the plasma does not transition to H-mode. Chapter 4 indicated that the nature of pedestal turbulence is also similar between I-mode and L-mode, in that the WCM dominates edge fluctuations. The difference between the I-mode and L-mode fluctuations may be that in I-mode, the WCM drive is strengthened due to increased heating power and ∇T_e, and this drive is stronger than damping via sheared $E \times B$ flow. When the WCM is driven strongly enough, it is able to impart energy to the LFEO. The WCM-LFEO coupling threshold is therefore one way to define the transition to I-mode regime. The nature of the edge turbulence does not change across this transition, but its drive and fluctuation amplitude increases. The role of the I-mode LFEO in aiding the overall turbulence shearing rate or turbulence energy flow, and thereby the LFEO's role in reducing or enhancing the turbulence-driven transport, is an important point for future study.

The I-mode confinement regime is the only phase during the presented favorable and unfavorable discharges in which the WCM center frequency experiences an upshift to 85 kHz. Although the change in frequency between the unfavorable configuration L-mode and I-mode would be consistent with a Doppler shift of a WCM-scale mode due to the measured increased $v_{E\times B}$, no such frequency shift appears in other discharge phases with similar changes in E_r. For example, the L-mode WCM is centered at 35 kHz in both favorable and unfavorable configuration discharges despite different $v_{E\times B}$ profiles in the favorable and unfavorable L-modes. There is also no change in the WCM or WCM-like feature's center frequency between favorable L-mode and H-mode, despite a significant difference in $v_{E\times B}$. One speculative explanation for the difference in frequency shift of the WCM in the favorable compared to the unfavorable configuration could be related to a difference in the three-dimensional nature of the edge turbulence in the difference magnetic configurations. In calculating expected Doppler shift of the WCM, an assumption of long toroidal wavelength was made. If the toroidal wavelength is instead small enough for the $k_\phi v_\phi$ term in the Doppler shift to be significant, then differences in toroidal flows between favorable and unfavorable configurations could contribute to differences in WCM frequency shift. Determining the toroidal structure of the WCM requires further measurement.

The observation of significant T_{rad} fluctuations in the H-mode pedestal contrast with the conventional picture of reduced ion scale turbulence in the H-mode pedestal due to increased $E\times B$ flow shear. However, if this pedestal mode is identified as the WCM, these observations could still be consistent with the reduction of transport-causing turbulence in H-mode. The WCM is known to exist in I-modes, which can have significant $E\times B$ flow shear, with E_r wells reaching almost as deep as those in H-mode. The WCM may therefore sit at the bottom of the E_r well where the shear is zero, with its frequency set by this radially localized injection point. I-modes also can have energy confinement quality approaching H-mode levels, so the existence of the WCM would appear not to drive enough energy transport to negatively impact confinement quality. The existence of T_{rad} fluctuations alone is not enough to draw conclusions about turbulence-driven transport. The direction and amplitude of electrostatic heat and particle transport are determined by density, temperature, and potential fluctuation amplitudes in addition to the phase relationships between these fluctuating quantities, and it is possible for a turbulent feature to have significant fluctuations without driving transport. Further investigation is needed to fully understand WCM-like fluctuations in the H-mode pedestal in order to determine what conditions lead to the H-mode WCM, and if comparable favorable and unfavorable configuration discharges have comparable pedestal fluctuations. Time-resolved studies that couple pedestal fluctuation measurements (e.g. from CECE) with SOL measurements (e.g. from probes) would better uncover the temporal and spatial relationship between changes in SOL fluctuations and confined region fluctuations across confinement regime transitions.

Chapter 6

Gyrokinetic investigation of outer core and pedestal top L-mode and I-mode plasmas

6.1 Introduction

As introduced in Section 2.3, the formation of the unique I-mode transport barrier is key to the transition from L-mode to I-mode and is defined by processes in the plasma edge near the last closed flux surface (LCFS). However, it has also been shown that transport properties in the plasma core change across confinement regime transitions, with fluctuations in the plasma *core* reducing in I-mode as compared to L-mode [147]. In contrast to these core measurements, the *pedestal* measurements presented in Chapter 4 show that edge and pedestal turbulence is dominated by the WCM and that its fluctuation amplitude increases between L and I-mode.

The region of the plasma that spans the outer core (OC) to the pedestal top (PT) is understudied, particularly in I-mode plasmas. The OC to PT region covers the radial range $\rho_{pol} = 0.85 - 0.95$, is understudied. This region is important to understand in particular because its properties such as stiffness may differ from the deep core [148]. The outer core region of L-modes has been studied computationally with a number of different gyrofluid and gyrokinetic codes, but these studies are largely focused on validation and limited to the region $r/a < 0.85$, or roughly $\rho_{pol} < 0.90$ [6], [149]–[151]. The region of I-mode plasmas from the outer core to the pedestal top has not been widely studied through either experiment or modeling. Studies from Alcator C-Mod, AUG, and EAST investigate I-mode pedestal turbulence experimentally, but the reported measurements do not extend inside the pedestal top [11], [12], [152]. As discussed in Chapter 1, a number of I-mode modeling studies have focused on the pedestal [15], [77], [153]. Some of these studies focus on the nature and identity of the WCM, although there is not yet consensus on the WCM identity. The core of I-modes have been studied experimentally and through gyrokinetic modeling in a very limited number of studies [76], [147]. These core studies find a reduction in and amplitude of core turbulence and between L and I-mode, and use these experimental measurements to validate gyrokinetic models (GYRO). An understanding of turbulence properties from the

OC to the PT is important to obtaining a complete picture of I-mode turbulence properties, as well as the difference between L and I-mode turbulence.

OC and PT T_e turbulence in L and I-modes has been measured with the CECE diagnostic in the recent experimental work from AUG presented in Chapter 4. In these locations, slight differences in temperature fluctuation amplitude are found between L and I-mode plasmas, but differences in the nature of the turbulence between the modes cannot be determined through these measurements alone. Gyrokinetic studies can provide information about turbulence physics which are not accessible via diagnostics. In this chapter, a gyrokinetic investigation of an L and I-mode OC and PT location is performed with the CGYRO code. Linear and nonlinear simulations are performed to assess turbulence growth rates and saturated heat fluxes. Scans over several drive and damping parameters are performed in the outer core. The simulated turbulence state of pedestal top is found to be sensitive to the method of kinetic profile fitting. In addition to this gyrokinetic analysis, gyrofluid simulations using the TGLF code [123] are performed for fine parameter scans to study the sensitivity of the L and I-mode plasmas to drive terms and to investigate the "stiffness" of the transport, or the response of the heat flux to a change in the profile gradients.

6.2 Experimental basis

A discharge at AUG with both L-mode and I-mode phases is used for comparative L and I-mode gyrokinetic studies. This well-diagnosed discharge is the "low n_e" plasma presented in Chapter 4. This discharge displays typical L and I-mode features, including the formation of an E_r well and edge energy transport barrier at the L to I transition. This discharge also features a WCM which undergoes upshift, broadening, and amplitude increase at the L to I transition.

6.2.1 Profiles

The kinetic profiles of the L and I-mode phases of this have been re-fitted for the following gyrokinetic analysis, as shown in Figure 6.1. The profiles were made by fitting modified hyberbolic tangent functions to Thomson scattering data for n_e and T_e and CXRS data for T_i. A Monte Carlo approach was applied to the fitting by varying data within their error bars and taking an average of 100 different fits. The density profile is nearly the same between L and I-modes and does not display an n_e pedestal. Both the electron and ion temperatures increase between L and I-modes and a T_e and T_i pedestal is formed. The gradient scale lengths calculated from the fitted profiles are also shown in Figure 5.2. The OC and PT locations chosen for gyrokinetic analysis are marked by the vertical dashed lines. Compared with the steeper gradient region of the pedestal ($\rho_{pol} > 0.95$), the gradient scale lengths are smaller at the OC and PT. The radial profiles of safety factor q and magnetic shear $\hat{s}$ are also shown in Figure 6.2, and are very similar between L and I-mode at both the OC and PT locations.

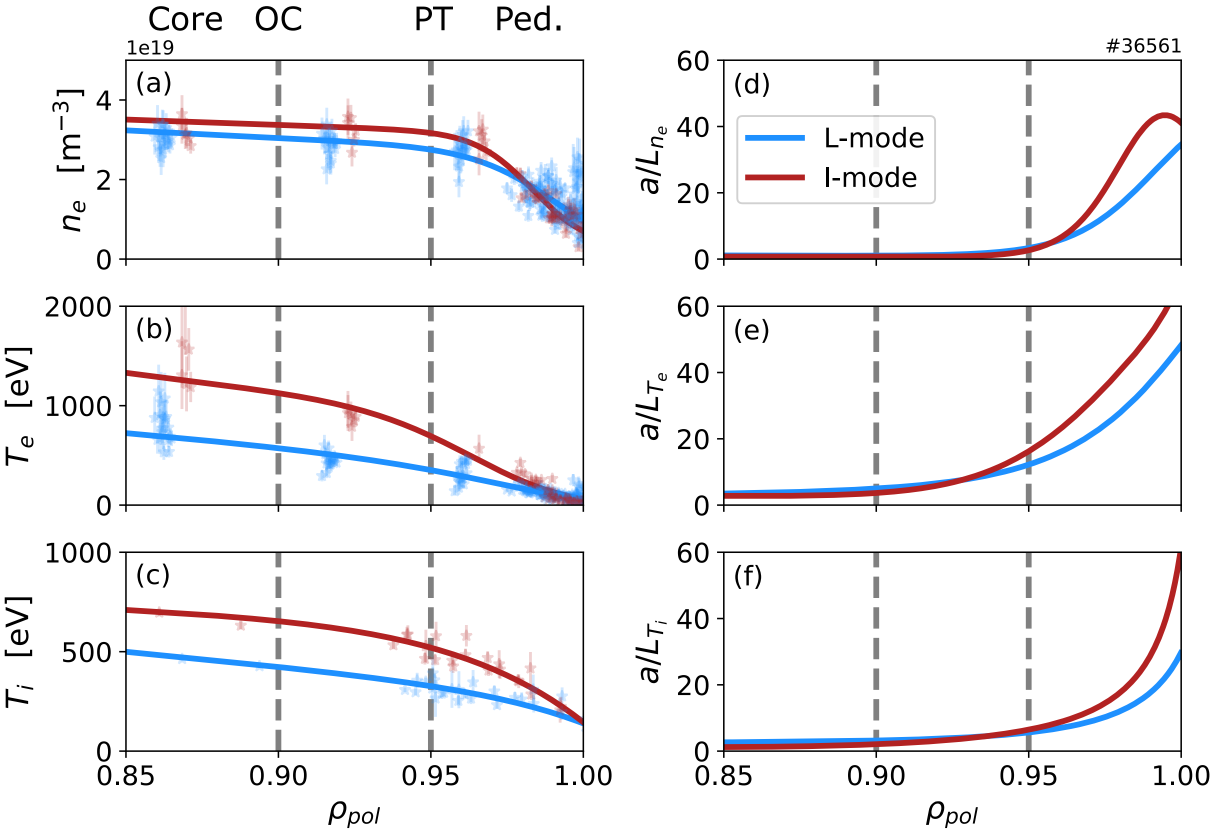

Figure 6.1: Kinetic profile fits to discharge #36561 at AUG during L-mode (4.3-4.6s) and I-mode (5.15-5.4s) phases for (a) n_e, (b) T_e, and (c) T_e. Profile data from Thomson (n_e and T_e) and CXRS (T_i) are also shown. Profiles are made with a Monte Carlo approach by varying data within their error bars 100 times, fitting modified hyperbolic tangent functions, and taking the average of all fits. Normalized gradient scale lengths a/L_n, a/L_{T_e}, and a/L_{T_e} (d-f) are calculated from the profile fits. The core, OC, PT, and pedestal areas are indicated. The locations selected for modeling are shown with vertical dashed lines.

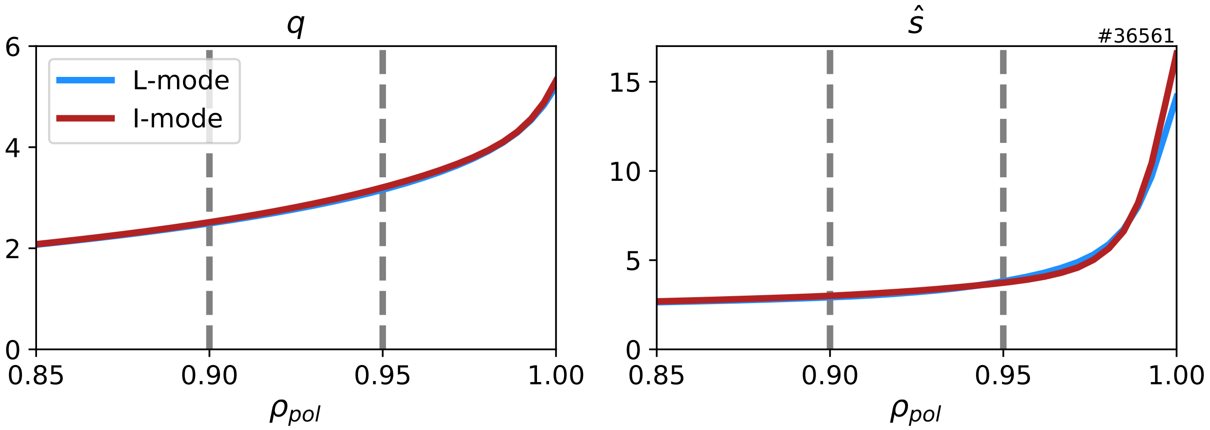

Figure 6.2: Profiles of safety factor q and magnetic shear $\hat{s}$ during the L and I-mode phases. The locations selected for modeling are shown with vertical dashed lines.

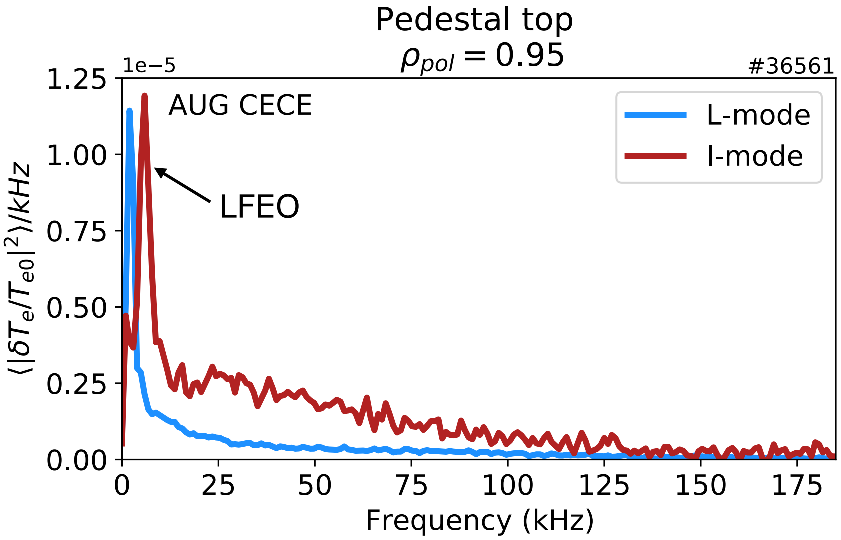

Figure 6.3: CECE cross-power spectra during L and I-mode phases at the pedestal top, $\rho_{pol} = 0.95$. Broadband fluctuations are higher in I-mode than L-mode. The coherent mode at 8 kHz in I-mode is the LFEO.

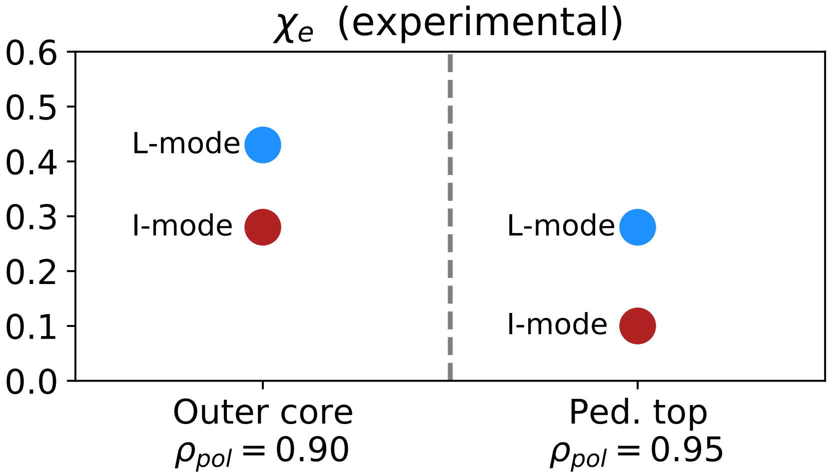

Figure 6.4: Experimental electron thermal diffusivity χ_e estimated from profile fits and input power, as in Reference [138]. χ_e decreases from the outer core to the pedestal top and decreases between L-mode and I-mode.

6.2.2 T_e fluctuation measurements at the pedestal top

Experimental turbulence observations during L and I-modes were reported in Chapter 4. The CECE diagnostic was used to measure the T_e fluctuations associated with the WCM in the pedestal region ($\rho_{pol} = 0.97 - 1.0$) of both the L-mode and I-mode phases, and broadband fluctuations near the pedestal top ($\rho_{pol} = 0.95$) were also captured. Fluctuation measurements farther inside the plasma were not captured in these experiments due to the finite radial extent of the diagnostic. Figure 6.3 shows the CECE cross power spectra for L-mode and I-mode at the radial location $\rho_{pol} = 0.95$. The I-mode spectrum has a higher value of cross-power than the L-mode spectrum. The I-mode phase features a coherent mode at 6.2 kHz, identified as the Low Frequency Edge Oscillation (LFEO) which is a characteristic of I-mode pedestals and may extend in breadth past the pedestal top [73].

A simple experimental transport analysis estimation to determine electron thermal conductivity χ_e from the fitted profiles is shown in Figure 6.4. This rough estimation follows the analysis of Reference [138], assuming that half the power flows through the electron channel and that all applied heating power is deposited in the core. χ_e is determined from $Q/2A = -\chi_e n_e \nabla T_e$, where Q is the total heat flux determined by heating power minus radiated power, A is the surface area at the location of interest, and n_e and ∇T_e are determined by the fitted profiles at the location of interest. From this simple analysis, it can be seen that the thermal diffusivity decreases from the outer core to the pedestal top, and at each location decreases between L and I-mode. This decrease in thermal conductivity follows with the expected increase in confinement quality between L and I-mode.

		OC		PT	
		L	I	L	I
Ion-scale	N_TOROIDAL	24	24	24	24
	N_RADIAL	512	512	528	528
	Box size (ρ_s)	100×100	100×100	100×100	100×100
Electron-scale	N_TOROIDAL	114	114	114	114
	N_RADIAL	280	264	270	252
	Box size (ρ_s)	9×12	9×12	9×12	9×12

Table 6.1: Resolution details for nonlinear simulations run at the OC and PT locations in L and I-mode. Box size is given in units of the ion gyroradius evaluated at the sound speed, ρ_s.

6.3 Simulation setup

The gyrokinetic simulations presented in this paper were performed with the CGYRO code [120]. To compare L and I-mode turbulence, two locations were investigated: the outer core at $\rho_{pol} = 0.90$ and the "pedestal top" at $\rho_{pol} = 0.95$. All four simulations feature three gyrokinetic species (electrons, ions, and the dominant impurity Boron), Miller geometry, the Sugama collision operator, electromagnetic effects, and rotation effects. Resolutions included 24 pitch angle points, 24 poloidal grid points, and 8 energy points. For linear simulations, 24 radial modes were considered. For the nonlinear simulations, the number of radial and toroidal modes, and the resulting simulation box size is given in Table ??.

6.4 Linear gyrokinetic simulations

Linear simulations were performed to study dominant mode properties during the L and I-mode phases at the ion and electron scales. The linear growth rates (γ) and real frequencies (ω) of these dominant modes are shown in Figure 6.5. In the outer core, the normalized dominant mode growth rate is higher in L than in I-mode at both the ion-scale ($k_\theta \rho_s 1.0$) and the electron-scale ($k_\theta \rho_s 1.0$) portions of the spectra. At this location, both L and I-mode display ion-directed ITG at the ion-scale and electron-directed ETG at the electron-scale. Sensitivity analysis confirms that the ion-scale instability is most sensitive to changes in a/L_{T_i} and the electron-scale instability is most sensitive to changes in a/L_{T_e}. At the pedestal top, the normalized dominant mode growth rates and real frequencies are very similar between L and I-mode at both the ion and electron-scales. At this location, the low wavenumber modes are electron-directed, indicating TEM rather than ITG dominates ion-scale turbulence. These linear simulations show that the dominant modes are of similar nature between L and I-mode both at the OC and the PT and that no significant changes in turbulence are apparent other than minor changes in linear growth rate amplitude.

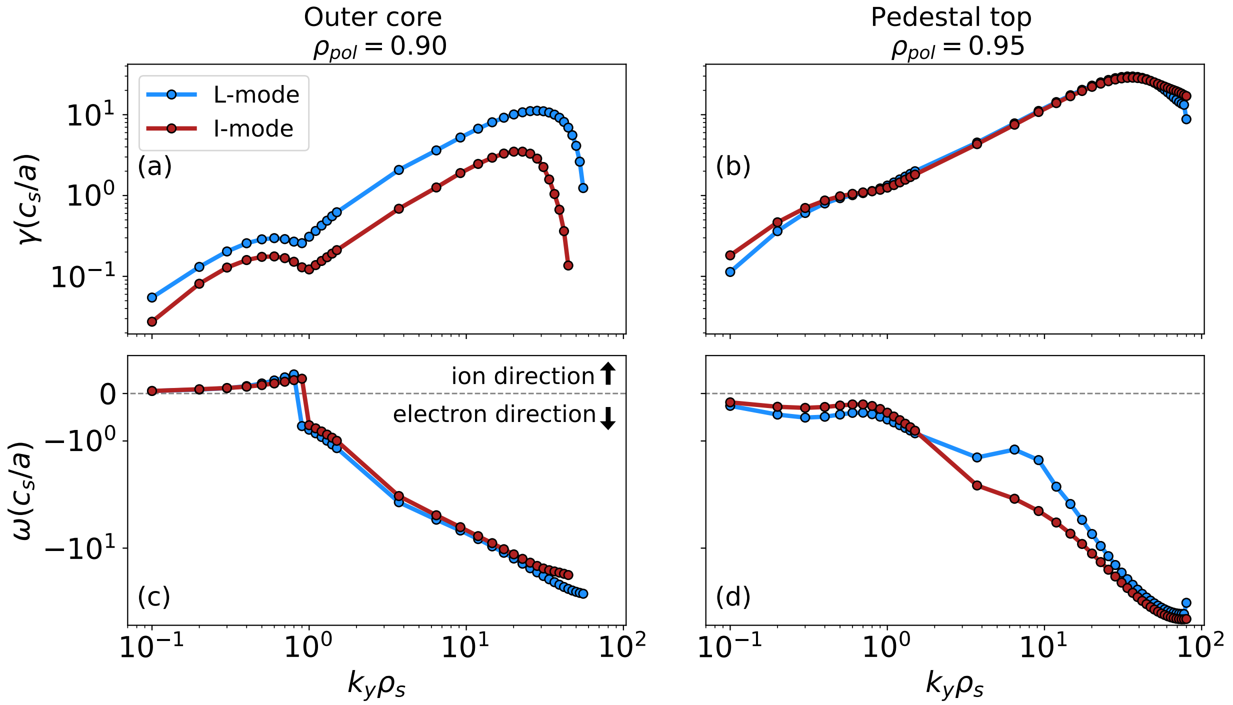

Figure 6.5: CGYRO linear stability analysis showing dominant mode linear growth rate (a, b) and real frequency (c, d) over $k_y\rho_s$ at the outer core and pedestal top for L-mode (blue) and I-mode (red). $k_y\rho_s$ values span both the ion ($k_y\rho_s < 1.0$) and electron-scales ($k_y\rho_s > 1.0$). For real frequency, positive(negative) indicates ion(electron) diamagnetic direction.

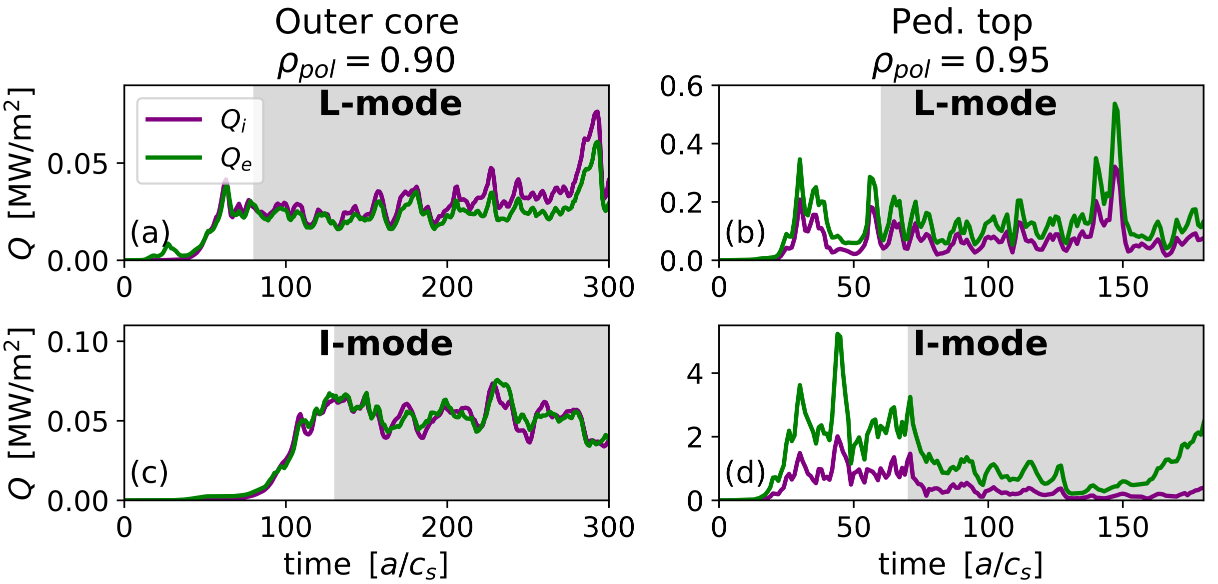

Figure 6.6: Ion (purple) and electron (green) heat flux over time for ion-scale simulations in L-mode (a,b) and I-mode (c,d) at the outer core and pedestal top. The shaded regions indicate the time period over which heat fluxes are averaged in Figure 6.8.

6.5 Nonlinear gyrokinetic simulations

6.5.1 Heat flux comparisons between L-mode and I-mode

Nonlinear simulations were performed at the outer core and pedestal top locations to investigate whether there are differences between L and I-mode in the saturated state of turbulence. The resolutions of these simulations were described in Section 6.3. The evolution of the heat fluxes over time are shown for ion-scale simulations in Figure 6.6 and electron-scale simulations in Figure 6.7. The time periods over which heat flux is averaged is shown by the dashed lines on these figures. Due to the computational expense of the PT simulations, these were not run for as long a time (in a/c_s) as the cheaper OC simulations. For the ion-scale cases, heat fluxes are averaged during the steady-state period after the initial linear instability growth until the end of the simulation. The appropriate periods for time-averaging the electron-scale simulations are more difficult to determine. For these electron-scale simulations, the averaging must occur after the period of electron-scale linear growth but before the ion modes undergo significant linear growth. As a result the choice of averaging windows in some cases must be short, such as the I-mode pedestal top simulation.

The time averaged ion and electron heat fluxes (in MW/m^2) at the ion and electron-scales from these simulations are shown in Figure 6.8. The ion and electron heat fluxes are seen to increase between L and I-mode at both the outer core and pedestal top location. The electron-scale heat flux also increases between L and I-mode, but this increase is much larger at the pedestal top than at the outer core. The large predicted heat flux at the I-mode pedestal top is accompanied by a large error bar, representing the 1σ uncertainty determined

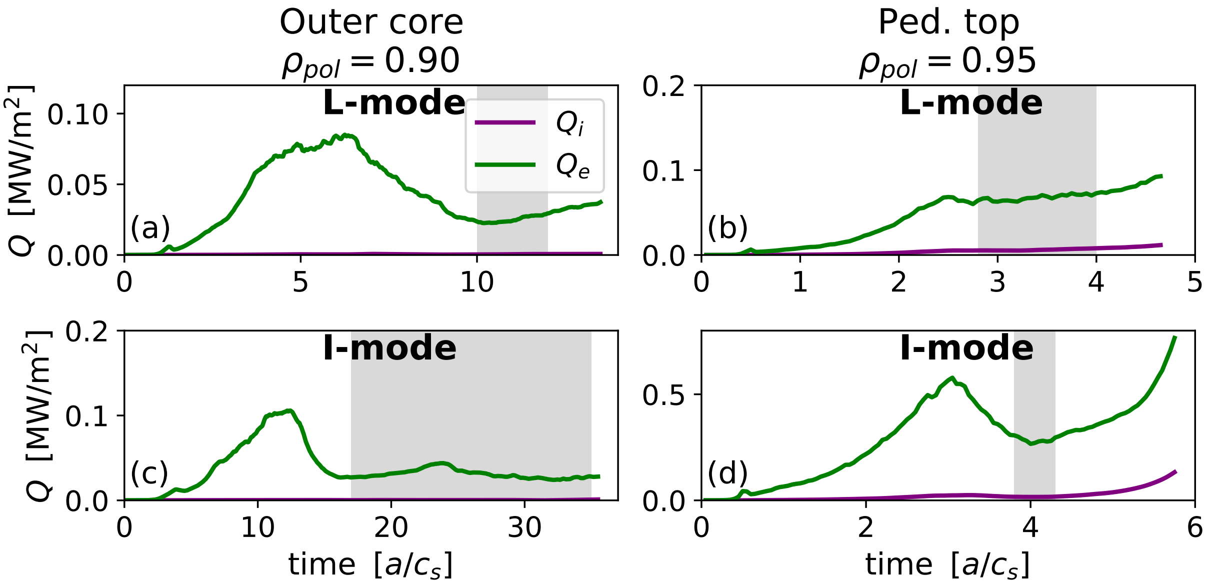

Figure 6.7: Ion (purple) and electron (green) heat flux over time for electron-scale simulations in L-mode (a,b) and I-mode (c,d) at the outer core and pedestal top. The shaded regions indicate the time period over which heat fluxes are averaged in Figure 6.8.

from the heat flux time averaging. The pedestal top heat flux time histories are more bursty in nature than those in the outer core. The experimental ion and electron heat fluxes have not been determined via the use of a transport solver (i.e. TRANSP) due to uncertainties in core profile measurements. However, from a qualitative P/A estimation of the heat flux (where P is the applied heating power minus radiated power and A is the plasma surface area), the experimental and simulated heat fluxes are far from agreement at both the OC and PT locations.

Trends in heat flux ratios are observed between L and I-mode and between the outer core and pedestal top. Figure 6.9 shows the ratio of the ion to electron heat flux, which is seen to decrease between the outer core and pedestal top and at both locations decrease between L and I-mode. This suggests that the pedestal top turbulence is more electron-dominated than the outer core, and I-mode turbulence is more electron-dominated than L-mode. Only the L-mode outer core appears to be ion-dominated in nature.

The ratio of the electron heat flux at the electron-scale to the ion-scale, $Q_{e,elec.-scale}/Q_{e,ion-scale}$, is shown in Figure 6.10. The ratio decreases from the outer core to the pedestal top and at each location decreases between L-mode and I-mode. The L-mode outer core has the most significant contribution from the electron-scale heat flux. The electron-scale heat flux is significant at this location.

The electromagnetic nature of the ion-scale heat fluxes was studied by computing the electromagnetic components of Q_i and Q_e. The electromagnetic portion of Q_i was negligible in all cases. In both the L-mode and I-mode outer core, the electromagnetic Q_e component was less than 5% and was negative, which is consistent with electromagnetic ITG [154]. At the pedestal top, the electromagnetic contribution to L-mode is Q_e negligible, but I-

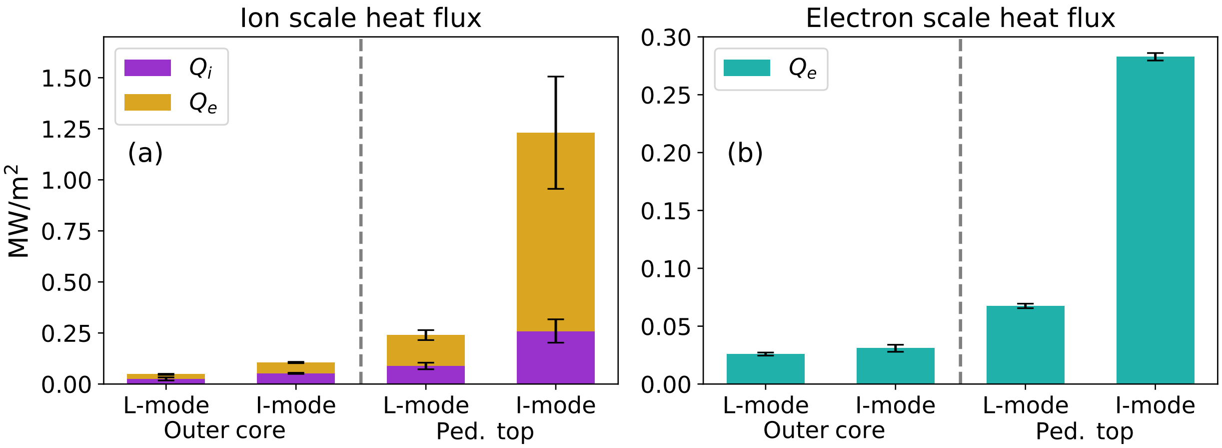

Figure 6.8: Time averaged heat fluxes from nonlinear simulations, including the ion-scale ion and electron heat fluxes and the electron-scale electron heat flux. Total heat flux increases from the outer core to the pedestal top and from L-mode to I-mode at each location.

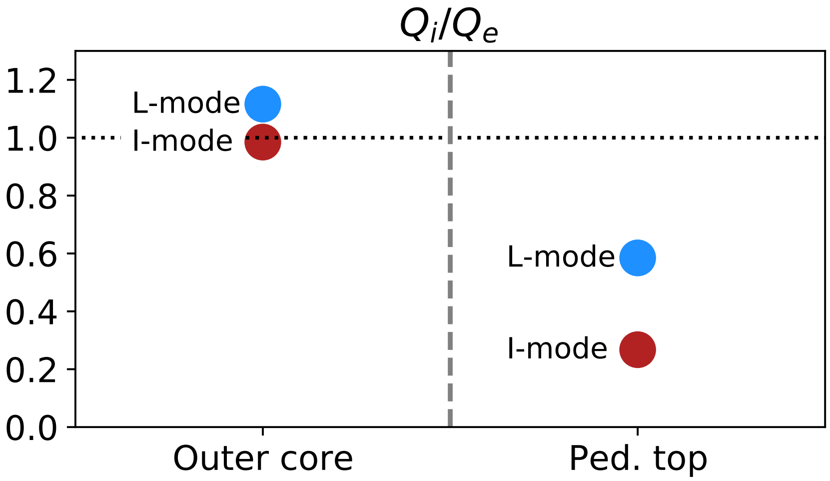

Figure 6.9: The ratio of ion-scale ion heat flux to electron heat flux, Q_i/Q_e, during L-mode and I-mode at the outer core and pedestal top locations. The Q_i/Q_e ratio decreases from the outer core to the pedestal top and decreases between L-mode and I-mode.

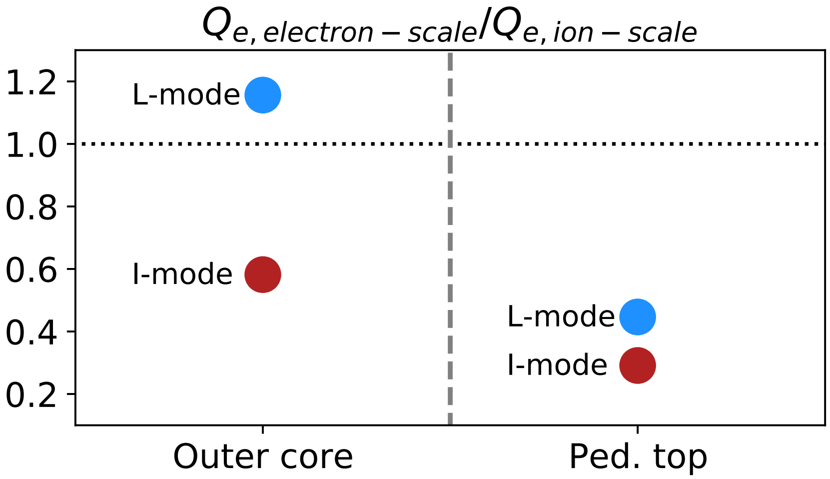

Figure 6.10: The ratio of electron heat flux at electron-scales to the ion-scale. The ratio decreases from the outer core to the pedestal top and between L-mode and I-mode at each location. The L-mode outer core has the largest electron-scale contribution.

mode exhibits a sizeable $+24\%$ electromagnetic contribution Q_e. This is a marked difference between L-mode and I-mode and could be indicative of the existence of electromagnetic modes such as MTM or KBM at the pedestal top in I-modes. These modes can be identified via their sensitivity to β and $\hat{s}$, wavenumber range, and linear parallel mode structure, however this analysis is left for future work.

6.5.2 Profile sensitivity

Due to limitations in experimental measurements such as core ion temperature measurements, experimental heat flux is difficult to determine for these plasmas and thus matching heat flux between simulations and experiment is not possible. In order to explore the sensitivity of the simulation results to the kinetic profile fitting method, alternative profile fits for n_e, T_e, and T_i were used. These "version 2" profiles and their associated inverse gradient scale lengths are shown in Figure 6.12. The profiles from Figure 6.1 used in the base cases will be referred to as "version 1". In the version 2 profiles, the integrated data analysis tool (IDA) [133] is used to determine the n_e and T_e profile fits from standard profile diagnostics including Thomson scattering and ECE [133]. This is a standard profile fitting routine at AUG but is not typically used for pedestal modeling exercises. T_i profiles are made using CXRS data and Gaussian process regression (GPR) fits. The two fitting methods result in differences in gradient scale lengths. The differences (in %) between version 1 and 2 profiles in a/L_{T_i}, a/L_{T_e}, and a/L_n are shown in Table ??.

Nonlinear CGYRO simulations were run holding all parameters constant compared to the previously performed simulation, other than the gradient scale lengths from these version 2 profile fits. Ion and electron-scale simulations were performed at both the OC and PT location. The resulting averaged time heat fluxes are shown in Figure 6.13, with the heat fluxes from profiles version 1 and Figure 6.8 repeated for comparison. At the OC there are

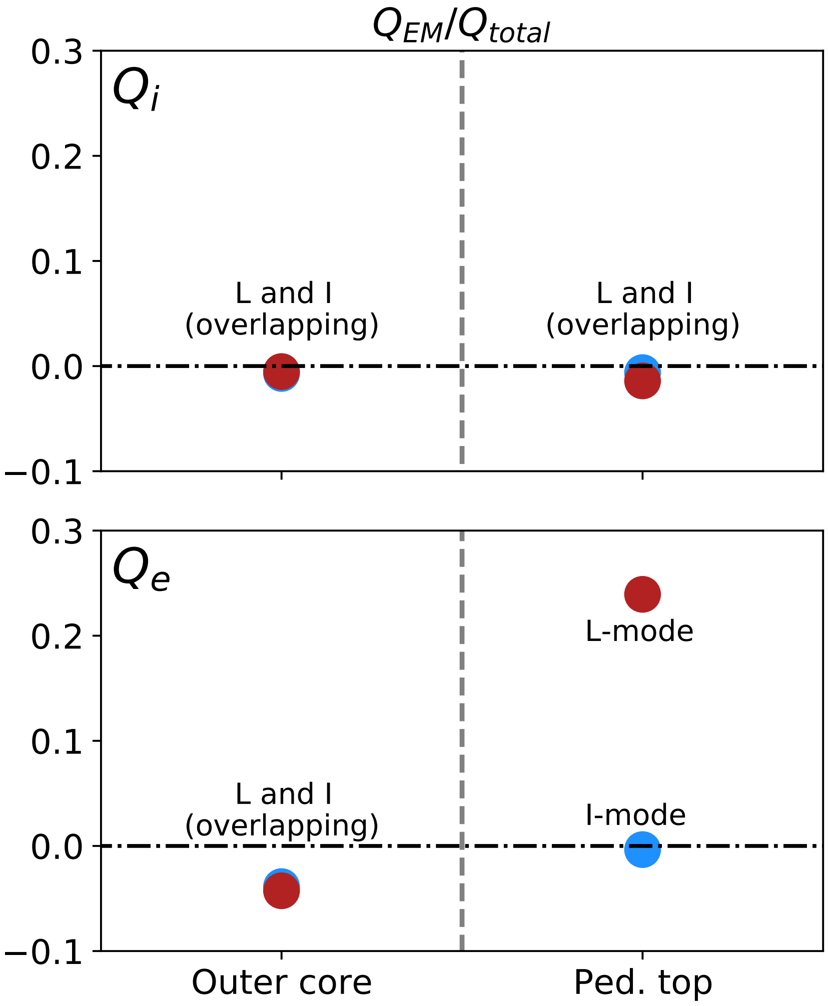

Figure 6.11: The ratio of the electromagnetic heat flux to the total heat flux in both the ion and electron channels. Q_i does not have a significant electromagnetic component in any of the four cases. Q_e displays a small negative electromagnetic component in both L-mode and I-mode in the outer core, and a significant positive electromagnetic component at the I-mode pedestal top.

	OC		PT	
	L	I	L	I
a/L_{T_i}	2	36	3	47
a/L_{T_e}	16	17	26	119
a/L_n	22	10	30	57

Table 6.2: Difference (represented in %) in gradient scale lengths between version 1 and version 2 profiles for the OC and PT locations in L and I-mode.

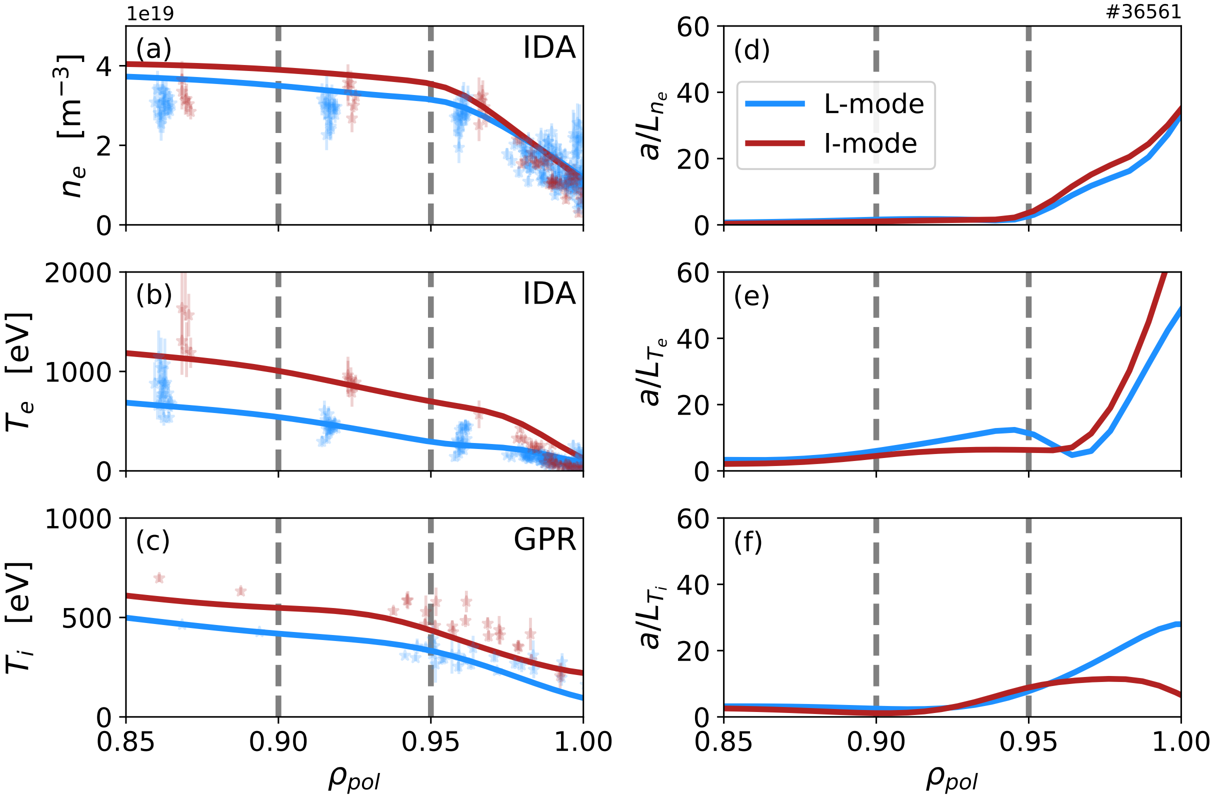

Figure 6.12: Alternative profile fits to discharge #36561 at AUG during L-mode (4.3-4.6s) and I-mode (5.15-5.4s) phases for (a) n_e, (b) T_e, and (c) T_e. IDA profiles are used for n_e and T_e and a GPR fit is used for T_i. Normalized gradient scale lengths a/L_n, a/L_{T_e}, and a/L_{T_e} (d-f) are calculated from these profile fits.

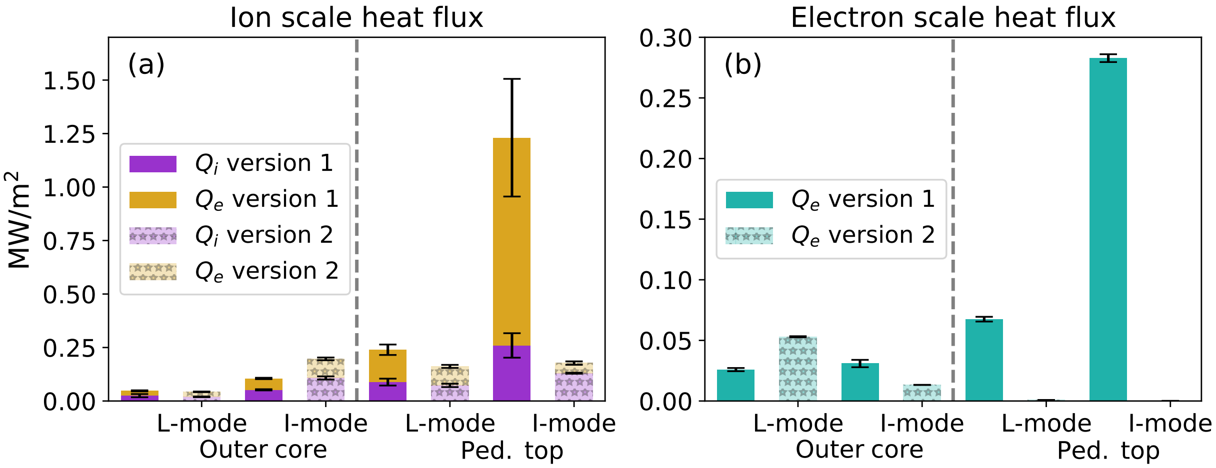

Figure 6.13: Comparison of time averaged heat fluxes from nonlinear simulations from profiles version 1 and profiles version 2, including the ion-scale ion and electron heat fluxes and the electron-scale electron heat flux.

differences in heat flux between simulations performed with the different profiles, however, the general trends in ion-scale heat fluxes between L and I-mode are consistent. Comparing version 2 with version 1 profiles at the ion-scale, Q_i is 22% lower and Q_e is 4% higher in L-mode. In I-mode, Q_i is over twice as high and Q_e is 67% higher. Both profile versions exhibit an increase in both Q_i and Q_e between L and I-mode. The trends in electron-scale heat flux are not consistent between the two versions of profiles. The electron-scale Q_e increases between L and I-mode with version 1 profiles, but decreases with version 2 profiles.

At the PT, the heat fluxes differ dramatically between the two profile fitting methods. Comparing version 2 to version 1 profiles at the ion-scale, Q_i is 17% lower and Q_e is 41% lower in L-mode. In I-mode, Q_i is 50% lower and Q_e is 21 times lower. The trends in heat flux at the PT are not overall consistent between the two profile fitting methods. While Q_i increases between L-mode and I-mode in both versions of the profiles, Q_e increases between L and I-mode with the version 1 profiles and decreases with the version 2 profiles. The electron-scale heat flux also increases between L and I-mode with the version 1 profiles, while it is negligible in both L and I-mode with version 2.

The larger differences in heat flux between the profile fitting methods are a result of the large differences in normalized gradients. In particular, the extreme differences in heat flux between the profile fitting methods at the I-mode pedestal top are correlated with profiles that change substantially between the two methods, as presented in Table ??. The differences in heat flux are striking, and indicate that any standalone gyrokinetic analysis in this region of the plasma could be affected by choices of profile fitting. This sensitivity to profile fitting method means that no definitive physics conclusions can be drawn about the PT simulations performed in this work.

6.6 Outer core parameter scans

6.6.1 Turbulence drive and damping scans

The heat flux results from both versions 1 and 2 profiles presented in Section 6.5 indicate an increase in heat flux between L-mode and I-mode in the outer core. The nature of the underlying turbulence can be better revealed with single and multi parameter scans. This parameter scan investigation is limited to the outer core radial location because uncertainties in pedestal top location profiles are too large to limit scans to reasonable ranges. To investigate several turbulent modes of interest, ion-scale scans over eight individual parameters and two combinations of parameters were performed. Due to the uncertainty in profile fitting, wide scans of ± 30% in each parameter were performed for both the L and I-mode outer core location, totaling 40 runs. The target turbulent modes under investigation were ITG (a/L_{T_i} scanned), TEM (a/L_n, a/L_{T_e}, and ν_{ee} scanned), electromagnetic modes such as KBM and MTM (β_e and $\hat{s}$ scanned). The ion to electron temperature ratio (T_i/T_e) and the $E \times B$ velocity shear ($\gamma_{E\times B}$) were also scanned.

The ITG investigation is shown in Figure 6.14. Both the L and I-mode ion and electron heat flux respond strongly to changes in a/L_{T_i}, indicating that ITG is an important factor for driving turbulence at this location. The response of heat flux to a change in gradient is similar between L and I-mode. Compared with the other scans, changing a/L_{T_i} causes the strongest response in Q_i.

The TEM investigation is shown in Figure 6.15. The terms scanned were a/L_n and a/L_{T_e}, which drive TEM, and ν_{ee}, which damps TEM. These terms were scanned individually (panels a-f) as well as combined (panels g-h). In the combined scan, the $+0.3$ factor scan indicates an increase of all drives, so a/L_n and a/L_{T_e} were increased by 30% while ν_{ee} was decreased by 30%. The opposite was performed for the -0.3 case combined scan. In the single parameter scans, neither L nor I-mode show a strong response to variations in a/L_n or ν_{ee}, but Q_i and Q_e both have a strong response to a/L_{T_e}. This indicates that electron temperature gradient driven TEM is important in driving transport in the outer core of both L and I-mode. Compared with the other scans, the Q_e response to a/L_{T_e} is the strongest, and the Q_i response is nearly as strong as to a/L_{T_i}. The combined scan shows a different trend than any of the three individual scans. In the combined scan, there is little change in Q_i in either L or I-mode and a more significant increase in Q_e with drive terms in I than in L-mode.

The impact of the ion to electron temperature ratio (T_i/T_e) is investigated by changing T_i alone. This ratio is important because it is thought to be a factor in determining whether turbulence is ion or electron dominated. Both L and I-mode Q_i and Q_e increase with increasing T_i/T_e. The heat flux response to the changing temperature ratio is nearly the same between L and I-mode. This indicates that while the I-mode outer core has lower T_i/T_e than L-mode due to its hotter and more decoupled nature, both L and I-mode fall in the same regime of turbulence in the range of these scans. The temperature ratio remains $T_i/T_e < 1$ over the range of these scans in both L and I-mode.

A selection of drives specific to electromagnetic modes, such as KBM and MTM instabilities, are shown in Figure 6.17. These instabilities can also be sensitive to kinetic profile and collision frequency drives previously discussed. The terms scanned to investigate elec-

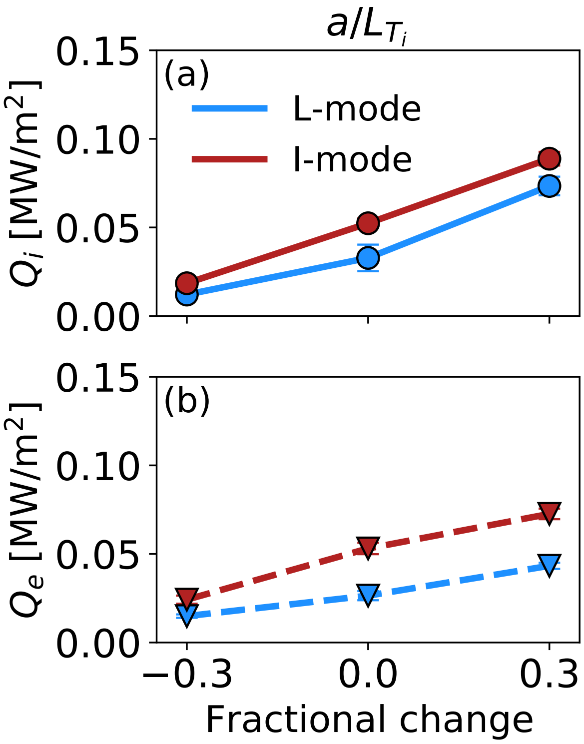

Figure 6.14: Scan of ITG mode drive term, a/L_{T_i}, and resulting time averaged Q_i (a) and Q_e (b) for L-mode (blue) and I-mode (red) outer core location.

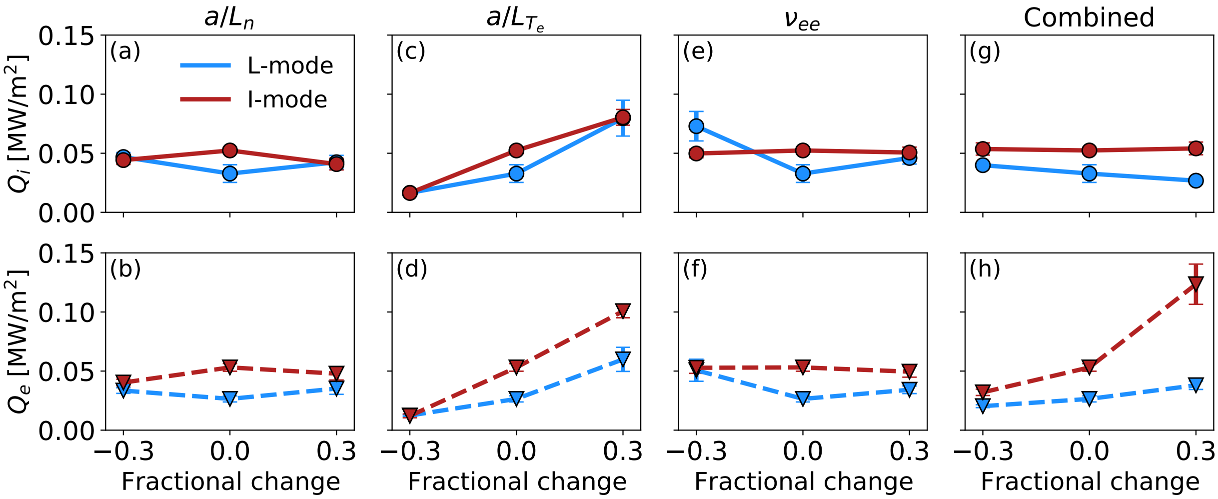

Figure 6.15: Scan of TEM mode drive/damping terms, a/L_n (a,b), a/L_{T_e} (c,d), and ν_{ee} (e,f), and resulting time averaged Q_i (a,c,e) and Q_e (b,d,f) for L-mode (blue) and I-mode (red) outer core location. Combined parameter scans (g,h) increase(decrease) a/L_n and a/L_{T_e} while decreasing(increasing) ν_{ee}.

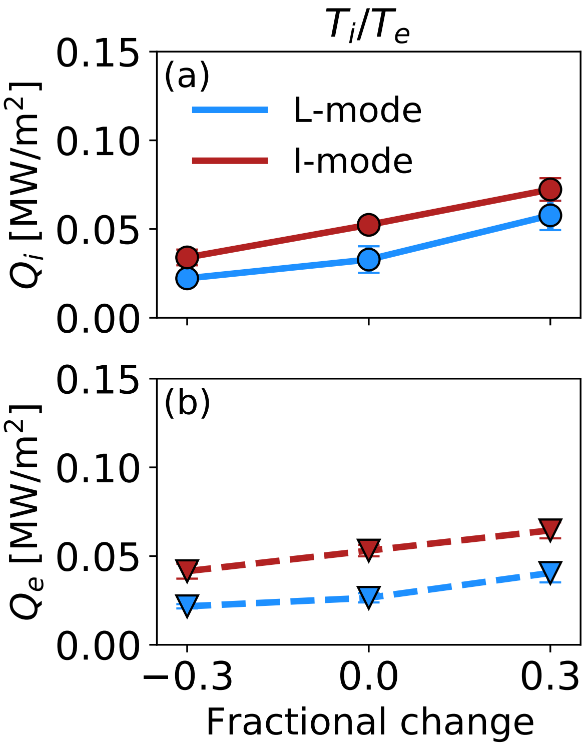

Figure 6.16: Scan of the ion to electron temperature ratio, T_i/T_e and resulting time averaged Q_i (a) and Q_e (b) for L-mode (blue) and I-mode (red) outer core location.

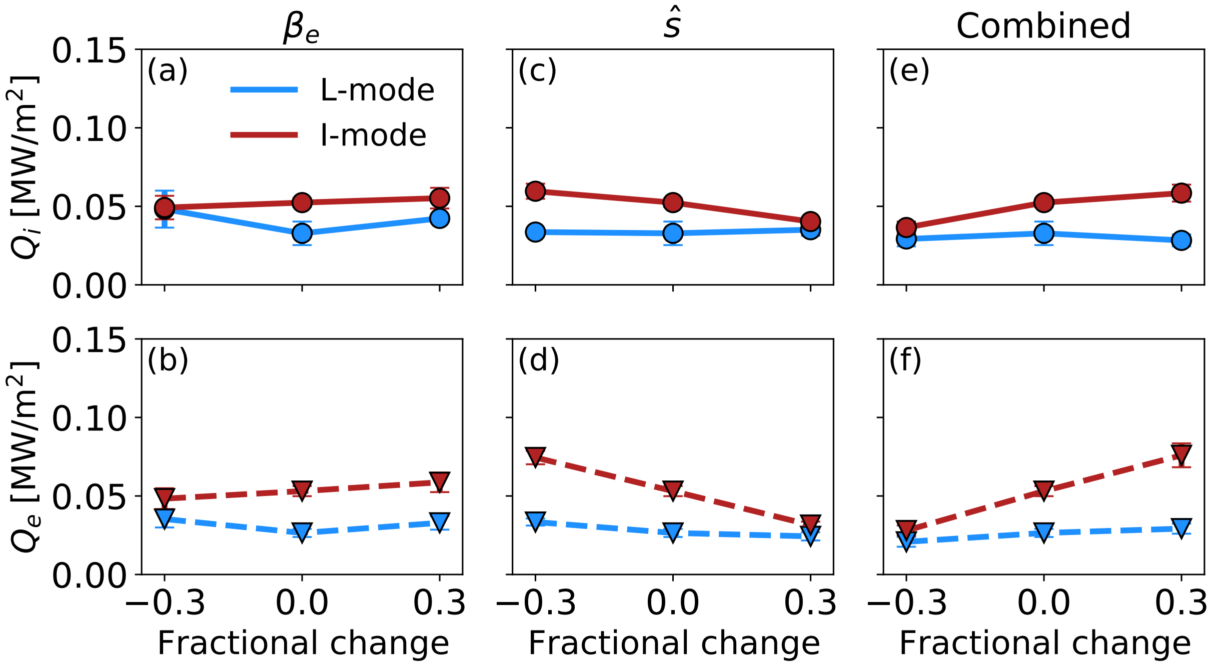

Figure 6.17: Scan of electromagnetic (e.g. KBM, MTM) mode drive/damping terms, β_e (a,b) and $\hat{s}$ (c,d), and resulting time averaged Q_i (a,c) and Q_e (b,d) for L-mode (blue) and I-mode (red) outer core location. Combined parameter scan (e,f) increases(decreases) β_e while decreasing(increasing) $\hat{s}$.

tromagnetic modes were β_e, a source of drive, and magnetic shear $\hat{s}$, a source of damping. Neither L nor I-mode display significant changes of Q_i or Q_e with β_e. The I-mode plasma Q_e decreases with increasing $\hat{s}$ but the L-mode plasma is not significantly affected. Figure 6.17 panels e and f show the result of these combined drives, with the -0.3 factor scan indicating decreased drive (decreased β_e and increased $\hat{s}$) and the $+0.3$ case indicating increased drive (increased β_e and decreased $\hat{s}$). The response of the heat fluxes to these combined drives is very similar to the response to $\hat{s}$ alone. Given the lack of heat flux response to β_e and the minimal electromagnetic heat flux in these simulations, it is unlikely that electromagnetic modes are an important factor in these plasmas. $\hat{s}$ is known to effect ITG and TEM modes [155], so the change of heat flux with $\hat{s}$ could also be due to electrostatic turbulence.

A scan of the $E \times B$ velocity shear, $\gamma_{E\times B}$, is shown in Figure 6.18. Neither the L nor the I-mode plasma show strong trends in heat flux with $\gamma_{E\times B}$. This is in contrast to the strong turbulence damping found with $\gamma_{E\times B}$ in previous L and I-mode core modeling at Alcator C-Mod [75]. This may be due to the low values of shear in these simulated outer core AUG plasmas, with $\gamma_{E\times B} = 0.019$ and 0.024 (c_s/a) in L-mode and I-mode respectively. The magnitude of this shear is significantly below the ion-scale linear growth rates determined from the linear simulations, with growth rate maxima $\gamma_{\max} = 0.30$ and 0.18 (c_s/a) in L and I-mode respectively. Therefore, the shear is likely too low to significantly damp turbulence and modify transport within the bounds of these scans.

In summary, changing the ITG drive through scanning a/L_{T_i} had the largest effect on

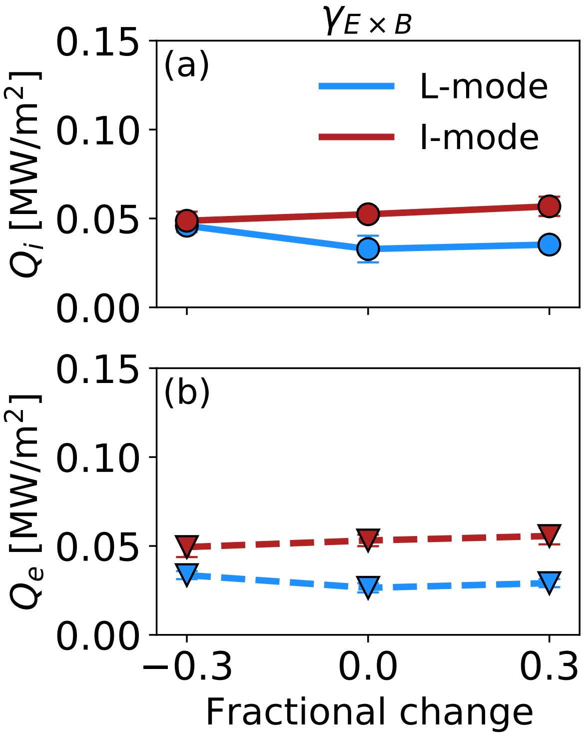

Figure 6.18: Scan of the $E \times B$ velocity shear, $\gamma_{E\times B}$, and resulting time averaged Q_i (a) and Q_e (b) for L-mode (blue) and I-mode (red) outer core location.

Q_i and had a similar magnitude effect on L and I-mode. Changing the TEM drive through scanning a/L_{T_e} had the largest effect on Q_e and had a larger effect on the I-mode than the L-mode plasma, particularly when combined with other TEM drives. The magnetic shear also had a larger impact on Q_e in I-mode than in L-mode. The T_i/T_e ratio impacted both Q_i and Q_e with a similar magnitude in both L and I-mode. Several parameters, such as a/L_n, ν_{ee}, β_e, and the $E \times B$ velocity shear, did not have strong impacts on the heat flux in either L nor I-mode within the range of these scans.

Many of the responses to these drives could be different at the pedestal top. Compared with the outer core, at the pedestal top the gradients are steeper, the plasma is cooler and more collisional, and both $E \times B$ velocity shear and magnetic shear are larger. The nature of the turbulence appears to be different at the pedestal top and the responses of heat fluxes to changes in parameters may be different. Simulation scans of the pedestal top are left for future work and with profiles that are better constrained.

6.6.2 TGLF stiffness tests

The gyrofluid code TGLF [124] is significantly computationally cheaper to run than CGYRO and TGLF is also well validated for core plasma scenarios. TGLF can therefore be used for fine scans of a/L_n, a/L_{T_e}, and a/L_{T_i}, which enables investigation of critical gradients and stiffness. As discussed in Chapter 2, stiffness can be thought of as the resistance of a particular profile to change, when that profile has a gradient above a particular threshold for turbulence drive. When a profiles is "stiff", an increase in heating power that would increase the profile gradient in turn increases the turbulence drive, and thereby increases the transport which regulates the profile.

The TGLF simulations performed for these stiffness tests were designed to have a setup as close as possible to the CGYRO simulations presented in the previous sections of this chapter. The same base gradients and geometric parameters were used, and electromagnetic effects were included. The saturation rule SAT2 [127] was used, and the default 4 parallel basis functions were used in these simulations.

The stiffness tests of these L and I-mode outer core plasmas are shown in Figure 6.19. The base case (version 1) gradient scale lengths in both L and I-mode are indicated by the vertical dashed lines, and several scans were performed on either side of these base gradient scale lengths. Both the L and I-mode base cases are found to be above the critical gradient, $a/L_{T_i} \sim 1.5$. The I-mode plasma has a larger response in both Q_i and Q_e than L-mode to changes in a/L_{T_i}, and the I-mode base case gradient sits closer to the critical gradient value. For these reasons, I-mode is more stiff than L-mode in terms of the T_i gradient. The a/L_{T_e} and a/L_n scans show that both L and I-mode sit below the critical gradients in T_e and n in these simulations. Above the T_e and n critical gradients, I-mode has a larger response in heat flux with changes in gradient, indicating that I-mode has higher stiffness.

The TGLF stiffness tests results are shown with heat fluxes normalized to gyro-Bohm heat flux units in Figure 6.20. When the gyro-Bohm normalization is considered, L and I-mode plasmas display very similar responses in heat flux to changes in a/L_{T_i} and a/L_{T_e}. This indicates that the higher stiffness in I-mode is due to its higher temperature and a corresponding change in terms of gyro-Bohm units, rather than a change in the nature of the turbulence. The response of the heat flux to changes in a/L_n does not match between L

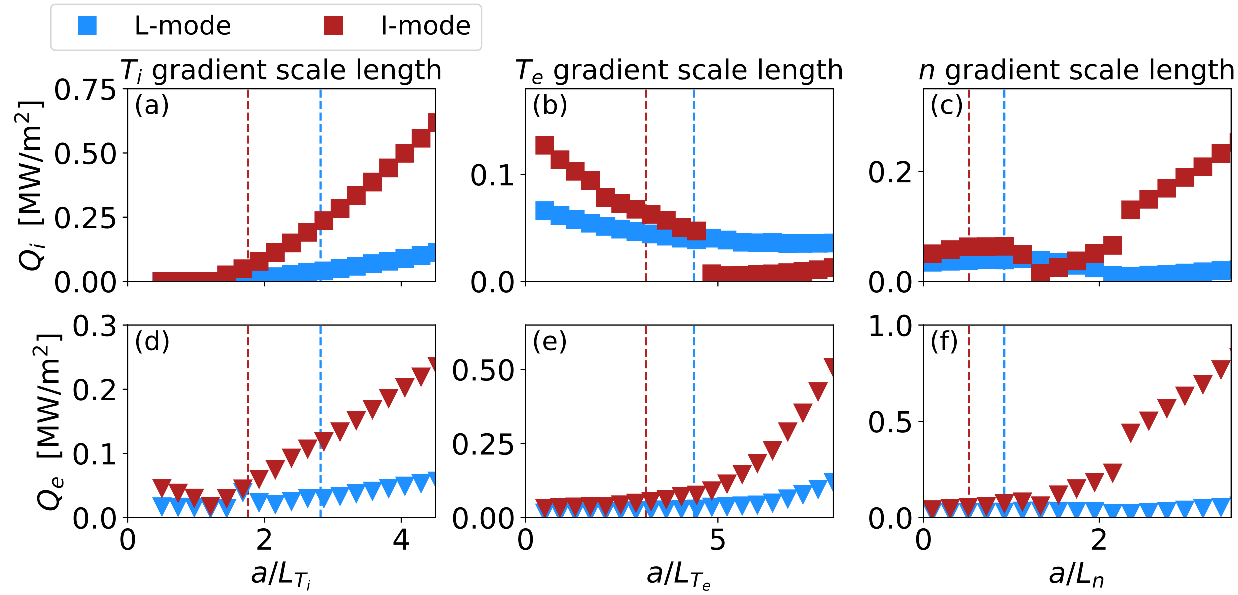

Figure 6.19: TGLF scans of normalized gradient scale lengths at the outer core location for L-mode (blue) and I-mode (red) plasmas. (a-c) show variation of Q_i and (d-f) show variation of Q_e in MW/m^2. Base case values are shown in the dashed lines for each normalized gradient scale length.

and I-mode in gyro-Bohm normalized units, but the base case values of a/L_n are far below the critical gradient in both L and I-mode.

6.7 Quantification of multi-scale effects

Multi-scale effects in gyrokinetic and gyrofluid simulations have been shown to be important to reproduce experimental heat flux levels in both the L-mode [156] and I-mode [76] core. The sizable contributions of the electron-scale heat flux contributions in some of the simulations presented here (Figure 6.10) may indicate that cross-scale coupling could play a role in the saturated turbulent state of these plasmas.

One metric for determining the relevance of multi-scale effects is the ratio of the maximum linear growth rate at the electron-scale, γ_{high-k}, to the maximum growth rate at the ion-scale, γ_{low-k}. One flagship multi-scale study suggests that as a rough rule-of-thumb, multi-scale effects become important when $\gamma_{high-k}/\gamma_{low-k} > 40$ [156]. The ratio of high to low wavenumber growth rates are shown in Table ??. Although the high to low-k ratio is below 40 for all simulations, it is close to 40 in the L-mode outer core. The ratio decreases from the outer core to the pedestal top in each plasma and decreases at each location between L-mode and I-mode. The location with the largest possibility of multi-scale effects is the L-mode outer core.

A second rule-of-thumb metric for qualifying the importance of multi-scale effects is the comparison of the ratio between the dominant mode linear growth rate to the wavenumber $(\gamma/k_y\rho_s)$ at low versus high wavenumbers. It has been suggested that when $(\gamma/k_y\rho_s)$ at the

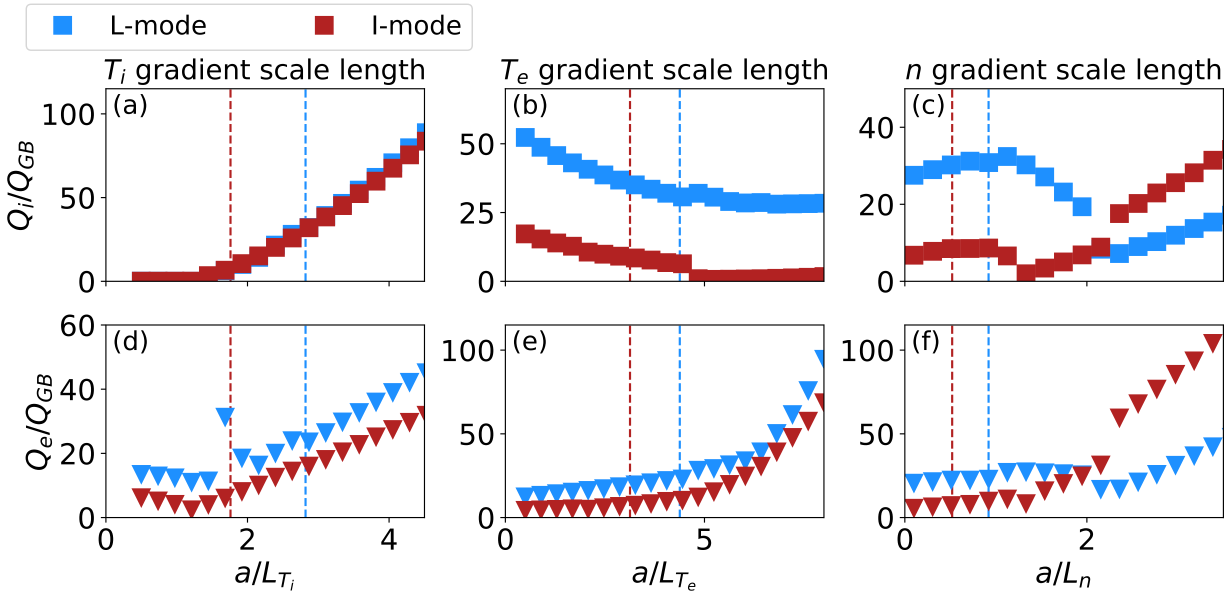

Figure 6.20: TGLF scans of normalized gradient scale lengths at the outer core location for L-mode and I-mode plasmas normalized to the gyroBohm heat flux units. (a-c) show variation of Q_i and (d-f) show variation of Q_e. Base case values are shown in the dashed lines for each normalized gradient scale length.

	$\gamma_{high-k}/\gamma_{low-k}$	
Location	Outer core	Pedestal top
L-mode	38	26
I-mode	19	3

Table 6.3: Ratio of the peak of the dominant mode growth rate at the electron-scale ($k_y\rho_s >$ 1.0) to the peak at the ion-scale ($k_y\rho_s <$ 1.0) at the outer core and pedestal top radial locations. The L-mode plasma in the outer core has the highest $\gamma_{high-k}/\gamma_{low-k}$, indicating the highest possibility of multi-scale effects.

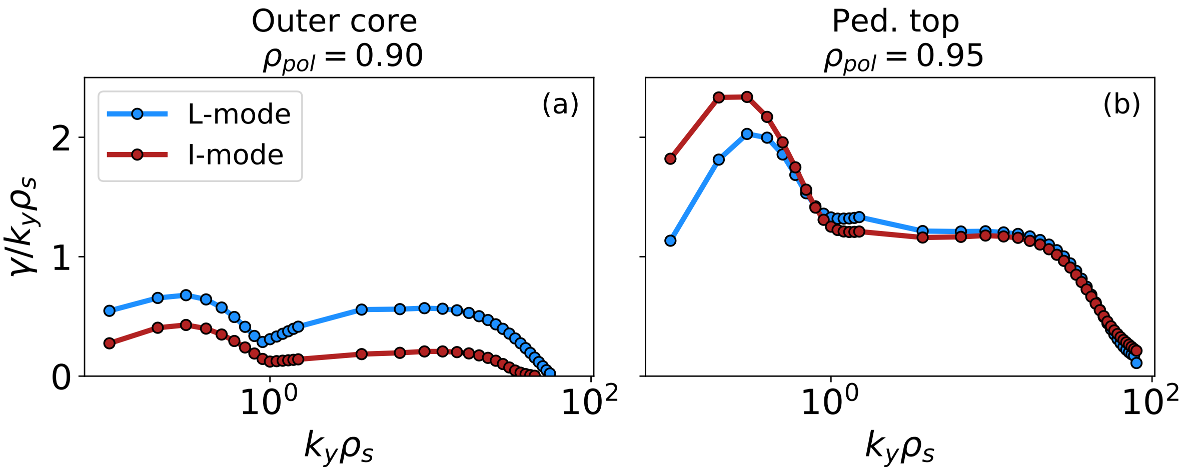

Figure 6.21: Dominant mode growth rate normalized to $k_y\rho_s$ over $k_y\rho_s$ for L-mode and I-mode linear simulations at the outer core (a) and pedestal top (b) radial locations.

electron-scale is comparable to or higher than that at the ion-scale, then multi-scale effects may be important [157]. The $\gamma/k_y\rho_s$ ratios against $k_y\rho_s$ are shown in Figure 6.21 for the simulated OC and PT L-mode and I-mode. In all cases, $\gamma/k_y\rho_s$ is larger at the ion scale than at the electron scale. However, in the L-mode outer core, $\gamma/k_y\rho_s$ at the electron scale approaches the same magnitude as at the ion scale. This once again indicates that the L-mode outer core has the greatest potential for multi-scale effects.

In addition to the $\gamma_{high-k}/\gamma_{low-k}$ and $\gamma/k_y\rho_s$ rules-of-thumb for determining the importance of multi-scale effects, the visual appearance of the turbulent eddies at the electron scale can indicate whether multi-scale effects may be important. A snapshot of the mid-plane electron density fluctuations from the L-mode outer core simulation is shown in Figure 6.22. In this snapshot, streamers the length of the $12\rho_s$ box can be seen, showing that the electron-scale turbulence can form ion-scale structures, which may be capable of interaction with the ion-scale turbulence [33].

Based on the discussed metrics, the outer core L-mode has the strongest possibility of multi-scale effects compared to the other simulations. Multi-scale phenomena can modify heat flux, as ETG streamers can cause significant transport at electron scales and may also enhance transport at ion scales by damping poloidal zonal flows [156], [158]. The reduction of multi-scale coupling between the L and I-mode cases could act to change the magnitude by which the turbulent heat flux changes between L and I-mode. Multi-scale effects have been suggested to have the largest impact on simulations where ITG is marginally unstable and electron modes dominate, because strongly-driven ITG can suppress electron-scale transport [159]. The observations here are not consistent with this trend; of the four simulations, the L-mode outer core appears to have the highest chance of multi-scale effects but also has the highest Q_i/Q_e ratio and sits farther above the a/L_{T_i} critical gradient than the I-mode outer core. Further simulations, including multi-scale simulations, are needed for a full understanding of the multi-scale nature of the L-mode and I-mode outer core.

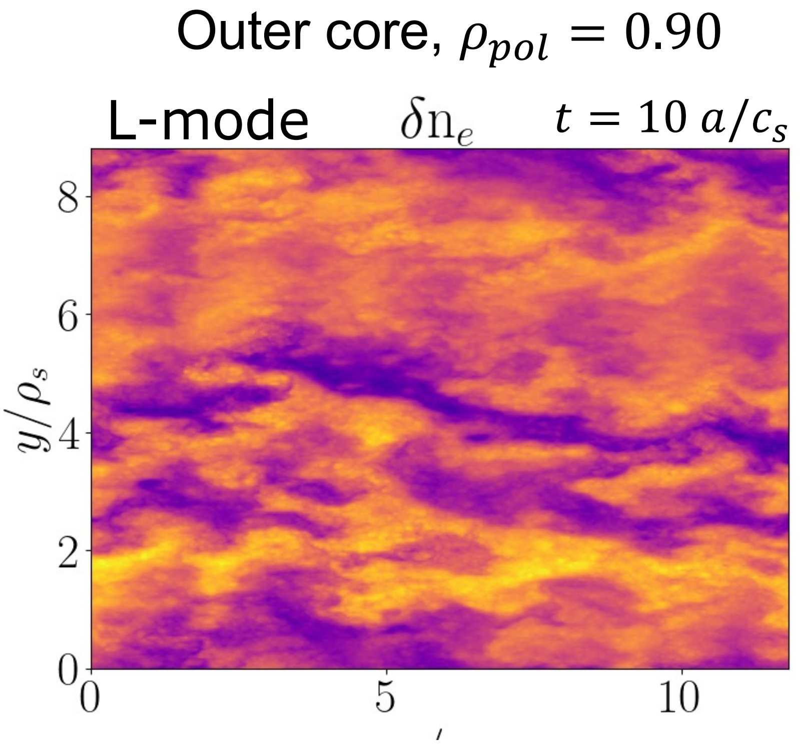

Figure 6.22: Snapshot of midplane electron density fluctuations from the electron-scale L-mode outer core simulation. Box-sized electron streamers can be seen.

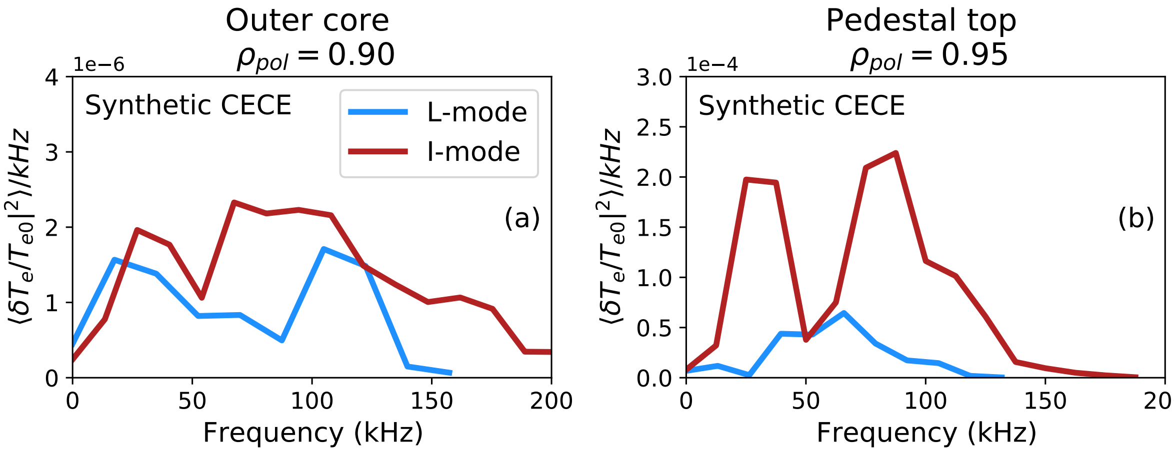

Figure 6.23: Synthetic CECE diagnostic crosspower spectra for the L and I-mode simulations at the outer core and pedestal top. In the outer core, the crosspower spectrum is similar between L-mode and I-mode. At the pedestal top the crosspower spectrum is higher in L-mode than I-mode, indicating higher T_e fluctuations in L-mode.

6.8 Qualitative comparison of fluctuations between experiment and simulations

6.8.1 Synthetic CECE diagnostic

A synthetic CECE diagnostic was applied to the L-mode and I-mode simulations to perform a qualitative comparison with experimental measurements presented in Section 6.2. This is not intended as a validation exercise but rather as a means to gain deeper understanding of the turbulence in this region. This synthetic diagnostic was developed for gyrokinetic validation work on DIII-D [160], and has been used here with modifications to represent the AUG CECE system. As an approximation of the beam pattern of the CECE diagnostic at AUG, the synthetic diagnostic applies a circular Gaussian beam with a 1/e power diameter of 7.6 mm in the poloidal direction. Two CECE channels each with a radial extent of 3.4 mm are spaced apart by 4.3 mm, consistent with the AUG CECE system's radial comb geometry.

The cross-power spectra calculated using this synthetic diagnostic on the L and I-mode CGYRO simulations are shown in Figure 6.23. At the outer core location, there is little difference between the L-mode and I-mode spectra. Unfortunately, there are no experimental measurements in these plasmas at this outer core location for qualitative comparison. Nevertheless, there is a difference in the cross-power spectra generated with the synthetic diagnostic at the pedestal top location. The I-mode cross-power spectrum is significantly higher than the L-mode spectrum, correlating with a higher fluctuation amplitude in I-mode compared to L-mode. This trend agrees qualitatively with the experimental CECE measurements shown in Figure 6.3, where the I-mode cross-power spectrum is higher than the L-mode spectrum. However, the experimental and synthetic measurements do not agree quantitatively, with the maximum experimental cross-power magnitude approximately 100 times smaller than the synthetic cross-power magnitude.

The synthetic diagnostic was also applied to the simulations performed with version 2 profiles, and while the T_e fluctuation crosspower spectra are still similar in the L and I-mode outer core, the opposite trend is found at the pedestal top location. With version 2 profiles at the pedestal top, the crosspower is lower in I-mode than in L-mode. This correlates with the decrease in heat flux between L and I-mode at the pedestal top with version 2 profiles. This trend is also the opposite of experimental observations. This investigation shows that simulated fluctuation levels are sensitive to the kinetic profiles, but without heat flux matched simulations a qualitative comparison between experiment and simulation is not possible.

6.9 Summary and discussion

In this chapter, a detailed gyrokinetic investigation of the L and I-mode outer core and pedestal top was performed. Electron and ion heat fluxes were found to increase between the outer core and the pedestal top, and heat fluxes increased at each location between L and I-mode. The Q_i/Q_e ratio was found to decrease between the outer core and pedestal top and at each location decrease between L and I-mode. The $Q_{e,elec.-scale}/Q_{e,ion-scale}$ ratio was also found to decrease between the outer core and pedestal top and at each location decrease between L and I-mode. A synthetic CECE diagnostic found that trends in T_e fluctuations agreed with experimental measurements and increased between L and I-mode, however, the simulations and experiment do not qualitatively agree. A caveat to note is that results at the pedestal top were found to be highly dependent on the method used for fitting kinetic profiles, with different fitting methods leading to large differences in the gradient scale lengths which drive the turbulence. Without the ability to match the heat flux with experiment, these simulations could not be further constrained.

The nature of the outer core turbulence was investigated through several parameter scans. Despite the differences in Q_i/Q_e and $Q_{e,elec.-scale}/Q_{e,ion-scale}$ between L and I-mode, the scans revealed that the nature of the turbulence in the L and I-mode outer core is very similar. The L and I-mode plasmas had similar responses to nearly all turbulence drive and damping terms. One exception was the stronger response of the I-mode plasma Q_e to changes in a/L_{T_e}, correlating with the higher dominance of electron turbulence in I-mode than L-mode. I-mode was found to have higher profile stiffness than L-mode, and this is linked to its higher temperature and therefore larger gyro-Bohm heat flux unit. In gyro-Bohm normalized units, the response of the L-mode and I-mode heat flux is nearly the same to changes in the a/L_{T_i} and a/L_{T_e}, above their critical gradients.

The linear gyrokinetic analysis performed further indicated that the dominant mode turbulent behavior is similar in the L and I-mode outer core. Linear analysis also allowed for qualification of the possible importance of multi-scale effects. A comparison of $\gamma_{high-k}/\gamma_{low-k}$ and $\gamma/k_y\rho_s$ indicate that the L-mode outer core has a higher potential for multi-scale effects than I-mode, and the outer core region has a higher potential for multi-scale effects than the pedestal top.

The finding that turbulence is of a similar nature between L-mode and I-mode in the outer core is consistent with the idea that the critical changes between L and I-mode occur near the edge of the plasma, where a transport barrier forms. This transport barrier region is farther in the edge of the plasma than the OC and PT top locations studied through gyrokinetic analysis in this chapter. The study of the turbulence in the OC and the PT, and the calculated heat fluxes, are important for understanding global confinement, validating models of turbulent transport, and making performance predictions for future reactors. However, the driving reason for the change in confinement between L-mode and I-mode likely occurs in the steep gradient region of the pedestal. Simulations in the pedestal region are difficult due to the steep gradients and computation expense, and are beyond the scope of this work. Different profile fitting methods give very different simulation results at the PT location, and towards the separatrix the uncertainties in profile fits and sensitivity to fitting technique are likely even higher, making standalone gyrokinetic simulations in this region of the plasma extremely challenging.

This modeling work suggests several paths for future study. Heat flux matching between experiment and simulation would help to converge simulation results to those of physical relevance. Better constrained profile fits would greatly assist in the study of the turbulence behavior at the pedestal top. In future experiments, obtaining CECE measurements at the outer core location in addition to the pedestal top would allow for a direct comparison between simulation and experiment at both locations. Extending this modeling to the steep gradient region and capturing the change in edge and pedestal turbulence between L-mode and I-mode would deepen our understanding of the I-mode confinement regime.

Chapter 7

Conclusions and future work

This thesis has described a range of experimental and modeling work aimed at understanding turbulence in the low confinement regime, L-mode, and the "improved" confinement regime I-mode. This work contributes to our understanding of turbulence in the tokamak edge, pedestal, and outer core in L-mode and I-mode, across a wide parameter space of experimental inputs. This chapter discusses key findings and points to directions for next steps for future research.

7.1 Key findings of this thesis

The investigation of edge fluctuations performed in this thesis were possible due to the extensive diagnostic suite at the ASDEX Upgrade (AUG) tokamak, including diagnostics for profile measurements and for turbulence measurements. The Correlation Electron Cyclotron Emission (CECE) diagnostic was the chief tool used in these studies, used for measuring radiated temperature (T_{rad}) fluctuation spectra, fluctuation amplitude, and correlation length with fine radial resolution. Challenges to ECE measurements in the plasma edge were carefully considered. As part of this work, the CECE system was extended from a 24 channel radial comb to 56 radial channels split across two toroidal locations. A Thermal Helium Beam diagnostic was also used for studying edge fluctuations, and Doppler reflectometers and a Helium II Spectroscopy system were used for studying the edge radial electric field. An overview of these diagnostics, including details of the newly expanded CECE system, were given in Chapter 3. These diagnostics were operated during dedicated experiments targeting open physics questions in I-mode and the L to H transition.

One open question addressed though experiment in this thesis was the reason for the higher power threshold in the unfavorable $B \times \nabla B$ configuration compared to the favorable configuration. In Chapter 5, we show that differences in edge fluctuations between the two magnetic configurations correlate with differences in E_r and its related $E \times B$ shear during L-mode phases prior to confinement regime transitions. These measurements show that there is a difference between the two configurations in the balance of turbulence drive and damping just prior to confinement regime transitions. The higher shear and lower fluctuation amplitude in the favorable configuration correlate with its easier access to the L to H transition. These fluctuation measurements provide new evidence for the importance of turbulence in determining confinement regime transitions.

This thesis also aimed to better understand edge turbulence in I-mode and across the L to I transition through detailed measurement of outer core and pedestal fluctuations. The I-mode confinement regime is accessed in the unfavorable $B \times \nabla B$ configuration because this configuration allows for application of higher heating power before transition to H-mode. Discharges with L and I-mode phases were performed across a range of densities, with an aim of scanning collisionality. The quality of global confinement, represented by the factor H_{98}, was found to be negatively correlated with collisionality in both L-mode and I-mode. However, the amplitude and character edge turbulence did not follow clear trends with either collisionality or confinement. Specifically, the Weakly Coherent Mode (WCM) dominated the edge fluctuations across all the plasmas studied.

Understanding the nature of WCM is an important aspect of understanding the I-mode as a whole. This motivates the studies described in Chapter 4, which use the AUG turbulence diagnostic suite to study the WCM in detail. Strikingly, the WCM was also found to be present in the L-mode T_e fluctuations preceding and following the I-mode transition in all discharges studied. A summary of the WCM characteristics observed in L-mode and I-mode was given in Table 4.2. The WCM was found to share several properties between L-mode and I-mode, including its wavenumber extent ($k_\theta = -0.5$ To -1.0 cm^{-1}) and location of peak amplitude ($\rho_{pol} = 0.98 - 0.99$). The phase between WCM n_e and T_e fluctuations, α_{nT}, is more out-of-phase in L-mode as compared to I-mode. This out of phase nature and the change in α_{nT} between L-mode and I-mode may assist in comparing the experimental WCM observations with theoretical candidates for its identity. A frequency upshift of the WCM occurs between L-mode and I-mode, and the value of this shift is consistent with the expected Doppler shift for a long-wavelength mode due to increased $E \times B$ rotation velocity. The existence of the L-mode WCM breaks the previously-held assumption that the WCM is the key defining feature of I-mode. It is still possible that the WCM plays an important role in the edge transport and regulating the pedestal, since the particle transport is expected to stay consistent between L-mode and I-mode.

Chapter 5 extended the study of the L-mode WCM from the unfavorable magnetic configuration to include the favorable magnetic configuration. In experiments designed to compare edge turbulence between favorable and unfavorable magnetic configurations, the development of the WCM was observed via pedestal T_{rad} fluctuations. The L-mode WCM first appeared during low power phases as a fluctuation with a low value of coherence $|\gamma_c(f)|$ in the CECE frequency spectra, low fluctuation amplitude, and a narrow radial extent. The mode was centered at the same radial location in the favorable and unfavorable phases and covered the same frequency extent. The WCM coherence, fluctuation amplitude, and radial extent grew in both the favorable and unfavorable configurations as more power was applied to the L-mode plasmas. However, the WCM grew to a higher coherence, fluctuation amplitude, and radial extent in the unfavorable configuration, which also had smaller $E \times B$ shear as compared to the favorable configuration. The presence of the WCM in both favorable and unfavorable L-modes is further evidence that this mode is not a unique or special feature of I-mode, but rather a type of edge fluctuation that can be present across a large parameter space of magnetic configuration, confinement regime, applied heating power, and kinetic profiles.

During the matched favorable and unfavorable experiments presented in Chapter 5, at high enough power, the unfavorable configuration plasma transitions to an I-mode and the WCM evolves to its I-mode character, shifting to higher frequency and a broader frequency range. At high enough power, the favorable configuration plasma transitions to the high confinement regime, H-mode. Notably, T_{rad} measurements show that a significant broadband fluctuation is present in the pedestal during the inter-ELM portion of the H-mode plasma. Here this feature is called a "WCM-like feature" due to its spectral properties alone. The measurements of broadband fluctuations in the H-mode pedestal show that the presence of turbulent fluctuations alone is not enough to drive transport. Rather, a particular combination of n_e, T_e, and ϕ fluctuations and the phases between these fluctuations is needed to drive transport.

During the I-mode phases of the discharges studied in this thesis, a Low Frequency Edge Oscillation (LFEO) appears in the T_{rad} fluctuation spectra. The LFEO does not appear in L-mode. The coupling between the WCM and the LFEO is unique to I-mode. The timing of the L to I-mode transition, the onset of the LFEO, and the frequency shift of the WCM coincide in the experiments presented here. Bicoherence analysis applied to the T_{rad} fluctuation signals in Chapter 4 showed that WCM and LFEO frequencies are coupled, as previously shown by References [74] and [144]. This previous work also suggests that the WCM transfers energy to the LFEO through this three-wave coupling. A new contribution of this thesis is the study of the radial structure of WCM-LFEO coupling. As shown in Chapter 4, there is radial coincidence between the location of the WCM peak amplitude, the LFEO peak amplitude, and the maximum bicoherence in the WCM-LFEO range of frequency coupling. The strength of coupling falls off sharply with radius. This indicates that important edge dynamics of I-mode are triggered at a single narrow location. One interpretation of this radial coincidence is that the WCM is driven most strongly at one particular location, most likely by ∇T_e. At this location of peak WCM drive, the LFEO then receives the most energy from the WCM. The role of these coupled fluctuations in maintaining the I-mode regime requires further study. One possible interpretation for the importance of the LFEO in I-mode is that its exchange of energy with the WCM influences the overall balance of turbulence drive and damping in the pedestal. The LFEO, whether its identity is a Geodesic Acoustic Mode (GAM) or a Zonal Flow Oscillation (ZFO), likely plays a role in the regulation of turbulence. The LFEO's role in the overall state of turbulence in the I-mode pedestal in turn affects the turbulence-driven transport of I-mode.

None of the studies here presented, or previously reported in the literature, show that the WCM is solely responsible for the unique transport barrier and beneficial transport properties of I-mode. In fact, the presence of the WCM in both L-mode and I-mode bring to question whether other changes in turbulence, not in the pedestal, are instead responsible for the change in transport between L-mode and I-mode. To probe this question, gyrokinetic simulations were performed with the CGYRO code to compare turbulence between L-mode and I-mode. These simulations were reported in Chapter 6 and were based off the L-mode and I-mode plasmas studied experimentally in Chapter 4. The simulations included one radial location in the outer core ($\rho_{pol} = 0.90$) and one at the pedestal top ($\rho_{pol} = 0.95$). At both locations, linear and nonlinear simulations run at the ion and electron scales. Uncertainties in profile fitting left the pedestal top simulations poorly constrained, but the outer core results showed greater robustness to kinetic profile fitting method.

In the outer core, the ratio of ion to electron heat flux (Q_i/Q_e) was found to decrease slightly between L-mode and I-mode. The electron-scale contribution to heat flux also decreased between L-mode and I-mode. However, the response of the L-mode and I-mode simulations to scans in turbulence drive and damping terms were the same, indicating that the nature of the L-mode and I-mode turbulence was similar at this location. Stiffness tests performed with the TGLF gyrofluid code showed that the I-mode outer core plasma was more stiff than the L-mode plasma, but this difference in stiffness disappeared when the heat fluxes were normalized by the gyroBohm heat flux. This is a further indication that the nature of turbulence in the L-mode and I-mode phases was similar: the turbulence-driven transport responds the same way to a change in gradient drive, the higher temperature of I-mode leads to a larger turbulent eddy correlation length, and thus a greater change in heat flux when gradient drive is changed. Rather than uncovering any significant differences between L-mode and I-mode, these simulations showed the core turbulence is of a similar nature between the L-mode and I-mode regimes.

The gyrokinetic simulation results of the L-mode and I-mode outer core complement the experimental findings presented in this thesis. The similarity of the outer core turbulence found in simulations (Chapter 6) indicates that the important phenomena separating L-mode and I-mode occur in the pedestal. While experimental investigation found that the WCM occurs in the edge of both L-mode and I-mode, the behavior of the WCM was different between L-mode and I-mode in terms of its fluctuation amplitude and, radial breadth, and coupling to the LFEO (Chapter 4). The balance of turbulence gradient drive of and shear flow damping is also found to be different between L-mode and I-mode, and different between favorable and unfavorable configurations in matched L-modes (Chapter 5). This experimental and modeling work deepens our understanding of L-mode and I-mode outer core and pedestal phenomena, and points to directions for future study.

7.2 Directions for work

To better understand the pedestal, and thereby I-mode as a whole, continued experimental and modeling work is needed. Key areas for future study include the separation of particle and energy transport in the I-mode pedestal, the identification of the WCM drive, the importance of WCM-LFEO coupling, and the triggering of the L to H and L to I transitions. From the experimental side, significant insight may be gained from further multi-channel turbulence measurements across the L, I, and H-mode confinement regimes. This thesis has primarily reported on T_{rad} fluctuations measured with CECE. Pedestal studies utilizing additional diagnostics such as reflectometers for n_e fluctuation measurements, the thermal He beam for n_e and T_e fluctuation measurements, and the coupled reflectometer-CECE system for α_{nT} measurements may provide valuable insight to the possible transport mechanisms in the pedestal, including transport from the Ion Temperature Gradient and Trapped Electron Mode drift wave turbulence, and from MHD-type instabilities.

In particular, measurements of α_{nT} can be used to test theories of turbulent transport in I-mode, such as recent work attributing changes in transport to changes in cross-phases [17] or theory that relates the WCM to a particular phase relation between fluctuating quantities [161]. Comparison of α_{nT} across L, I, and H-mode can provide insight to the types of turbulent modes present in these regimes, and the possible transport these modes drive. Simulations can be used to provide further understanding of transport across these regimes, with α_{nT} and other turbulence measurements used to constrain the possible regimes of turbulence. For example, simulations could be used to explore the turbulent modes or mixtures of modes which result in the expected density and temperature fluctuation amplitudes, α_{nT} value, and transport of the L and I-mode WCM. It should be noted that in order to unambiguously understand experimental α_{nT} measurements, more work must be done to understand the relationship between measured cross-phase and the reflectometer wave path, the differences between ECE-ECE and ECE-reflectometer correlations, and how density fluctuation information is carried by the reflectometer amplitude and reflectometer phase.

Several aspects of pedestal fluctuations require further study, including both WCM fluctuations and non-WCM turbulence. This thesis has largely focused on T_e fluctuations, using CECE measurements to provide information about WCM localization and fluctuation amplitude in L and I-mode. The n_e fluctuation amplitude has been shown to be higher than the T_e fluctuation amplitude in I-mode [72], [128]. A comparison of the location of the peak fluctuation amplitude in n_e and T_e would be useful, because if the localization differs between these two channels, this could provide insight to the formation of the unique I-mode transport barrier. The mechanism for the formation of the I-mode transport barrier still remains an open question. In this thesis, we have not unambiguously determined how this transport barrier forms and is maintained. However, the measurements of fluctuations across L and I-mode regimes, in terms of fluctuation amplitude and cross-phase, could be consistent with the transport required for the I-mode regime. The presence of the WCM itself and its T_e fluctuation amplitude do not appear to be linked to energy confinement, further indicating that this mode may play a role in particle but not energy transport. Non-WCM turbulence is likely playing an important role in the change in transport across the L to I transition, as previous studies note the reduction of low frequency fluctuations in I-mode [11], [72]. One possible interpretation is that the background turbulence drives significant heat flux in L-mode but is damped in I-mode, while the WCM is strengthened in I-mode but does not drive significant heat flux. In order to test this hypothesis, the WCM and the background turbulence must be decoupled through measurement and data analysis techniques.

The conditions which lead to the appearance of the WCM in L-mode is an area that requires further study. CECE fluctuation measurements consistently captured the WCM in L-mode phases in the experiments presented in this thesis. In these studies, the plasma conditions varied in terms of power level, favorable and unfavorable ∇B drift, and density. However, all experiments were performed in the USN configuration at AUG, because this configuration allows operation in the unfavorable ∇B drift configuration, and thus I-mode, for the standard current direction at AUG. Operation with unfavorable ∇B drift in LSN at AUG requires a reverse I_p campaign. LSN is the typical configuration for standard experiments at AUG, due to the lower divertor and its controlled pumping. Further experiments targeting L-modes in the typical LSN configuration, or during a reverse I_p campaign, could provide insight to relationship between the specifics of the configuration and the presence of the WCM. The height of the X-point is an important factor in achieving I-mode, so this parameter should be scanned when investigating the factors leading to the appearance or disappearance of the WCM in L-mode.

The identity of the LFEO and its importance to I-mode is an area of current study. The

LFEO's identity as a GAM could be confirmed through measurement of its plasma potential perturbations and resulting E_r perturbations, and perturbation in the perpendicular $v_{E\times B}$, all with the expected $m = n = 0$ mode structure. These quantities may be accessed by diagnostics such as the Heavy Ion Beam Probe, Beam Emission Spectroscopy, and reflectometry diagnostics. The GAM pressure sideband with $m = 1$, $n = 0$ structure can be accessed through diagnostics that measure density and temperature fluctuations, like ECE or reflectometers. Whether or not the WCM is identified as a GAM, its importance in maintaining the I-mode pedestal can be investigated through higher order spectral analysis techniques. The bicoherence analysis of T_e fluctuation signals presented in this thesis only shows that the WCM and LFEO frequencies are coupled, which is necessary for energy transfer, but this analysis does not determine the presence or direction of energy transfer. To study the spectral transfer of energy, the transfer function must be formulated as in [74] with fluctuations in density, density gradient, and poloidal velocity.

Broadband fluctuations in the H-mode pedestal measured with CECE are a new area of study. These measurements have only been briefly touched upon in Chapter 5 of this thesis. One clear direction for future work is further qualification and identification of the inter-ELM H-mode pedestal turbulence at AUG. Previous work across different machines has reported on inter-ELM fluctuations, as summarized in Reference [162], and the references therein. However, there remain open questions related to the impact of these inter-ELM modes, including their role in regulating the pedestal and triggering the ELM crash. The distinction between the broadband drift-wave turbulence and MHD-type modes is not always clear experimentally. By using CECE in parallel with other diagnostics to target inter-ELM phases of H-modes, we can understand the situations in which broadband fluctuations are present, and their possible correlations with transport.

In addition to further experimental measurements, new data analysis techniques applied to already existing data can lead to physical insights. For example, the onset of the pedestal in both I-mode and H-mode is of great interest. The temporal relationship between turbulence damping and the onset of the $E \times B$ shear layer in the H-mode edge is an open question, as is the relationship between onset of the LFEO in I-mode and the frequency shift of the WCM. By utilizing high temporal resolution of the CECE diagnostic, the change of turbulence over small time windows during transitions may be studied. Applying higher order spectral analysis such as bicoherence and spectral transfer functions to these transition periods may provide insight to the balance between turbulence and zonal flows, and coupling between the WCM, LFEO, and zonal flows.

Upcoming CECE diagnostic upgrades will allow investigation of not only edge physics, but also the coupling between the core and the edge in future experiments. It has previously been shown that core fluctuations can be reduced in I and H-mode compared to L-mode [147], [163], but the experimental and modeling work presented here show that outer core turbulence can be of similar nature between L-mode and I-mode. The changes in outer core turbulence across confinement regime transitions in comparison to deep core turbulence is one area of future study. The relationship between turbulence damping by edge sheared flows and core turbulence reduction must also be understood. Expansions to the current AUG CECE diagnostic are underway that include an upgrade to 96 radial channels. With this radial coverage, turbulence in the core and edge can simultaneously be measured, and changes in turbulence can be tracked across confinement regime transitions at different locations.

The diagnostic expansion is aimed to be modular, so that two groups of 32 channels can overlap radially, but be separated vertically so poloidal correlation measurements can also be attempted. Such measurements can be used to compare the poloidal structure of fluctuations in the core plasma with that at the edge. This poloidally separated system of CECE radial combs will allow for the study of both radial and perpendicular correlation lengths of turbulence, both of which are important for understanding transport and how transport can change between regimes. For example, in Chapter 6 the gyroBohm heat flux unit was shown to increase between L and I-mode in the outer core region due to the higher temperature in I-mode. Measurements of the change in correlation length between L and I-mode could confirm whether typical turbulent eddy sizes change between L and I-mode.

The outer core and pedestal top gyrokinetic modeling work presented in this thesis point to next steps for the modeling pathway of investigating I-mode. As a first step, obtaining experimental heat flux measurements for comparison with simulation can help constrain simulation inputs. In particular, uncertainties at the pedestal top may be targeted through heat flux matching. Beyond this outer core and pedestal top simulations, the pedestal region is the next frontier for modeling work. An accurate pedestal model needs to contain the important physical effects in the pedestal. These include the large variation of parameters over a small radial region, leading to large gradient scale lengths and drastic changes in collisionality over the pedestal. The pedestal is also thought to be multiscale in nature, with important transport drivers ranging from small-scale ETG to the large-scale ELMs. A first step in comparing the L, I, and H-mode pedestals could be electron-scale gyrokinetic simulations that capture the ETG transport. Ultimately, creative new approaches are needed to model the complete dynamics of the pedestal, such as coupled core to edge codes.

The studies presented in this thesis increase our understanding of the turbulence and transport processes at in the edge region of I-mode plasmas, which is important to the extrapolation of this operational regime to future machines. As the heating power window for I-mode access widens as magnetic field increases [69], future high field devices such as SPARC will have the opportunity to operate in I-mode. A high performance operating regime like I-mode would assist future devices in achieving their $Q > 1$ mission without the material damage from ELMs that would accompany H-mode operation. Predicting the performance of I-mode in future devices is an important area of current research. By constructing cross-machine I-mode scaling laws using today's tokamaks, the I-mode confinement time and power threshold can be predicted for future tokamaks. If I-mode is achieved on future tokamaks diagnostic techniques such as CECE can be used to study the fluctuations and fluctuation-driven transport.

I-mode is not the only candidate regime for ELM-free high confinement operation in future reactors. Regimes such as Enhanced D-alpha H-mode, Quiescent H-mode, and Negative Triangularity L-mode might also fulfill the requirements of a future power plant. A survey of edge turbulence behavior in these other high confinement regimes is given in Appendix B. The experimental, data analysis, and modeling techniques outlined for next steps could be just as readily applied to these other regimes. In conclusion, further study of fluctuations in the tokamak edge informs our understanding of the operational regimes needed for future fusion reactors. The newest advances in diagnostics, data analysis techniques, and computational modeling are required in order to gain a more complete understanding of the physically rich edge region. This active area of research plays a critical role in the success of tokamak fusion as a whole.

Appendix A

Poloidal impurity asymmetries, flow, and neoclassical transport in pedestals in the plateau and banana regimes

This appendix describes a neoclassical model of impurity and main ion behavior in the pedestal. The description is adapted from Reference [130], in which the authors made equal contributions. This model extends previous impurity neoclassical pedestal models slightly by retaining impurity diamagnetic effects, which are shown to have no substantial impact on the model. The more significant extension of this model from previous work is the more comprehensive treatment of main ions in the plateau and banana regimes. This model provides valuable insight by which to understand pedestal impurity distribution and particle fluxes, including the differences in these quantities between L, I, and H-mode.

A.1 Introduction

As described in Chapter 2, the reduction of edge turbulence by sheared flows during the L to H-mode, and L to I-mode, transitions is expected to reduce the turbulent fluxes that drive the transport of heat and particles. This process allows the development of the pedestal and is important for attaining the high energy confinement needed for future reactor operation. In the pedestal region of reduced turbulence, neoclassical collisional transport is often assumed to explain lower order particle transport behavior, such as impurity flows [18], [164]–[169]. Pedestal measurements indicate that impurity transport can be at or near neoclassical levels in improved confinement regimes [170], [171].

Accumulation of impurities in a tokamak plasma can lead to loss of energy, and ultimately result in radiative collapse. ELMy H-mode relies on ELMs to expel impurities. I-mode, which exhibits a heat transport barrier without a particle transport barrier, has impurity confinement properties similar to L-mode [170]. The behavior of impurities in the pedestal of both H-mode and I-mode is important to understand in order to have a complete picture of pedestal transport processes and to predict future reactor operation.

Conventional neoclassical orderings [172] are limited in the pedestal because the scale lengths of E_r can be as small as the poloidal ion gyroradius. In Reference [164], a high charge number ordering for impurities was employed to cope with limitations of conventional neoclassical orderings, but maintain a local treatment of transport. This treatment allowed some behavior of impurities to be understood for banana regime main ions, demonstrating that large main ion gradients poloidally redistribute impurity ions to reduce their parallel friction with main ions, as well as their neoclassical particle flux. This resulted in accumulation on the high field side of the tokamak. Further work considered the cases of strong rotation [166] and plateau regime main ions [168]. The Charge Exchange Recombination Spectroscopy (CXRS) diagnostic measures spectroscopic emission from impurities, and its measurements can be used to infer the pedestal radial electric field E_r as well as in-out poloidal asymmetries in E_r and impurity density [129], [173]–[177]. In more recent neoclassical impurity models, the banana regime formulation of Reference [164] has been recast into a form that utilizes CXRS measurement capabilities, using a poloidal impurity flow term in place of a term that requires solving the kinetic equation for the main ions in the presence of impurities [18], [178], [179]. In all these models, the poloidal variation of the magnetic field is responsible for the poloidal variation of the impurity density, which is in turn responsible for the poloidal variation of the electric field.

The pedestal region of I-mode and H-mode can be in either the plateau or banana regime of collisionality, depending on the exact parameters of the plasma and the location in the pedestal. The material that follows will show that these regimes share the same characteristics in terms of poloidal impurity density variation. We will also show that the impurity pressure gradient term can be retained by allowing moderate impurity charge numbers (e.g. nitrogen, carbon, and boron) rather than very large (e.g. tungsten) charge numbers, and using an aspect ratio expansion for the impurity pressure gradient terms. This impurity diamagnetic term will be shown to be small. In this model, the plateau regime solution of the main ion kinetic equation and treatment of ambipolarity are improved.

The rest of this appendix will develop a model of impurity transport in the pedestal, beginning in Section A.2 with an introduction to the tokamak notation and coordinates used. Next, in Section A.3, general expressions will be presented for the parallel impurity momentum equation, quasineutrality, radial impurity flux, and the impurity flow, all with the impurity pressure term retained. In Sections A.4 and A.5 the general expressions are applied to banana regime main ions and plateau regime main ions separately. Approximate solutions for the poloidal variation of impurity density in the plateau and banana regimes will be presented in Section A.6, and diffusion and convection forms of the impurity continuity equation are discussed in Section A.7. Finally in Section A.8, predictions of impurity density accumulation and radial fluxes from the model are given for I-mode and H-mode scenarios.

A.2 Geometry

Before describing the behavior of impurities and main ions, the tokamak geometry used must be introduced. The magnetic field of an axisymmetric tokamak can be written as:

$$\vec{B} = I\nabla\zeta + \nabla\zeta \times \nabla\psi = \nabla\left(\zeta - q\vartheta\right) \times \nabla\psi = B\vec{b} \tag{A.1}$$

where ψ is the poloidal flux function, ζ is the toroidal angle with $|\nabla\zeta| = R^{-1}$, ϑ is the poloidal angle, q is the safety factor, $\vec{b}$ is the unit vector along $\vec{B}$, and $I = I\left(\psi\right) = RB_t$ with

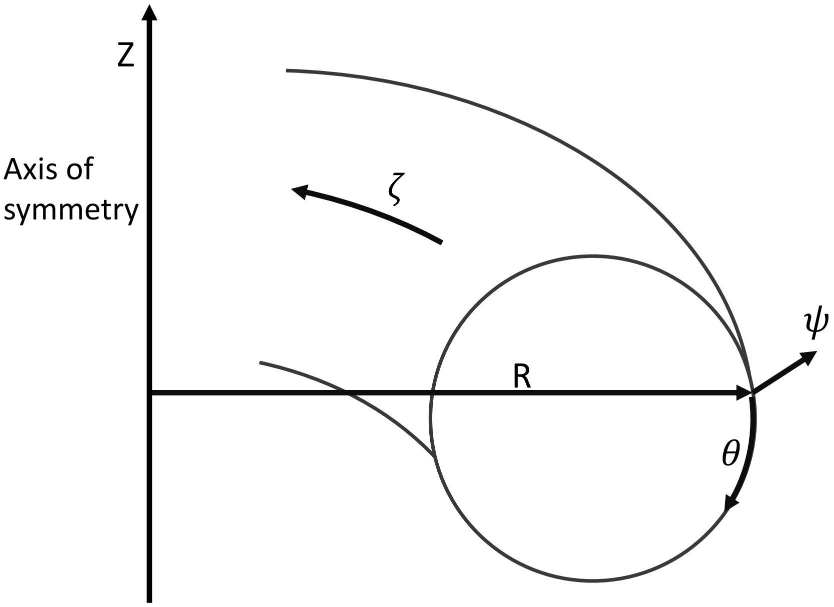

Figure A.1: Tokamak geometry.

R the major radius and B_t the toroidal magnetic field. This geometry is shown in Figure A.1. By picking ϑ such that

$$\vec{B} \cdot \nabla\vartheta = \frac{|I|}{qR^2} = \frac{1}{q}|\vec{B} \cdot \nabla\zeta|, \tag{A.2}$$

q will be a flux function $q = q\left(\psi\right)$.

Additional useful relations include:

$$\vec{B} \times \nabla\psi = I\vec{B} - B^2R^2\nabla\zeta \tag{A.3}$$

$$|\nabla\psi| = RB_p \tag{A.4}$$

$$\nabla\zeta \cdot \nabla\psi = 0 = \nabla\zeta \cdot \nabla\vartheta \tag{A.5}$$

$$\nabla\psi \times \nabla\vartheta \cdot \nabla\zeta = \vec{B} \cdot \nabla\vartheta \tag{A.6}$$

where B_p is the poloidal magnetic field. The toroidal current is taken to be in the $\nabla\zeta$ direction, making $B_p > 0$ and $\vec{B} \cdot \nabla\vartheta > 0$. The low field side (LFS) equatorial plane is taken to be $\vartheta = 0$ with ϑ increasing in the $\vec{B}_p = \nabla\zeta \times \nabla\psi$ direction. The toroidal magnetic field can be in the co-current ($B_t > 0$) or counter-current ($B_t < 0$) direction.

In ψ, ϑ, ζ variables, the components of any vector $\vec{A}$ can be written as:

$$\vec{A} = \frac{1}{\nabla\psi \times \nabla\vartheta \cdot \nabla\zeta}\left[\left(\vec{A} \cdot \nabla\psi\right)\left(\nabla\vartheta \times \nabla\zeta\right) + \left(\vec{A} \cdot \nabla\vartheta\right)\left(\nabla\zeta \times \nabla\psi\right) + \left(\vec{A} \cdot \nabla\zeta\right)\left(\nabla\psi \times \nabla\vartheta\right)\right] \tag{A.7}$$

In this form, the divergence is formed as:

$$\nabla \cdot \vec{A} = \left[\frac{\partial}{\partial \psi} \left(\frac{\vec{A} \cdot \nabla \psi}{\vec{B} \cdot \nabla \vartheta} \right) + \frac{\partial}{\partial \vartheta} \left(\frac{\vec{A} \cdot \nabla \vartheta}{\vec{B} \cdot \nabla \vartheta} \right) \right] \vec{B} \cdot \nabla \vartheta \tag{A.8}$$

In a tokamak, the flux surface average of a scalar quantity A is defined as:

$$\langle A \rangle = \frac{1}{V'} \oint \frac{d\vartheta \ A}{\vec{B} \cdot \nabla \vartheta} \tag{A.9}$$

with $V' = \oint \frac{d\vartheta}{\vec{B} \cdot \nabla \vartheta}$ and the ϑ integral over a full 2π when $A = A(\psi, \vartheta)$. The flux surface average operating on the divergence of a vector $\vec{A}$ gives:

$$\left\langle \nabla \cdot \vec{A} \right\rangle = \frac{1}{V'} \frac{\partial}{\partial \psi} \left(V' \left\langle \vec{A} \cdot \nabla \psi \right\rangle \right) \tag{A.10}$$

For current density $\vec{J}$, $\left\langle \nabla \cdot \vec{J} \right\rangle = 0$ will give the ambipolarity condition $\left\langle \vec{J} \cdot \nabla \psi \right\rangle = 0$ upon integration from the magnetic axis.

A.3 Impurity treatment

The lowest order momentum conservation equation for impurities (subscript z) with charge Z_z and mass M_z is:

$$Z_z e n_z \left(\nabla \Phi - \frac{1}{c} \vec{V}_z \times \vec{B} \right) + \nabla p_z = \vec{b} F_{zi}^{\parallel} = \vec{b} M_z \int d^3 v v_{\parallel} C_{zi} \tag{A.11}$$

Here, e is the proton charge, c is the speed of light, $F_{zi}^{\parallel}$ is the parallel collisional friction between impurities and main ions (subscript i), C_{zi} is the collision operator for impurities colliding with main ions, n_z and $p_z = n_z T_i(\psi)$ are the impurity density and pressure, $\vec{V}_z$ is the impurity velocity, and Φ is the electrostatic potential. Equilibration with main ions is assumed to give $T_z = T_i$. Only low flow speeds are considered here, making the inertial term negligible. Sonic rotation was considered in Reference [166].

The ordering

$$Z_z e \Phi \sim T_i \gg Z_i e \Phi \tag{A.12}$$

is assumed, where Z_i and n_i are the main ion charge number and density. This allows $Z_z e n_z \nabla \Phi \sim \nabla p_z$, and allows the formulation of a theoretical description where all the terms in Eq. A.11 are the same magnitude. While this ordering allows for insight into pedestal neoclassical impurity transport, it is not as general as a true pedestal ordering that requires $Z_i e \Phi \sim T_i$ to permit $Z_i e n_i \frac{\partial \Phi}{\partial \psi} \sim \frac{\partial p_i}{\partial \psi}$ [180]. The theoretical model developed here assumes:

$$\frac{\partial p_i}{\partial \psi} \gg Z_e e n_i \frac{\partial \Phi}{\partial \psi} \gg Z_z e n_z \frac{\partial \Phi}{\partial \psi} \sim \frac{\partial p_z}{\partial \psi} \tag{A.13}$$

An expression for the radial electric field, E_r, is found by dotting momentum balance by $\nabla \vartheta \times \nabla \zeta$ and neglecting the friction contribution as small to give:

$$E_r = -RB_p\frac{\partial \Phi}{\partial \psi} \approx \frac{RB_p}{Z_z e n_z}\frac{\partial p_z}{\partial \psi} + \frac{RB_p}{c}\vec{V}_z \cdot \nabla\zeta - \frac{IB_p}{cR}\frac{\vec{V}_z \cdot \nabla\vartheta}{\vec{B} \cdot \nabla\vartheta} \approx \frac{RB_p}{Z_z e n_z}\frac{\partial p_z}{\partial \psi} + \frac{1}{c}\left(V_t B_p - V_p B_t\right) \tag{A.14}$$

E_r can be determined experimentally by measuring the diamagnetic, toroidal, and poloidal flow contributions in Eq. A.14 using injected or intrinsic impurities in the plasma [129], [173], [174], [181]. The orderings given in A.12 and A.13 allow all terms in Eq. A.14 to be the same order.

The flux surface averaged electrostatic potential, $\langle\Phi\rangle$, is largely determined by the main ions through conservation of toroidal angular momentum. The poloidal variation of the electrostatic potential is given by $\Phi - \langle\Phi\rangle$. The poloidal variation of the impurity density is found from conservation of impurity parallel momentum. Due to the need to maintain quasineutrality, impurities can result in strong poloidal variation in $\Phi - \langle\Phi\rangle$. E_r can also vary poloidally due to contributions from $\frac{\partial}{\partial\psi}\left(\Phi - \langle\Phi\rangle\right)$.

Momentum balance yields the perpendicular flow velocity $\vec{V}_{\perp z}$, giving:

$$n_z\vec{V}_z = n_z\vec{V}_{\perp z} + n_z\vec{V}_{\parallel z}\vec{b} = c\frac{\vec{B}}{B^2} \times \left[n_z\nabla\Phi + \frac{\nabla p_z}{Z_z e}\right] + n_z V_{\parallel z}\frac{\vec{B}}{B} \tag{A.15}$$

The impurity flow can also be written as:

$$n_z\vec{V}_z = L_z\vec{B} + n_z\omega_z R^2\nabla\zeta - \Upsilon\nabla\vartheta \times \nabla\zeta \tag{A.16}$$

Here, the Υ term allows a radial flow departure from a flux surface:

$$n_z\vec{V}_z \cdot \nabla\psi = -\Upsilon\vec{B} \cdot \nabla\vartheta = \frac{cI}{Z_z e B^2}\left(\vec{B} \cdot \nabla p_z + Z_z e n_z \vec{B} \cdot \nabla\Phi\right). \tag{A.17}$$

The angular frequency $\omega_z = \omega_z(\psi, \vartheta)$ contributes to the toroidal flow:

$$\vec{V}_z \cdot \nabla\zeta = \omega_z + \frac{1}{n_z}L_z\vec{B} \cdot \nabla\zeta. \tag{A.18}$$

The parallel flow coefficient L_z is related to the poloidal flow and leads to the expression:

$$n_z\vec{V}_z \cdot \nabla\vartheta = L_z\vec{B} \cdot \nabla\vartheta = \left[\frac{n_z V_{\parallel z}}{B} + \frac{cI}{Z_z e B^2}\left(\frac{\partial p_z}{\partial\psi} + Z_z e n_z\frac{\partial\Phi}{\partial\psi}\right)\right]\vec{B} \cdot \nabla\vartheta. \tag{A.19}$$

Additionally, the impurity continuity equation gives:

$$0 = \nabla \cdot \left(n_z\vec{V}_z\right) - \vec{B} \cdot \nabla\vartheta\left(\frac{\partial L_z}{\partial\vartheta} - \frac{\partial\Upsilon}{\partial\psi}\right). \tag{A.20}$$

L_z is not a flux function, due to the retention of the radial impurity pressure gradient and the poloidal variation of electrostatic potential and the impurity pressure. The poloidal variation of the potential and impurity density are responsible for the radial impurity flow. Standard banana and plateau regime treatments assume these quantities are flux functions, so a radial impurity flow does not occur [172]. Treatments focused on measuring poloidal variation of impurity flow on a flux surface do not consider the small radial flow correction Υ [182], [183]. In Reference [164], the $\frac{\partial\Upsilon}{\partial\psi}$ term is ignored because Z_z is assumed to be very large.

The parallel impurity momentum equation is given by:

$$\vec{B}\cdot\nabla p_z + Z_z e n_z \vec{B}\cdot\nabla\Phi = BF_{zi}^{\|} = -BF_{iz}^{\|} = -M_i B\int d^3v v_\| C_{iz}. \tag{A.21}$$

To evaluate this, collisional momentum conservation

$$M_z\int d^3v v_\| C_{zi} + M_i\int d^3v v_\| C_{iz} = 0 \tag{A.22}$$

is employed since it is convenient to use the collision operator C_{iz} for the faster background ions colliding with the slower impurities:

$$C_{iz}\{f_{i1}\} = \frac{3\sqrt{2\pi}T_i^{3/2}\nu_{iz}}{4M_i^{3/2}}\nabla_v\cdot\left[\nabla_v\nabla_v v\cdot\nabla_v\left(f_{i1} - \frac{M_i}{T_i}V_{\|z}v_\| f_{i0}\right)\right] \tag{A.23}$$

where $f_i = f_{i0} + f_{i1}$, with f_{i1} the non-adiabatic perturbed ion distribution function and f_{i0} the Maxwellian (which must be a flux function and depend on total energy in the banana and plateau regimes):

$$f_{i0} = n_i\left(\frac{M_i}{2\pi T_i}\right)^{3/2} \mathrm{e}^{-M_i v^2/2T_i} \approx \langle n_i\rangle\left[1 - Z_i e\left(\Phi - \langle\Phi\rangle\right)\frac{1}{T_i}\right]\mathrm{e}^{-M_i v^2/2T_i} \tag{A.24}$$

with $n_e \approx \langle n_i\rangle\left[1 - Z_i e\left(\Phi - \langle\Phi\rangle\right)\frac{1}{T_i}\right]$. It is convenient to keep the perturbed Maxwell-Boltzmann response in f_{i0}. The ion-impurity collision frequency ν_{iz} is defined as:

$$\nu_{iz} = n_z\frac{4\sqrt{2\pi}Z_i^2 Z_z^2 e^4}{3M_i^{1/2}T_i^{3/2}}\ln\Lambda \tag{A.25}$$

where ln Λ is the Coulomb logarithm, M_i is the background ion mass, and $\nu_{iz}/\nu_{zi} = M_z n_z/2M_i n_i \ll 1$, where ν_{zi} is the impurity-ion collision frequency. Evaluating the parallel friction gives:

$$F_{iz}^{\|} = M_i\int d^3v v_\| C_{iz} = M_i n_i \nu_{iz}\left(V_{\|z} - \frac{3\sqrt{2\pi}T_i^{3/2}}{2M_i^{3/2}n_i}\int d^3v\frac{v_\| f_{i1}}{v_3}\right) = -F_{zi}^{\|}. \tag{A.26}$$

Only unlike particle collisions cause particle transport. The banana regime diffusivity for electrons colliding with the main ions, D_e, is roughly $D_e \sim q^2\rho_e^2\nu_{ei}/\epsilon^{3/2} \propto n_e M_e^{1/2}$, with ρ_e the electron gyroradius, ν_{ei} the electron-ion collision frequency, and M_e the electron mass. The banana regime diffusivity for the faster main ions colliding with the slower impurities, D_i, is roughly $D_i \sim q^2\rho_i^2\nu_{iz}/\epsilon^{3/2} \propto Z_z^2 n_z M_i^{1/2}$, with ρ_i the ion gyroradius. Therefore, as long as $Z_z^2 n_z/n_e \gg (M_e/M_i)^{1/2}$, electron transport can be ignored. Then, ambipolarity between ions and impurities requires:

$$Z_i \left\langle n_i \vec{V}_i \cdot \nabla\psi \right\rangle = -Z_z \left\langle n_z \vec{V}_z \cdot \nabla\psi \right\rangle = Z_z \left\langle \Upsilon \vec{B} \cdot \nabla\vartheta \right\rangle = -\frac{cI}{e} \left\langle \frac{F_{iz}^{\|}}{B} \right\rangle \tag{A.27}$$

with the poloidal variation of Υ essential to obtain finite particle fluxes. The poloidal variation of the magnetic field in the parallel friction gives rise to poloidal variation of the potential and densities. These poloidal density variations must satisfy quasineutrality, which upon taking hte poloidal derivative yields:

$$\vec{B} \cdot \nabla n_e = Z_i \vec{B} \cdot \nabla n_i + Z_z \vec{B} \cdot \nabla n_z \tag{A.28}$$

Assuming the temperatures are flux functions, and using a Maxwell-Boltzmann response for the electrons, $n_e \approx \langle n_e \rangle \left[1 + e\left(\Phi - \langle\Phi\rangle\right)/T_e(\psi)\right]$, and background ions, leads to:

$$Z_z \vec{B} \cdot \nabla n_z = \langle n_e \rangle \left(\frac{e}{T_e} + \frac{Z_i e}{T_i} \right) \vec{B} \cdot \nabla\Phi, \tag{A.29}$$

where the impurity density is assumed small in order not to alter lowest order quasineutrality, $\langle n_e \rangle = Z_i \langle n_i \rangle \gg Z_z \langle n_z \rangle$. Consequently, the potential can be eliminated from the parallel momentum constraint, and the solution for n_z must satisfy the solubility constraint $\left\langle B F_{iz}^{\|} \right\rangle = 0$. Using quasineutrality to rewrite the parallel impurity equation yields:

$$\left(1 + \frac{\alpha n_z}{\langle n_z \rangle}\right) \vec{B} \cdot \nabla n_z = \frac{B F_{iz}^{\|}}{T_i} \tag{A.30}$$

where

$$\alpha = \frac{Z_z^2 \langle n_z \rangle \tau}{Z_i \langle n_e \rangle (1+\tau)} \tag{A.31}$$

is allowed to be order unity or less, and $\tau = Z_i T_e / T_i$. Equations A.29 and A.14 and the preceding orderings allow $Z_z e\left(\Phi - \langle\Phi\rangle\right)/T_i \sim \left(n_z - \langle n_z \rangle\right)/\langle n_z \rangle \sim 1$ as well as $Z_z e \langle\Phi\rangle \sim T_i$, but assume $Z_i e\left(\Phi - \langle\Phi\rangle\right)/T_i \ll 1$.

The poloidal variation of the impurity density is due to the poloidal variation of the magnetic field in $B F_{iz}^{\|}$. Using the normalizations $n = n_z/\langle n_z \rangle$ and $b^2 = B^2/\langle B^2 \rangle$, and introducing $d\theta = \left\langle \vec{B} \cdot \nabla\vartheta \right\rangle d\vartheta / \vec{B} \cdot \nabla\vartheta$ to remove the ϑ dependence of $\vec{B} \cdot \nabla\vartheta$, the parallel impurity momentum equation becomes:

$$(1 + \alpha n) \frac{\partial n}{\partial \theta} = -\frac{M_i n_i \langle \nu_{iz} \rangle \langle B^2 \rangle}{\langle n_z \rangle \langle p_z \rangle \left\langle \vec{B} \cdot \nabla\vartheta \right\rangle} b^2 \left(\frac{n_z V_{\|z}}{B} - \frac{3\sqrt{2\pi} T_i^{3/2} n_z}{2 M_i^{3/2} n_i} \int d^3v \frac{v_\| f_{i1}}{B v^3} \right) \tag{A.32}$$

where $n_i \simeq \langle n_i \rangle$ is used in the coefficients on the right side, since it gives a negligible correction of order $Z_i e\left(\Phi - \langle\Phi\rangle\right)/T_i \sim Z_z\left(n_z \langle n_z \rangle\right)/\langle n_e \rangle \ll 1$. Here, and in the remainder of this appendix, $n_i \approx \langle n_i \rangle$ and $p_i \approx \langle p_i \rangle = \langle n_i \rangle T_i$ but $n_z \neq \langle n_z \rangle$.

Taking the poloidal derivative of quasineutrality also allows Υ to be written as:

$$\Upsilon = \frac{cIT_i}{Z_z e B^2}\left(1+\frac{\alpha n_z}{\langle n_z\rangle}\right)\frac{\partial n_z}{\partial \vartheta} = \frac{cI\left\langle p_z\right\rangle}{Z_z e B^2}\frac{\partial}{\partial \vartheta}\left[n-1+\frac{\alpha}{2}\left(n^2-1\right)\right]. \tag{A.33}$$

Notice that when Z_z is very large, $\Upsilon \to 0$ giving $\partial L_z/\partial\vartheta \to 0$, which is the limit considered in Reference [164]. The lowest order poloidal variation of L_z due to impurity diamagnetic effects can be retained by assuming the poloidal variation of the magnetic field is weak by ordering:

$$\frac{1}{\langle n_z\rangle}\frac{\partial n_z}{\partial\vartheta} \sim \frac{1}{\langle B^2\rangle}\frac{\partial B^2}{\partial \vartheta} \sim \epsilon \ll 1. \tag{A.34}$$

This ordering is consistent with the inverse aspect ratio $\epsilon = a/R$ expansion necessary in the plateau regime, where a is minor radius. In the banana regime, this expansion is only necessary to treat impurity pressure terms, but illustrates how their behavior enters in a limited extent. In the banana regime, all other terms can be retained for general B, and therefore, for quite general n_z as long as the poloidal ion gyroradius is small compared to the radial scale lengths. The aspect ratio expansion means:

$$\frac{1}{b^2}\frac{\partial}{\partial\vartheta}\left[n-1+\frac{\alpha}{2}\left(n^2-1\right)\right] = \frac{\partial}{\partial\vartheta}\left[\frac{n-1}{b^2}+\frac{\alpha}{2b^2}\left(n^2-1\right)\right] - \left[n-1+\frac{\alpha}{2}\left(n^2-1\right)\right]\frac{\partial}{\partial\vartheta}\left(\frac{1}{b^2}\right) \tag{A.35}$$

where the last term is order ϵ^2. Consequently, impurity diamagentic modifications of order $Z_i\epsilon/Z_z$ are retained by writing Υ as:

$$\Upsilon = \frac{cI\left\langle p_z\right\rangle}{Z_z e\left\langle B^2\right\rangle}\frac{\partial}{\partial\vartheta}\left[\frac{n-1}{b^2}+\frac{\alpha}{2b^2}\left(n^2-1\right)\right]+\Delta, \tag{A.36}$$

with $\left\langle \Upsilon\vec{B}\cdot\nabla\vartheta\right\rangle = \left\langle \Delta\vec{B}\cdot\nabla\vartheta\right\rangle$ and $Z_i\epsilon^2/Z_z$ corrections from Δ:

$$\Delta = \frac{cI\left\langle p_z\right\rangle}{Z_z e\left\langle B^2\right\rangle}\left[n-1+\frac{\alpha}{2}\left(n^2-1\right)\right]\frac{\partial}{\partial\vartheta}\left(1-\frac{1}{b^2}\right). \tag{A.37}$$

Ignoring the Δ term as small in $\nabla\cdot\left(n_z\vec{V}_z\right) = 0$ and integrating Eq. A.20 leads to:

$$\frac{n_z\vec{V}_z\cdot\nabla\vartheta}{\vec{B}\cdot\nabla\vartheta} = L_z \approx K_z\left(\psi\right) + \frac{\partial}{\partial\psi}\left\{\frac{cI\left\langle p_z\right\rangle}{Z_z e\left\langle B^2\right\rangle}\left[\frac{n-1}{b^2}+\frac{\alpha}{2b^2}\left(n^2-1\right)\right]\right\} \tag{A.38}$$

with K_z a flux function associated with the poloidal flow. The preceding and

$$\frac{n_z\vec{V}_z\cdot\nabla\vartheta}{\vec{B}\cdot\nabla\vartheta} = \frac{n_z V_{\|z}}{B} + \frac{cI}{B^2}\left(n_z\frac{\partial\Phi}{\partial\psi}+\frac{1}{Z_z e}\frac{\partial p_z}{\partial\psi}\right) \tag{A.39}$$

allow the parallel impurity flow to be written as:

$$\frac{n_z V_{\|z}}{B} = K_z\left(\psi\right) - \frac{cI}{B^2}\left(n_z\frac{\partial\Phi}{\partial\psi}+\frac{1}{Z_z e}\frac{\partial\left\langle p_z\right\rangle}{\partial\psi}\right) + \frac{cI}{Z_z e B^2}\frac{\partial}{\partial\psi}\left[\alpha\left\langle p_z\right\rangle\left(n-1\right)\right], \tag{A.40}$$

where in $\langle p_z\rangle$ terms, the radial variation of B is weak compared to that of n_z, n_i, and T_i.

To make further progress, more details for the solution f_{i1} are required. These details can be obtained by considering the background ions to be in either the banana ($\nu_* < 1$) or plateau ($1 < \nu_* < 1/\epsilon^{3/2}$) regimes, where collisionality $\nu_* \equiv \nu_{ii} qR/v_i\epsilon^{3/2}$ with $\nu_{ii} = n_i \frac{4\sqrt{\pi}Z_i^4 e^4}{3M_i^{1/2}T_i^{3/2}} \ln\Lambda$ the ion-ion collision frequency and $v_i = \sqrt{2T_i/M_i}$ the ion thermal speed. We will consider these two regimes separately, beginning with the banana regime. In both cases, the impurities may be collisional even for moderate Z_z/Z_i, as $\nu_{zz}/\nu_{ii} = Z_z^4 n_z M_i^{1/2}/Z_i^4 n_i M_z^{1/2} \sim \alpha\left(Z_z/Z_i\right)^2\left(\nu_{ii}qR/v_i\right)$ with ν_{zz} the impurity-impurity collision frequency and $v_z = \sqrt{2T_i/M_z}$ the impurity thermal speed. The preceding indicates the impurities become collisional when $\alpha\left(Z_z/Z_i\right)^2 > 1$. Collisional background ions are not considered here, but were were investigated in References [167], [184], [185].

A.4 Background ions: banana regime

In the banana regime the background ion kinetic equation is formulated to be solved in total energy, $E = v^2/2 + Z_i e\Phi/M_i$, and magnetic moment, $\mu = v_\perp^2/2B$, variables. The kinetic equation is:

$$v_\parallel \vec{b}\cdot\nabla h_1 = C_1\Big\{ h_1 - \frac{Iv_\parallel}{\Omega_i}\frac{\partial f_{i0}}{\partial\psi}\bigg|_E \Big\} \tag{A.41}$$

where C_1 is the ion-ion plus ion-impurity collision operator, $\Omega_i = Z_i eB/M_i c$ is the ion cyclotron frequency,

$$f_{i0} = \eta(\psi)\left(\frac{M_i}{2\pi T_i}\right)^{3/2} \mathrm{e}^{-M_i E/T_i} \approx \langle n_i\rangle\left[1 - \frac{1}{T_i}Z_i e\left(\Phi - \langle\Phi\rangle\right)\right]\mathrm{e}^{-M_i v^2/2T_i} \tag{A.42}$$

with $n_i = \eta\mathrm{e}^{-Z_i e\Phi/T_i} \approx \langle n_i\rangle\left[1 - \frac{1}{T_i}Z_i e\left(\Phi - \langle\Phi\rangle\right)\right]$ as before, with $\eta = \langle n_i\rangle\,\mathrm{e}^{Z_i e\langle\Phi\rangle/T_i}$ a pseudo-density, and h_1 related to f_1 by:

$$f_{i1} = h_1 - \frac{Iv_\parallel}{\Omega_i}\frac{\partial f_{i0}}{\partial\psi}\bigg|_E = h_1 - \frac{Iv_\parallel f_{i0}}{\Omega_i}\left[\frac{1}{p_i}\frac{\partial p_i}{\partial\psi} + \frac{Z_i e}{T_i}\frac{\partial\Phi}{\partial\psi} + \left(\frac{M_i v^2}{2T_i} - \frac{5}{2}\right)\frac{1}{T_i}\frac{\delta T_i}{\delta\psi}\right]. \tag{A.43}$$

Evaluating the integrals for the explicit friction terms yields:

$$\frac{3\sqrt{2\pi}T_i^{3/2}n_z}{2M_i^{3/2}n_i}\int d^3v\frac{v_\parallel(f_{i1} - h_1)}{Bv^3} = -\frac{cIn_z}{B^2}\frac{\partial\Phi}{\partial\psi} - \frac{cIn_z}{Z_i e n_i B^2}\left(\frac{\partial p_i}{\partial\psi} - \frac{3n_i}{2}\frac{\partial T_i}{\partial\psi}\right). \tag{A.44}$$

In the banana regime, $v_\parallel\vec{b}\cdot\nabla h_1 = 0$ to lowest order, making:

$$u \equiv \frac{3\sqrt{2\pi}T_i^{3/2}}{2M_i^{3/2}}\int d^3v\frac{v_\parallel h_1}{Bv_3} \tag{A.45}$$

a flux function. The trapped ion portion of h_1 vanishes, as can be seen by transit averaging the next order kinetic equation and noting $v_\parallel$ changes sign upon reflection. Then the terms in Eq. A.26 on the right side of the parallel momentum equation combine to give:

$$\begin{aligned}\frac{n_z V_{\parallel z}}{B} - \frac{3\sqrt{2\pi}T_i^{3/2} n_z}{2M_i^{3/2} n_i}\int d^3v\, \frac{v_\parallel f_{i1}}{Bv^3} = K_z - \frac{n_z u}{n_i} &+ \frac{cI}{Z_z e B^2}\frac{\partial}{\partial\psi}\left[\alpha\left\langle p_z\right\rangle(n-1) - \left\langle p_z\right\rangle\right] \\ &+ \frac{cIn_z}{Z_i e n_i B^2}\left(\frac{\partial p_i}{\partial\psi} - \frac{3n_i}{2}\frac{\partial T_i}{\partial \psi}\right)\end{aligned} \tag{A.46}$$

In addition, the radial particle flux is:

$$\begin{aligned}Z_i\left\langle n_i\vec{V}_i\cdot\nabla\psi\right\rangle = \frac{cI}{e}\left\langle\frac{F_{iz}^{\parallel}}{B}\right\rangle = -\frac{cIM_i n_i\left\langle\nu_{iz}\right\rangle}{e\left\langle n_z\right\rangle}\Bigg\{K_z - \frac{\left\langle n_z\right\rangle u}{n_i} &+ \frac{cI}{Z_z e}\left\langle\frac{1}{B^2}\frac{\partial}{\partial\psi}\left[\alpha\left\langle p_z\right\rangle(n-1)\right.\right. \\ &\left.\left. - \left\langle p_z\right\rangle\right]\right\rangle + \frac{cI}{Z_i e n_i}\left\langle\frac{n_z}{B^2}\right\rangle\left(\frac{\partial p_i}{\partial\psi} - \frac{3n_i}{2}\frac{\partial T_i}{\partial\psi}\right)\Bigg\}\end{aligned} \tag{A.47}$$

Defining the gradient flux function G by:

$$G = G(\psi) = -\frac{cIM_i\left\langle\nu_{iz}\right\rangle}{Z_i e\left\langle p_z\right\rangle\left\langle\vec{B}\cdot\nabla\vartheta\right\rangle}\left(\frac{\partial p_i}{\partial\psi} - \frac{3n_i}{2}\frac{\partial T_i}{\partial\psi}\right), \tag{A.48}$$

an impurity diamagnetic flux function $D \propto 1/Z_z$ by:

$$D = D(\psi) = -\frac{cIM_i n_i\left\langle\nu_{iz}\right\rangle}{Z_z e\left\langle p_z\right\rangle\left\langle n_z\right\rangle\left\langle\vec{B}\cdot\nabla\vartheta\right\rangle}\frac{\partial\left\langle p_z\right\rangle}{\partial\psi}, \tag{A.49}$$

a poloidal flow function K:

$$K = K(\psi) = \frac{M_i n_i\left\langle\nu_{iz}\right\rangle\left\langle B^2\right\rangle}{\left\langle p_z\right\rangle\left\langle n_z\right\rangle\left\langle\vec{B}\cdot\nabla\vartheta\right\rangle}K_z, \tag{A.50}$$

and a flow quantity U (that is only a flux function in the banana regime):

$$U = \frac{M_i\left\langle\nu_{iz}\right\rangle\left\langle B^2\right\rangle u}{\left\langle p_z\right\rangle\left\langle\vec{B}\cdot\nabla\vartheta\right\rangle}, \tag{A.51}$$

then the parallel impurity momentum equation in the banana regime becomes:

$$(1+\alpha n)\frac{\partial n}{\partial\theta} = Gn - Kb^2 + Unb^2 - D\left[1 - \frac{\partial\left[\alpha\left\langle p_z\right\rangle(n-1)\right]/\partial\psi}{\partial\left\langle p_z\right\rangle/\partial\psi}\right]. \tag{A.52}$$

To obtain the last term it is necessary to make an aspect ratio expansion, A.34, but the other terms are valid for general B and n_z. Notice that the final term in the expression multiplying D vanishes to lowest order upon flux surface averaging. Except for the generalization to include poloidal variation due to impurity diamagnetic effects, the orderings here are essentially the same as in References [164] and [168], where the impurity diamagnetic term is ignored by assuming very large Z_z/Z_i. The treatment here retains D to lowest order in the parallel impurity momentum equation. Consequently, moderate $Z_z/Z_i \gg 1$ (e.g. carbon or boron) are allowed, but very large Z_z/Z_i (e.g. tungsten) need not be assumed.

This treatment, as well as that in References [164] and [168] allow:

$$G \sim \frac{\rho_{ip}}{L_\perp}\frac{Z_z^2}{Z_i^2}\frac{qR\nu_{ii}}{v_i} \sim 1 \tag{A.53}$$

where the poloidal ion gyroradius, $\rho_{ip} = v_i B/\Omega_i B_p$ is assumed much smaller than the radial scale length $L_\perp$. At the banana-plateau transition, $G \sim (\rho_{ip}/L_\perp)\,(Z_z/Z_i)^2\,\epsilon^{3/2}$, indicating that for $G \sim 1$, $(Z_z/Z_i)^2\,\epsilon^{3/2} \gg 1$ is required.

Recalling that in the banana regime, the quantity U is a flux function, the solubility constraint

$$K = G + U\left\langle nb^2\right\rangle - D \tag{A.54}$$

can be employed to eliminate K:

$$(1+\alpha n)\frac{\partial n}{\partial \theta} = G\left(n - b^2\right) + Ub^2\left(n - \left\langle nb^2\right\rangle\right) - D\left[1 - b^2 - \frac{\partial\left[\alpha\left\langle p_z\right\rangle(n-1)\right]/\partial\psi}{\partial\left\langle p_z\right\rangle/\partial\psi}\right], \tag{A.55}$$

which agrees with Reference [164] when $Z_z \to \infty$. The orderings assume $D/G \sim Z_i/Z_z \ll 1$. The D term assumes $\epsilon \ll 1$ and enters because then $D(1-b^2)/G(n-b^2) \sim Z_i/\epsilon Z_z \sim 1$ is allowed. Measurements on Alcator C-Mod for $B_t > 0$ indicate $K > 0$ and $D > 0$ over most of the pedestal in both H-mode and I-mode [129]. In I-mode $\eta_i \equiv d\ln T_i/d\ln n_i > 2$ is expected, giving $G < 0$ in C-Mod and the flow term $U > 0$ in the banana regime. In H-mode, $\eta_i < 2$ is anticipated, givien $G > 0$ in C-Mod, so U can be of either sign.

With CXRS one can measure impurity flows as well as impurity density and temperature variations. Therefore, it is useful to use solubility to eliminate U instead of K to rewrite the parallel impurity momentum equation in the banana regime as:

$$\begin{aligned}(1+\alpha n)\frac{\partial n}{\partial \theta} = G\left(n - \frac{nb^2}{\left\langle nb^2\right\rangle}\right) - K\left(b^2 - \frac{nb^2}{\left\langle nb^2\right\rangle}\right) + D\left[(n-1) + \left(b^2-1\right)\right.\\ \left. + \frac{\partial\left[\alpha\left\langle p_z\right\rangle(n-1)\right]/\partial\psi}{\partial\left\langle p_z\right\rangle/\partial\psi}\right.,\end{aligned} \tag{A.56}$$

which generalizes the $Z_z \to \infty$ form in Reference [178] to include poloidal variation driven by the impurity pressure terms. To obtain this form, $Z_i/Z_z \sim \epsilon$ is assumed to simplify the D term by using $nb^2/\left\langle nb^2\right\rangle - b^2 \approx n - 1$. The orderings allow $G \sim 1 \sim K \sim Z_z D/Z_i$. For this ordering, impurity pressure effects are only allowed to alter the poloidal variation of the impurity density by terms of order ϵ. For a realistic, strongly varying magnetic field, this equation could be solved numerically to find strong poloidal variation in the impurity density. However, due to the difficulty of determining the various coefficients with the requisite certainty, only a simple limiting solution will be given once the plateau regime equation is derived. In the weak gradient and flow, low confinement limit (L-mode), the small up-down asymmetry satisfies $(1+\alpha)\partial n/\partial\theta \approx G(1-b^2)$ as in [164].

In addition to the poloidal impurity density variation, the particle flux can be evaluated for banana regime background ions from friction. Using the same orderings,

$$\begin{aligned}\frac{F_{iz}^{\|}}{B} = \frac{\langle p_z \rangle \left\langle \vec{B} \cdot \nabla\vartheta \right\rangle}{\langle B^2 \rangle} \Bigg\{ & G\left(\frac{n}{b^2} - \frac{n}{\langle nb^2 \rangle}\right) - K\left(1 - \frac{1}{\langle nb^2 \rangle}\right) + \\ & D\left[\frac{n}{b^2} + 1 - \frac{2}{b^2} + \frac{\partial\left[\alpha \langle p_z \rangle (n-1)\right]/\partial\psi}{b^2 \partial \langle p_z \rangle / \partial\psi}\right]\Bigg\}.\end{aligned} \tag{A.57}$$

The D term is negligible once Eq. A.57 is averaged (recall it is derived assuming $\epsilon \ll 1$), leading to the particle flux of the banana regime background ions being:

$$\left\langle n_i \vec{V}_i \cdot \nabla\psi \right\rangle = \frac{cI}{Z_i e}\left\langle \frac{F_{iz}^{\|}}{B} \right\rangle = -\frac{cI \langle p_z \rangle \left\langle \vec{B} \cdot \nabla\vartheta \right\rangle}{Z_i e \langle B^2 \rangle}\left[G\left(\left\langle \frac{n}{b^2} \right\rangle - \frac{1}{\langle nb^2 \rangle}\right) - K\left(1 - \frac{1}{\langle nb^2 \rangle}\right)\right], \tag{A.58}$$

as in [18], [178], [179], which also assume $T_i = T_z = \langle T_z \rangle$. This flux vanishes as desired for $n_z \to 0$. Also large gradient ($G \gg 1$ and $D \gg 1$) and flow ($K \gg 1$) drives make the right side of Eq. A.56 vanish and thereby reduce the friction (Eq. A.57) and radial transport (Eq. A.58), as pointed out in [164]. When K is retained instead of U with $G \sim K \gg 1 \sim D$, Eq. A.56 reduces to:

$$G\left(n - \frac{nb^2}{\langle nb^2 \rangle}\right) \approx K\left(b^2 - \frac{nb^2}{\langle nb^2 \rangle}\right), \tag{A.59}$$

indicating that for $G > 0$ and $K > 0$ (or $G < 0$ and $K < 0$), impurity accumulation will be large on the high field side (HFS), while impurity accumulation will occur on the low field side (LFS) when G and K are of opposite sign. The general form of Eq. A.57 and the approximate form Eq. A.59 allow strong poloidal variation in the magnetic field and the impurity density. For example, Eq. A.59 can be solved for a specified b^2 by defining $g \equiv G/K$ to obtain the lowest order result:

$$n = b^2 / \left[g + (1-g)b^2 / \left\langle nb^2 \right\rangle\right] \tag{A.60}$$

for a fixed g. The constant $\langle nb^2 \rangle$ determined implicitly from the constraint:

$$\left\langle b^2 / \left[g + (1-g)b^2 / \left\langle nb^2 \right\rangle\right] \right\rangle = 1. \tag{A.61}$$

The special case $g = 1$ gives $n = b^2$ to lowest order. It allows Eq. A.56 to be solved to next order to find:

$$n = b^2 + 1K\left[\left(1 + \alpha b^2\right)\frac{\partial b^2}{\partial \theta} - D\left(b^2 - 1\right)\frac{\partial\left(\alpha \langle p_z \rangle\right)/\partial\psi}{2 + \partial \langle p_z \rangle / \partial\psi}\right], \tag{A.62}$$

demonstrating impurity diamagnetic modifications occur for $G = K \gg D \sim 1$.

The plateau regime parallel momentum equation and particle flux for the impurities are derived next, before approximate solutions are presented.

A.5 Background ions: plateau regime

In the plateau regime, ($1 > \nu_{ii} qR/v_i > \epsilon^{3/2}$), the form of the collision operator C_{iz} makes it necessary to let:

$$f_{iz} = H_1 + \frac{M_i}{T_i} V_{\parallel z} v_\parallel f_{i0}, \tag{A.63}$$

with H_1 and h_1 related by:

$$h_1 - H_1 = \frac{I v_\parallel}{\Omega_i} \frac{\partial f_{i0}}{\partial \psi}\bigg|_E + \frac{M_i}{T_i} V_{\parallel z} v_\parallel f_{i0}, \tag{A.64}$$

and, unlike the banana regime, $v_\parallel \vec{b} \cdot \nabla h_1 \neq 0$. Then the plateau regime background ion kinetic equation to be solved for $\epsilon \ll 1$ is:

$$v_\parallel \vec{b} \cdot \nabla \vartheta \frac{\partial H_1}{\partial \vartheta} - C_1\{H_1\} = -v_\parallel \vec{b} \cdot \nabla \vartheta \frac{\partial}{\partial \vartheta} \left(\frac{I V_\parallel}{\Omega_i} \frac{\partial f_{i0}}{\partial \psi} \bigg| + \frac{M_i}{T_i} V_{\parallel z} v_\parallel f_{i0} \right). \tag{A.65}$$

In addition, the parallel impurity momentum equation to be solved for $\epsilon \ll 1$ is:

$$(1 + \alpha n) \frac{\partial n}{\partial \theta} = -\frac{B F_{iz}^{\parallel}}{\langle p_z \rangle \left\langle \vec{B} \cdot \nabla \vartheta \right\rangle} = \frac{3\sqrt{2\pi} T_i^{3/2} \nu_{iz} B}{2 M_i^{1/2} \langle p_z \rangle \left\langle \vec{B} \cdot \nabla \vartheta \right\rangle} \int d^3 v \frac{v_\parallel H_1}{v^3} \tag{A.66}$$

Solving in the plateau regime, there are subtleties that need to be explained in some detail as the procedure used here differs from that of Reference [168], which assumes differences in poloidal variation are unimportant by making the replacement:

$$V_{\parallel z} \to -\frac{cI}{Z_i e B n_i} \left[\frac{\partial p_i}{\partial \psi} + Z_i n_i \frac{\partial \Phi}{\partial \psi} + \frac{y b^2 n_i}{2} \frac{\partial T_i}{\partial \psi} \right] \equiv V_{\parallel I}^{\text{plat}}. \tag{A.67}$$

Reference [168] assumes very large Z_z so no $\langle p_z \rangle$ terms enter, and determine y from ambipolarity to recover $V_{\parallel I}^{\text{plat}}$, the usual plateau expression [172] for the parallel ion flow when $y = 1$.

For a plateau regime to exist, $\epsilon \approx r/R_0 \ll 1$ is required, where R_0 is the major radius of the magnetic axis. In addition to $d\theta = \left\langle \vec{B} \cdot \nabla \vartheta \right\rangle / \vec{B} \cdot \nabla \vartheta$ and $B = B_0 \left(1 - \epsilon \cos\theta + \dots\right)$, with $B_0^2 = \langle B^2 \rangle$ and $\left\langle \vec{B} \cdot \vartheta \right\rangle \approx B_0/qR_0$, a large aspect ratio for for n,

$$n = 1 + \epsilon \left(n_c \cos\theta + n_s \sin\theta \right), \tag{A.68}$$

must be employed in the drive terms $K_z \frac{\partial}{\partial \theta} \left(\frac{B}{n_z} \right)$, $\frac{\partial \langle p_z \rangle}{\partial \psi} \frac{\partial}{\partial \theta} \left(\frac{1}{B n_z} \right)$, and $\frac{\partial}{\partial \psi} \alpha \langle p_z \rangle \frac{\partial (n-1)}{\partial \theta}$ of $V_{\parallel z}$. Here, n_c and n_s are the coefficients that will be determined by solving Eq. A.66. Then the plateau regime kinetic equation is written as:

$$v_\parallel \frac{\partial H_1}{\partial \vartheta} - qR_0 C_1\{H_1\} = Q_s \sin\theta + Q_c \cos\theta, \tag{A.69}$$

where θ dependence enters only via $\sin\theta$ and $\cos\theta$. The coefficients are:

$$Q_s = \frac{\epsilon M_i}{2T_i}\Bigg\{\frac{cI\left(v_\perp^2 + 2v_\parallel^2\right)}{Z_i e B_0 n_i}\left[\frac{\partial p_i}{\partial \psi} - \frac{Z_i n_i}{Z_z \langle n_z \rangle}\frac{\partial \langle p_z \rangle}{\partial \psi} + \left(\frac{M_i v^2}{2T_i} - \frac{5}{2}\right) n_i \frac{\partial T_i}{\partial \psi}\right] \\ + \frac{K_z B_0}{\langle n_z \rangle}\left[v_\perp^2 - 2(1+n_c)v_\parallel^2\right] + \frac{2cIv_\parallel^2}{Z_z e B_0 \langle n_z \rangle}\left[n_c \frac{\partial \langle p_z \rangle}{\partial \psi} + \frac{\partial}{\partial \psi}\left(\alpha \langle p_z \rangle n_c\right)\right]\Bigg\} f_{i0}, \tag{A.70}$$

and

$$Q_c = -\frac{\epsilon M_i}{T_i}\Bigg\{\frac{cI}{Z_z e B_0 \langle n_z \rangle}\left[n_s \frac{\partial \langle p_z \rangle}{\partial \psi} + \frac{\partial}{\partial \psi}\left(\alpha \langle p_z \rangle n_s\right)\right] - \frac{K_z B_0}{\langle n_z \rangle} n_s\Bigg\} v_\parallel^2 f_{i0}. \tag{A.71}$$

Even in the $Z_z \to \infty$ limit, the poloidal variation of the impurity density matters and enters through the $K_z n_c$ and $K_z n_s$ terms. In the plateau regime, most ions are collisionless, requiring $qR\nu_{ii}/v_i \ll 1$. Nevertheless, collisions must be strong enough that no ions are trapped. The ξ boundary layer width, ξ_w is found by balancing streaming with collisions, $\xi_w v_i \sim \nu_{ii} qR/\xi_w^2$, to give the plateau ordering $1 \gg \xi_w \sim (\nu_{ii} qR/v_i)^{1/3} \gg \epsilon^{1/2}$, with $\epsilon^{1/2}$ the trapped fraction.

Once the kinetic equation is in the proper form for the plateau regime, the details of the collision operator do not matter in most situations. However to check, the unlike collision operator Eq. A.23 is used for ion-impurity collisions and the following momentum conserving, model ion-ion collisions operator is employed:

$$C_{ii}\{f_{i1}\} = \frac{3\sqrt{pi}T_i^{3/2}\nu_{ii}}{2M_i^{3/2}}\nabla_v \cdot \left[\nabla_v \nabla_v v \cdot \nabla_v \left(f_{i1} - \frac{M_i}{T_i} W_{\parallel I} v_\parallel f_{i0}\right)\right], \tag{A.72}$$

with

$$W_{\parallel i} = \frac{3T_i \int d^3v \frac{v_\parallel}{v^3} f_{i1}}{M_i \int d^3v \frac{1}{v} f_{i0}} \tag{A.73}$$

and, for $v_\parallel = \xi v$,

$$\nabla_v \cdot \left(\nabla_v \nabla_v v \cdot \nabla_v f\right) = \frac{1}{v^3}\frac{\partial}{\partial \xi}\left[\left(1-\xi^2\right)\frac{\partial f}{\partial \xi}\right]. \tag{A.74}$$

Only the diffusive terms matter in the plateau regime, giving:

$$C_1\{H_1\} = \nu \frac{\partial}{\partial \xi}\left[\left(1-\xi^2\right)\frac{\partial H_1}{\partial \xi}\right] \approx \nu \frac{\partial^2 H_1}{\partial \xi^2}, \tag{A.75}$$

with

$$\nu = \frac{2\sqrt{2\pi}T_i^{3/2}}{4M_i^{3/2}v^3}\left(\sqrt{2}\nu_{ii} + \nu_{iz}\right). \tag{A.76}$$

Then the plateau kinetic equation in v, ξ variables becomes

$$\xi v\frac{\partial H_1}{\partial\vartheta} - \nu q R_0\frac{\partial^2 H_1}{\partial\xi^2} = \mathrm{Im}\big\{(Q_s + \mathrm{i}Q_c)\,\mathrm{e}^{\mathrm{i}\theta}\big\}, \tag{A.77}$$

where the mirror force term, $\frac{\epsilon\mu B_0}{v}\sin\theta\frac{\partial H_1}{\partial\xi} \sim \frac{\epsilon v H_1}{\xi_w}$, is negligible compared to $\xi v\frac{\partial H_1}{\partial\vartheta} \sim \xi_w v H_1$ in the ξ boundary layer of width ξ_w since $\epsilon\,(v_i/\nu_{ii}qR)^{2/3} \ll 1$.

The flux function K_z must be chosen in a manner ensuring ion transport vanishes in the absence of impurities. It is tempting to think of the ion-impurity transport problem as being very much the same as the electron-ion transport problem. Nonetheless, there are important and subtle differences. In particular, impurity collisions cannot modify the ion distribution function when $n_z \to 0$, while the electron distribution is always modified by the ion collisions (see the Appendix of Reference [186] for a summary of the e-i treatment).

Letting $u = \gamma\xi$, defining:

$$\gamma = \left(\frac{v}{\nu q R_0}\right)^{1/3} \gg 1, \tag{A.78}$$

and noting that the localized solution to $\frac{\partial^2 h}{\partial u^2} - \mathrm{i}uh = -1$ is $h = \int_0^\infty dx\mathrm{e}^{-x^3/3-\mathrm{i}ux}$, the plateau kinetic equation solution is found to be:

$$\begin{aligned} H_1 &= \frac{\gamma}{v}\mathrm{Im}\Big\{(Q_s + \mathrm{i}Q_c)\,\mathrm{e}^{\mathrm{i}\theta}\int_0^\infty dx\mathrm{e}^{-x^3/3-\mathrm{i}\gamma\xi x}\Big\} \\ &= \frac{\gamma Q_s}{v}\left[\sin\theta\int_0^\infty dx\mathrm{e}^{-x^3/3}\cos(\gamma\xi x) - \cos\theta\int_0^\infty dx\mathrm{e}^{-x^3/3}\sin(\gamma\xi x)\right] \\ &\quad + \frac{\gamma Q_c}{v}\left[\cos\theta\int_0^\infty dx\mathrm{e}^{-x^3/3}\cos(\gamma\xi x) - \sin\theta\int_0^\infty dx\mathrm{e}^{-x^3/3}\sin(\gamma\xi x)\right], \end{aligned} \tag{A.79}$$

where all $\xi\sqrt{\epsilon}$ ions are collisional and $\xi \sim 1$ ions are collision less. For this solution

$$\gamma\int_{-1}^{1} d\xi\int_0^1 dx\mathrm{e}^{-x^3/3}\cos(\gamma\xi x) = 2\int_0^1 dx\frac{1}{x}\mathrm{e}^{-x^3/3}\sin(\gamma x) \xrightarrow[\gamma\gg 1]{} \pi \tag{A.80}$$

implying

$$\gamma\int_0^1 dx\mathrm{e}^{-x^3/3}\cos(\gamma\xi x) \xrightarrow[\gamma\gg 1]{} \pi\delta(\xi) \tag{A.81}$$

while

$$\gamma\int_{-1}^{1} d\xi\int_0^1 dx\mathrm{e}^{-x^3/3}\sin(\gamma\xi x) = -\int_0^1 dx\frac{1}{x}\mathrm{e}^{-x^3/3}\int_{-1}^{1} d\xi\frac{d}{d\xi}\cos(\gamma\xi x) = 0, \tag{A.82}$$

and

$$\gamma\int_0^1 dx\mathrm{e}^{-x^3/3}\sin(\gamma\xi x) = -\frac{1}{\xi}\int_0^1 dx\mathrm{e}^{-x^3/3}\frac{d}{dx}\cos(\gamma\xi x) \xrightarrow[\gamma\gg 1]{} \frac{1}{\xi} \tag{A.83}$$

To evaluate the integrals needed here, all that is required is:

$$H_1 = Q_s\left[\frac{\pi}{v}\delta(\xi)\sin\theta - \frac{\cos\theta}{v_\parallel}\right] + Q_c\left[\frac{\pi}{v}\delta(\xi)\cos\theta - \frac{\sin\theta}{v_\parallel}\right] \tag{A.84}$$

implying the replacement $C_1\{H_1\} \rightarrow \nu_{\text{eff}} H_1$ with $\nu_{\text{eff}} \sim \nu/\xi_w^2$ can be employed in Eq. A.69.

Only H_1 terms odd in $v_\parallel$ contribute to the friction, giving

$$\int d^3v \frac{v_\parallel H_1}{v^3} = \sin\theta \int d^3v \frac{Q_c}{v^3} - \cos\theta \int d^3v \frac{Q_s}{v^3}, \tag{A.85}$$

where

$$\int d^3v \frac{Q_c}{v^3} = \epsilon \frac{2M_i^{3/2} n_i B_0}{3\sqrt{2\pi} T_i^{3/2} \langle n_z \rangle} \left\{ n_s K_z - \frac{cI}{Z_z e B_0^2} \left[n_s \frac{\partial \langle p_z \rangle}{\partial \psi} + \frac{\partial}{\partial \psi} \left(\alpha \langle p_z \rangle n_s \right) \right] \right\}, \tag{A.86}$$

and

$$\begin{aligned} \int d^3v \frac{Q_s}{v^3} = {} & \epsilon \frac{4cIM_i^{3/2}}{3\sqrt{2\pi} Z_i e T_i^{3/2} B_0} \left(\frac{\partial p_i}{\partial \psi} - \frac{Z_i n_i}{Z_z \langle n_z \rangle} \frac{\partial \langle p_z \rangle}{\partial \psi} - \frac{3}{2} n_i \frac{\partial T_i}{\partial \psi} \right) \\ & - \epsilon \frac{2M_i^{3/2} n_i B_0}{3\sqrt{2\pi} T_i^{3/2} \langle n_z \rangle} \left\{ n_c K_z - \frac{cI}{Z_z e B_0^2} \left[n_c \frac{\partial \langle p_z \rangle}{\partial \psi} + \frac{\partial}{\partial \psi} \left(\alpha \langle p_z \rangle n_c \right) \right] \right\}, \end{aligned} \tag{A.87}$$

where $\partial\epsilon/\partial\psi \approx 1/R_0^2 B_p = q/rR_0B_0$ terms are ignored as unimportant compared to those varying on the radial scale of the pedestal and $\left\langle \frac{1}{B} \int d^3v \frac{v_\parallel}{v^3} H_1 \right\rangle = 0$ for any plateau regime solution. As a result, the parallel impurity momentum equation to order ϵ for plateau regime background ions is:

$$(1 + \alpha n) \frac{\partial n}{\partial \theta} = 2\epsilon (G - D) \cos\theta + (K + D)(n - 1) + D \frac{\partial \left[\alpha \langle p_z \rangle (n-1) \right] / \partial \psi}{\partial \langle p_z \rangle / \partial \psi}; \tag{A.88}$$

exactly the same as for banana regime background ions when $\epsilon \ll 1$ and Eq. A.68 is inserted, implying that A.55 can be used for both regimes! All D terms are local, except $\frac{\partial}{\partial\psi}(n-1)$, since it implicitly leads to second derivatives in radius. The solution n is also local since it depends on radial first derivatives. The full expression for the D terms was not recovered in Reference [187] due to a less accurate treatment of the parallel friction.

A.6 Approximate solutions for impurity density variation and radial particle transport

The parallel impurity momentum equation can be solved in detail if all radial profiles are accurately known. Here, we give approximate solutions for $Z_i/Z_z\epsilon \ll 1$. A $G \sim 1 \sim K \sim Z_z D/Z_i$, in this limit the lowest order parallel impurity momentum equation is simply:

$$(1 + \alpha n) \frac{\partial n}{\partial \theta} = 2\epsilon G \cos\theta + K (n - 1) \tag{A.89}$$

and the solution for both the banana and plateau regime background ions is:

$$n = 1 + 2\epsilon G \frac{(1+\alpha)\sin\theta - K\cos\theta}{(1+\alpha)^2 + K^2}. \tag{A.90}$$

The clear features of the solution are that the sign of G determines the up-down asymmetry. The in-out asymmetry depends on the sign and size of both K and G where the sign of the flux surface averaged poloidal flow gives the sign of K:

$$\frac{\left\langle n_z \vec{V}_z \cdot \nabla\vartheta \right\rangle}{\left\langle \vec{B} \cdot \nabla\vartheta \right\rangle} \approx K_z(\psi) = \frac{\langle p_z \rangle \langle n_z \rangle \left\langle \vec{B} \cdot \nabla\vartheta \right\rangle}{M_i n_i \langle \nu_{iz} \rangle \langle B^2 \rangle} K, \tag{A.91}$$

as $\nabla\vartheta$ and $\nabla\zeta \times \nabla\psi$ are roughly in the same direction and $\vec{B} \cdot \nabla\vartheta \approx \left\langle \vec{B} \cdot \nabla\vartheta \right\rangle$ to lowest order.

Banana regime transport

The large aspect ratio background ion particle flux for banana regime ions colliding with impurities is:

$$\left\langle n_i \vec{V}_i \cdot \nabla\psi \right\rangle = \epsilon^2 \frac{cI \langle p_z \rangle \left\langle \vec{B} \cdot \nabla\vartheta \right\rangle}{Z_i e \langle B^2 \rangle} (2G + n_c K) = \frac{2\epsilon c I (1+\alpha)^2 \langle p_z \rangle \left\langle \vec{B} \cdot \nabla\vartheta \right\rangle G}{Z_i e \langle B^2 \rangle [(1+\alpha)^2 + K^2]} \tag{A.92}$$

.

Here we use:

$$\left\langle \frac{n}{b^2} \right\rangle - 1 = \left\langle \frac{\left(b^2 - 1\right)^2}{b^2} \right\rangle - \left\langle \frac{(n-1)\left(b^2-1\right)}{b^2} \right\rangle \approx (2 + n_c)\,\epsilon^2, \tag{A.93}$$

$$\left\langle nb^2 \right\rangle - 1 = \left\langle (n-1)\left(b^2 - 1\right) \right\rangle \approx n_c \epsilon^2, \tag{A.94}$$

$$\left\langle \frac{n}{b^2} \right\rangle - \frac{1}{\langle nb^2 \rangle} \approx 2\epsilon^2, \tag{A.95}$$

and

$$K = G + \left\langle nb^2 \right\rangle U + D \approx G + U. \tag{A.96}$$

Consequently, the direction of the radial ion particle flux for banana regime background ions depends on the sign of $IG \propto -I^2 \left(2T_i \frac{\partial n_i}{\partial\psi} - n_i \frac{\partial T_i}{\partial\psi}\right)$, while the direction of the poloidal flow is unimportant as only K^2 enters to reduce the transport. When $IG > 0$ or $\eta_i = d\ln T_i / d\ln n_i < 2$ (as in H-mode) the background particle flux is outward, while for $IG < 0$ or $\eta_i = d\ln T_i / d\ln n_i > 2$ (as in I-mode) the background ions are transported inward [177] and provide natural fueling. This desirable $\eta_i > 2$ case is sometimes referred to as temperature screening because the radial flux of impurities is outward [188].

Plateau regime transport

The lowest order expression for the friction used to obtain the parallel impurity momentum equation for the plateau regime background ions is not good enough to evaluate the particle flux since $\left\langle n_z \vec{V}_z \cdot \nabla\psi \right\rangle = \frac{cI}{Z_z e}\left\langle \frac{F_{iz}^{\parallel}}{B} \right\rangle = 0$. As a result, the particle flux for plateau regime ions is negligibly small and K_z must be found from:

$$\left\langle n_i \vec{V}_i \cdot \nabla\psi \right\rangle = \left\langle d^3v f_{i1} \vec{v}_d \cdot \nabla\psi \right\rangle = \left\langle d^3v H_1 \vec{v}_d \cdot \nabla\psi \right\rangle \tag{A.97}$$

where

$$\vec{v}_d \cdot \nabla\psi = I v_\parallel \vec{b} \cdot \nabla \left(\frac{v_\parallel}{\Omega_i} \right) \Bigg|_{E,\mu} \approx -\frac{\epsilon M_i c}{2 Z_i e q} \left(v_\perp^2 + 2 v_\parallel^2 \right) \sin\theta, \tag{A.98}$$

as the poloidal variation of the potential is very weak. Evaluating the integrals by noting only the sin terms even in $v_\parallel$ contribute, with $\left\langle \sin^2\theta \right\rangle = 1/2$ and $d^3v = 2\pi v^2 dv\, d\xi$, yields:

$$\begin{aligned} \left\langle n_i \vec{V}_i \cdot \nabla\psi \right\rangle &= -\frac{\pi\epsilon M_i c}{4 Z_i e q} \int d^3v \; v \delta(\xi) Q_s \\ &= \frac{\sqrt{2\pi}\epsilon^2 I B_0 T_i^{3/2} n_i}{2 q \Omega_0^2 M_i^{3/2}} \left(\frac{1}{p_i}\frac{\partial p_i}{\partial\psi} - \frac{Z_i}{Z_z \langle p_z \rangle} \frac{\partial \langle p_z \rangle}{\partial\psi} + \frac{1}{2T_i}\frac{\partial T_i}{\partial\psi} + \frac{Z_i e B_0^2}{cI \langle p_z \rangle} K_z \right) \end{aligned} \tag{A.99}$$

where $\Omega_0 = Z_i e B_0 / M_i c$. The main ion density and temperature gradient terms give a plateau diffusivity of $q v_i^3 / \Omega_0^2 R$ (which is $M_i^{1/2}/M_e^{1/2} \gg 1$ larger than the electron particle diffusivity).

Comparing the size of the $\partial p_i / \partial\psi$ terms from both ways of evaluating the particle flux and accounting for $\left\langle F_{iz}^{\parallel}/B \right\rangle = 0$ leads to:

$$\frac{(cI/Z_i e)\left\langle F_{iz}^{\parallel}/B \right\rangle}{\left\langle \int d^3v \; H_1 \vec{v}_d \cdot \nabla\psi \right\rangle} \ll \frac{\nu_{iz} q R_0}{\epsilon v_i} \sim \frac{\alpha \nu_{ii} q R_0}{\epsilon v_i}, \tag{A.100}$$

where electron transport is assumed negligible, $\alpha 1$, and $\sqrt{\epsilon} < \nu_{ii} q R / \epsilon v_i < 1/\epsilon$ in the plateau regime. The preceding estimate indicates the need to use $\left\langle \int d^3v \; H_1 \vec{v}_d \cdot \nabla\psi \right\rangle$ to evaluate K_z.

Based on these estimates and the need to maintain ambipolarity between the ions and impurities, the radial ion particle transport must vanish to lowest order:

$$\left\langle n_i \vec{V}_i \cdot \nabla\psi \right\rangle \approx 0, \tag{A.101}$$

thereby determining K_z to be given by:

$$\frac{1}{p_i}\frac{\partial p_i}{\partial\psi} - \frac{Z_i}{Z_z \langle p_z \rangle} \frac{\partial \langle p_z \rangle}{\partial\psi} + \frac{1}{2T_i}\frac{\partial T_i}{\partial\psi} + \frac{Z_i e \langle B^2 \rangle}{cI \langle p_z \rangle} K_z = 0. \tag{A.102}$$

Again, friction seems to be acting to reduce the neoclassical particle flux.

Ignoring poloidally varying terms, the preceding equation inserted into A.40 leads to the lowest order relation between the parallel impurity and background ion flows:

$$V_{\parallel z} \approx -\frac{cI}{B}\frac{\partial \Phi}{\partial \psi} - \frac{cIB}{Z_i e \left\langle B^2 \right\rangle n_i}\left(\frac{\partial p_i}{\partial \psi} + \frac{n_i}{2}\frac{\partial T_i}{\partial \psi}\right) \approx V_{\parallel i}^{\mathrm{plat}}, \tag{A.103}$$

where $V_{\parallel i}^{\mathrm{plat}}$ is the usual plateau expression for the parallel ion flow [172]. All the poloidally varying terms can be evaluated using $n_i V_{\parallel i} = \int d^3 v v_\parallel f_{i1}$ to obtain the full relation between the parallel ion and impurity flows in the plateau regime:

$$V_{\parallel i} - V_{\parallel z} = \frac{1}{n_i}\int d^v v_\parallel H_1 = \frac{1}{n_i}\left(\sin\theta \int d^3 v Q_c - \cos\theta \int d^3 v Q_s\right) \sim \frac{\epsilon v_i \rho_{ip}}{L_\perp}, \tag{A.104}$$

but as there are many terms and they are small in ϵ, they are not given here. These terms account for the difference between the results here and in Reference [168] for $Z_z \to \infty$.

Using the preceding expression for $V_{\parallel z}$ gives a consistency check on the lowest order plateau regime poloidal impurity flow to be:

$$\begin{aligned}\frac{\left\langle n_z \vec{V}_z \cdot \nabla\vartheta \right\rangle}{\left\langle \vec{B} \cdot \nabla\vartheta \right\rangle} \approx K_z(\psi) &= -\frac{cI\left\langle p_z \right\rangle}{Z_i e \left\langle B^2 \right\rangle}\left(\frac{1}{p_i}\frac{\partial p_i}{\partial \psi} - \frac{Z_i}{Z_z \left\langle p_z \right\rangle}\frac{\partial \left\langle p_z \right\rangle}{\partial \psi} + \frac{1}{2T_i}\frac{\delta T_i}{\delta \psi}\right) \\ &\approx -\frac{cI\left\langle p_z \right\rangle}{Z_i e \left\langle B^2 \right\rangle}\left(\frac{1}{p_i}\frac{\partial p_i}{\partial \psi} + \frac{1}{2T_i}\frac{\delta T_i}{\delta \psi}\right).\end{aligned} \tag{A.105}$$

On Alcator C-Mod, a positive poloidal flow ($K > 0$) is typically observed when $I > 0$ [129]. In AUG, when $I < 0$, a negative poloidal flow ($K < 0$) occurs [174], [181].

The plateau solution in Reference [168] is sensibly formulated to recover the standard result without impurities, but to do so it assumes $K_z/n_z = y\left(cI/2Z_i e\left\langle B^2\right\rangle\right)\partial T_i/\partial\psi$ in $V_{\parallel z}$, with the parameter y determined from ambipolarity. This procedure replaces $V_{\parallel z}$ by $V_{\parallel i}$ in f_{i1} so it does not properly account for various poloidally varying drive terms in $C_{iz}\{(V_{\parallel z} - V_{\parallel i})v_\parallel f_{i0}\} \neq 0$, and thereby misses impurity drive terms which require writing $n = 1 + \epsilon(n_c\cos\theta + n_s\sin\theta)$. Moreover, like all plateau regime treatment, Reference [168] should only find H_1 to lowest order in ϵ and be unable to evaluate the radial flux from friction as $\left\langle F_{iz}^{\parallel}/B \right\rangle = 0$.

A.7 Diffusion and convection form of impurity continuity

The diffusion and convection form of the continuity equation is useful for understanding transport. For the banana regime, impurity continuity equation can be cast as:

$$\frac{\partial \left\langle n_z \right\rangle}{\partial t} = \frac{1}{r}\frac{\partial}{\partial r}\left[r\left(D_z\frac{\partial \left\langle n_z \right\rangle}{\partial r} - V_z\left\langle n_z \right\rangle\right)\right] \tag{A.106}$$

.
The small term D must be retained in Eq. A.58 by making the replacement $G \to G - D$ as suggested by Equations A.52 and A.99. The orderings used here imply the particle diffusivity term D_z is less important than the radial convection velocity V_z. Using ambipolarity and

the large aspect ratio approximation $RB_p\frac{\partial}{\partial\psi} \approx \frac{\partial}{\partial r}$ for $|\nabla\psi| = RB_p$ gives the impurity flux as:

$$\left\langle n_z\vec{V}_z \cdot \nabla\psi \right\rangle = -Z_i \left\langle n_i\vec{V}_i \cdot \nabla\psi \right\rangle \approx -RB_p \left(D_z \frac{\partial \langle n_z \rangle}{\partial r} - V_z \langle n_z \rangle \right). \tag{A.107}$$

Then, Eq. A.92 Leads to:

$$D_z = \frac{2\epsilon^2 c^2 M_i p_i \langle \nu_{iz} \rangle}{Z_z^2 e^2 B_p^2 \langle n_z \rangle (1 + K^2)} \tag{A.108}$$

and:

$$\frac{RV_z}{D_z} = -\frac{R}{T_i}\frac{\partial T_i}{\partial r} + \frac{Z_z}{Z_i}\left(\frac{R}{n_i}\frac{\partial n_i}{\partial r} - \frac{R}{2T_i}\frac{\partial T_i}{\partial r}\right) \approx \frac{Z_z}{Z_i}\left(\frac{R}{n_i}\frac{\partial n_i}{\partial r} - \frac{R}{2T_i}\frac{\partial T_i}{\partial r}\right) \tag{A.109}$$

where the diffusivity and the first term in RV_z/D_z are small by Z_i/Z_z. In the diffusion and convection form, the outward diffusion ($\partial \langle n_z \rangle / \partial r < 0$) can be counteracted by a pinch ($V_z < 0$). The convection velocity changes sign at $\eta_i = 2$, with a pinch ($V_z < 0$) for $\eta_i < 2$ and outward $V_z > 0$ for $\eta_i > 2$. The direction of the poloidal flow is unimportant as only K^2 enters. In the plateau regime, the vanishing of the radial impurity diffusion determines the unknown flux function K_z, making the poloidal flow positive ($K > 0$). In this case, it is not possible to write a diffusion-convection form of impurity continuity.

The treatment here and in Reference [164] assumes that in the banana regime, the time for the impurities to diffuse across the magnetic field, $L_\perp^2/D_z$, is large compared to the the time for the impurities to equilibrate along the magnetic field, $q^2R^2\nu_{zz}/v_z^2$. The ratio yields a restriction:

$$1 \gg \frac{q^2R^2\nu_{zz}/v_z^2}{L_\perp^2/D_z} \sim \left(\frac{\rho_{ip}}{L_\perp}\frac{Z_z^2}{Z_i^2}\frac{qR\nu_{ii}}{v_i}\right)^2 \frac{\epsilon^2\alpha}{(Z_z/Z_i)^{3/2}} \sim G^2\frac{\epsilon^2\alpha}{(Z_z/Z_i)^{3/2}}, \tag{A.110}$$

consistent with allowing $G \sim 1$. However, radial impurity convection is Z_z/Z_i faster than diffusion, making the restriction more severe by requiring $G^2\epsilon^2\alpha \ll (Z_z/Z_i)^{1/2}$. In the plateau regime, the time for impurities to diffuse across the field is very long, as the radial transport is negligible, so the impurities are more easily able to equilibrate along the magnetic field.

A.8 Summary

This appendix formulated and solved a pedestal treatment that evaluates the poloidal variation of the impurity density and electrostatic potential, as related by Eq. A.29. The radial transport of main ions and impurities in both the banana and plateau regimes has been evaluated, with the impurity diamagnetic pressure term maintained. Weak poloidal variation in the plasma density is retained, but poloidal variation of ion and impurity temperatures (which are assumed equal) is neglected. This model takes the important assumption that the poloidal ion gyro radius is small compared to the radial pedestal scale lengths. This may not necessarily be true in the pedestal, in which case more advanced treatments are needed [180].

However, the model herein still provides valuable insight by which to understand pedestal impurity distribution and particle fluxes.

The banana and plateau regime treatments are found to have the same parallel impurity momentum equation (A.88) at large aspect ratio when the subtleties of the plateau treatment are taken into account. When the impurity diamagnetic terms are negligible, the banana regime treatment reduces to the original treatment of Reference [164], with a gradient drive term in addition to a second drive term that requires solving the perturbed ion kinetic equation (A.41). This reduced model would also recover the formulation of References [18], [178], [179], in which the drives are the gradient drive term (A.48) and a poloidal flow term (A.50). This poloidal flow term can in principle be determined experimentally with the aid of the CXRS diagnostic.

The new impurity pressure gradient drive terms in the model presented here have the coefficient defined by Eq. A.49 and account for non-local behavior due to drift departure from flux surfaces, which comes from the poloidal variation of the impurity density. All impurity pressure gradient effects are obtained by assuming that the aspect ratio is large. This assumption does not need to be made for the other terms in the banana regime, but must always be made in the plateau regime. The impurity pressure gradient terms provide an additional source of poloidal impurity density variation, as can be seen from Equations A.56 and A.88. However, because $Z_i/Z_z \ll 1$, these terms do not significantly alter the radial transport and poloidal flow in the plateau regime or in the large aspect ratio limit of the banana regime.

Even within the limitations and assumptions of this model, the neoclassical results derived for particle transport and flows provide useful means for understanding and checking experimental measurements. This is true even when the poloidal variation of the impurity density is not strong. In the banana regime, when the gradient coefficient G and the poloidal flow coefficient K are order unity or larger, large poloidal impurity variation occurs. Only these large G and K solutions are presented here. No attempt is made to explain heat fluxes, as they are expected to be a combination of neoclassical shear-regulated turbulent processes [189], [190]. In addition, the Pfirsch-Schlüter regime for the main ions is not considered here as it requires $\rho_{ip}/L_\perp \ll v_i/qR\nu_{ii} \ll 1$, leading to different results [167], [185].

The signs of $I = RB_t$, G (the gradient drive term), and K (the poloidal flow drive term) vary depending on geometry and operation mode. As a summary, notable results are given in Table A.1 for the two directions of magnetic field relative to the Ohmic current: termed aligned (co) and opposed (counter). The entries in this table are based on Equations A.90, A.91, A.92, A.101, and A.105. Additional information follows from the general banana regime solution of Reference [166] in the trace impurity limit, for which:

$$u \approx -\frac{0.33 J I n_i}{M_i \omega_0 B_0} \frac{\partial T_i}{\partial \psi} \tag{A.111}$$

with $J \approx 1 - 1.46\sqrt{\epsilon}$. Based on this $\alpha \ll 1$ limit, $U/I > 0$ for a negative temperature gradient as expected in the pedestal. Consequently, using the lower order solubility constraint, $K = G + U$, in the H-mode limit the poloidal flow is expected to be in the direction of the poloidal magnetic field for $B = RB_t > 0$ and opposite to the poloidal magnetic field for $I = RB_t < 0$. I-mode measurements on Alcator C-Mod [129] and AUG [174] normally find $V_p B_t > 0$, giving $KI > 0$, except perhaps near the last closed flux surface. This leads to co $\vec{B}_p$ flow for $B_t > 0$

and counter $\vec{B}_p$ flow for $B_t < 0$. In making the table, the stronger density gradient limit ($\eta_i < 2$) is presumed to be H-mode, while the weaker density gradient limit ($\eta_i > 2$) is assumed to be I-mode. L-mode has the weakest temperature gradient and poloidal variation in G and K are thought to be very small. Impurity accumulation is then also expected to be very negligible in both the banana and plateau regimes, and banana regime radial transport is expected to be weak. Therefore, L-mode is not considered in the table. The table is based on the results presented here, except for the experimental observation that the poloidal flow term in I-mode makes a negative radial electric field contribution. The results presented in the table indicate that in-out impurity accumulation is a key difference between H-mode and I-mode pedestals, while the sign of the toroidal magnetic field and the poloidal impurity flow are the same ($KI > 0$).

The simplest, large aspect ratio results presented here can be qualitatively compared to experimental results. General aspect ratio results can be obtained from Equations A.60 and A.61 for $|G| \gg 1$, where normally $g = G/K > 0$ in H-mode and $G/K < 0$ is expected in I-mode. In C-Mod, with $I = RB_t > 0$ a positive poloidal flow ($K > 0$) and negative radial impurity pressure gradient ($D > 0$) are measured in H-mode and I-mode [129]. In H-mode at C-Mod, the HFS impurity density is found to be larger than that on the LFS [176], [177], in agreement with our model. The poloidal variations in AUG are weaker than in C-Mod. In AUG, when $I = RB_t < 0$ the poloidal flow is negative in H-mode and I-mode [174]. In H-mode at AUG, the impurity accumulation is on the HFS [181] in agreement with our model. Impurity density variation is weak in I-mode [177], [181]. Based on Eq. A.14, neither the radial electric field nor the electrostatic potential is a flux function. Moreover, the poloidal variation of the impurity density may be responsible for some of the poloidal variation of the poloidal impurity flow, since $n_z\vec{V}_z\cdot\nabla\vartheta/\vec{B}\cdot\nabla\vartheta = L_z(\psi,\vartheta)$ is not a flux function because of impurity pressure gradient terms in Eq. A.38. Then, perhaps the assumption that the impurity flow in the pedestal is confined to a flux surface [182] is inadequate and the poloidally varying radial impurity flow, $n_z\vec{V}_z \cdot \nabla\psi = \Upsilon\vec{B} \cdot \nabla\vartheta$, is playing a role.

Finally, the large aspect ratio results reported here predict up-down asymmetries in the impurity accumulation. We are unable to treat X-points or strong poloidal variation in this model. Normally, the direction of the up-down asymmetry in core L-mode plasmas reverses when the toroidal magnetic field reverses to change the direction of $\vec{B} \times \nabla B$ [191]–[194], with the impurity accumulation usually opposite to $\vec{B} \times \nabla B$ and independent of X-point location. Based on the simple model considered here, pedestal impurity accumulation occurs away from (toward) $\vec{B} \times \nabla B$ drift in H-mode (I-mode) operation. Based on experimental observations, H-mode (I-mode) access is favorable when $\vec{B}\times\nabla B$ drift is towards (away from) the X-point.

Model predictions	**H-mode**: $\eta_i < 2$		**I-mode**: $\eta_i > 2$	
	co $\vec{\mathbf{B}}_\mathbf{t}$ ($I > 0$, $G > 0$)	**counter** $\vec{\mathbf{B}}_\mathbf{t}$ ($I < 0$, $G < 0$)	**co** $\vec{\mathbf{B}}_\mathbf{t}$ ($I > 0$, $G < 0$)	**counter** $\vec{\mathbf{B}}_\mathbf{t}$ ($I < 0$, $G > 0$)
Banana regime radial transport (recall Eq. A.92)	Impurities inward Ions outward	Impurities inward Ions outward	Impurities outward Ions inward	Impurities outward Ions inward
Plateau regime radial transport	negligible	negligible	negligible	negligible
Poloidal impurity flow in banana regime	co $\vec{B}_p$ $K > 0$ implies $U > 0$ in $K = G + U$	counter $\vec{B}_p$ $K > 0$ implies $U > 0$ in $K = G + U$	co $\vec{B}_p$ $V_p B_t > 0$ in Eq. A.14 for $E_r < 0$	counter $\vec{B}_p$ $V_p B_t > 0$ in Eq. A.14 for $E_r < 0$
Poloidal impurity flow in plateau regime (recall Eq. A.105)	co $\vec{B}_p$ since $K > 0$	counter $\vec{B}_p$ since $K < 0$	co $\vec{B}_p$ since $K > 0$	counter $\vec{B}_p$ since $K < 0$
In-out impurity accumulation: banana & plateau	HFS since $K > 0$	HFS since $K < 0$	LFS since $K > 0$	LFS since $K < 0$
Up-down impurity accumulation: banana & plateau	accumulation opposite $\vec{B} \times \nabla B$ direction	accumulation opposite $\vec{B} \times \nabla B$ direction	accumulation in $\vec{B} \times \nabla B$ direction	accumulation in $\vec{B} \times \nabla B$ direction

Table A.1: Summary of notable for the two directions of magnetic field relative to Ohmic current: aligned (co) and opposed (counter), for I-mode and H-mode profiles. Entries are based on Equations A.90, A.91, A.92, A.101, and A.105.

Appendix B

ELM free H-mode pedestal fluctuations

Future fusion reactors will require high energy confinement operation without ELMs, which damage plasma facing components. Several candidate ELM-free high confinement regimes are under exploration at tokamak research facilities around the world. Examples of these regimes include the Enhanced D-α H-mode (EDA H-mode), the Quiescent H-mode (QH-mode), Negative Triangularity (NT) L-mode, and the “Improved” confinement regime (I-mode). This thesis has largely focused on I-mode operation in AUG, reporting on the edge fluctuations unique to this regime using the CECE diagnostic as the primary turbulence measurement tool. In recent years, EDA H-mode, QH-mode, and NT plasmas have also undergone development at AUG. Here we will show examples of CECE edge fluctuation measurements in the EDA H-mode and QH-mode regimes at AUG.

B.1 EDA H-mode

Enhanced D-alpha (EDA) H-mode is a steady-state ELM-free high confinement regime accessed with auxiliary heating above the L to H-mode threshold and high fueling compared to standard ELMy H-modes. This regime was first discovered and extensively studied at Alcator C-Mod [195], and has more recently been developed at AUG [82]. EDA H-mode is characterized by high energy confinement, high pedestal pressure, and low impurity confinement despite the lack of ELMs. Due to the highly beneficial properties of EDA H-mode for future reactor operation, the ability to extrapolate its access and performance is desirable. Cross-machine study of its properties is important for gaining fundamental understanding of the regime.

One of the most prominent characteristics of EDA H-mode is an edge-localized quasi-coherent mode (QCM), which dominates the pedestal fluctuations. The QCM has been studied in detail at C-Mod [196]–[198], and is currently under investigation at AUG. This edge fluctuation is thought to be responsible for a continuous relaxation of edge pressure gradients in place of ELMs, driving a significant particle flux and preventing the accumulation of impurities.

EDA H-mode experiments at AUG feature the QCM across several channels including magnetic, density, and temperature fluctuations. Here, we briefly present an example of the QCM δT_e fluctuation properties captured by CECE. The time histories of the discharge studied are given in Figure B.1. A steady-state phase 3.5-6.0s is used for CECE analysis. The CECE coherence $|\gamma_c(f)|$ spectra at several radial locations are shown in Figure B.2. The QCM is identified in the spectrum as the feature centered at $\sim$ 30 kHz, with a coherence level approaching 1.0. The broadened portion of the spectrum $>$ 60 kHz could be due to background broadband fluctuations, or could be related to the interaction between the QCM and background turbulence.

In CECE coherence spectra, the QCM is observed on channels in the pedestal, as well as channels which map to locations in the core plasma. In Figure B.2, the QCM coherence appears highest in the channels closest to the core. However, reflectometer measurements find no evidence of QCM fluctuations in the core plasma, and magnetics measurements indicate that the QCM is highly localized to the pedestal region [82]. The appearance of the QCM in core channels of ECE diagnostics is therefore in contrast with the mode's expected location. Recent analysis work has shown that refractive effects can explain the appearance of the WCM on core ECE and CECE channels [199].

B.2 QH-mode

The Quiescent H-mode (QH-mode) is typically achieved with counter-current NBI injection and divertor cryopumping for density control. QH-mode was first discovered at DIII-D [200], [201] and has since been reproduced at AUG [202] and the Joint European Torus (JET) [83], and JT60-U [203]. Studies at DIII-D have shown that QH-mode can also be attained with NBI co-injection [204]. QH-mode has highly favorable qualities, including high confinement without ELMs and without impurity accumulation.

An edge electromagnetic fluctuation known as the Edge Harmonic Oscillation (EHO) is thought to regulate the pedestal pressure and expel impurities in place of ELMs [83], [205]. This mode has a low frequency (fundamental f10kHz), with several harmonics typically visible on ECE, magnetics, and reflectometry diagnostics. A high frequency MHD oscillation from 300-450kHz has also been observed in the pedestal of QH-mode plasmas at AUG and JET [83], [206].

The previous studies of QH-mode at AUG occurred prior to 2007 when the machine still had carbon plasma-facing components. Since AUG became a fully tungsten-walled machine, QH-mode has not been reproduced in steady-state. Experiments were performed more recently to assess the possibility of accessing QH-mode on a tungsten-walled machine [207]. The time histories of one such QH-mode development discharge are shown in Figure B.3. A brief QH-mode period is highlighted between 3.5-3.7s. This period is transient and not steady-state, but still displays the characteristic fluctuation features of QH-mode.

Figure B.4 shows CECE coherence spectra during the transient QH-mode period. The EHO fundamental can be seen at around 10 kHz. A broadband mode centered around 90 kHz is also seen in the spectra. The EHO only appears in CECE channels in the edge and pedestal region and has a maximum amplitude at $\rho_{pol} = 0.96$. The broadband mode appears during the same time period as the EHO and is also localized near the pedestal bottom. Figure B.5 shows the $\delta T_e/T_e$ fluctuation amplitude during the QH-mode phase, calculated from CECE. The frequency integration window used for determining $\delta T_e/T_e$ is chosen as 15-250 kHz. This range excludes the EHO fundamental but does include the higher

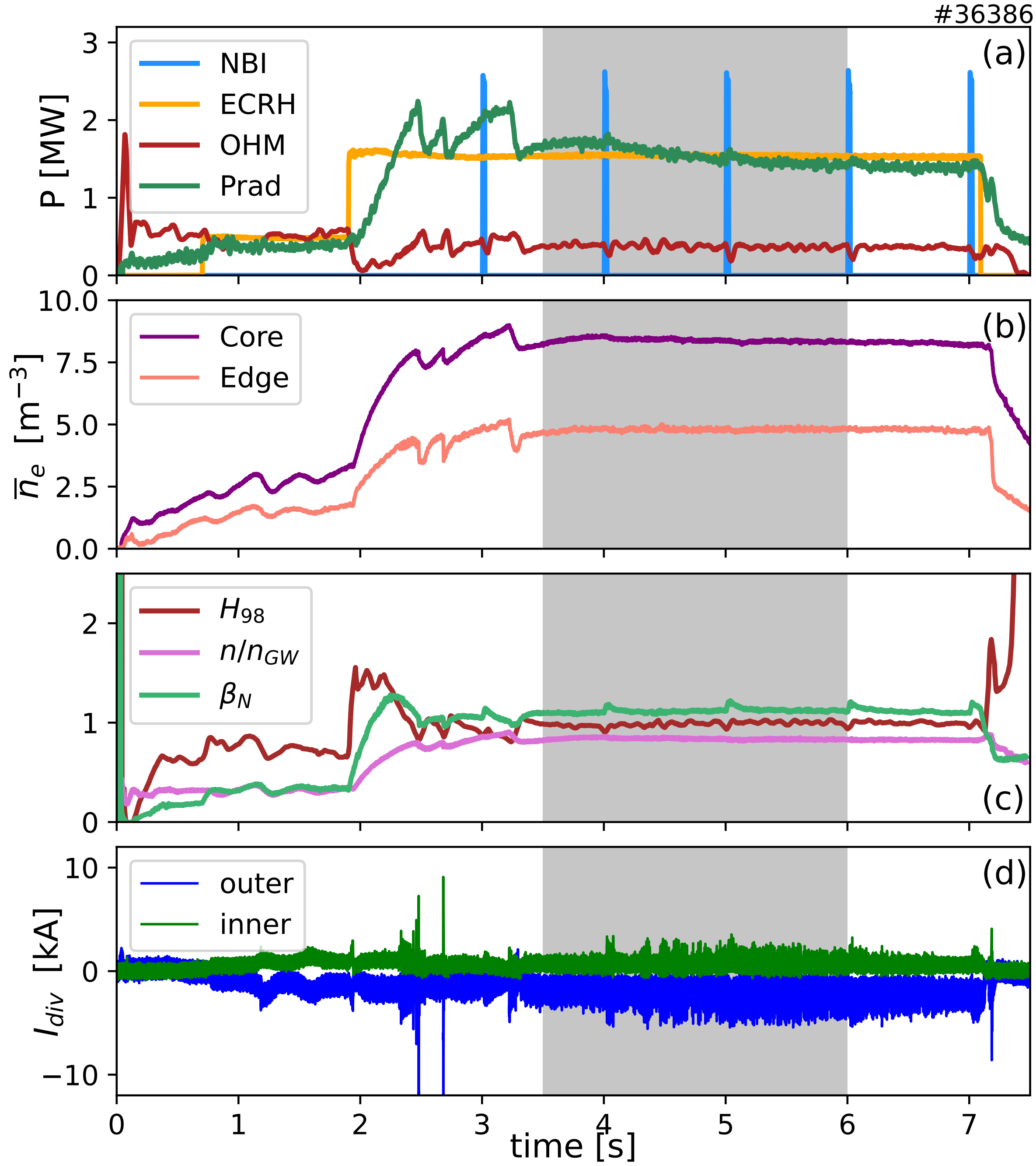

Figure B.1: Time histories of QH-mode development discharge #36386, including (a) Heating and radiated power, (b) core and edge line averaged density, (c) H_{98}, Greenwald fraction, and normalized β_N, and (d) inner and outer divertor shunt current as an ELM marker. A steady-state EDA H-mode phase begins at 3.4s and remains for the remainder of the discharge. The phase used for CECE analysis is shaded.

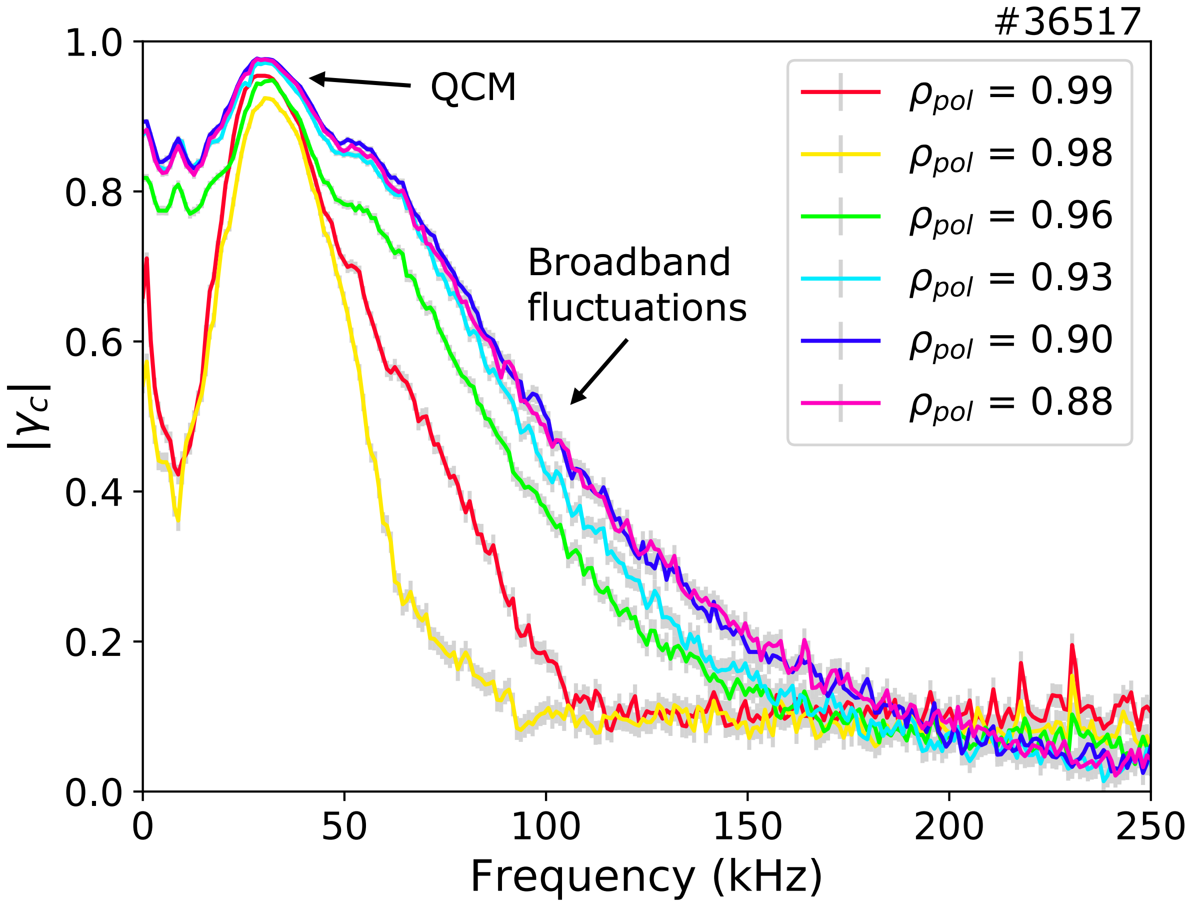

Figure B.2: CECE coherence spectra of outer core edge fluctuations for EDA H-mode discharge #36386, calculated for the time window 3.5-6.0s. The QCM can be seen on all channels, centered at 30 kHz. Broadband fluctuations can be seen in the outer core channels.

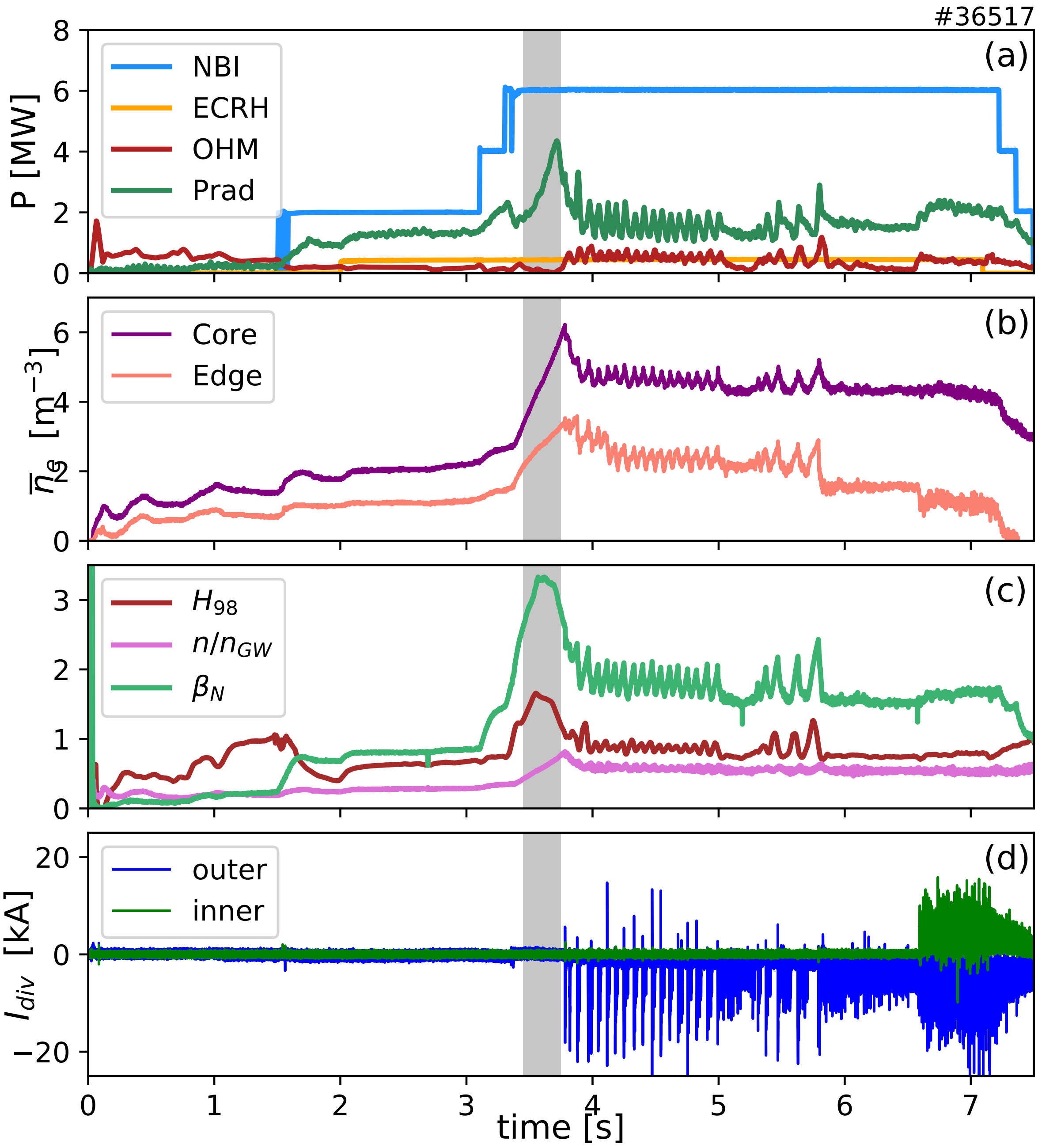

Figure B.3: Time histories of QH-mode development discharge #36517, including (a) Heating and radiated power, (b) core and edge line averaged density, (c) H_{98}, Greenwald fraction, and normalized β_N, and (d) inner and outer divertor shunt current as an ELM marker. A transient QH-mode type period occurs 3.5-3.7s, and this time window is used for CECE analysis.

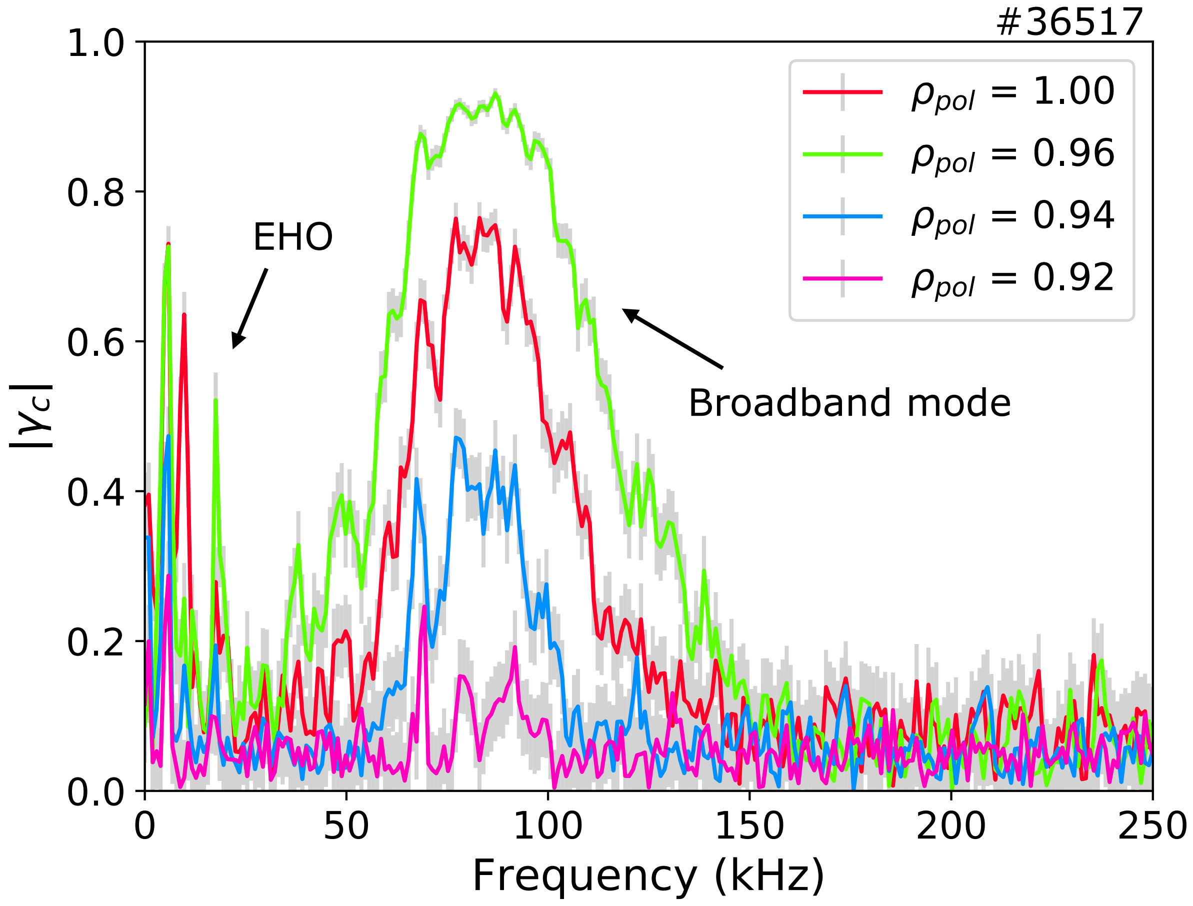

Figure B.4: CECE coherence spectra of outer core edge fluctuations for QH-mode discharge #36399, determined using the time window 3.5-3.7s. The EHO is identified as a coherent mode with a fundamental at 10 kHz. In addition, a broadband mode is seen, centered at 90kHz. The EHO and broadband mode both peak in amplitude at $\rho_{pol} = 0.96$.

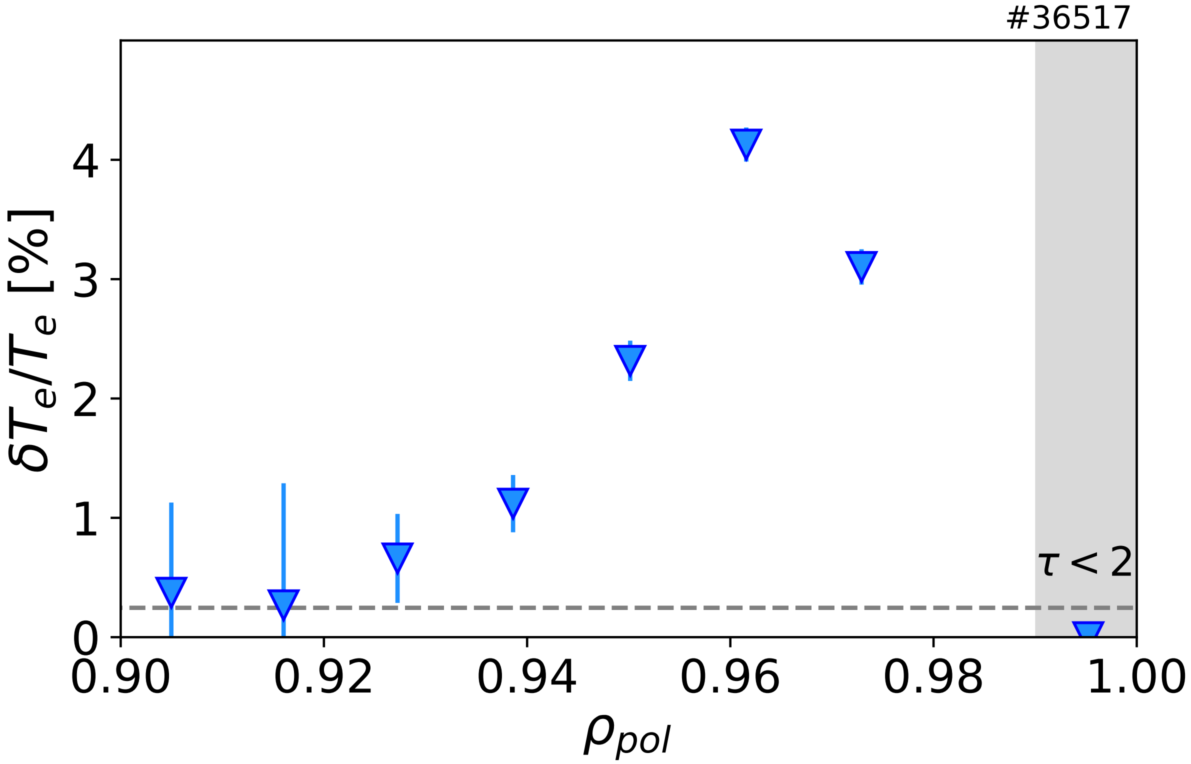

Figure B.5: CECE fluctuation amplitude, calculated from integration of $|\gamma_c|$ spectra, as described in Chapter 3. The integration range was 15-250kHz. The 4.1% fluctuation amplitude near $\rho_{pol} = 0.96$ correlates with the maximum amplitude of the broadband pedestal fluctuation. The region of low optical depth ($\tau < 2$) is shaded.

harmonics, which make negligible contributions to the calculated $\delta T_e/T_e$. The sharp increase of fluctuation amplitude near $\rho_{pol} = 0.96$ is due to the broadband pedestal fluctuation, reaching a maximum fluctuation amplitude of $\delta T_e/T_e = 4.1\%$

The EHO fundamental and harmonics are present on several diagnostics during the transient QH-mode. Figure B.6 shows the autopower spectra from a CECE channel, a Q-band reflectometer, and a Mirnov coil. All three diagnostics display the EHO harmonics at the same frequency.

These preliminary measurements show that CECE can capture characteristic QH-mode pedestal fluctuations and provide useful information about their nature including localization, $\delta T_e/T_e$, and spectral features. It is unclear whether steady-state QH-modes can be achieved on a tungsten-walled device, so study of QH-mode fluctuations may be limited to transient phases at AUG.

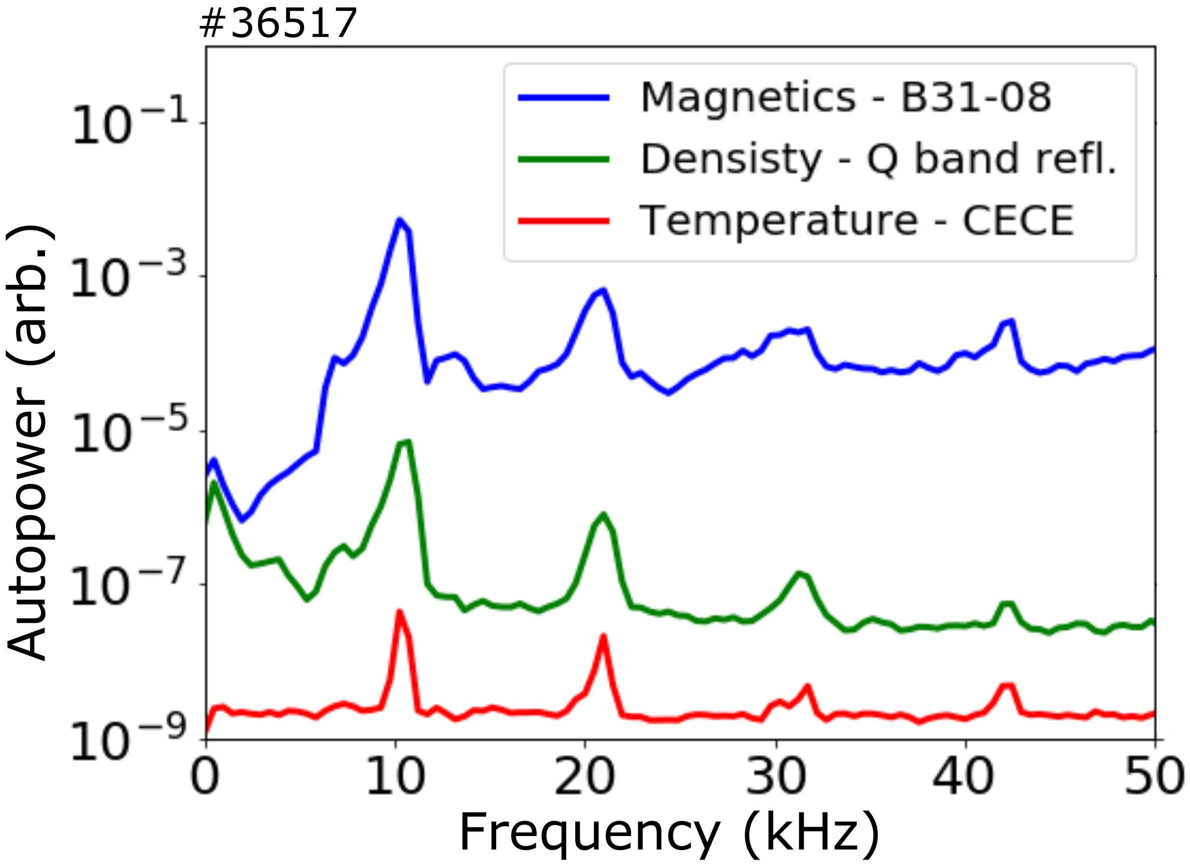

Figure B.6: EHO fundamental and harmonics appear at the same frequency in signals from magnetics (Mirnov coil B31-08), density (Q-band reflectometer) and CECE (pedestal channel) during transient QH-mode phase.

B.3 Summary

CECE measurements from an EDA H-mode discharge and a QH-mode development discharge have been presented. These measurements capture pedestal fluctuations of coherent modes important to the transport of these regimes. In EDA H-mode, CECE coherence spectra capture the QCM. In QH-mode, the EHO is identified, in addition to a higher-frequency broadband pedestal fluctuation. The study of NT plasmas at AUG is a current active area of research [208], [209], and ongoing analysis is likely to provide insight to the nature of edge fluctuations in this regime. Although these regimes were not the focus of the body of this thesis, these measurements point to the study of other ELM-free high confinement regimes with CECE as fruitful pathways for future research.

Appendix C

Data access and analysis tools

This Appendix describes the data analysis and simulation workflows performed in this thesis. Access to several computer systems is needed, as described below.

C.1 Computer access

- Max Planck IPP computing, including access to TOK-I machines for AUG data analysis: `https://www.aug.ipp.mpg.de/wwwaug/documentation/computerIT/`
- MFEWS at the PSFC
- Engaging cluster at MIT: `https://engaging-web.mit.edu/eofe-wiki/`
- NERSC: `https://www.nersc.gov/`
- Cybele and Iris cluster at General Atomics

C.2 AUG experimental data analysis workflow

The python executable files used for AUG data analysis are stored on IPP workstations and contained within the directory: `/shares/users/work/rbiel/thesis`. Important routines for data analysis are stored within:
`/shares/users/work/rbiel/cece_aug_repo`.

C.2.1 CECE analysis

CECE localization

- For an estimation the measurement location of CECE channels, mapping cold resonance positions to the magnetic field equilibrium, `localizations_new.py` within the data analysis repository can be used. The script `anaCECE.py` calls this mapping routine.

- For a calculation of CECE channel warm resonance positions, the ECRad code [103] can be used. Instructions for running ECRad can be found at `https://www.aug.ipp.mpg.de/foswiki/bin/view/CorrelationECE/ECRAd`.

Coherence spectra

Coherence between all selected channels of the CECE comb is performed in: `/shares/users/work/rbiel/cece_aug_repo/analysis/cece_data.py`. The general data analysis plotting tool, which plots coherence spectra and autopower spectra is `anaCECE.py`. Scripts with modified plotting parameters (e.g. channel numbers, frequency limits, shot numbers) have been saved for the coherence plots generated in this thesis.

These include:

- Figure 4.6: `anaCECE_spectra_highne.py` and `anaCECE_spectra_lowne.py`
- Figures 5.4, 5.5, and 5.8: `anaCECE_spectra_fav_unfav.py`
- Figure 6.3: `anaCECE_spectra_lowne.py`
- Figure B.2: `anaCECE_spectra_EDAH.py`
- Figure B.4: `anaCECE_spectra_QH.py`

Fluctuation amplitude calculation

The general fluctuation amplitude plotting tool is `anaCECE_dT.py`. Scripts with modified plotting parameters have been saved for the fluctuation amplitude plots generated in this thesis.

- Figure 4.7: `anaCECE_dT_lowne.py` and `anaCECE_dT_lowne.py`
- Figure B.5: `anaCECE_dT_QH.py`

Long range toroidal correlations

Long range correlations are calculated using the same principles as correlations between radially neighboring CECE channels, but the routines are adjusted to read data from the toroidally separated CECE systems. The long-range correlations represented in Figure 4.11 are performed in `long_range_correlations.py`

Radial correlation length

The calculation of the WCM radial correlation length and peak amplitude represented in text in Table 5.1 is performed in `correlation_length_41285_and_41286.py`.

Spectrograms

Spectrograms shown in Figure 4.4 can be reproduced using `spectrograms_cece.py`.

Bicoherence analysis

The bicoherence calculation is performed in `higherOrderSpectra.py`. These calculations are applied in the following scripts to generate plots for this thesis:

- Figure 4.12: `bispectra_WCM.py`
- Figure 5.9: `bispectra_LIH.py`

C.2.2 nT phase calculations

The α_{nT} calculation used to produce Figure 4.9 can be found in `nTphase.py`.

C.2.3 Thermal Helium beam analysis

The dispersion relation in Figure 4.8 can be reproduced by executing `HEB_plots.py`.

C.2.4 Kinetic profile plotting routines

Several methods of fitting profiles to experimental data are used in this thesis. These methods and the accompanyign routines are described here.

- AUGPED is an in-house profile fitter. It is run by executing "`augped`" in the terminal of an IPP machine. Through choices in the GUI, one can select the data to fit for each profile. The fit can be saved as a shotfile or textfile.
- A Gaussian Process Regression technique is applied to the ion profile fits in Figure 4.2. These calculations are housed at: `AUGPED_GPR_fits.py` and require a saved text file from AUGPED which includes the diagnostic data points.
- The Integrated Data Analysis (IDA) tool is used for preliminary profile analysis. These profiles are stored under the 'IDA' shotfile. Figure 2.9 uses IDA profiles and is generated using the script `profiles_IDA.py`.
- A Monte Carlo Thomson fitting routine is used for the profiles in Chapters 4 and 5. This routine randomly varies Thomson Scattering and CXRS data within their experimental error bars, makes modified hyperbolic tangent fits with each iteration, and makes an average fit based on all iterations.

The scripts used for the profiles in Chapters 4, 5, and 6 are:

- Figure 4.2: `profilesPlot_36561.py` and `profilesPlot_40891and2.py`
- Figure 5.2 and 5.3: `fit_profiles_fav_unfav.py`
- Figure 6.1: `fit_profiles_LI.py`
- Figure 6.12 is reproduced from Chapter 4.

C.2.5 Time history plots

The time history plots which represent an experiment are based on the `CECE_scope.py` script. This script is used for making Figure 3.2. Modified scripts have been saved to generate the figures in Chapters 4, 5, and Appendix B as follows:

- Figure 4.1: `CECE_scope_low_and_highne.py`
- Figure 5.1: `CECE_scope_favunfav.py`
- Figure B.1: `CECE_scope_EDAH.py`
- Figure B.3: `CECE_scope_QH.py`

C.2.6 E_r plots

E_r profiles in this thesis are generated with Doppler reflectometry and the Helium Beam Spectroscopy diagnostics in this thesis. The scipts to generate E_r profile plots are as follows:

- Figure 4.3: `read_Doppler_corrected.py`
- Figures 5.4, 5.5, and 5.7: `read_HES2.py`

C.2.7 AUG vessel and flux surface plots

The AUG vessel and flux surfaces in Figures 2.8, 5.1, and 5.2 are generated with the script: `equ_compare.py`.

C.2.8 L-mode and I-mode H_{98} and ν_{eff} database

The script for reading the shotfiles and performing calculations of H_{98} and ν_{eff} to generate Figure 4.5 is `database_parameters.py`.

C.3 Modeling workflow

C.3.1 TRANSP transport solver

Preparing runs through TRVIEW

On IPP TOK-I worstations, the `trview` gui can be run to generate the TR.DAT and UFILE input files needed for running TRANSP. UFILES can also be created outside of `trview` using the scripts contained within `/shares/users/work/rbiel/thesis/transpTools/`.

Running and interpreting TRANSP through PORTALS

Once the TRANSP input files are created, they are transferred to the MFEWS computers. Here, TRANSP runs may be submitted through the PORTALS framework: `https://portals-tutorial.readthedocs.io/en/latest/` [210].

The following scripts can be executed to run and plot TRANSP runs, as well as use TRANSP output to generate input files needed for TGLF and CGYRO. The scripts are located on MFEWS computers, at `/home/rachelbi/transp/`.

- `run_transp.py` submits TRANSP runs to the PPPL grid and fetches them once complete.
- `plot_transp.py` plots outputs of a TRANSP run in a notebook style.
- `prep_cgyro.py` uses the output of a TRANSP run to generate an input file for TGLF at a selected location, as well as the `input.gacode` file needed for CGYRO simulations.

C.3.2 TGLF

Scripts to run TGLF and plots outputs through the PORTALS framework are stored on MFEWS computers. To run TGLF over a parameter scan and output the heat flux to make Figures 6.19 and 6.20, `/home/rachelbi/TGLF/run_scans.py` is run.

C.3.3 Linear CGYRO simulations

Linear CGYRO is run on the MIT Engaging cluster to determine the growth rate and real frequency of the dominant turbulent mode at a given wavenumber. The GACODE suite (`https://gafusion.github.io/doc/`) must first be built on Engaging. To scan over a range of wavenumber, the program `/pool001/rachelbi/cgyro_scan.pro` is run in IDL. To plot the growth rate and real frequency spectra to produce plots such as Figure 6.5 and 6.21, `/pool001/rachelbi/plot_spectra.py` is then run.

C.3.4 Nonlinear CGYRO simulations

Nonlinear CGYRO is run on NERSC to investigate the saturated state of turbulence and determine turbulent fluxes. The GACODE suite must first be built on NERSC. The `input.cgyro` and `input.gacode` files can be copied over to NERSC from Engaging, resolutions must be adjusted to set the simulation box size and the wavenumber resolution, and the nonlinear flag in the input file must be turned on.

Once runs are complete, to plot the heat flux over simulation time as in Figures 6.6, and 6.7 `cgyro_outputs.py` is run. This script also prints the average heat flux and its standard deviation over a determined period, so it is also used to output the values which are used in Figures 6.8, 6.10, 6.11, 6.13, 6.14, 6.15, 6.16, 6.17, and 6.18.

The snapshot of density fluctuations in Figure 6.22 uses built-in CGYRO plotting routines and is executed by running within the CGYRO output directory:

```
cgyro_plot -plot fluct -t 100 -moment n -s 2.
```

Synthetic CECE diagnostic for CGYRO

A synthetic CECE diagnostic residing on the GA Iris cluster is used for producing Figure 6.23. This tool was designed for validation work on DIII-D [160] and here we use a modified version to match the CECE beam pattern at AUG. In order to use the synthetic diagnostic, the outputs of a nonlinear CGYRO run must be copied over to the Iris machines. The synthetic diagnostic is then run through OMFIT and saved in the project `/home/bielajewr/synCGYRO_tools_AUGedit.zip`.

References

[1] M. Bell, K. McGuire, and et. al, "Overview of DT results from TFTR," *Nuclear Fusion*, vol. 35, no. 12, p. 1429, 1995.

[2] E. Gibney, "Reactor smashes energy record," *Nature*, vol. 602, p. 371, 2022.

[3] A. J. Wootton, B. A. Carreras, H. Matsumoto, K. McGuire, W. A. Peebles, C. P. Ritz, P. W. Terry, and S. J. Zweben, "Fluctuations and anomalous transport in tokamaks," *Physics of Fluids B: Plasma Physics*, vol. 2, no. 12, pp. 2879–2903, Dec. 1, 1990, ISSN: 0899-8221. DOI: 10.1063/1.859358. [Online]. Available: https://doi.org/10.1063/1.859358 (visited on 06/15/2023).

[4] W. Horton, "Drift waves and transport," *Reviews of Modern Physics*, vol. 71, no. 3, pp. 735–778, Apr. 1, 1999. DOI: 10.1103/RevModPhys.71.735. [Online]. Available: https://link.aps.org/doi/10.1103/RevModPhys.71.735.

[5] T. Görler, A. E. White, D. Told, F. Jenko, C. Holland, and T. L. Rhodes, "A flux-matched gyrokinetic analysis of DIII-d l-mode turbulence," *Physics of Plasmas*, vol. 21, no. 12, p. 122 307, Dec. 17, 2014, ISSN: 1070-664X. DOI: 10.1063/1.4904301. [Online]. Available: https://doi.org/10.1063/1.4904301 (visited on 07/08/2023).

[6] T. Görler, A. E. White, D. Told, F. Jenko, C. Holland, and T. L. Rhodes, "On the validation of gyrokinetic l-mode simulations," *Fusion Science and Technology*, vol. 69, no. 2, pp. 537–545, Apr. 1, 2016, ISSN: 1536-1055. DOI: 10.13182/FST15-182. [Online]. Available: https://doi.org/10.13182/FST15-182.

[7] S. Freethy, T. Görler, A. Creely, G. Conway, S. Denk, T. Happel, C. Koenen, P. Hennequin, and A. White, "Validation of gyrokinetic simulations with measurements of electron temperature fluctuations and density-temperature phase angles on ASDEX upgrade," *Physics of Plasmas*, vol. 25, no. 5, p. 055 903, May 1, 2018, ISSN: 1070-664X. DOI: 10.1063/1.5018930. [Online]. Available: https://doi.org/10.1063/1.5018930 (visited on 03/19/2023).

[8] A. E. White, "Validation of nonlinear gyrokinetic transport models using turbulence measurements," *Journal of Plasma Physics*, vol. 85, no. 1, p. 925 850 102, 2019, ISSN: 0022-3778. DOI: 10.1017/S0022377818001253. [Online]. Available: https://www.cambridge.org/core/article/validation-of-nonlinear-gyrokinetic-transport-models-using-turbulence-measurements/D659391275AB4B71D37BEF8BB2241D45.

[9] J. Ruiz Ruiz, W. Guttenfelder, A. E. White, N. T. Howard, J. Candy, Y. Ren, D. R. Smith, N. F. Loureiro, C. Holland, and C. W. Domier, "Validation of gyrokinetic simulations in NSTX and projections for high-k turbulence measurements in NSTX-u," *Physics of Plasmas*, vol. 27, no. 12, p. 122 505, Dec. 8, 2020, ISSN: 1070-664X. DOI: 10.1063/5.0009620. [Online]. Available: https://doi.org/10.1063/5.0009620 (visited on 07/08/2023).

[10] D. Whyte, A. Hubbard, J. Hughes, *et al.*, "I-mode: An h-mode energy confinement regime with l-mode particle transport in alcator c-mod," *Nuclear Fusion*, vol. 50, no. 10, p. 105 005, Oct. 1, 2010, ISSN: 0029-5515. DOI: 10.1088/0029-5515/50/10/105005. [Online]. Available: https://dx.doi.org/10.1088/0029-5515/50/10/105005.

[11] A. Hubbard, D. Whyte, R. Churchill, *et al.*, "Edge energy transport barrier and turbulence in the i-mode regime on alcator c-mod," *Physics of Plasmas*, vol. 18, no. 5, p. 056 115, May 1, 2011, ISSN: 1070-664X. DOI: 10.1063/1.3582135. [Online]. Available: https://doi.org/10.1063/1.3582135 (visited on 02/15/2023).

[12] T. Happel, P. Manz, F. Ryter, *et al.*, "The i-mode confinement regime at ASDEX upgrade: Global properties and characterization of strongly intermittent density fluctuations," *Plasma Physics and Controlled Fusion*, vol. 59, no. 1, p. 014 004, Oct. 18, 2016, ISSN: 0741-3335. DOI: 10.1088/0741-3335/59/1/014004. [Online]. Available: https://dx.doi.org/10.1088/0741-3335/59/1/014004.

[13] B. Coppi and T. Zhou, "Interpretation of the i-regime and transport associated with relevant heavy particle modes," *Physics of Plasmas*, vol. 19, no. 1, p. 012 302, Jan. 1, 2012, Publisher: American Institute of Physics, ISSN: 1070-664X. DOI: 10.1063/1.3671944. [Online]. Available: https://doi.org/10.1063/1.3671944 (visited on 03/13/2023).

[14] Z. Liu, X. Xu, X. Gao, *et al.*, "The physics mechanisms of the weakly coherent mode in the alcator c-mod tokamak," *Physics of Plasmas*, vol. 23, no. 12, p. 120 703, Dec. 1, 2016, ISSN: 1070-664X. DOI: 10.1063/1.4972088. [Online]. Available: https://doi.org/10.1063/1.4972088 (visited on 03/13/2023).

[15] H. Yang, T. Zhou, and Y. Xiao, "Gyrokinetic simulation of turbulent transport for i-mode edge plasmas," *Nuclear Fusion*, vol. 61, no. 5, p. 056 006, Apr. 13, 2021, ISSN: 0029-5515. DOI: 10.1088/1741-4326/abebcd. [Online]. Available: https://dx.doi.org/10.1088/1741-4326/abebcd.

[16] P. Manz, T. Happel, U. Stroth, T. Eich, D. Silvagni, and the ASDEX Upgrade team, "Physical mechanism behind and access to the i-mode confinement regime in tokamaks," *Nuclear Fusion*, vol. 60, no. 9, p. 096 011, Jul. 31, 2020, ISSN: 0029-5515. DOI: 10.1088/1741-4326/ab9e17. [Online]. Available: https://dx.doi.org/10.1088/1741-4326/ab9e17.

[17] P. Terry and D. Newman, "Cross phases of temperature-gradient-driven turbulence as a model basis for i-mode particle transport," *Physics of Plasmas*, vol. 30, no. 10, p. 102 304, Oct. 31, 2023, ISSN: 1070-664X. DOI: 10.1063/5.0159677. [Online]. Available: https://doi.org/10.1063/5.0159677 (visited on 11/18/2023).

[18] S. Espinosa and P. Catto, "Theoretical explanation of i-mode impurity removal and energy confinement," *Plasma Physics and Controlled Fusion*, vol. 60, no. 9, p. 094 001, Jul. 16, 2018, ISSN: 0741-3335. DOI: 10.1088/1361-6587/aad0c9. [Online]. Available: https://dx.doi.org/10.1088/1361-6587/aad0c9.

[19] C. Chen, *Introduction to Plasma Physics and Controlled Fusion*, Second. New Yrok: Plenium Press, 1974.

[20] R. Goldston and P. Rutherford, *Introduction to Plasma Physics* (Plasma Physics Series). CRC Press, 1995.

[21] J. Weiland, *Collective Modes in Inhomogeneous Plasmas: Kinetic and Advanced Fluid Theory* (Series in Plasma Physics). CRC Press, 1999.

[22] P. Diamond, S.-I. Itoh, K. Itoh, and T. Hahm, "Zonal flows in plasma—a review," *Plasma Physics and Controlled Fusion*, vol. 47, no. 5, R35, Apr. 1, 2005, ISSN: 0741-3335. DOI: 10.1088/0741-3335/47/5/R01. [Online]. Available: https://dx.doi.org/10.1088/0741-3335/47/5/R01.

[23] P. Rodriguez-Fernandez, "Perturbative transport experiments and time-dependent modeling in alcator c-mod and DIII-d," Ph.D Thesis, Massachusetts Institute of Technology, 2019, Ph.D. dissertation, Massachusetts Institute of Technology, Cambridge, MA, 2019.

[24] G. Conway, "Turbulence measurements in fusion plasmas," *Plasma Physics and Controlled Fusion*, vol. 50, no. 12, p. 124 026, Nov. 4, 2008, ISSN: 0741-3335. DOI: 10.1088/0741-3335/50/12/124026. [Online]. Available: https://dx.doi.org/10.1088/0741-3335/50/12/124026.

[25] D. Ross, "On standard forms for transport equations and quasilinear fluxes," *Plasma Physics and Controlled Fusion*, vol. 34, no. 2, p. 137, Feb. 1, 1992, ISSN: 0741-3335. DOI: 10.1088/0741-3335/34/2/001. [Online]. Available: https://dx.doi.org/10.1088/0741-3335/34/2/001.

[26] F. Romanelli, "Ion temperature-gradient-driven modes and anomalous ion transport in tokamaks," *Physics of Fluids B: Plasma Physics*, vol. 1, no. 5, pp. 1018–1025, May 1, 1989, ISSN: 0899-8221. DOI: 10.1063/1.859023. [Online]. Available: https://doi.org/10.1063/1.859023 (visited on 06/16/2023).

[27] H. Nordman and J. Weiland, "Transport due to toroidal eta_i mode turbulence in tokamaks," *Nuclear Fusion*, vol. 29, no. 2, p. 251, Feb. 1, 1989, ISSN: 0029-5515. DOI: 10.1088/0029-5515/29/2/008. [Online]. Available: https://dx.doi.org/10.1088/0029-5515/29/2/008.

[28] C. Primmerman, L. Lidsky, and P. Politzer, "Trapped-electron mode in cylindrical geometry," *Physical Review Letters*, vol. 33, no. 16, pp. 957–960, Oct. 14, 1974. DOI: 10.1103/PhysRevLett.33.957. [Online]. Available: https://link.aps.org/doi/10.1103/PhysRevLett.33.957.

[29] F. Ryter, C. Angioni, A. Peeters, F. Leuterer, H.-U. Fahrbach, W. Suttrop, and A. U. Team, "Experimental study of trapped-electron-mode properties in tokamaks: Threshold and stabilization by collisions," *Physical Review Letters*, vol. 95, no. 8, p. 085 001, Aug. 16, 2005. DOI: 10.1103/PhysRevLett.95.085001. [Online]. Available: https://link.aps.org/doi/10.1103/PhysRevLett.95.085001.

[30] W. Horton, B. Hong, and W. Tang, "Toroidal electron temperature gradient driven drift modes," *The Physics of Fluids*, vol. 31, no. 10, pp. 2971–2983, Oct. 1, 1988, ISSN: 0031-9171. DOI: 10.1063/1.866954. [Online]. Available: https://doi.org/10.1063/1.866954 (visited on 06/15/2023).

[31] A. Hirose, "Electron temperature gradient modes in tokamaks," *Physics of Fluids B: Plasma Physics*, vol. 2, no. 4, pp. 850–853, Apr. 1, 1990, ISSN: 0899-8221. DOI: 10.1063/1.859272. [Online]. Available: https://doi.org/10.1063/1.859272 (visited on 06/15/2023).

[32] W. Dorland, F. Jenko, M. Kotschenreuther, and B. Rogers, "Electron temperature gradient turbulence," *Physical Review Letters*, vol. 85, no. 26, pp. 5579–5582, Dec. 25, 2000. DOI: 10.1103/PhysRevLett.85.5579. [Online]. Available: https://link.aps.org/doi/10.1103/PhysRevLett.85.5579.

[33] N. Howard, C. Holland, A. White, M. Greenwald, and J. Candy, "Synergistic cross-scale coupling of turbulence in a tokamak plasma," *Physics of Plasmas*, vol. 21, no. 11, p. 112 510, Nov. 24, 2014, ISSN: 1070-664X. DOI: 10.1063/1.4902366. [Online]. Available: https://doi.org/10.1063/1.4902366 (visited on 06/15/2023).

[34] L. Chen, P. Rutherford, and W. Tang, "Drift-modified tearing instabilities due to trapped electrons," *Physical Review Letters*, vol. 39, no. 8, pp. 460–463, Aug. 22, 1977. DOI: 10.1103/PhysRevLett.39.460. [Online]. Available: https://link.aps.org/doi/10.1103/PhysRevLett.39.460.

[35] J. Connor, S. Cowley, and R. Hastie, "Micro-tearing stability in tokamaks," *Plasma Physics and Controlled Fusion*, vol. 32, no. 10, p. 799, Oct. 1, 1990, ISSN: 0741-3335. DOI: 10.1088/0741-3335/32/10/004. [Online]. Available: https://dx.doi.org/10.1088/0741-3335/32/10/004.

[36] J. Kesner and S. Migliuolo, "Microtearing modes and fast edge fluctuations in alcator c-mod plasmas," *Nuclear Fusion*, vol. 39, no. 2, p. 163, Feb. 1, 1999, ISSN: 0029-5515. DOI: 10.1088/0029-5515/39/2/303. [Online]. Available: https://dx.doi.org/10.1088/0029-5515/39/2/303.

[37] W. Tang, J. Connor, and R. Hastie, "Kinetic-ballooning-mode theory in general geometry," *Nuclear Fusion*, vol. 20, no. 11, p. 1439, Nov. 1, 1980, ISSN: 0029-5515. DOI: 10.1088/0029-5515/20/11/011. [Online]. Available: https://dx.doi.org/10.1088/0029-5515/20/11/011.

[38] C. Cheng, "Kinetic theory of collisionless ballooning modes," *The Physics of Fluids*, vol. 25, no. 6, pp. 1020–1026, Jun. 1, 1982, ISSN: 0031-9171. DOI: 10.1063/1.863858. [Online]. Available: https://doi.org/10.1063/1.863858 (visited on 06/16/2023).

[39] M. Kotschenreuther, X. Liu, D. Hatch, *et al.*, "Gyrokinetic analysis and simulation of pedestals to identify the culprits for energy losses using 'fingerprints'," *Nuclear Fusion*, vol. 59, no. 9, p. 096 001, Jul. 12, 2019, ISSN: 0029-5515. DOI: 10.1088/1741-4326/ab1fa2. [Online]. Available: https://dx.doi.org/10.1088/1741-4326/ab1fa2.

[40] ASDEX Team, "The h-mode of ASDEX," *Nuclear Fusion*, vol. 29, no. 11, p. 1959, Nov. 1, 1989, ISSN: 0029-5515. DOI: 10.1088/0029-5515/29/11/010. [Online]. Available: https://dx.doi.org/10.1088/0029-5515/29/11/010.

[41] U. Plank, "The effect of the radial electric field around the separatrix on the access to the high confinement mode at ASDEX upgrade," Ph.D Thesis, Ludwig Maximilian University of Munich, 2021, Ph.D. dissertation, Ludwig Maximilian University of Munich, Munich, Germany, Oct. 2021.

[42] E. Viezzer, "Radial electric field studies in the plasma edge of ASDEX upgrade," Ph.D Thesis, Ludwig Maximilian University of Munich, 2012, Ph.D. dissertation, Ludwig Maximilian University of Munich, Munich, Germany, 2012.

[43] P. Terry, "Suppression of turbulence and transport by sheared flow," *Reviews of Modern Physics*, vol. 72, no. 1, pp. 109–165, Jan. 1, 2000. DOI: 10.1103/RevModPhys.72.109. [Online]. Available: https://link.aps.org/doi/10.1103/RevModPhys.72.109.

[44] H. Zohm, "Edge localized modes (ELMs)," *Plasma Physics and Controlled Fusion*, vol. 38, no. 2, p. 105, Feb. 1, 1996, ISSN: 0741-3335. DOI: 10.1088/0741-3335/38/2/001. [Online]. Available: https://dx.doi.org/10.1088/0741-3335/38/2/001.

[45] A. Leonard, "Edge-localized-modes in tokamaksa)," *Physics of Plasmas*, vol. 21, no. 9, p. 090 501, Sep. 11, 2014, ISSN: 1070-664X. DOI: 10.1063/1.4894742. [Online]. Available: https://doi.org/10.1063/1.4894742 (visited on 09/03/2023).

[46] H. Biglari, P. H. Diamond, and P. W. Terry, "Influence of sheared poloidal rotation on edge turbulence," *Physics of Fluids B: Plasma Physics*, vol. 2, no. 1, pp. 1–4, Jan. 1, 1990, ISSN: 0899-8221. DOI: 10.1063/1.859529. [Online]. Available: https://doi.org/10.1063/1.859529 (visited on 02/15/2023).

[47] P. H. Diamond and Y.-B. Kim, "Theory of mean poloidal flow generation by turbulence," *Physics of Fluids B: Plasma Physics*, vol. 3, no. 7, pp. 1626–1633, Jul. 1, 1991, ISSN: 0899-8221. DOI: 10.1063/1.859681. [Online]. Available: https://doi.org/10.1063/1.859681 (visited on 06/21/2023).

[48] T. Eich, P. Manz, and the ASDEX Upgrade team, "The separatrix operational space of ASDEX upgrade due to interchange-drift-alfvén turbulence," *Nuclear Fusion*, vol. 61, no. 8, p. 086 017, Jul. 8, 2021, ISSN: 0029-5515. DOI: 10.1088/1741-4326/ac0412. [Online]. Available: https://dx.doi.org/10.1088/1741-4326/ac0412.

[49] G. Conway, A. Smolyakov, and T. Ido, "Geodesic acoustic modes in magnetic confinement devices," *Nuclear Fusion*, vol. 62, no. 1, p. 013 001, Dec. 14, 2021, ISSN: 0029-5515. DOI: 10.1088/1741-4326/ac0dd1. [Online]. Available: https://dx.doi.org/10.1088/1741-4326/ac0dd1.

[50] Y. Martin, T. Takizuka, and I. C. H.-m. T. D. W. Group, "Power requirement for accessing the h-mode in ITER," *Journal of Physics: Conference Series*, vol. 123, p. 012 033, 2008. DOI: 10.1088/1742-6596/123/1/012033.

[51] ITER Physics Expert Group on Confinement and Transport, ITER Physics Expert Group on Confinement Modelling and Database, and ITER Physics Basis Editors, "Chapter 2: Plasma confinement and transport," *Nuclear Fusion*, vol. 39, no. 12, p. 2175, Dec. 1, 1999, ISSN: 0029-5515. DOI: 10.1088/0029-5515/39/12/302. [Online]. Available: https://dx.doi.org/10.1088/0029-5515/39/12/302.

[52] P. Yushmanov, T. Takizuka, K. Riedel, O. Kardaun, J. Cordey, S. Kaye, and D. Post, "Scalings for tokamak energy confinement," *Nuclear Fusion*, vol. 30, no. 10, p. 1999, Oct. 1, 1990, ISSN: 0029-5515. DOI: 10.1088/0029-5515/30/10/001. [Online]. Available: https://dx.doi.org/10.1088/0029-5515/30/10/001.

[53] F. Ryter, R. Fischer, J. Fuchs, *et al.*, "I-mode studies at ASDEX upgrade: L-i and i-h transitions, pedestal and confinement properties," *Nuclear Fusion*, vol. 57, no. 1, p. 016 004, Sep. 28, 2016, ISSN: 0029-5515. DOI: 10.1088/0029-5515/57/1/016004. [Online]. Available: https://dx.doi.org/10.1088/0029-5515/57/1/016004.

[54] U. Plank, D. Brida, G. Conway, *et al.*, "Experimental study of the edge radial electric field in different drift configurations and its role in the access to h-mode at ASDEX upgrade," *Physics of Plasmas*, vol. 30, no. 4, p. 042 513, Apr. 17, 2023, ISSN: 1070-664X. DOI: 10.1063/5.0102763. [Online]. Available: https://doi.org/10.1063/5.0102763 (visited on 04/21/2023).

[55] T. Carlstrom, R. Groebner, C. Fenzi, G. McKee, R. Moyer, and T. Rhodes, "Evidence for the role of velocity shear on the l-h transition in DIII-d," *Plasma Physics and Controlled Fusion*, vol. 44, no. 5, A333, Apr. 29, 2002, ISSN: 0741-3335. DOI: 10.1088/0741-3335/44/5A/335. [Online]. Available: https://dx.doi.org/10.1088/0741-3335/44/5A/335.

[56] H. Meyer, P. Carolan, G. Conway, *et al.*, "H-mode physics of near double null plasmas in MAST and its applications to other tokamaks," *Nuclear Fusion*, vol. 46, no. 1, p. 64, Dec. 14, 2005, ISSN: 0029-5515. DOI: 10.1088/0029-5515/46/1/008. [Online]. Available: https://dx.doi.org/10.1088/0029-5515/46/1/008.

[57] J. Schirmer, G. Conway, H. Zohm, W. Suttrop, and the ASDEX Upgrade Team, "The radial electric field and its associated shear in the ASDEX upgrade tokamak," *Nuclear Fusion*, vol. 46, no. 9, S780, Aug. 17, 2006, ISSN: 0029-5515. DOI: 10.1088/0029-5515/46/9/S13. [Online]. Available: https://dx.doi.org/10.1088/0029-5515/46/9/S13.

[58] L. Vermare, P. Hennequin, C. Honoré, *et al.*, "Formation of the radial electric field profile in the WEST tokamak," *Nuclear Fusion*, vol. 62, no. 2, p. 026 002, Dec. 16, 2021, ISSN: 0029-5515. DOI: 10.1088/1741-4326/ac3c85. [Online]. Available: https://dx.doi.org/10.1088/1741-4326/ac3c85.

[59] L. Aho-Mantila, M. Wischmeier, H. Müller, S. Potzel, D. Coster, X. Bonnin, G. Conway, and the ASDEX Upgrade Team, "Outer divertor of ASDEX upgrade in low-density l-mode discharges in forward and reversed magnetic field: I. comparison between measured plasma conditions and SOLPS5.0 code calculations," *Nuclear Fusion*, vol. 52, no. 10, p. 103 006, Aug. 20, 2012, ISSN: 0029-5515. DOI: 10.1088/0029-5515/52/10/103006. [Online]. Available: https://dx.doi.org/10.1088/0029-5515/52/10/103006.

[60] A. Chankin, E. Delabie, G. Corrigan, D. Harting, C. Maggi, H. Meyer, and JET Contributors, "EDGE2d-EIRENE modelling of near SOL er: Possible impact on the h-mode power threshold," *Plasma Physics and Controlled Fusion*, vol. 59, no. 4, p. 045 012, Mar. 9, 2017, ISSN: 0741-3335. DOI: 10.1088/1361-6587/aa5ecc. [Online]. Available: https://dx.doi.org/10.1088/1361-6587/aa5ecc.

[61] B. LaBombard, J. Rice, A. Hubbard, *et al.*, "Transport-driven scrape-off layer flows and the x-point dependence of the l-h power threshold in alcator c-mod," *Physics of Plasmas*, vol. 12, no. 5, p. 056 111, May 1, 2005, ISSN: 1070-664X. DOI: 10.1063/1.1876294. [Online]. Available: https://doi.org/10.1063/1.1876294 (visited on 02/15/2023).

[62] T. Versloot, P. de Vries, C. Giroud, *et al.*, "Momentum losses by charge exchange with neutral particles in h-mode discharges at JET," *Plasma Physics and Controlled Fusion*, vol. 53, no. 6, p. 065 017, Apr. 14, 2011, ISSN: 0741-3335. DOI: 10.1088/0741-3335/53/6/065017. [Online]. Available: https://dx.doi.org/10.1088/0741-3335/53/6/065017.

[63] R. Brzozowski, F. Jenko, R. Bilato, and M. Cavedon, "A geometric model of ion orbit loss under the influence of a radial electric field," *Physics of Plasmas*, vol. 26, no. 4, p. 042 511, Apr. 1, 2019, ISSN: 1070-664X. DOI: 10.1063/1.5075613. [Online]. Available: https://doi.org/10.1063/1.5075613 (visited on 04/05/2023).

[64] P. Manz, A. Stegmeir, B. Schmid, T. Ribeiro, G. Birkenmeier, N. Fedorczak, S. Garland, K. Hallatschek, M. Ramisch, and B. Scott, "Magnetic configuration effects on the reynolds stress in the plasma edge," *Physics of Plasmas*, vol. 25, no. 7, p. 072 508, Jul. 1, 2018, ISSN: 1070-664X. DOI: 10.1063/1.5037511. [Online]. Available: https://doi.org/10.1063/1.5037511 (visited on 04/05/2023).

[65] N. Fedorczak, P. Ghendrih, P. Hennequin, G. Tynan, P. Diamond, and P. Manz, "Dynamics of tilted eddies in a transversal flow at the edge of tokamak plasmas and the consequences for l–h transition," *Plasma Physics and Controlled Fusion*, vol. 55, no. 12, p. 124 024, Nov. 28, 2013, ISSN: 0741-3335. DOI: 10.1088/0741-3335/55/12/124024. [Online]. Available: https://dx.doi.org/10.1088/0741-3335/55/12/124024.

[66] F. Ryter, W. Suttrop, B. Brüsehaber, *et al.*, "H-mode power threshold and transition in ASDEX upgrade," *Plasma Physics and Controlled Fusion*, vol. 40, no. 5, p. 725, May 1, 1998, ISSN: 0741-3335. DOI: 10.1088/0741-3335/40/5/032. [Online]. Available: https://dx.doi.org/10.1088/0741-3335/40/5/032.

[67] A. Marinoni, J. Rost, M. Porkolab, *et al.*, "Characterization of density fluctuations during the search for an i-mode regime on the DIII-d tokamak," *Nuclear Fusion*, vol. 55, no. 9, p. 093 019, Aug. 17, 2015, ISSN: 0029-5515. DOI: 10.1088/0029-5515/55/9/093019. [Online]. Available: https://dx.doi.org/10.1088/0029-5515/55/9/093019.

[68] X. Feng, A. Liu, C. Zhou, *et al.*, "I-mode investigation on the experimental advanced superconducting tokamak," *Nuclear Fusion*, vol. 59, no. 9, p. 096 025, Jul. 29, 2019, ISSN: 0029-5515. DOI: 10.1088/1741-4326/ab28a7. [Online]. Available: https://dx.doi.org/10.1088/1741-4326/ab28a7.

[69] A. Hubbard, S.-G. Baek, D. Brunner, *et al.*, "Physics and performance of the i-mode regime over an expanded operating space on alcator c-mod," *Nuclear Fusion*, vol. 57, no. 12, p. 126 039, Oct. 4, 2017, ISSN: 0029-5515. DOI: 10.1088/1741-4326/aa8570. [Online]. Available: https://dx.doi.org/10.1088/1741-4326/aa8570.

[70] D. Silvagni, T. Eich, T. Happel, *et al.*, "I-mode pedestal relaxation events at ASDEX upgrade," *Nuclear Fusion*, vol. 60, no. 12, p. 126 028, Oct. 14, 2020, ISSN: 0029-5515. DOI: 10.1088/1741-4326/abb423. [Online]. Available: https://dx.doi.org/10.1088/1741-4326/abb423.

[71] R. Fischer, C. Fuchs, B. Kurzan, W. Suttrop, and E. Wolfrum, "Integrated data analysis of profile diagnostics at ASDEX upgrade," *Fusion Science and Technology*, vol. 58, no. 2, pp. 675–684, Oct. 1, 2010, ISSN: 1536-1055. DOI: 10.13182/FST10-110. [Online]. Available: https://doi.org/10.13182/FST10-110.

[72] T. Happel, M. Griener, D. Silvagni, *et al.*, "Stationarity of i-mode operation and i-mode divertor heat fluxes on the ASDEX upgrade tokamak," *Nuclear Materials and Energy*, vol. 18, pp. 159–165, Jan. 1, 2019, ISSN: 2352-1791. DOI: 10.1016/j.nme.2018.12.022. [Online]. Available: https://www.sciencedirect.com/science/article/pii/S2352179118301017.

[73] W. McCarthy, "The low frequency edge oscillation in alcator c-mod and ASDEX upgrade i-mode," Ph.D. dissertation, Massachusetts Institute of Technology, Cambridge, MA, May 2022.

[74] I. Cziegler, P. Diamond, N. Fedorczak, *et al.*, "Fluctuating zonal flows in the i-mode regime in alcator c-mod," *Physics of Plasmas*, vol. 20, no. 5, p. 055 904, May 1, 2013, ISSN: 1070-664X. DOI: 10.1063/1.4803914. [Online]. Available: https://doi.org/10.1063/1.4803914 (visited on 02/15/2023).

[75] A. White, N. Howard, A. Creely, *et al.*, "Nonlinear gyrokinetic simulations of the i-mode high confinement regime and comparisons with experiment," *Physics of Plasmas*, vol. 22, no. 5, p. 056 109, May 1, 2015, ISSN: 1070-664X. DOI: 10.1063/1.4921150. [Online]. Available: https://aip.scitation.org/doi/abs/10.1063/1.4921150 (visited on 02/21/2023).

[76] A. J. Creely, N. T. Howard, P. Rodriguez-Fernandez, *et al.*, “Validation of nonlinear gyrokinetic simulations of l- and i-mode plasmas on alcator c-mod,” *Physics of Plasmas*, vol. 24, no. 5, p. 056 104, May 1, 2017, ISSN: 1070-664X. DOI: 10.1063/1.4977466. [Online]. Available: https://doi.org/10.1063/1.4977466 (visited on 02/21/2023).

[77] X. Liu, M. Kotschenreuther, D. Hatch, S. Mahajan, J. Hughes, and A. Hubbard, “Gyrokinetics investigations of an i-mode pedestal on alcator c-mod,” *arXiv*, 2020. DOI: 10.48550/ARXIV.2005.08924.

[78] B. Coppi and T. Zhou, “Heavy particle modes and signature of the i-regime,” *Physics Letters A*, vol. 375, no. 32, pp. 2916–2920, Jul. 25, 2011, ISSN: 0375-9601. DOI: 10.1016/j.physleta.2011.06.018. [Online]. Available: https://www.sciencedirect.com/science/article/pii/S0375960111007274.

[79] U. Stroth, D. Aguiam, E. Alessi, *et al.*, “Progress from ASDEX upgrade experiments in preparing the physics basis of ITER operation and DEMO scenario development,” *Nuclear Fusion*, vol. 62, no. 4, p. 042 006, Mar. 15, 2022, ISSN: 0029-5515. DOI: 10.1088/1741-4326/ac207f. [Online]. Available: https://dx.doi.org/10.1088/1741-4326/ac207f.

[80] M. Bernert, T. Eich, A. Kallenbach, *et al.*, “The h-mode density limit in the full tungsten ASDEX upgrade tokamak,” *Plasma Physics and Controlled Fusion*, vol. 57, no. 1, p. 014 038, Nov. 28, 2014, ISSN: 0741-3335. DOI: 10.1088/0741-3335/57/1/014038. [Online]. Available: https://dx.doi.org/10.1088/0741-3335/57/1/014038.

[81] P. Sauter, T. Pütterich, F. Ryter, *et al.*, “L- to h-mode transitions at low density in ASDEX upgrade,” *Nuclear Fusion*, vol. 52, no. 1, p. 012 001, Dec. 5, 2011, ISSN: 0029-5515. DOI: 10.1088/0029-5515/52/1/012001. [Online]. Available: https://dx.doi.org/10.1088/0029-5515/52/1/012001.

[82] L. Gil, C. Silva, T. Happel, *et al.*, “Stationary ELM-free h-mode in ASDEX upgrade,” *Nuclear Fusion*, vol. 60, no. 5, p. 054 003, Apr. 6, 2020, ISSN: 0029-5515. DOI: 10.1088/1741-4326/ab7d1b. [Online]. Available: https://dx.doi.org/10.1088/1741-4326/ab7d1b.

[83] W. Suttrop, V. Hynönen, T. Kurki-Suonio, *et al.*, “Studies of the ‘quiescent h-mode’ regime in ASDEX upgrade and JET,” *Nuclear Fusion*, vol. 45, no. 7, p. 721, Jul. 5, 2005, ISSN: 0029-5515. DOI: 10.1088/0029-5515/45/7/021. [Online]. Available: https://dx.doi.org/10.1088/0029-5515/45/7/021.

[84] P. Molina Cabrera, P. Rodriguez-Fernandez, T. Görler, *et al.*, “Isotope effects on energy transport in the core of ASDEX-upgrade tokamak plasmas: Turbulence measurements and model validation,” *Physics of Plasmas*, vol. 30, no. 8,

[85] H. Murmann, S. Götsch, H. Röhr, H. Salzmann, and K. H. Steuer, “The thomson scattering systems of the ASDEX upgrade tokamak,” *Review of Scientific Instruments*, vol. 63, no. 10, pp. 4941–4943, Oct. 1, 1992, ISSN: 0034-6748. DOI: 10.1063/1.1143504. [Online]. Available: https://doi.org/10.1063/1.1143504 (visited on 06/04/2023).

[86] B. Kurzan and H. Murmann, "Edge and core thomson scattering systems and their calibration on the ASDEX upgrade tokamak," *Review of Scientific Instruments*, vol. 82, no. 10, p. 103 501, Oct. 4, 2011, ISSN: 0034-6748. DOI: 10.1063/1.3643771. [Online]. Available: https://doi.org/10.1063/1.3643771 (visited on 05/15/2023).

[87] H. Hartfuss, T. Geist, and M. Hirsch, "Heterodyne methods in millimetre wave plasma diagnostics with applications to ECE, interferometry and reflectometry," *Plasma Physics and Controlled Fusion*, vol. 39, no. 11, p. 1693, Nov. 1, 1997, ISSN: 0741-3335. DOI: 10.1088/0741-3335/39/11/001. [Online]. Available: https://dx.doi.org/10.1088/0741-3335/39/11/001.

[88] S. Rathgeber, L. Barrera, T. Eich, R. Fischer, B. Nold, W. Suttrop, M. Willensdorfer, E. Wolfrum, and the ASDEX Upgrade Team, "Estimation of edge electron temperature profiles via forward modelling of the electron cyclotron radiation transport at ASDEX upgrade," *Plasma Physics and Controlled Fusion*, vol. 55, no. 2, p. 025 004, Dec. 21, 2012, ISSN: 0741-3335. DOI: 10.1088/0741-3335/55/2/025004. [Online]. Available: https://dx.doi.org/10.1088/0741-3335/55/2/025004.

[89] E. Viezzer, T. Pütterich, R. Dux, R. McDermott, and ASDEX Upgrade Team, "High-resolution charge exchange measurements at ASDEX upgrade," *Review of Scientific Instruments*, vol. 83, no. 10, p. 103 501, Oct. 2, 2012, ISSN: 0034-6748. DOI: 10.1063/1.4755810. [Online]. Available: https://doi.org/10.1063/1.4755810 (visited on 05/15/2023).

[90] R. McDermott, A. Lebschy, B. Geiger, *et al.*, "Extensions to the charge exchange recombination spectroscopy diagnostic suite at ASDEX upgrade," *Review of Scientific Instruments*, vol. 88, no. 7, p. 073 508, Jul. 19, 2017, ISSN: 0034-6748. DOI: 10.1063/1.4993131. [Online]. Available: https://doi.org/10.1063/1.4993131 (visited on 05/15/2023).

[91] G. Conway, C. Angioni, R. Dux, F. Ryter, A. Peeters, J. Schirmer, C. Troester, CFN Reflectometry Group, and the ASDEX Upgrade team, "Observations on core turbulence transitions in ASDEX upgrade using doppler reflectometry," *Nuclear Fusion*, vol. 46, no. 9, S799, Aug. 17, 2006, ISSN: 0029-5515. DOI: 10.1088/0029-5515/46/9/S15. [Online]. Available: https://dx.doi.org/10.1088/0029-5515/46/9/S15.

[92] T. Happel, A. B. Navarro, G. Conway, *et al.*, "Core turbulence behavior moving from ion-temperature-gradient regime towards trapped-electron-mode regime in the ASDEX upgrade tokamak and comparison with gyrokinetic simulation," *Physics of Plasmas*, vol. 22, no. 3, p. 032 503, Mar. 1, 2015, ISSN: 1070-664X. DOI: 10.1063/1.4914153. [Online]. Available: https://doi.org/10.1063/1.4914153 (visited on 03/19/2023).

[93] A. Dinklage, H. Dreier, R. Fischer, S. Gori, R. Preuss, and U. Toussaint, "Integrated data analysis for fusion: A bayesian tutorial for fusion diagnosticians," *AIP Conference Proceedings*, vol. 988, no. 1, pp. 471–480, Mar. 12, 2008, ISSN: 0094-243X. DOI: 10.1063/1.2905117. [Online]. Available: https://doi.org/10.1063/1.2905117 (visited on 06/04/2023).

[94] I. Hutchinson, *Principles of Plasma Diagnostics*. Cambridge University Press, 2002, ISBN: 978-0-511-61363-0.

[95] A. Creely, S. Freethy, W. Burke, G. Conway, R. Leccacorvi, W. Parkin, D. Terry, and A. White, "Correlation electron cyclotron emission diagnostic and improved calculation of turbulent temperature fluctuation levels on ASDEX upgrade," *Review of Scientific Instruments*, vol. 89, no. 5, p. 053 503, May 1, 2018, ISSN: 0034-6748. DOI: 10.1063/1.5005507. [Online]. Available: https://doi.org/10.1063/1.5005507 (visited on 02/15/2023).

[96] J. Bendat and A. Piersol, *Random Data: Analysis and Measurement Procedures*, Fourth. John Wiley & Sons, Inc., 2010, ISBN: 978-1-118-03242-8.

[97] D. Smith, E. Powers, and G. Caldwell, "Fast-fourier-transform spectral-analysis techniques as a plasma fluctuation diagnostic tool," *IEEE Transactions on Plasma Science*, vol. 2, no. 4, pp. 261–272, Dec. 1974, ISSN: 1939-9375. DOI: 10.1109/TPS.1974.4316849.

[98] G. Cima, R. Bravenec, A. Wootton, T. Rempel, R. Gandy, C. Watts, and M. Kwon, "Core temperature fluctuations and related heat transport in the texas experimental tokamak-upgrade," *Physics of Plasmas*, vol. 2, no. 3, pp. 720–726, Mar. 1, 1995, ISSN: 1070-664X. DOI: 10.1063/1.871423. [Online]. Available: https://doi.org/10.1063/1.871423 (visited on 09/04/2023).

[99] C. Watts, Y. In, J. Heard, P. Phillips, A. Lynn, A. Hubbard, and R. Gandy, "Upper limit on turbulent electron temperature fluctuations in the core of alcator c-mod," *Nuclear Fusion*, vol. 44, no. 9, p. 987, Aug. 5, 2004, ISSN: 0029-5515. DOI: 10.1088/0029-5515/44/9/007. [Online]. Available: https://dx.doi.org/10.1088/0029-5515/44/9/007.

[100] M. Bornatici, F. Engelmann, S. Novak, and V. Petrillo, "Absorption of a plasma of finite density around the electron cyclotron harmonics," *Plasma Physics*, vol. 23, no. 12, p. 1127, Dec. 1, 1981, ISSN: 0032-1028. DOI: 10.1088/0032-1028/23/12/003. [Online]. Available: https://dx.doi.org/10.1088/0032-1028/23/12/003.

[101] M. Bornatici, R. Cano, O. De Barbieri, and F. Engelmann, "Electron cyclotron emission and absorption in fusion plasmas," *Nuclear Fusion*, vol. 23, no. 9, p. 1153, Sep. 1, 1983, ISSN: 0029-5515. DOI: 10.1088/0029-5515/23/9/005. [Online]. Available: https://dx.doi.org/10.1088/0029-5515/23/9/005.

[102] B. Tobias, M. Austin, J. Boom, K. Burrell, I. Classen, C. Domier, N. Luhmann Jr., R. Nazikian, and P. Snyder, "ECE-imaging of the h-mode pedestal (invited)a)," *Review of Scientific Instruments*, vol. 83, no. 10, 10E329, Jul. 17, 2012, ISSN: 0034-6748. DOI: 10.1063/1.4733742. [Online]. Available: https://doi.org/10.1063/1.4733742 (visited on 05/24/2023).

[103] S. Denk, R. Fischer, H. Smith, *et al.*, "Analysis of electron cyclotron emission with extended electron cyclotron forward modeling," *Plasma Physics and Controlled Fusion*, vol. 60, no. 10, p. 105 010, Sep. 7, 2018, ISSN: 0741-3335. DOI: 10.1088/1361-6587/aadb2f. [Online]. Available: https://dx.doi.org/10.1088/1361-6587/aadb2f.

[104] T. Rempel, R. Gandy, and A. Wootton, "Density fluctuation effects on electron cyclotron emission correlation measurements in optically gray plasmas," *Review of Scientific Instruments*, vol. 65, no. 6, pp. 2044–2048, Jun. 1, 1994, ISSN: 0034-6748. DOI: 10.1063/1.1144810. [Online]. Available: https://doi.org/10.1063/1.1144810 (visited on 03/19/2023).

[105] K. Borrass, "Assessment of the impact of cyclotron emission on the performance of next-generation tokamaks in the presence of an absorbing wall," *Fusion Technology*, vol. 16, no. 2, pp. 172–184, Sep. 1, 1989, ISSN: 0748-1896. DOI: 10.13182/FST89-A29146. [Online]. Available: https://doi.org/10.13182/FST89-A29146.

[106] J. Hillesheim, W. Peebles, T. Rhodes, L. Schmitz, A. White, and T. Carter, "New plasma measurements with a multichannel millimeter-wave fluctuation diagnostic system in the DIII-d tokamak (invited)a)," *Review of Scientific Instruments*, vol. 81, no. 10, p. 10D907, Oct. 6, 2010, ISSN: 0034-6748. DOI: 10.1063/1.3466900. [Online]. Available: https://doi.org/10.1063/1.3466900 (visited on 06/01/2023).

[107] A. E. White, W. A. Peebles, T. L. Rhodes, *et al.*, "Measurements of the cross-phase angle between density and electron temperature fluctuations and comparison with gyrokinetic simulations," *Physics of Plasmas*, vol. 17, no. 5, p. 056 103, May 1, 2010, ISSN: 1070-664X. DOI: 10.1063/1.3323084. [Online]. Available: https://doi.org/10.1063/1.3323084 (visited on 03/19/2023).

[108] J. Hillesheim, J. DeBoo, W. Peebles, *et al.*, "Observation of a critical gradient threshold for electron temperature fluctuations in the DIII-d tokamak," *Physical Review Letters*, vol. 110, no. 4, p. 045 003, Jan. 23, 2013. DOI: 10.1103/PhysRevLett.110.045003. [Online]. Available: https://link.aps.org/doi/10.1103/PhysRevLett.110.045003.

[109] T. Rhodes, W. Peebles, E. Doyle, P. Pribyl, M. Gilmore, R. Moyer, and R. Lehmer, "Signal amplitude effects on reflectometer studies of density turbulence in tokamaks," *Plasma Physics and Controlled Fusion*, vol. 40, no. 4, p. 493, Apr. 1, 1998, ISSN: 0741-3335. DOI: 10.1088/0741-3335/40/4/005. [Online]. Available: https://dx.doi.org/10.1088/0741-3335/40/4/005.

[110] G. Conway, "2d modelling of radial correlation reflectometry," *Plasma Physics and Controlled Fusion*, vol. 39, no. 3, p. 407, 1997, ISSN: 0741-3335. DOI: 10.1088/0741-3335/39/3/006. [Online]. Available: https://dx.doi.org/10.1088/0741-3335/39/3/006.

[111] G. Conway, "2d physical optics simulation of fluctuation reflectometry," presented at the 3rd International Reflectometer Workshop for Fusion Plasmas, Informes Técnicos Ciemat, 1997, p. 39.

[112] G. Conway, "Effects of reflectometer asymmetries on fluctuation measurements," *Plasma Physics and Controlled Fusion*, vol. 41, no. 1, p. 65, Jan. 1, 1999, ISSN: 0741-3335. DOI: 10.1088/0741-3335/41/1/005. [Online]. Available: https://dx.doi.org/10.1088/0741-3335/41/1/005.

[113] M. Griener, J. M. Burgos, M. Cavedon, *et al.*, "Qualification and implementation of line ratio spectroscopy on helium as plasma edge diagnostic at ASDEX upgrade," *Plasma Physics and Controlled Fusion*, vol. 60, no. 2, p. 025 008, Dec. 14, 2017, ISSN: 0741-3335. DOI: 10.1088/1361-6587/aa97e8. [Online]. Available: https://dx.doi.org/10.1088/1361-6587/aa97e8.

[114] M. Griener, E. Wolfrum, M. Cavedon, R. Dux, V. Rohde, M. Sochor, J. Muñoz Burgos, O. Schmitz, and U. Stroth, "Helium line ratio spectroscopy for high spatiotemporal resolution plasma edge profile measurements at ASDEX upgrade (invited)," *Review of Scientific Instruments*, vol. 89, no. 10, p. 10D102, Oct. 1, 2018, ISSN: 0034-6748. DOI: 10.1063/1.5034446. [Online]. Available: https://doi.org/10.1063/1.5034446 (visited on 03/19/2023).

[115] X. Garbet, Y. Idomura, L. Villard, and T. Watanabe, "Gyrokinetic simulations of turbulent transport," *Nuclear Fusion*, vol. 50, no. 4, p. 043 002, Mar. 16, 2010, ISSN: 0029-5515. DOI: 10.1088/0029-5515/50/4/043002. [Online]. Available: https://dx.doi.org/10.1088/0029-5515/50/4/043002.

[116] P. Catto, W. Tang, and D. Baldwin, "Generalized gyrokinetics," *Plasma Physics*, vol. 23, no. 7, p. 639, Jul. 1, 1981, ISSN: 0032-1028. DOI: 10.1088/0032-1028/23/7/005. [Online]. Available: https://dx.doi.org/10.1088/0032-1028/23/7/005.

[117] E. Frieman and L. Chen, "Nonlinear gyrokinetic equations for low-frequency electromagnetic waves in general plasma equilibria," *The Physics of Fluids*, vol. 25, no. 3, pp. 502–508, Mar. 1, 1982, ISSN: 0031-9171. DOI: 10.1063/1.863762. [Online]. Available: https://doi.org/10.1063/1.863762 (visited on 06/09/2023).

[118] G. Howes, S. Cowley, W. Dorland, G. Hammett, E. Quataert, and A. Schekochihin, "Astrophysical gyrokinetics: Basic equations and linear theory," *The Astrophysical Journal*, vol. 651, no. 1, p. 590, Nov. 1, 2006, ISSN: 0004-637X. DOI: 10.1086/506172. [Online]. Available: https://dx.doi.org/10.1086/506172.

[119] A. Brizard and T. Hahm, "Foundations of nonlinear gyrokinetic theory," *Reviews of Modern Physics*, vol. 79, no. 2, pp. 421–468, Apr. 2, 2007, Publisher: American Physical Society. DOI: 10.1103/RevModPhys.79.421. [Online]. Available: https://link.aps.org/doi/10.1103/RevModPhys.79.421.

[120] J. Candy, E. Belli, and R. Bravenec, "A high-accuracy eulerian gyrokinetic solver for collisional plasmas," *Journal of Computational Physics*, vol. 324, pp. 73–93, Nov. 1, 2016, ISSN: 0021-9991. DOI: 10.1016/j.jcp.2016.07.039. [Online]. Available: https://www.sciencedirect.com/science/article/pii/S0021999116303400.

[121] H. Sugama, T.-H. Watanabe, and M. Nunami, "Linearized model collision operators for multiple ion species plasmas and gyrokinetic entropy balance equations," *Physics of Plasmas*, vol. 16, no. 11, p. 112 503, Nov. 4, 2009, ISSN: 1070-664X. DOI: 10.1063/1.3257907. [Online]. Available: https://doi.org/10.1063/1.3257907 (visited on 06/08/2023).

[122] P. Helander and D. Sigmar, *Collisional Transport in Magnetized Plasmas*. Cambridge: Cambridge University Press, 2005, ISBN: 978-0-521-02098-5.

[123] G. Staebler, J. Kinsey, and R. Waltz, "Gyro-landau fluid equations for trapped and passing particles," *Physics of Plasmas*, vol. 12, no. 10, p. 102 508, Oct. 10, 2005, ISSN: 1070-664X. DOI: 10.1063/1.2044587. [Online]. Available: https://doi.org/10.1063/1.2044587 (visited on 06/07/2023).

[124] G. Staebler, J. Kinsey, and R. Waltz, "A theory-based transport model with comprehensive physics," *Physics of Plasmas*, vol. 14, no. 5, p. 055 909, May 11, 2007, ISSN: 1070-664X. DOI: 10.1063/1.2436852. [Online]. Available: https://doi.org/10.1063/1.2436852 (visited on 04/23/2023).

[125] G. Staebler, J. Candy, N. Howard, and C. Holland, "The role of zonal flows in the saturation of multi-scale gyrokinetic turbulence," *Physics of Plasmas*, vol. 23, no. 6, p. 062 518, Jun. 29, 2016, ISSN: 1070-664X. DOI: 10.1063/1.4954905. [Online]. Available: https://doi.org/10.1063/1.4954905 (visited on 06/07/2023).

[126] G. Staebler, N. Howard, J. Candy, and C. Holland, "A model of the saturation of coupled electron and ion scale gyrokinetic turbulence," *Nuclear Fusion*, vol. 57, no. 6, p. 066 046, May 9, 2017, ISSN: 0029-5515. DOI: 10.1088/1741-4326/aa6bee. [Online]. Available: https://dx.doi.org/10.1088/1741-4326/aa6bee.

[127] G. Staebler, E. A. Belli, J. Candy, J. Kinsey, H. Dudding, and B. Patel, "Verification of a quasi-linear model for gyrokinetic turbulent transport," *Nuclear Fusion*, vol. 61, no. 11, p. 116 007, Sep. 23, 2021, ISSN: 0029-5515. DOI: 10.1088/1741-4326/ac243a. [Online]. Available: https://dx.doi.org/10.1088/1741-4326/ac243a.

[128] A. White, P. Phillips, D. Whyte, A. Hubbard, C. Sung, J. Hughes, A. Dominguez, J. Terry, and I. Cziegler, "Electron temperature fluctuations associated with the weakly coherent mode in the edge of i-mode plasmas," *Nuclear Fusion*, vol. 51, no. 11, p. 113 005, Oct. 12, 2011, ISSN: 0029-5515. DOI: 10.1088/0029-5515/51/11/113005. [Online]. Available: https://dx.doi.org/10.1088/0029-5515/51/11/113005.

[129] C. Theiler, R. Churchill, B. Lipschultz, *et al.*, "Inboard and outboard radial electric field wells in the h- and i-mode pedestal of alcator c-mod and poloidal variations of impurity temperature," *Nuclear Fusion*, vol. 54, no. 8, p. 083 017, Jun. 18, 2014, ISSN: 0029-5515. DOI: 10.1088/0029-5515/54/8/083017. [Online]. Available: https://dx.doi.org/10.1088/0029-5515/54/8/083017.

[130] R. Bielajew and P. Catto, "Poloidal impurity asymmetries, flow and transport in conventional neoclassical pedestals in the plateau and banana regimes," *Journal of Plasma Physics*, vol. 89, no. 4, 2023.

[131] R. Bielajew, G. Conway, M. Griener, *et al.*, "Edge turbulence measurements in l-mode and i-mode at ASDEX upgrade," *Physics of Plasmas*, vol. 29, no. 5, p. 052 504, May 1, 2022, ISSN: 1070-664X. DOI: 10.1063/5.0088062. [Online]. Available: https://doi.org/10.1063/5.0088062 (visited on 02/15/2023).

[132] R. McDermott, C. Angioni, G. Conway, R. Dux, E. Fable, R. Fischer, T. Pütterich, F. Ryter, E. Viezzer, and the ASDEX Upgrade Team, "Core intrinsic rotation behaviour in ASDEX upgrade ohmic l-mode plasmas," *Nuclear Fusion*, vol. 54, no. 4, p. 043 009, Mar. 12, 2014, ISSN: 0029-5515. DOI: 10.1088/0029-5515/54/4/043009. [Online]. Available: https://dx.doi.org/10.1088/0029-5515/54/4/043009.

[133] R. Fischer, A. Dinklage, and E. Pasch, "Bayesian modelling of fusion diagnostics," *Plasma Physics and Controlled Fusion*, vol. 45, no. 7, p. 1095, May 30, 2003, ISSN: 0741-3335. DOI: 10.1088/0741-3335/45/7/304. [Online]. Available: https://dx.doi.org/10.1088/0741-3335/45/7/304.

[134] G. Conway, J. Schirmer, S. Klenge, W. Suttrop, E. Holzhauer, and the ASDEX Upgrade Team, "Plasma rotation profile measurements using doppler reflectometry," *Plasma Physics and Controlled Fusion*, vol. 46, no. 6, p. 951, Apr. 27, 2004, ISSN: 0741-3335. DOI: 10.1088/0741-3335/46/6/003. [Online]. Available: https://dx.doi.org/10.1088/0741-3335/46/6/003.

[135] L. Frassinetti, M. Beurskens, S. Saarelma, *et al.*, "Global and pedestal confinement and pedestal structure in dimensionless collisionality scans of low-triangularity h-mode plasmas in JET-ILW," *Nuclear Fusion*, vol. 57, no. 1, p. 016 012, Oct. 11, 2016, ISSN: 0029-5515. DOI: 10.1088/0029-5515/57/1/016012. [Online]. Available: https://dx.doi.org/10.1088/0029-5515/57/1/016012.

[136] F. Ryter, C. Angioni, G. Tardini, *et al.*, "The upgraded ASDEX upgrade contribution to the ITPA confinement database: Description and analysis," *Nuclear Fusion*, vol. 61, no. 4, p. 046 030, Mar. 17, 2021, ISSN: 0029-5515. DOI: 10.1088/1741-4326/abe4b0. [Online]. Available: https://dx.doi.org/10.1088/1741-4326/abe4b0.

[137] J. Walk, "Pedestal structure and stability in high-performance plasmas on alcator c-mod," Ph.D Thesis, Massachusetts Institue of Technology, 2014, Ph.D. dissertation, Massachusetts Institute of Technology, Cambridge, MA, 2014.

[138] A. Hubbard, B. Carreras, R. Boivin, J. Hughes, E. Marmar, D. Mossessian, and S. Wukitch, "Variation of edge gradients with heat flux across l-h and h-l transitions in alcator c-mod," *Plasma Physics and Controlled Fusion*, vol. 44, no. 5, A359, Apr. 29, 2002, ISSN: 0741-3335. DOI: 10.1088/0741-3335/44/5A/338. [Online]. Available: https://dx.doi.org/10.1088/0741-3335/44/5A/338.

[139] C. Theiler, J. L. Terry, E. Edlund, I. Cziegler, R. M. Churchill, J. W. Hughes, B. LaBombard, T. Golfinopoulos, and the Alcator C-Mod Team, "Radial localization of edge modes in alcator c-mod pedestals using optical diagnostics," *Plasma Physics and Controlled Fusion*, vol. 59, no. 2, p. 025 016, Jan. 17, 2017, ISSN: 0741-3335. DOI: 10.1088/1361-6587/aa52e5. [Online]. Available: https://dx.doi.org/10.1088/1361-6587/aa52e5.

[140] J. M. Beall, Y. C. Kim, and E. J. Powers, "Estimation of wavenumber and frequency spectra using fixed probe pairs," *Journal of Applied Physics*, vol. 53, no. 6, pp. 3933–3940, Jun. 1, 1982, ISSN: 0021-8979. DOI: 10.1063/1.331279. [Online]. Available: https://doi.org/10.1063/1.331279 (visited on 03/19/2023).

[141] D. Silvagni, J. Terry, W. McCarthy, *et al.*, "I-mode pedestal relaxation events in the alcator c-mod and ASDEX upgrade tokamaks," *Nuclear Fusion*, vol. 62, no. 3, p. 036 004, Jan. 19, 2022, ISSN: 0029-5515. DOI: 10.1088/1741-4326/ac4296. [Online]. Available: https://dx.doi.org/10.1088/1741-4326/ac4296.

[142] Z. Yan, G. McKee, L. Schmitz, P. Gohil, S. Haskey, and D.-D. Team, "Turbulence characteristics and flow dynamics impacts on the h-mode transition in favourable magnetic geometry with lower power threshold," vol. 381, no. 2242, Jan. 2, 2023.

[143] R. Bielajew, U. Plank, G. Conway, A. Hubbard, P. Rodriguez-Fernandez, B. Vanovac, C. Yoo, and A. White, "Edge radiated temperature fluctuations across confinement regime transitions in favorable and unfavorable drift configurations at ASDEX upgrade (accepted)," *Nuclear Fusion*, 2023.

[144] P. Manz, P. Lauber, V. Nikolaeva, *et al.*, "Geodesic oscillations and the weakly coherent mode in the i-mode of ASDEX upgrade," *Nuclear Fusion*, vol. 55, no. 8, p. 083 004, Jun. 30, 2015, ISSN: 0029-5515. DOI: 10.1088/0029-5515/55/8/083004. [Online]. Available: https://dx.doi.org/10.1088/0029-5515/55/8/083004.

[145] I. Cziegler, A. Hubbard, J. Hughes, J. Terry, and G. Tynan, "Turbulence nonlinearities shed light on geometric asymmetry in tokamak confinement transitions," *Phys. Rev. Lett.*, vol. 118, no. 10, p. 105 003, Mar. 2017. DOI: 10.1103/PhysRevLett.118.105003. [Online]. Available: https://link.aps.org/doi/10.1103/PhysRevLett.118.105003.

[146] M. Xu, G. Tynan, P. Diamond, *et al.*, "Frequency-resolved nonlinear turbulent energy transfer into zonal flows in strongly heated l-mode plasmas in the HL-2a tokamak," *Phys. Rev. Lett.*, vol. 108, no. 24, p. 245 001, Jun. 2012. DOI: 10.1103/PhysRevLett.108.245001. [Online]. Available: https://link.aps.org/doi/10.1103/PhysRevLett.108.245001.

[147] A. White, M. Barnes, A. Dominguez, *et al.*, "Reduction of core turbulence in i-mode plasmas in alcator c-mod," *Nuclear Fusion*, vol. 54, no. 8, p. 083 019, Jun. 26, 2014, ISSN: 0029-5515. DOI: 10.1088/0029-5515/54/8/083019. [Online]. Available: https://dx.doi.org/10.1088/0029-5515/54/8/083019.

[148] O. Sauter, S. Brunner, D. Kim, *et al.*, "On the non-stiffness of edge transport in l-mode tokamak plasmasa)," *Physics of Plasmas*, vol. 21, no. 5, p. 055 906, May 21, 2014, ISSN: 1070-664X. DOI: 10.1063/1.4876612. [Online]. Available: https://doi.org/10.1063/1.4876612 (visited on 04/20/2023).

[149] T. Rhodes, C. Holland, S. Smith, *et al.*, "L-mode validation studies of gyrokinetic turbulence simulations via multiscale and multifield turbulence measurements on the DIII-d tokamak," *Nuclear Fusion*, vol. 51, no. 6, p. 063 022, May 13, 2011, ISSN: 0029-5515. DOI: 10.1088/0029-5515/51/6/063022. [Online]. Available: https://dx.doi.org/10.1088/0029-5515/51/6/063022.

[150] C. Holland, L. Schmitz, T. Rhodes, *et al.*, "Advances in validating gyrokinetic turbulence models against l- and h-mode plasmas a)," *Physics of Plasmas*, vol. 18, no. 5, p. 056 113, May 9, 2011, ISSN: 1070-664X. DOI: 10.1063/1.3574518. [Online]. Available: https://doi.org/10.1063/1.3574518 (visited on 04/20/2023).

[151] J. Chowdhury, W. Wan, Y. Chen, S. E. Parker, R. J. Groebner, C. Holland, and N. Howard, "Study of the l-mode tokamak plasma "shortfall" with local and global nonlinear gyrokinetic f particle-in-cell simulation," *Physics of Plasmas*, vol. 21, no. 11, p. 112 503, Nov. 6, 2014, ISSN: 1070-664X. DOI: 10.1063/1.4901031. [Online]. Available: https://doi.org/10.1063/1.4901031 (visited on 04/20/2023).

[152] A. Liu, X. Zou, M. Han, *et al.*, "Experimental identification of edge temperature ring oscillation and alternating turbulence transitions near the pedestal top for sustaining stationary i-mode," *Nuclear Fusion*, vol. 60, no. 12, p. 126 016, Sep. 30, 2020, ISSN: 0029-5515. DOI: 10.1088/1741-4326/abb14a. [Online]. Available: https://dx.doi.org/10.1088/1741-4326/abb14a.

[153] K. Stimmel, A. Bañón Navarro, T. Happel, D. Told, T. Görler, E. Wolfrum, J. Martin Collar, R. Fischer, P. Schneider, and F. Jenko, "Gyrokinetic investigation of the ASDEX upgrade i-mode pedestal," *Physics of Plasmas*, vol. 26, no. 12, p. 122 504, Dec. 1, 2019, ISSN: 1070-664X. DOI: 10.1063/1.5124986. [Online]. Available: https://doi.org/10.1063/1.5124986 (visited on 02/21/2023).

[154] D. R. Hatch, M. J. Pueschel, F. Jenko, W. M. Nevins, P. W. Terry, and H. Doerk, "Magnetic stochasticity and transport due to nonlinearly excited subdominant microtearing modes," *Physics of Plasmas*, vol. 20, no. 1, p. 012 307, Jan. 31, 2013, ISSN: 1070-664X. DOI: 10.1063/1.4789448. [Online]. Available: https://doi.org/10.1063/1.4789448 (visited on 04/22/2023).

[155] J. Kinsey, R. Waltz, and J. Candy, "The effect of safety factor and magnetic shear on turbulent transport in nonlinear gyrokinetic simulations," *Physics of Plasmas*, vol. 13, no. 2, p. 022 305, Feb. 8, 2006, ISSN: 1070-664X. DOI: 10.1063/1.2169804. [Online]. Available: https://doi.org/10.1063/1.2169804 (visited on 04/23/2023).

[156] N. Howard, C. Holland, A. White, M. Greenwald, J. Candy, and A. Creely, "Multi-scale gyrokinetic simulations: Comparison with experiment and implications for predicting turbulence and transport," *Physics of Plasmas*, vol. 23, no. 5, p. 056 109, Apr. 20, 2016, ISSN: 1070-664X. DOI: 10.1063/1.4946028. [Online]. Available: https://doi.org/10.1063/1.4946028 (visited on 04/23/2023).

[157] A. Creely, P. Rodriguez-Fernandez, G. Conway, S. Freethy, N. Howard, A. White, and the ASDEX Upgrade Team, "Criteria for the importance of multi-scale interactions in turbulent transport simulations," *Plasma Physics and Controlled Fusion*, vol. 61, no. 8, p. 085 022, Jun. 25, 2019, Publisher: IOP Publishing, ISSN: 0741-3335. DOI: 10.1088/1361-6587/ab24ae. [Online]. Available: https://dx.doi.org/10.1088/1361-6587/ab24ae.

[158] S. Maeyama, Y. Idomura, T.-H. Watanabe, M. Nakata, M. Yagi, N. Miyato, A. Ishizawa, and M. Nunami, "Cross-scale interactions between electron and ion scale turbulence in a tokamak plasma," *Physical Review Letters*, vol. 114, no. 25, p. 255 002, Jun. 23, 2015. DOI: 10.1103/PhysRevLett.114.255002. [Online]. Available: https://link.aps.org/doi/10.1103/PhysRevLett.114.255002.

[159] T. Neiser, F. Jenko, T. Carter, L. Schmitz, D. Told, G. Merlo, A. Bañón Navarro, P. Crandall, G. R. McKee, and Z. Yan, "Gyrokinetic GENE simulations of DIII-d near-edge l-mode plasmas," *Physics of Plasmas*, vol. 26, no. 9, p. 092 510, Sep. 24, 2019, ISSN: 1070-664X. DOI: 10.1063/1.5052047. [Online]. Available: https://doi.org/10.1063/1.5052047 (visited on 04/25/2023).

[160] N. Howard, P. Rodriguez-Fernandez, C. Holland, *et al.*, "Simultaneous reproduction of experimental kinetic profiles, fluxes, transport coefficients, and turbulence characteristics via nonlinear gyrokinetic profile predictions in a DIII-d ITER similar shape plasma," *Physics of Plasmas*, 2023.

[161] P. Manz, D. Silvagni, O. Grover, T. Happel, T. Eich, M. Griener, and ASDEX Upgrade Team, "Gyrofluid simulation of an i-mode pedestal relaxation event," *Physics of Plasmas*, vol. 28, no. 10, p. 102 502, Oct. 4, 2021, ISSN: 1070-664X. DOI: 10.1063/5.0059295. [Online]. Available: https://doi.org/10.1063/5.0059295 (visited on 06/29/2023).

[162] F. Laggner, A. Diallo, M. Cavedon, and E. Kolemen, "Inter-ELM pedestal localized fluctuations in tokamaks: Summary of multi-machine observations," *Nuclear Materials and Energy*, vol. 19, pp. 479–486, May 1, 2019, ISSN: 2352-1791. DOI: 10.1016/j.nme.2019.02.030. [Online]. Available: https://www.sciencedirect.com/science/article/pii/S2352179118301911.

[163] L. Schmitz, A. E. White, T. A. Carter, W. A. Peebles, T. L. Rhodes, K. H. Burrell, W. Solomon, and G. M. Staebler, "Observation of reduced electron-temperature fluctuations in the coreof h-mode plasmas," *Physical Review Letters*, vol. 100, no. 3, p. 035 002, Jan. 23, 2008. DOI: 10.1103/PhysRevLett.100.035002. [Online]. Available: https://link.aps.org/doi/10.1103/PhysRevLett.100.035002.

[164] P. Helander, "Bifurcated neoclassical particle transport," *Physics of Plasmas*, vol. 5, no. 11, pp. 3999–4004, Nov. 1, 1998, ISSN: 1070-664X. DOI: 10.1063/1.873121. [Online]. Available: https://doi.org/10.1063/1.873121 (visited on 07/10/2023).

[165] M. Romanelli and M. Ottaviani, "Effects of density asymmetries on heavy impurity transport in a rotating tokamak plasma," *Plasma Physics and Controlled Fusion*, vol. 40, no. 10, p. 1767, Oct. 1, 1998, ISSN: 0741-3335. DOI: 10.1088/0741-3335/40/10/007. [Online]. Available: https://dx.doi.org/10.1088/0741-3335/40/10/007.

[166] T. Fülöp and P. Helander, "Nonlinear neoclassical transport in a rotating impure plasma with large gradients," *Physics of Plasmas*, vol. 6, no. 8, pp. 3066–3075, Aug. 1, 1999, ISSN: 1070-664X. DOI: 10.1063/1.873593. [Online]. Available: https://doi.org/10.1063/1.873593 (visited on 07/09/2023).

[167] T. Fülöp and P. Helander, "Nonlinear neoclassical transport in toroidal edge plasmas," *Physics of Plasmas*, vol. 8, no. 7, pp. 3305–3313, Jul. 1, 2001, ISSN: 1070-664X. DOI: 10.1063/1.1372179. [Online]. Available: https://doi.org/10.1063/1.1372179 (visited on 07/11/2023).

[168] M. Landreman, T. Fülöp, and D. Guszejnov, "Impurity flows and plateau-regime poloidal density variation in a tokamak pedestal," *Physics of Plasmas*, vol. 18, no. 9, p. 092 507, Sep. 20, 2011, ISSN: 1070-664X. DOI: 10.1063/1.3631819. [Online]. Available: https://doi.org/10.1063/1.3631819 (visited on 07/11/2023).

[169] C. Angioni and P. Helander, "Neoclassical transport of heavy impurities with poloidally asymmetric density distribution in tokamaks," *Plasma Physics and Controlled Fusion*, vol. 56, no. 12, p. 124 001, Nov. 7, 2014, ISSN: 0741-3335. DOI: 10.1088/0741-3335/56/12/124001. [Online]. Available: https://dx.doi.org/10.1088/0741-3335/56/12/124001.

[170] J. Rice, M. Reinke, C. Gao, *et al.*, "Core impurity transport in alcator c-mod l-, i- and h-mode plasmas," *Nuclear Fusion*, vol. 55, no. 3, p. 033 014, Feb. 20, 2015, ISSN: 0029-5515. DOI: 10.1088/0029-5515/55/3/033014. [Online]. Available: https://dx.doi.org/10.1088/0029-5515/55/3/033014.

[171] T. Pütterich, R. Dux, M. Janzer, and R. McDermott, "ELM flushing and impurity transport in the h-mode edge barrier in ASDEX upgrade," *Proceedings of the 19th International Conference on Plasma-Surface Interactions in Controlled Fusion*, vol. 415, no. 1, S334–S339, Aug. 1, 2011, ISSN: 0022-3115. DOI: 10.1016/j.jnucmat.2010.09.052. [Online]. Available: https://www.sciencedirect.com/science/article/pii/S0022311510005623.

[172] F. L. Hinton and R. D. Hazeltine, "Theory of plasma transport in toroidal confinement systems," *Reviews of Modern Physics*, vol. 48, no. 2, pp. 239–308, Apr. 1, 1976. DOI: 10.1103/RevModPhys.48.239. [Online]. Available: https://link.aps.org/doi/10.1103/RevModPhys.48.239.

[173] R. M. McDermott, B. Lipschultz, J. W. Hughes, *et al.*, "Edge radial electric field structure and its connections to h-mode confinement in alcator c-mod plasmasa)," *Physics of Plasmas*, vol. 16, no. 5, p. 056 103, Mar. 12, 2009, ISSN: 1070-664X. DOI: 10.1063/1.3080721. [Online]. Available: https://doi.org/10.1063/1.3080721 (visited on 07/10/2023).

[174] E. Viezzer, T. Pütterich, G. Conway, *et al.*, "High-accuracy characterization of the edge radial electric field at ASDEX upgrade," *Nuclear Fusion*, vol. 53, no. 5, p. 053 005, Apr. 19, 2013, ISSN: 0029-5515. DOI: 10.1088/0029-5515/53/5/053005. [Online]. Available: https://dx.doi.org/10.1088/0029-5515/53/5/053005.

[175] E. Viezzer, T. Pütterich, E. Fable, A. Bergmann, R. Dux, R. M. McDermott, R. M. Churchill, M. G. Dunne, and the ASDEX Upgrade Team, "Rotation and density asymmetries in the presence of large poloidal impurity flows in the edge pedestal," *Plasma Physics and Controlled Fusion*, vol. 55, no. 12, p. 124 037, Nov. 28, 2013, ISSN: 0741-3335. DOI: 10.1088/0741-3335/55/12/124037. [Online]. Available: https://dx.doi.org/10.1088/0741-3335/55/12/124037.

[176] R. Churchill, B. Lipschultz, C. Theiler, and the Alcator C-Mod Team, "In–out impurity density asymmetry in the pedestal region of alcator c-mod," *Nuclear Fusion*, vol. 53, no. 12, p. 122 002, Nov. 13, 2013, ISSN: 0029-5515. DOI:

10.1088/0029-5515/53/12/122002. [Online]. Available: https://dx.doi.org/10.1088/0029-5515/53/12/122002.

[177] R. M. Churchill, C. Theiler, B. Lipschultz, *et al.*, "Poloidal asymmetries in edge transport barriersa)," *Physics of Plasmas*, vol. 22, no. 5, p. 056 104, Apr. 24, 2015, ISSN: 1070-664X. DOI: 10.1063/1.4918353. [Online]. Available: https://doi.org/10.1063/1.4918353 (visited on 07/11/2023).

[178] S. Espinosa and P. Catto, "Radial impurity flux measuring method with plasma heating in general geometry," *Plasma Physics and Controlled Fusion*, vol. 59, no. 10, p. 105 001, Aug. 2, 2017, ISSN: 0741-3335. DOI: 10.1088/1361-6587/aa7ad2. [Online]. Available: https://dx.doi.org/10.1088/1361-6587/aa7ad2.

[179] S. Espinosa and P. Catto, "Pedestal radial flux measuring method to prevent impurity accumulation," *Physics of Plasmas*, vol. 24, no. 5, p. 055 904, Mar. 23, 2017, ISSN: 1070-664X. DOI: 10.1063/1.4978886. [Online]. Available: https://doi.org/10.1063/1.4978886 (visited on 07/11/2023).

[180] S. Trinczek, F. I. Parra, P. J. Catto, I. Calvo, and M. Landreman, "Neoclassical transport in strong gradient regions of large aspect ratio tokamaks," *Journal of Plasma Physics*, vol. 89, no. 3, p. 905 890 304, 2023, ISSN: 0022-3778. DOI: 10.1017/S0022377823000430. [Online]. Available: https://www.cambridge.org/core/article/neoclassical-transport-in-strong-gradient-regions-of-large-aspect-ratio-tokamaks/5EB1AB70D362590114F0D128A721B0DB.

[181] D. Cruz-Zabala, E. Viezzer, U. Plank, *et al.*, "In-out charge exchange measurements and 3d modelling of diagnostic thermal neutrals to study edge poloidal impurity asymmetries," *Plasma Physics and Controlled Fusion*, vol. 64, no. 4, p. 045 021, Mar. 9, 2022, ISSN: 0741-3335. DOI: 10.1088/1361-6587/ac5917. [Online]. Available: https://dx.doi.org/10.1088/1361-6587/ac5917.

[182] K. D. Marr, B. Lipschultz, P. J. Catto, R. M. McDermott, M. L. Reinke, and A. N. Simakov, "Comparison of neoclassical predictions with measured flows and evaluation of a poloidal impurity density asymmetry," *Plasma Physics and Controlled Fusion*, vol. 52, no. 5, p. 055 010, Apr. 9, 2010, ISSN: 0741-3335. DOI: 10.1088/0741-3335/52/5/055010. [Online]. Available: https://dx.doi.org/10.1088/0741-3335/52/5/055010.

[183] T. Pütterich, E. Viezzer, R. Dux, R. McDermott, and the ASDEX Upgrade Team, "Poloidal asymmetry of parallel rotation measured in ASDEX upgrade," *Nuclear Fusion*, vol. 52, no. 8, p. 083 013, Jul. 11, 2012, ISSN: 0029-5515. DOI: 10.1088/0029-5515/52/8/083013. [Online]. Available: https://dx.doi.org/10.1088/0029-5515/52/8/083013.

[184] P. Maget, J. Frank, T. Nicolas, O. Agullo, X. Garbet, and H. Lütjens, "Natural poloidal asymmetry and neoclassical transport of impurities in tokamak plasmas," *Plasma Physics and Controlled Fusion*, vol. 62, no. 2, p. 025 001, Nov. 20, 2019, ISSN: 0741-3335. DOI: 10.1088/1361-6587/ab53ab. [Online]. Available: https://dx.doi.org/10.1088/1361-6587/ab53ab.

[185] P. Maget, P. Manas, J. Frank, T. Nicolas, O. Agullo, and X. Garbet, "An analytic model for the collisional transport and poloidal asymmetry distribution of impurities in tokamak plasmas," *Plasma Physics and Controlled Fusion*, vol. 62, no. 10, p. 105 001, Aug. 14, 2020, ISSN: 0741-3335. DOI: 10.1088/1361-6587/aba7f9. [Online]. Available: https://dx.doi.org/10.1088/1361-6587/aba7f9.

[186] I. Pusztai and P. J. Catto, "Neoclassical plateau regime transport in a tokamak pedestal," *Plasma Physics and Controlled Fusion*, vol. 52, no. 7, p. 075 016, Jun. 17, 2010, ISSN: 0741-3335. DOI: 10.1088/0741-3335/52/7/075016. [Online]. Available: https://dx.doi.org/10.1088/0741-3335/52/7/075016.

[187] S. Espinosa and P. Catto, "Non-linear neoclassical model for poloidal asymmetries in tokamak pedestals: Diamagnetic and radial effects included," 2019.

[188] M. R. Wade, W. A. Houlberg, and L. R. Baylor, "Experimental confirmation of impurity convection driven by the ion-temperature gradient in toroidal plasmas," *Physical Review Letters*, vol. 84, no. 2, pp. 282–285, Jan. 10, 2000. DOI: 10.1103/PhysRevLett.84.282. [Online]. Available: https://link.aps.org/doi/10.1103/PhysRevLett.84.282.

[189] E. Viezzer, E. Fable, M. Cavedon, *et al.*, "Investigation of inter-ELM ion heat transport in the h-mode pedestal of ASDEX upgrade plasmas," *Nuclear Fusion*, vol. 57, no. 2, p. 022 020, Oct. 4, 2016, ISSN: 0029-5515. DOI: 10.1088/0029-5515/57/2/022020. [Online]. Available: https://dx.doi.org/10.1088/0029-5515/57/2/022020.

[190] E. Viezzer, M. Cavedon, E. Fable, *et al.*, "Ion heat transport dynamics during edge localized mode cycles at ASDEX upgrade," *Nuclear Fusion*, vol. 58, no. 2, p. 026 031, Jan. 9, 2018, ISSN: 0029-5515. DOI: 10.1088/1741-4326/aaa22f. [Online]. Available: https://dx.doi.org/10.1088/1741-4326/aaa22f.

[191] J. L. Terry, E. S. Marmar, K. I. Chen, and H. W. Moos, "Observation of poloidal asymmetry in impurity-ion emission due to grad-b drifts," *Physical Review Letters*, vol. 39, no. 25, pp. 1615–1618, Dec. 19, 1977. DOI: 10.1103/PhysRevLett.39.1615. [Online]. Available: https://link.aps.org/doi/10.1103/PhysRevLett.39.1615.

[192] K. Brau, S. Suckewer, and S. Wong, "Vertical poloidal asymmetries of low-z element radiation in the PDX tokamak," *Nuclear Fusion*, vol. 23, no. 12, p. 1657, Dec. 1, 1983, ISSN: 0029-5515. DOI: 10.1088/0029-5515/23/12/009. [Online]. Available: https://dx.doi.org/10.1088/0029-5515/23/12/009.

[193] R.D. Durst, "Vertical asymmetries in soft x-ray emissivity in COMPASS-c," *Nuclear Fusion*, vol. 32, no. 12, p. 2238, Dec. 1, 1992, ISSN: 0029-5515. DOI: 10.1088/0029-5515/32/12/I13. [Online]. Available: https://dx.doi.org/10.1088/0029-5515/32/12/I13.

[194] J. Rice, J. Terry, E. Marmar, and F. Bombarda, "X-ray observations of up-down impurity density asymmetries in alcator c-mod plasmas," *Nuclear Fusion*, vol. 37, no. 2, p. 241, Feb. 1, 1997, ISSN: 0029-5515. DOI: 10.1088/0029-5515/37/2/I09. [Online]. Available: https://dx.doi.org/10.1088/0029-5515/37/2/I09.

[195] M. Greenwald, R. Boivin, P. Bonoli, *et al.*, "Characterization of enhanced d high-confinement modes in alcator c-mod," *Physics of Plasmas*, vol. 6, no. 5, pp. 1943–1949, May 1, 1999, ISSN: 1070-664X. DOI: 10.1063/1.873451. [Online]. Available: https://doi.org/10.1063/1.873451 (visited on 07/17/2023).

[196] A. E. Hubbard, R. L. Boivin, R. S. Granetz, *et al.*, "Pedestal profiles and fluctuations in c-mod enhanced d-alpha h-modes," *Physics of Plasmas*, vol. 8, no. 5, pp. 2033–2040, May 1, 2001, ISSN: 1070-664X. DOI: 10.1063/1.1348329. [Online]. Available: https://doi.org/10.1063/1.1348329 (visited on 07/17/2023).

[197] Snipes, B. LaBombard, M. Greenwald, I. Hutchinson, J. Irby, Y. Lin, A. Mazurenko, and M. Porkolab, "The quasi-coherent signature of enhanced d h-mode in alcator c-mod," *Plasma Physics and Controlled Fusion*, vol. 43, no. 4, p. L23, Apr. 1, 2001, ISSN: 0741-3335. DOI: 10.1088/0741-3335/43/4/101. [Online]. Available: https://dx.doi.org/10.1088/0741-3335/43/4/101.

[198] B. LaBombard, T. Golfinopoulos, J. L. Terry, D. Brunner, E. Davis, M. Greenwald, J. W. Hughes, and Alcator C-Mod Team, "New insights on boundary plasma turbulence and the quasi-coherent mode in alcator c-mod using a mirror langmuir probea)," *Physics of Plasmas*, vol. 21, no. 5, p. 056 108, May 5, 2014, ISSN: 1070-664X. DOI: 10.1063/1.4873918. [Online]. Available: https://doi.org/10.1063/1.4873918 (visited on 07/17/2023).

[199] B. Vanovac, J. Stober, E. Wolfrum, *et al.*, "Electron temperature fluctuation levels of the quasi-coherent mode across the plasma radius," *EPJ Web Conf.*, vol. 277, 2023. DOI: 10.1051/epjconf/202327703003. [Online]. Available: https://doi.org/10.1051/epjconf/202327703003.

[200] C. M. Greenfield, K. H. Burrell, J. C. DeBoo, *et al.*, "Quiescent double barrier regime in the DIII-d tokamak," *Physical Review Letters*, vol. 86, no. 20, pp. 4544–4547, May 14, 2001. DOI: 10.1103/PhysRevLett.86.4544. [Online]. Available: https://link.aps.org/doi/10.1103/PhysRevLett.86.4544.

[201] K. H. Burrell, W. P. West, E. J. Doyle, *et al.*, "Advances in understanding quiescent h-mode plasmas in DIII-da)," *Physics of Plasmas*, vol. 12, no. 5, p. 056 121, Apr. 28, 2005, ISSN: 1070-664X. DOI: 10.1063/1.1894745. [Online]. Available: https://doi.org/10.1063/1.1894745 (visited on 07/18/2023).

[202] W. Suttrop, G. Conway, L. Fattorini, *et al.*, "Study of quiescent h-mode plasmas in ASDEX upgrade," *Plasma Physics and Controlled Fusion*, vol. 46, no. 5, A151, Apr. 21, 2004, ISSN: 0741-3335. DOI: 10.1088/0741-3335/46/5A/016. [Online]. Available: https://dx.doi.org/10.1088/0741-3335/46/5A/016.

[203] N. Oyama, Y. Sakamoto, A. Isayama, *et al.*, "Energy loss for grassy ELMs and effects of plasma rotation on the ELM characteristics in JT-60u," *Nuclear Fusion*, vol. 45, no. 8, p. 871, Jul. 28, 2005, ISSN: 0029-5515. DOI: 10.1088/0029-5515/45/8/014. [Online]. Available: https://dx.doi.org/10.1088/0029-5515/45/8/014.

[204] K. Burrell, T. Osborne, P. Snyder, W. West, M. Fenstermacher, R. J. Groebner, P. Gohil, A. Leonard, and W. Solomon, "Quiescent h-mode plasmas with strong edge rotation in the cocurrent direction," *Physical Review Letters*, vol. 102, no. 15, p. 155 003, Apr. 17, 2009. DOI: 10.1103/PhysRevLett.102.155003. [Online]. Available: https://link.aps.org/doi/10.1103/PhysRevLett.102.155003.

[205] K. Burrell, M. Austin, D. Brennan, *et al.*, "Quiescent h-mode plasmas in the DIII-d tokamak," *Plasma Physics and Controlled Fusion*, vol. 44, no. 5, A253, Apr. 29, 2002, ISSN: 0741-3335. DOI: 10.1088/0741-3335/44/5A/325. [Online]. Available: https://dx.doi.org/10.1088/0741-3335/44/5A/325.

[206] W. Suttrop, M. Maraschek, G. Conway, *et al.*, "ELM-free stationary h-mode plasmas in the ASDEX upgrade tokamak," *Plasma Physics and Controlled Fusion*, vol. 45, no. 8, p. 1399, Jun. 30, 2003, ISSN: 0741-3335. DOI: 10.1088/0741-3335/45/8/302. [Online]. Available: https://dx.doi.org/10.1088/0741-3335/45/8/302.

[207] E. Viezzer, "Access and sustainment of naturally ELM-free and small-ELM regimes," *Nuclear Fusion*, vol. 58, no. 11, p. 115 002, Sep. 27, 2018, ISSN: 0029-5515. DOI: 10.1088/1741-4326/aac222. [Online]. Available: https://dx.doi.org/10.1088/1741-4326/aac222.

[208] T. Happel, T. Pütterich, D. Told, M. Dunne, R. Fischer, J. Hobirk, R. McDermott, U. Plank, and A. U. T. the, "Overview of initial negative triangularity plasma studies on the ASDEX upgrade tokamak," *Nuclear Fusion*, vol. 63, no. 1, p. 016 002, Nov. 24, 2022, ISSN: 0029-5515. DOI: 10.1088/1741-4326/ac8563. [Online]. Available: https://dx.doi.org/10.1088/1741-4326/ac8563.

[209] B. Vanovac, "Pedestal properties of negative triangularity plasma with favorable/unfavorable grad b drift direction in ASDEX upgrade," Poster, Poster, 49th European Physical Society Plasma Physics Division, Bordeaux, France, 2023.

[210] P. Rodriguez-Fernandez, N. Howard, and J. Candy, "Nonlinear gyrokinetic predictions of SPARC burning plasma profiles enabled by surrogate modeling," *Nuclear Fusion*, vol. 62, no. 7, p. 076 036, May 13, 2022, ISSN: 0029-5515. DOI: 10.1088/1741-4326/ac64b2. [Online]. Available: https://dx.doi.org/10.1088/1741-4326/ac64b2.